

3-D NUMERICAL SIMULATIONS OF FLUID FLOW AND HEAT TRANSFER  
IN VARIOUS MICRO CONDUITS

A THESIS SUBMITTED TO  
THE GRADUATE SCHOOL OF NATURAL AND APPLIED SCIENCES  
OF  
MIDDLE EAST TECHNICAL UNIVERSITY

BY

METİN BİLGEHAN TURGAY

IN PARTIAL FULFILLMENT OF THE REQUIREMENTS  
FOR  
THE DEGREE OF DOCTOR OF PHILOSOPHY  
IN  
MECHANICAL ENGINEERING

SEPTEMBER 2017



Approval of the thesis:

**3-D NUMERICAL SIMULATIONS OF FLUID FLOW AND HEAT  
TRANSFER IN VARIOUS MICRO CONDUITS**

submitted by **METİN BİLGEHAN TURGAY** in partial fulfillment of the requirements for the degree of **Doctor of Philosophy in Mechanical Engineering Department, Middle East Technical University** by,

Prof. Dr. Gülbin Dural Ünver  
Dean, Graduate School of **Natural and Applied Sciences**

\_\_\_\_\_

Prof. Dr. Tuna Balkan  
Head of Department, **Mechanical Engineering**

\_\_\_\_\_

Assoc. Prof. Dr. Almıla Güvenç Yazıcıoğlu  
Supervisor, **Mechanical Engineering Dept., METU**

\_\_\_\_\_

**Examining Committee Members:**

Assoc. Prof. Dr. M. Metin Yavuz  
Mechanical Engineering Dept., METU

\_\_\_\_\_

Assoc. Prof. Dr. Almıla Güvenç Yazıcıoğlu  
Mechanical Engineering Dept., METU

\_\_\_\_\_

Prof. Dr. Murat Köksal  
Mechanical Engineering Dept., Hacettepe University

\_\_\_\_\_

Assoc. Prof. Dr. Murat K. Aktaş  
Mechanical Engineering Dept.,  
TOBB University of Economics and Technology

\_\_\_\_\_

Asst. Prof. Dr. Feyza Kazanç  
Mechanical Engineering Dept., METU

\_\_\_\_\_

**Date:** 08.09.2017

**I hereby declare that all information in this document has been obtained and presented in accordance with academic rules and ethical conduct. I also declare that, as required by these rules and conduct, I have fully cited and referenced all material and results that are not original to this work.**

Name, Last Name: Metin Bilgehan TURGAY

Signature:

## ABSTRACT

### **3-D NUMERICAL SIMULATIONS OF FLUID FLOW AND HEAT TRANSFER IN VARIOUS MICRO CONDUITS**

Turgay, Metin Bilgehan

Ph.D., Department of Mechanical Engineering

Supervisor: Assoc. Prof. Dr. Almıla Güvenç Yazıcıoğlu

September 2017, 232 pages

In this work, it is aimed to investigate the effect of roughness geometrical properties and configurations on laminar flow and heat transfer characteristics in microchannels, numerically. For this purpose, two-dimensional parallel plate, and three-dimensional trapezoidal microchannels with different roughness properties are modeled along with the smooth ones. Fluid flow and heat transfer simulations are conducted with COMSOL Multiphysics. Roughness is modeled as triangular obstructions on one of the plates in two-dimensions, and conical obstructions in three-dimensions on the base of the trapezoidal channel, to mimic the natural roughness in silicon microchannels and microstructures on lotus leaves. Numerically obtained results, for smooth and rough channels, are compared with each other, and with the results that exist in the literature. It is found that, both in 2D and 3D tested geometries, local Nusselt number increases through the tip of the roughness elements due to increased velocity of the subjected flow. However, near the base of the roughness elements and between them, reduction in local Nusselt number is observed due to reduced velocity fields reduced convective heat flux in the fluid, and increased thermal conductivity of the fluid through the exit of the

channels. Frictional characteristics of the tested rough geometries showed nonlinear behavior with the complexity of the surface parameters. It is shown that widely used relative roughness height concept is not enough to define the roughness effect in microchannels. Additionally, effects of stabilization methods, element discretization order, and relative tolerance level on the results of microfluidic simulations with COMSOL are investigated.

Keywords: microchannel, flow, heat transfer, surface roughness, numerical simulation.

## ÖZ

### ÇEŞİTLİ MİKROKANALLARDAKİ AKIŞKAN AKIŞI VE ISI TRANSFERİNİN 3 BOYUTLU SAYISAL SİMÜLASYONU

Turgay, Metin Bilgehan

Doktora, Makine Mühendisliği Bölümü

Tez Yöneticisi: Doç. Dr. Almila Güvenç Yazıcıoğlu

Eylül 2017, 232 sayfa

Bu çalışmada, mikrokanallarda bulunan farklı konfigürasyonlardaki ve geometrik özelliklerdeki yüzey pürüzlülüğünün laminar akışa ve ısı transferine etkisinin sayısal olarak incelenmesi amaçlanmıştır. Bunun için düz yüzeyli kanallarla birlikte, farklı yüzey pürüzlülük özelliklerine sahip, iki boyutlu paralel plakalardan oluşan ve üç boyutlu eşkenar yamuk kesitli kanallar oluşturulmuştur. Akış ve ısı transferi simülasyonları COMSOL Multiphysics programı ile yapılmıştır. Yüzey pürüzlülüğü, iki boyutlu kanallarda, bir plakaya yerleştirilen üçgen şekilli çıkıntılar ile modellenirken, üç boyutlu kanallarda, silikon kanallarda oluşan doğal pürüzleri ve lotus yapraklarındaki mikro yapıları taklit edebilmek için, konik çıkıntılar ile modellenmiştir. Düz ve pürüzlü kanallar için sayısal olarak elde edilen sonuçlar hem birbirleriyle, hem de literatürde varolan sonuçlar ile karşılaştırılmıştır. Hem iki hem de üç boyutlu kanallarda, pürüzlerin uç noktalara doğru, çevresel akış hızının artmasına bağlı olarak, yerel Nusselt sayılarında artış gözlemlenmiştir. Fakat, pürüzlerin taban kısımlarında ve pürüz elemanlarının arasında, konveksiyonla ısı transferini azaltan düşük hız bölgelerinin oluşması ve akışkan termal iletkenliğinin

kanal çıkışına doğru artması nedeniyle yerel Nusselt sayısının azaldığı görülmüştür. Pürüzlü geometrilerdeki sürtünme karakteristikleri ise, oluşturulan yüzeylerin karmaşıklık seviyesiyle doğrusal olmayan bir davranış sergilemiştir. Pürüzlü geometrilerdeki akış analizlerde yaygın olarak kullanılan relatif yüzey pürüzlülüğü konseptinin, mikrokanallardaki pürüzlülüğün etkisini tanımlamak için yeterli olmadığı gösterilmiştir. Ayrıca, COMSOL Multiphysics programında kullanılan sayısal stabilizasyon metodlarının, ağ yapısında kullanılan elemanların seviyesinin ve bağıl hata seviyesinin mikroakışkan simülasyonlarından elde edilen sonuçlara etkisi de incelenmiştir.

Anahtar Kelimeler: mikrokanallar, akış, ısı transferi, yüzey pürüzlülüğü, sayısal simülasyon.

*LLAP*

## ACKNOWLEDGEMENTS

First of all, I would like to thank to my supervisor, Assoc. Prof. Dr. Almıla G. YAZICIOĞLU, for her guidance, patience, trust and encouragement.

I also would like to thank to Assoc. Prof. Dr. Murat K. AKTAŞ and Assoc. Prof. Dr. M. Metin YAVUZ for their valuable contributions during this work, Mr. Mustafa YALÇIN for his support.

Finally, greatest appreciation is for my family members, my friends, ARIK and YURTÖREN families, and most importantly for my Zeynep. Life would be unbearable without her.

This study was supported by BAP-03-02-2011-003.

## TABLE OF CONTENTS

ABSTRACT.....	v
ÖZ.....	vii
ACKNOWLEDGEMENTS.....	x
TABLE OF CONTENTS.....	xi
LIST OF TABLES.....	xiv
LIST OF FIGURES.....	xvi
NOMENCLATURE.....	xxvii
CHAPTERS	
1. INTRODUCTION.....	1
2. LITERATURE REVIEW.....	7
2.1 Experimental and Numerical Studies in Trapezoidal Microchannels.....	9
2.2 Studies in Rough Microchannels.....	23
2.3 Studies Conducted with COMSOL Multiphysics.....	46
2.4 Summary of Literature Review and Objectives.....	54
3. GOVERNING EQUATIONS.....	57
4. 2D FLOW AND HEAT TRANSFER SIMULATIONS BETWEEN PARALLEL PLATES.....	63
5. 3D FLOW SIMULATIONS IN TRAPEZOIDAL CHANNELS.....	79

5.1	Flow Simulations in Macroscale Smooth Channels.....	79
5.2	Flow Simulations in Microscale Smooth Channels.....	83
5.3	Flow Simulations in Microscale Rough Channels.....	85
5.4	Discussions.....	90
6.	3D FLOW AND HEAT TRANSFER SIMULATIONS IN TRAPEZOIDAL MICROCHANNELS.....	93
6.1	Reference Problem Definition.....	93
6.2	Smooth Microchannel Simulations.....	97
6.2.1	Mesh Independence Studies.....	97
6.2.2	Results and Discussions.....	103
6.3	Rough Microchannel Simulations with <i>1LineCone</i> ( <i>R1LC</i> ) Configuration.....	108
6.3.1	Mesh Independence Studies.....	108
6.3.2	Results and Discussions.....	116
6.4	Rough Microchannel Simulations with <i>2LineCone</i> ( <i>R2LC</i> ) Configuration.....	134
6.4.1	Mesh Independence Studies.....	134
6.4.2	Results and Discussions.....	142
6.5	Rough Microchannel Simulations with RDC Configuration.....	159
6.5.1	Mesh Independence Studies.....	159
6.5.2	Results and Discussions.....	167
6.6	Comparisons of Smooth and Rough Channels.....	186

7. SUMMARY, CONCLUSIONS AND SUGGESTIONS FOR FUTURE WORK.....	191
REFERENCES.....	197
APPENDICES	
A. NOTES ON BOUNDARY LAYER MESH.....	211
A.1 Tests in 2D Geometry.....	211
A.2 Tests in 3D Geometry.....	215
A.3 Conclusion.....	219
B. NUMERICAL CONSIDERATIONS IN COMSOL MULTIPHYSICS.....	221
B.1 Memory Reduction Studies.....	221
B.2 Effect of Stabilization Methods.....	223
B.3 Effect of Element Discretization.....	226
B.4 Effect of Relative Tolerance.....	228
CURRICULUM VITAE.....	231

## LIST OF TABLES

Table 4.1	Test cases for 2D water flow simulations.....	65
Table 4.2	Properties of mesh used in the mesh independence studies of <i>Geometry (b) Case-04</i> .....	66
Table 4.3	Properties of selected meshes for each 2D rough geometry....	70
Table 4.4	Percent differences in temperature and pressure compared to the smooth channel between $x = 200 \mu\text{m}$ and $x = 600 \mu\text{m}$ locations.....	74
Table 5.1	Geometrical properties of the smooth macro trapezoidal channels used in simulations.....	80
Table 5.2	Accepted mesh element numbers for each case with corresponding $Po$ values and percentage differences from analytical values.....	82
Table 5.3	Geometrical properties of smooth microchannels used in simulations.....	84
Table 5.4	Accepted mesh element numbers for each case with corresponding $Po$ values.....	84
Table 5.5	Accepted mesh element numbers for each micro case with corresponding $Po$ values.....	90
Table 5.6	Comparison of calculated $Po$ values for macro and microscale smooth channels.....	91
Table 5.7	Comparison of calculated $Po$ values for microscale smooth and rough channels.....	92
Table 6.1	Cone heights ( $h$ ), base radiuses ( $r$ ), and total number of cones used in each geometry.....	97
Table 6.2	Summary of mesh properties and calculated values used in mesh independence tests of smooth channel simulations ( $S$ : Solver, $I$ : Iterative, $D$ : Direct, $PM$ : Physical Memory, $VM$ : Virtual Memory, $HS$ : Heated Surface).....	99

Table 6.3	Summary of mesh properties and calculated values used in mesh independence tests of <i>1LineCone</i> configuration ( <i>PM</i> : Physical Memory, <i>VM</i> : Virtual Memory, <i>HS</i> : Heated Surface).....	109
Table 6.4	Summary of mesh properties and calculated values used in mesh independence tests of <i>2LineCone</i> configuration ( <i>PM</i> : Physical Memory, <i>VM</i> : Virtual Memory, <i>HS</i> : Heated Surface).....	135
Table 6.5	Summary of mesh properties and calculated values used in mesh independence tests of <i>DaisyCone</i> configuration ( <i>PM</i> : Physical Memory, <i>VM</i> : Virtual Memory, <i>HS</i> : Heated Surface).....	160
Table 6.6	Mean <i>Re</i> , <i>f</i> , and <i>Po</i> values with temperature and pressure difference between the inlet and exit of the heated section for each geometry.....	190
Table A.1	Coordinates of the data extraction lines.....	213
Table A.2	Properties of constructed meshes and solution times.....	213
Table A.3	Percentage differences of mean velocities calculated along the lines around <i>R1</i> and <i>R3</i> for meshes 7, 8, 9, 11, and 12.....	215
Table A.4	Coordinates of the data extraction lines (all in $\mu\text{m}$ ).....	217
Table A.5	Properties of the used meshes and solution times.....	217
Table B.1	Memory usage and CPU times of two test cases with and without row reordering option.....	222
Table B.2	Some of the checked parameters for <i>Mesh-2</i> of row reordering test ( <i>mh</i> : microheater).....	222
Table B.3	<i>Po</i> values, average, and maximum heater surface temperatures for stabilization method test cases.....	224
Table B.4	Mesh properties and parameters for discretization comparison.....	226
Table B.5	Used cases for the relative tolerance tests and obtained results for $300 \text{ kW/m}^2$ effective heat flux and $1016 \text{ kg/(m}^2\text{s)}$ inlet mass flux.....	229

## LIST OF FIGURES

Figure 1.1	(a) Silicon trapezoidal microchannel produced by wet etching [6], and (b) glassy carbon microchannel produced by reactive ion etching [7].....	3
Figure 2.1	Schematic of the rough microchannel and roughness elements used in [62].....	27
Figure 2.2	Representative channel geometries used in [63].....	27
Figure 2.3	Representative channel geometries used in [69] (A) ridge-shaped grooves, (B) V-shaped grooves, (C) shield-shaped grooves, (D) straight slot grooves, and (E) smooth surface..	32
Figure 2.4	Bionic surface geometries considered in [70] (a) placoid-shaped grooves, (b) V-shaped grooves, (c) riblet-shaped grooves, and (d) ridge-shaped grooves.....	33
Figure 2.5	Schematics of the corrugated channel used in [72].....	35
Figure 2.6	Image of the micro pin fins used in [73].....	35
Figure 2.7	Schematic view of the channel with micro cylinders (left), and SEM image of a silicon micro cylinder array [74].....	37
Figure 2.8	Schematic views of the channels considered in [76].....	38
Figure 2.9	Schematics of simulated channels in [77], regular rectangular (left), with offset fan-shaped reentrant cavities (middle), and with triangular reentrant cavities (right).....	39
Figure 2.10	Schematics of channels used in [78] ( <i>Rec</i> : Rectangular, <i>Tri</i> : Triangular, <i>Fan</i> : Fan shaped, <i>Tra</i> : Trapezoidal, <i>Dia</i> : Diamond, <i>C</i> : Cavity, <i>F</i> : Fin, <i>CR</i> : Conventional Rectangular).....	41
Figure 2.11	SEM images of PMMA surfaces at the bottom of microchannels formed by means of etching in O <sub>2</sub> plasma prior to (left) and after (right) immersion in water and drying [80].....	42

Figure 2.12	Image of denticles from the surface of the mid-body region in a bonnethead shark (Scale bar = 50 $\mu m$ ) [81].....	43
Figure 2.13	Images of the biomimetic riblet silicone material (Scale bars = 200 $\mu m$ ). (A) Front side. (B) Cross-section view, $h = 87 \mu m$ , $s = 340 \mu m$ [81].....	43
Figure 2.14	Images of Speedo shark skin-like swimsuit fabric (Fastskin FS II) (Scale bars = 500 $\mu m$ ). (A) Underside surface image (non-biomimetic), (B) Outside surface image (biomimetic), (C) Cross-section image showing the dents on the biomimetic side (red arrows) [81].....	44
Figure 2.15	Images of a lotus leaf showing micro and nano structures [82].....	45
Figure 2.16	Piranha Pin Fin (PPF) array used in [91].....	49
Figure 2.17	Wall thickening patterns used in the simulations of [96].....	50
Figure 3.1	Schematics of 2D parallel plate microchannel and boundary conditions.....	58
Figure 3.2	Representative schematic for channels having trapezoidal cross-section.....	60
Figure 4.1	Schematics of the rough parallel-plate channels and geometrical properties of roughness elements [106].....	64
Figure 4.2	Selected cell $Re$ plots for mesh independence studies of <i>Geometry (b) Case-04</i> (with 1.325% relative roughness).....	67
Figure 4.3	Selected cell $Pe$ plots for mesh independence studies of <i>Geometry (b) Case-04</i> (with 1.325% relative roughness).....	68
Figure 4.4	Local $Nu$ distribution at the inlet of the channel and at the middle of the rough section for <i>Case-04</i> of <i>Geometry (b)</i> and $Re = 100$ .....	69
Figure 4.5	Distribution of chosen meshes around the first two roughness elements of 2D parallel plate channels.....	71
Figure 4.6	Streamlines around the middle roughness elements for <i>Case-03</i> of 2D rough channel geometries for $Re = 100$ .....	72
Figure 4.7	Velocity contour plots around the middle roughness elements for <i>Case-03</i> of 2D smooth and rough channel geometries for $Re = 100$ .....	73
Figure 4.8	Local $Nu$ distribution along the 2D <i>Geometry (a) (smooth)</i> and close-up view of entrance section.....	76

Figure 4.9	Local $Nu$ distribution along the 2D <i>Geometry (b)</i> ( $\varepsilon = 1.325\%$ ) and close-up view between the two consecutive roughness elements.....	76
Figure 4.10	Local $Nu$ distribution along the 2D <i>Geometry (c)</i> ( $\varepsilon = 2.00\%$ ) and close-up view between the two consecutive roughness elements.....	77
Figure 4.11	Local $Nu$ distribution along the 2D <i>Geometry (d)</i> ( $\varepsilon = 2.65\%$ ) and close-up view between the two consecutive roughness elements.....	78
Figure 5.1	Schematics of the cross-sections of trapezoidal channel used in macroscale flow simulations.....	81
Figure 5.2	(a) Change of $Po$ values with respect to element number for mesh independence runs of <i>Macro_G01</i> case, (b) Solution time and memory usage with respect to element numbers.....	82
Figure 5.3	Schematics of the side view of microchannel geometry along the flow direction used in smooth microscale flow simulations.....	84
Figure 5.4	Change in $Po$ with respect to mesh element number for <i>Micro_G03</i> and <i>Micro_G04</i> cases.....	85
Figure 5.5	Model of <i>Micro_G06 (1LineCone)</i> case and geometrical properties of its roughness elements.....	86
Figure 5.6	Model of <i>Micro_G07 (2LineCone)</i> case and geometrical properties of its roughness elements.....	87
Figure 5.7	Model of <i>Micro_G08 (DaisyCone)</i> case and geometrical properties of its roughness elements.....	88
Figure 5.8	Calculated $Po$ values with respect to mesh element numbers for mesh independence studies of micro smooth and rough geometries.....	89
Figure 6.1	Schematic of trapezoidal microchannel and placement of heated section in the reference work [26].....	95
Figure 6.2	Wall mean temperatures over the microheaters for the mesh independence tests cases (a) Cases with predefined meshes, (b) Cases with manually adjusted meshes ( $q_{eff} = 300 \text{ kW/m}^2$ , $G = 1016 \text{ kg/(m}^2\text{s)}$ ).....	101
Figure 6.3	Local Nusselt numbers over the microheaters for the mesh independence test cases (a) Cases with predefined meshes, (b) Cases with manually adjusted meshes ( $q_{eff} = 300 \text{ kW/m}^2$ , $G = 1016 \text{ kg/(m}^2\text{s)}$ ).....	102

Figure 6.4	Wall temperatures over the first two microheaters (at $z = 6000 \mu\text{m}$ and $z = 8000 \mu\text{m}$ ) along $x$ -direction for various inlet mass fluxes.....	104
Figure 6.5	Wall temperatures over the last two microheaters (at $z = 32000 \mu\text{m}$ and $z = 34000 \mu\text{m}$ ) along $x$ -direction for various inlet mass fluxes.....	104
Figure 6.6	Wall temperatures along $x$ -direction for various $z$ -locations for inlet mass fluxes of $200 \text{ kg}/(\text{m}^2\text{s})$ and $1016 \text{ kg}/(\text{m}^2\text{s})$ .....	105
Figure 6.7	Wall mean temperatures for inlet mass fluxes of $294 \text{ kg}/(\text{m}^2\text{s})$ and $1016 \text{ kg}/(\text{m}^2\text{s})$ with reference results ( <i>P.S.</i> : Present Study, <i>Ref.</i> : Reference Work, <i>Exp.</i> : Experimental, <i>Num.</i> : Numerical).....	105
Figure 6.8	Calculated $Nu$ values for various inlet mass fluxes with the reference results ( <i>P.S.</i> : Present Study, <i>Ref.</i> : Reference Work).....	106
Figure 6.9	Comparison of $Po$ values obtained from the equations proposed in literature.....	107
Figure 6.10	Comparison of $Nu$ values obtained from the equations proposed in literature ( <i>Prs. Std.</i> : Present Study, <i>Ref. Std.</i> : Reference Study [26], <i>MH.15</i> : 15 <sup>th</sup> microheater).....	108
Figure 6.11	Surface meshes around the conical elements of R1LC configuration for <i>Case-1</i> (coarsest), <i>Case-6</i> , and <i>Case-8</i> (densest).....	110
Figure 6.12	Fluid bulk mean temperature distribution for mesh independence test cases of R1LC configuration around the first two roughness elements.....	111
Figure 6.13	Fluid bulk mean temperature distribution for mesh independence test cases of R1LC configuration around the last two roughness elements.....	111
Figure 6.14	Wall temperature distributions for mesh independence test cases of R1LC configuration along the $x$ -direction at $z = 20000 \mu\text{m}$ and $z = 20015 \mu\text{m}$ locations.....	112
Figure 6.15	Wall mean temperature distribution for mesh independence test cases of R1LC configuration around the first two roughness elements.....	113
Figure 6.16	Wall mean temperature distribution for mesh independence test cases of R1LC configuration around the last two roughness elements.....	113

Figure 6.17	Local Nusselt distribution for mesh independence test cases of R1LC configuration around the first two roughness elements.....	114
Figure 6.18	Local Nusselt distribution for mesh independence test cases of R1LC configuration around the middle roughness elements.....	115
Figure 6.19	Local Nusselt distribution for mesh independence test cases of R1LC configuration around the last two roughness elements.....	115
Figure 6.20	Velocity magnitude profiles along $y$ -direction at $x = 50 \mu\text{m}$ and various $z$ locations for the first conical element of R1LC configuration.....	117
Figure 6.21	Velocity magnitude profiles along $y$ -direction at $x = 50 \mu\text{m}$ and various $z$ locations for the last conical element of R1LC configuration.....	117
Figure 6.22	Velocity magnitude profiles along $x$ -direction at $y = 5 \mu\text{m}$ and various $z$ locations for the first conical element of R1LC configuration.....	118
Figure 6.23	Velocity magnitude profiles along $x$ -direction at $y = 5 \mu\text{m}$ and various $z$ locations for the last conical element of R1LC configuration.....	118
Figure 6.24	Velocity distribution at various cross-sections around the middle cone of R1LC configuration in the flow direction ( $G = 1016 \text{ [kg/(m}^2\text{s)]}$ ).....	119
Figure 6.25	Wall temperature distribution at $z = 6000 \mu\text{m}$ location for various inlet mass fluxes for R1LC configuration with corresponding smooth values.....	120
Figure 6.26	Wall temperature distribution at $z = 34000 \mu\text{m}$ location for various inlet mass fluxes for R1LC configuration with corresponding smooth values.....	121
Figure 6.27	Wall temperature distribution around the middle cone of R1LC configuration for inlet mass fluxes of $200 \text{ kg/(m}^2\text{s)}$ and $1016 \text{ kg/(m}^2\text{s)}$ for (a) flow facing side of the cone, (b) back side of the cone.....	122
Figure 6.28	Temperature distribution at various cross-sections around the middle cone of R1LC configuration in the flow direction ( $G = 1016 \text{ [kg/(m}^2\text{s)]}$ ).....	123
Figure 6.29	Fluid bulk mean temperature distribution over the $10^{\text{th}}$ roughness element of R1LC configuration.....	124

Figure 6.30	Fluid bulk mean temperature distribution over the last two roughness elements of R1LC configuration.....	124
Figure 6.31	Wall mean temperature distribution over the first two roughness elements of R1LC configuration.....	125
Figure 6.32	Wall mean temperature distribution near the middle roughness element of R1LC configuration.....	126
Figure 6.33	Wall mean temperature distribution over the last two roughness elements of R1LC configuration.....	126
Figure 6.34	Surface temperature and convective heat flux around the middle cone of R1LC configuration for $G = 1016$ [kg/(m <sup>2</sup> s)] ( <i>Top</i> : heat flux around the half of the cone, <i>Bottom</i> : heat flux at $y = 7.5 \mu\text{m}$ plane).....	128
Figure 6.35	Change of density at $x = 50 \mu\text{m}$ plane through the inlet to outlet of the rough section of R1LC configuration ( $G = 1016$ [kg/(m <sup>2</sup> s)]).....	129
Figure 6.36	Change of viscosity at $x = 50 \mu\text{m}$ plane through the inlet to outlet of the rough section of R1LC configuration ( $G = 1016$ [kg/(m <sup>2</sup> s)]).....	130
Figure 6.37	Change of thermal conductivity at $x = 50 \mu\text{m}$ plane through the inlet to outlet of the rough section of R1LC configuration ( $G = 1016$ [kg/(m <sup>2</sup> s)]).....	131
Figure 6.38	Local Nusselt distribution over the first two roughness elements of R1LC configuration.....	132
Figure 6.39	Local Nusselt distribution near the middle roughness element of R1LC configuration.....	133
Figure 6.40	Local Nusselt distribution over the last two roughness elements of R1LC configuration.....	133
Figure 6.41	Surface meshes around the conical elements of R2LC configuration for <i>Case-1</i> (coarsest), <i>Case-8</i> , and <i>Case-10</i> (densest).....	135
Figure 6.42	Fluid bulk mean temperature distribution for mesh independence test cases of R2LC configuration around the last two roughness elements.....	136
Figure 6.43	Wall temperature distributions for mesh independence test cases of R2LC configuration along the $x$ -direction at $z = 20000 \mu\text{m}$ and $z = 20015 \mu\text{m}$ locations.....	137
Figure 6.44	Wall temperature distributions for mesh independence test cases of R2LC configuration along the $x$ -direction at $z = 34890 \mu\text{m}$ and $z = 34910 \mu\text{m}$ locations.....	138

Figure 6.45	Wall mean temperature distribution for mesh independence test cases of R2LC configuration around the first two roughness elements.....	139
Figure 6.46	Wall mean temperature distribution for mesh independence test cases of R2LC configuration around the middle roughness element.....	139
Figure 6.47	Local Nusselt distribution for mesh independence test cases of R2LC configuration around the first two roughness elements.....	140
Figure 6.48	Local Nusselt distribution for mesh independence test cases of R2LC configuration around the middle roughness elements.....	141
Figure 6.49	Local Nusselt distribution for mesh independence test cases of R2LC configuration around the last two roughness elements.....	141
Figure 6.50	Velocity magnitude profiles along $y$ -direction at $x = 23 \mu\text{m}$ and various $z$ locations for the first conical element of R2LC configuration.....	143
Figure 6.51	Velocity magnitude profiles along $y$ -direction at $x = 69 \mu\text{m}$ and various $z$ locations for the last conical element of R2LC configuration.....	143
Figure 6.52	Velocity magnitude profiles along $x$ -direction at $y = 5 \mu\text{m}$ and various $z$ locations for the first conical element of R2LC configuration.....	144
Figure 6.53	Velocity magnitude profiles along $x$ -direction at $y = 5 \mu\text{m}$ and various $z$ locations for the last conical element of R2LC configuration.....	144
Figure 6.54	Velocity distribution at various cross-sections around the middle cone of R2LC configuration in the flow direction ( $G = 1016 \text{ [kg/(m}^2\text{s)]}$ ).....	145
Figure 6.55	Wall temperature distribution at $z = 6000 \mu\text{m}$ location for various inlet mass fluxes for R2LC configuration with corresponding smooth values.....	146
Figure 6.56	Wall temperature distribution at $z = 34000 \mu\text{m}$ location for various inlet mass fluxes for R2LC configuration with corresponding smooth values.....	147

Figure 6.57	Wall temperature distribution around the middle cone of R2LC configuration for inlet mass fluxes of 200 kg/(m <sup>2</sup> s) and 1016 kg/(m <sup>2</sup> s) for (a) flow facing side of the cone, (b) back side of the cone.....	148
Figure 6.58	Temperature distribution at various cross-sections around the middle cone of R2LC configuration in the flow direction ( $G = 1016$ [kg/(m <sup>2</sup> s)]).....	149
Figure 6.59	Fluid bulk mean temperature distribution over the 10 <sup>th</sup> roughness elements of R2LC configuration.....	150
Figure 6.60	Fluid bulk mean temperature distribution over the last two roughness elements of R2LC configuration.....	151
Figure 6.61	Wall mean temperature distribution over the first two roughness elements of R2LC configuration.....	152
Figure 6.62	Wall mean temperature distribution near the middle roughness elements of R2LC configuration.....	152
Figure 6.63	Wall mean temperature distribution over the last two roughness elements of R2LC configuration.....	153
Figure 6.64	Surface temperature around the middle conical elements of R2LC configuration and convective heat flux in the fluid at $y = 7.5 \mu\text{m}$ plane ( $G = 1016$ [kg/(m <sup>2</sup> s)]).....	154
Figure 6.65	Local Nusselt distribution over the first two roughness elements of R2LC configuration.....	155
Figure 6.66	Local Nusselt distribution near the middle roughness element of R2LC configuration.....	155
Figure 6.67	Local Nusselt distribution over the last two roughness elements of R2LC configuration.....	156
Figure 6.68	Change of thermal conductivity at $x = 23 \mu\text{m}$ plane through the inlet to outlet of the rough section of R2LC configuration ( $G = 1016$ [kg/(m <sup>2</sup> s)]).....	157
Figure 6.69	Change of thermal conductivity at $x = 69 \mu\text{m}$ plane through the inlet to outlet of the rough section of R2LC configuration ( $G = 1016$ [kg/(m <sup>2</sup> s)]).....	158
Figure 6.70	Surface meshes around the conical elements of RDC configuration for <i>Case-1</i> (coarsest), <i>Case-6</i> , and <i>Case-8</i> (densest).....	160
Figure 6.71	Fluid bulk mean temperature distribution for mesh independence test cases of RDC configuration over the last roughness element set.....	162

Figure 6.72	Wall temperature distributions for mesh independence test cases of RDC configuration along the $x$ -direction at $z = 5135 \mu\text{m}$ and $z = 5170 \mu\text{m}$ locations.....	162
Figure 6.73	Wall temperature distributions for mesh independence test cases of RDC configuration along the $x$ -direction at $z = 19940 \mu\text{m}$ and $z = 19975 \mu\text{m}$ locations.....	163
Figure 6.74	Wall temperature distributions for mesh independence test cases of RDC configuration along the $x$ -direction at $z = 34815 \mu\text{m}$ and $z = 34850 \mu\text{m}$ locations.....	163
Figure 6.75	Wall mean temperature distribution for mesh independence test cases of RDC configuration around the first roughness element set.....	164
Figure 6.76	Wall mean temperature distribution for mesh independence test cases of RDC configuration around the middle roughness element set.....	164
Figure 6.77	Local Nusselt distribution for mesh independence test cases of RDC configuration around the first roughness element set.....	165
Figure 6.78	Local Nusselt distribution for mesh independence test cases of RDC configuration around the middle roughness element set.....	166
Figure 6.79	Local Nusselt distribution for mesh independence test cases of RDC configuration around the last roughness element set.....	166
Figure 6.80	Velocity magnitude profiles around the small side cones of first and last roughness element set of RDC configuration along $y$ -direction at $x = 15 \mu\text{m}$ and $x = 85 \mu\text{m}$ for various $z$ locations.....	168
Figure 6.81	Velocity magnitude profiles along $y$ -direction at $x = 50 \mu\text{m}$ and various $z$ locations for the first and last roughness element set of RDC configuration.....	169
Figure 6.82	Velocity magnitude profiles along $x$ -direction at $y = 5 \mu\text{m}$ and various $z$ locations for the first and last roughness element set of RDC configuration.....	170
Figure 6.83	Velocity distribution at various cross-sections through the middle roughness element set of RDC configuration in the flow direction ( $G = 1016 \text{ [kg/(m}^2\text{s)]}$ ).....	171

Figure 6.84	Wall temperature distribution at $z = 5975 \mu\text{m}$ location for various inlet mass fluxes for RDC configuration with corresponding smooth values.....	174
Figure 6.85	Wall temperature distribution at $z = 33975 \mu\text{m}$ location for various inlet mass fluxes for RDC configuration with corresponding smooth values.....	174
Figure 6.86	Wall temperature distribution around the bigger cone of middle roughness element set of RDC configuration for inlet mass fluxes of $200 \text{ kg}/(\text{m}^2\text{s})$ and $1016 \text{ kg}/(\text{m}^2\text{s})$ for (a) flow facing side of the cone, (b) back side of the cone.....	175
Figure 6.87	Temperature distribution at various cross-sections through the middle roughness element set of RDC configuration in the flow direction ( $G = 1016 \text{ [kg}/(\text{m}^2\text{s})]$ ).....	176
Figure 6.88	Fluid bulk mean temperature distribution over the 7 <sup>th</sup> roughness element set of RDC configuration.....	179
Figure 6.89	Fluid bulk mean temperature distribution over the last two roughness element sets of RDC configuration.....	179
Figure 6.90	Wall mean temperature distribution over the first two roughness element sets of RDC configuration.....	180
Figure 6.91	Wall mean temperature distribution over the middle roughness element set of RDC configuration.....	181
Figure 6.92	Wall mean temperature distribution over the last two roughness element sets of RDC configuration.....	181
Figure 6.93	Surface temperature around the middle roughness element set of RDC configuration and convective heat flux in the fluid at $y = 5 \mu\text{m}$ plane (top) and $y = 7.5 \mu\text{m}$ plane (bottom) for $G = 1016 \text{ kg}/(\text{m}^2\text{s})$ .....	183
Figure 6.94	Variation of $\rho$ , $\mu$ , and $k$ over the last two roughness element set of RDC configuration at $x = 50 \mu\text{m}$ plane for $G = 1016 \text{ kg}/(\text{m}^2\text{s})$ .....	184
Figure 6.95	Local Nusselt distribution over the first two roughness element sets of RDC configuration.....	185
Figure 6.96	Local Nusselt distribution over the middle roughness element set of RDC configuration.....	185
Figure 6.97	Local Nusselt distribution over the last two roughness element sets of RDC configuration.....	186
Figure 6.98	Pressure drop between the inlet and exit of heated section of smooth and rough channels for various inlet mass fluxes.	187

Figure 6.99	Temperature difference between the inlet and outlet of heated section of smooth and rough channels for various inlet mass fluxes.....	188
Figure 6.100	Change in $Po$ value with inlet mass flux in smooth and rough channels.....	189
Figure A.1	Schematics of 2D test channel and the locations of data extraction lines.....	212
Figure A.2	Close-up views of velocity distributions near the base and around the middle of the $R1-L4$ line.....	214
Figure A.3	Velocity distributions over the tip point of middle roughness element (along the $R2-L3$ line) and close-up view near the tip point.....	214
Figure A.4	Schematics of 3D test channel and the locations of data extraction lines.....	216
Figure A.5	$w$ -velocity distributions along the second line of first roughness element and close-up view of the base section.....	218
Figure A.6	$w$ -velocity distributions along the second line of first roughness element and close-up view of the middle section.....	219
Figure B.1	Wall mean temperatures calculated with COMSOL v4.4 and v5.2a for test cases of stabilization methods.....	225
Figure B.2	Local $Nu$ values for test cases of stabilization methods.....	225
Figure B.3	Wall mean temperature distribution over the heated section for first and second order mesh elements.....	227

## NOMENCLATURE

$Br$	Brinkman number, $Br = \mu U_m / (k(T_i - T_w))$
$C_p$	Constant pressure specific heat, J/(kg K)
$D_h$	Hydraulic diameter
$e$	Average height of the roughness elements
$f$	Friction constant
$G$	Mass flux, kg/(m <sup>2</sup> s)
$H$	Channel height, m
$h$	Convective heat transfer coefficient
$k$	Thermal conductivity of the fluid, W/(m K)
$Kn$	Knudsen number, $Kn = \lambda / L_c$
$L$	Length of channel, m
$L_c$	Characteristic length, m
$Nu$	Nusselt number, $Nu = q D_h / (k \Delta T)$
$p$	Pressure, Pa
$Pe$	Peclet number, $Pe = Re Pr$
$Po$	Poiseuille number, $Po = f Re$
$Pr$	Prandtl number, $Pr = \vartheta / \alpha$
$q$	Heat flux, W/m <sup>2</sup>
$Re$	Reynolds number, $Re = \rho U D_h / \mu$
$T$	Temperature, K

$u, v, w$	Velocity components in $x, y, z$ directions, m/s
$W_b$	Base width of trapezoidal microchannel
$W_t$	Top width of trapezoidal microchannel
$x, y, z$	Geometric coordinates

### **Greek Symbols**

$\alpha$	Thermal diffusivity, $\text{m}^2/\text{s}$
$\alpha$	Aspect ratio of the channel, $W_b/H$
$\gamma$	Specific heat ratio
$\gamma$	Aspect ratio of the channel, $H/W_t$
$\varepsilon$	Relative roughness of surface, $\varepsilon = e/D_h$
$\theta$	Sidewall angle of trapezoid channel
$\lambda$	Mean free path, m
$\mu$	Dynamic viscosity, Pa.s
$\rho$	Density, $\text{kg}/\text{m}^3$
$\vartheta$	Kinematic viscosity, $\text{kg}/\text{m}^3$

### **Subscripts**

$eff$	Effective
$HS$	Heated surface
$i$	Inlet values
$m$	Mean values
$max$	Maximum
$vh$	Viscous heating
$w$	Wall values
$x, z$	Local values

## CHAPTER 1

### INTRODUCTION

Micro-Electro-Mechanical Systems (MEMS) can be defined as miniaturized mechanical and electro-mechanical devices and structures that are produced by micro fabrication techniques [1]. Their dimensions can vary from well below one micron to a few millimeters and they can be in the form of relatively simple structures without moving elements, or can be extremely complex with multiple moving parts. Studies in microscale phenomena started well before a century ago. However, the MEMS technology developed rapidly during the late 1980s and throughout the 1990s with the expertise, know-how, and physical infrastructure developed for the silicon integrated circuit (IC) industry [2]. Nowadays, MEMS devices are used nearly in every area due to their important advantages and developments that they possess, such as high efficiency in production, low costs per samples, very small dimensions of the resulting product which improves portability and transport, much better accuracy and reliability, and in heat transfer area, increased convective and radiative heat transfer rates due to high surface area to volume ratios of heat sinks or heat exchangers.

Various MEMS devices include fluid flow and heat transfer at microscale. In microfluidic devices, micro flows are generally characterized by Knudsen number ( $Kn$ ) which is the ratio of mean free path to characteristic length ( $Kn = \lambda/L_c$ ), where the mean free path is the average distance traveled by the molecules without colliding with each other. For  $Kn < 0.001$  flow is considered as continuum, where micro liquid flows with hydraulic diameters greater than  $1 \mu\text{m}$  generally falls in this category and no-slip wall boundary condition is applicable with Navier-Stokes

equations. For  $0.001 \leq Kn \leq 0.10$  flow is considered in slip-flow regime and most gas micro flows belong to this category. In gas micro flows, rarefaction, compressibility, viscous heating, and thermal creep might become important in some cases. In liquid micro flows, wetting, adsorption, or electrokinetics might become effective [3].

Disregarding the experimental and measurement errors, experimental studies in the literature have shown that microchannel flow, heat and mass transfer phenomena cannot be explained by conventional theories of transport phenomena all the time. As the size scale decrease, the fundamental physics changes drastically. To explain the unusual behavior in microscale some important scaling effects, namely the entrance effect, conjugate heat transfer, viscous heating, rarefaction, compressibility, electric double layer effect, and so on, should be considered that are not considered or deliberately neglected due to their miniscule effect, in macroscale [4].

Other than the mentioned effects, one of the reasons causing different results in the experiments is the surface roughness characteristics of the channels, which can be natural and in random order or deliberately engineered. When the surfaces of the microfluidic devices are investigated, it can be seen that roughness characteristics of microchannel surfaces depend on the manufacturing processes and materials that the channels are made of. For example, photolithography is widely used in microsystems with silicon wafers. When chemical wet etching with KOH is applied on the silicon substrate, specific cross-sectional shapes of rectangle, trapezoid, and triangle are obtained [5]. These cross-sectional shapes of the microchannels depend on the crystallographic nature of the silicon used, and the concentration and temperature of the KOH solution, which result in relatively smooth sidewalls and rough bottom walls for rectangular and trapezoidal cross-sections as shown in Fig. (1.1) with glassy carbon microchannel produced by reactive ion etching.

Surface roughness is not always an unwanted or undesired result of the manufacturing process. In some research fields, such as in biomimetics, it is one of

the main driving factors. By definition, biomimetics is mimicking the nature of biological creatures in design [8]. By investigating the unique properties of living beings such as water repellent superhydrophobic and self-cleaning lotus leaves, drag reducing denticles of shark's skin, adhesive lamella of gecko's legs, or feathers of some colorful butterflies [8, 9], importance and the use of surface roughness-like structures by nature can be understood. A common property of these examples is that all show the mentioned unique feature by hierarchical micro and nano structures on their leaves, skins, and feathers, which can be called engineered rough surfaces due to similarities in appearance to natural rough surfaces. By mimicking these geometries, self-cleaning windows and paints for buildings, drag reducing and antifouling coatings for air and sea vehicles, and textiles with changeable optical properties can be manufactured [8, 9].

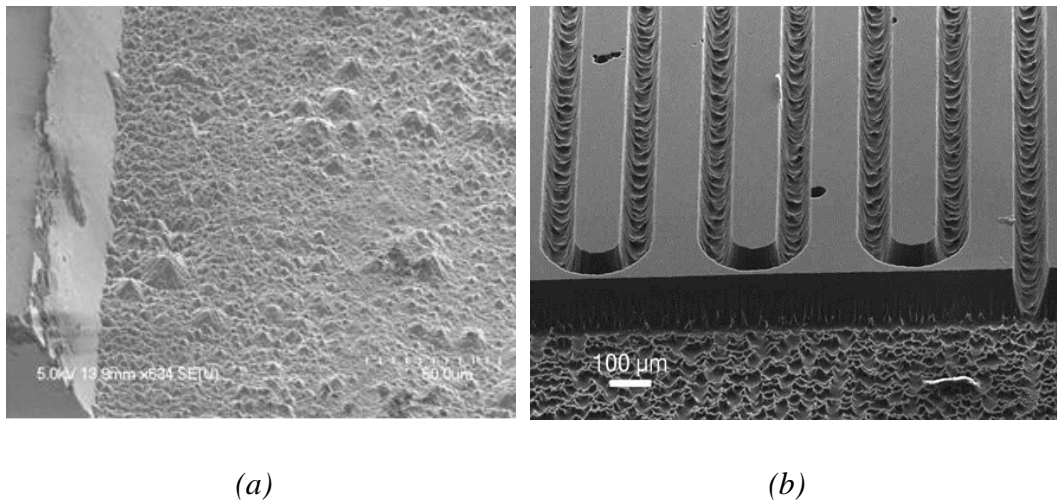


Figure 1.1: (a) Silicon trapezoidal microchannel produced by wet etching [6], and (b) glassy carbon microchannel produced by reactive ion etching [7].

In macroscale laminar flow, roughness of the walls is generally neglected since its overall effect on the fluid physics is small. However, published studies show that

surface roughness could have great effects on flow and heat transfer characteristics in microchannels depending on the geometrical parameters of roughness elements such as shape, height, spacing between each element, density and so on. Changing these parameters can yield either increase or decrease in flow friction, pressure drop or heat transfer.

Moreover, increasing knowledge and understanding the importance of small features in living beings, such as the water repelling self-cleaning property of lotus leaves, adhesion capability of geckos, drag reducing shark skins due to their micro and nano structures, lead the researchers to applying specific engineered surfaces that mimic the nature. In these applications, roughness is used deliberately on the surfaces to obtain a specific goal. However, since every geometrical parameter and their combination affects the outcome differently, need for a large amount of data has arisen.

In this work, it is intended to investigate the effect of different roughness configurations and properties on laminar flow and heat transfer characteristics in microchannels, numerically. For this purpose, two-dimensional parallel plate, and three-dimensional trapezoidal microchannels with different roughness properties are modeled along with the smooth ones. Modelling of channels, and fluid flow and heat transfer simulations are conducted with the commercial CFD program COMSOL Multiphysics. For the post-processing, MATLAB and COMSOL's LiveLink for MATLAB module are used. In two-dimensions, roughness is modeled as triangular obstructions on one of the parallel plates. In three-dimensions, roughness is modeled as conical obstructions with different heights and base radii, and placed on the base of the trapezoidal channel. Numerically obtained results, for smooth and rough channels, are compared with each other, and with numerical and experimental results existing in the literature.

A review of studies in literature about microscale flow and heat transfer, both in smooth and rough channels, is given in Chapter – 2 with a focus on laminar liquid flow and heat transfer in microchannels with trapezoidal cross-sections. Engineered

surfaces are also considered with the natural roughness. In addition, studies concerning simulations with COMSOL Multiphysics are reviewed briefly. Theory and governing equations are provided in Chapter – 3. Model descriptions and results of two-dimensional smooth and rough microchannel simulations are presented in Chapter – 4. Three-dimensional simulations are considered in two sections. First, flow simulations, without any means of heat transfer, in macro and micro scale smooth and rough trapezoidal channels are conducted. Geometries and flow conditions are explained, and comparative results are given in Chapter – 5. Second, flow and heat transfer simulations in smooth and rough microchannels are conducted and presented in Chapter – 6. Considered problems are summarized in Chapter – 7 with the main findings. In addition, brief information on the use of boundary layer mesh, and some numerical considerations on the options of COMSOL are given in Appendix – A, and Appendix – B, respectively.



## CHAPTER 2

### LITERATURE REVIEW

In this section, review of studies in literature about microscale flow and heat transfer, both in smooth and rough channels is presented with a focus on laminar liquid flow and heat transfer in microchannels with trapezoidal cross-sections. Engineered surfaces, which are generally regarded as roughness, are also considered as well as the natural roughness. In addition, studies concerning simulations with COMSOL Multiphysics are reviewed briefly.

Early experimental studies of fluid flow and heat transfer in microchannels and microfluidic devices are reviewed and compared with the conventional macroscale theories in [5, 10-12]. In these reviews, the authors draw attention to conflicting results published in the reviewed studies. While in some experiments higher Nusselt ( $Nu$ ) and higher Poiseuille ( $Po$ ) numbers are reported, in the others, with similar flow conditions and in similar geometries, lower  $Nu$  and  $Po$  values are reported. Authors stated and explained the possible error sources as experimental uncertainties, measurement errors, miscalculations, neglecting pressure losses, neglecting entrance/exit effects, and not considering the surface effects.

More recent reviews on the subject are presented in [13-16]. Dey *et al.* [13] reviewed the experimental studies of single-phase liquid flows that are investigating the friction and heat transfer in microchannels. They grouped the studies as leading higher, lower or equivalent results than the results of conventional theories, and discussed the possible deviation sources, such as surface roughness, nano bubble formation, surface hydrophobicity, fluid slippage, liquid-solid interactions, and

geometrical properties of the microchannels which generally do not have important effect on macroscale counterparts. Adham *et al.* [14] reviewed the experimental studies of microchannel heat sinks and defined the trends of published works on used materials, coolant types, flow conditions, and channel shapes. Asadi *et al.* [15] reviewed the experimental works about heat transfer and pressure drop in microchannels, and stated that discrepancies between the experimental results of microchannel studies and theoretical ones are lower in newer studies while the discrepancies were large in the earlier ones. Moreover, both in Refs. [14] and [15], the authors stated that earlier studies are mostly experimental and prone to high errors, while newer studies are mostly numerical.

Dai *et al.* [16] reviewed experimental works in literature about liquid flow in rough micro and minichannels. They analyzed the data taken from these studies by means of the critical Reynolds numbers ( $Re_c$ ) and friction factors ( $f$ ). Authors compared the results with prediction models that exist in the literature. The channel cross-sections in the reviewed studies were mostly circular or rectangular. Based on the analyzed data, authors stated that, when the relative roughness in the microchannels is below 1%, the channels could be treated as smooth. However, when the relative roughness is above 1%,  $f$  and  $Re_c$  gradually deviate from predictions of smooth channels, while this limit is 5% for the macroscale channels.

Morini [17] defined the important scaling effects as axial conduction in the fluid, conjugate heat transfer between fluid and channel walls, non-uniform surface roughness, and viscous dissipation for the single phase flows in microchannels. Then, he discussed the effects of viscous dissipation, entrance region, and conjugate heat transfer in various microchannel geometries on  $f$  and  $Nu$  for incompressible, laminar, fully developed flow. The author showed that the dependence of  $Nu$  value on Reynolds ( $Re$ ) number can be explained by taking the mentioned scaling effects into account, especially the conjugate effects and temperature dependent liquid properties at low  $Re$  flows, and viscous dissipation and entrance effects at high  $Re$  flows. In another study, Morini [18] examined the results of experiments in literature

about laminar to turbulent transition in microchannels and presented a model to explain the effects of channel geometries on the discrepancy between micro and macro flows. This model is based on the Obot-Jones Model, which was developed for macrosized channels to set the similarity between circular and noncircular channels on the use of hydraulic diameter in  $Re$  and related definitions, by the help of channel aspect ratios ( $\gamma$ ). The author also proposed a polynomial function to predict fully developed  $Po$  value for steady, isothermal, laminar flows with constant thermophysical properties in rectangular, trapezoidal, and hexagonal channels, which is given in Eq. (2.1), and compared the obtained results with the available data from the literature. Morini stated that the model is promising and valid for channels with 40  $\mu\text{m}$  and greater hydraulic diameters. In Eq. (2.1), the aspect ratio for the trapezoidal channel is defined as the ratio of height to longer base width and the constants  $g_i$  are tabulated for the mentioned cross-sectional geometries.

$$fRe_{fd} = \sum_{i=0}^5 g_i \gamma^i \quad (2.1)$$

These reviews of experimental studies indicated that variation of thermophysical properties of liquids with temperature, surface conditions of microchannels, channel cross-sectional shapes and geometrical properties are important factors on determination of  $f$  and  $Nu$  values.

## 2.1 EXPERIMENTAL AND NUMERICAL STUDIES IN TRAPEZOIDAL MICROCHANNELS

Qu *et al.* [19] conducted experiments of deionized water flowing through trapezoidal silicon microchannels with hydraulic diameters ranging from 51  $\mu\text{m}$  to 169  $\mu\text{m}$  and having relative surface roughness up to 3.5%. They measured the volume flow rate and pressure drop at fully developed conditions and calculated the friction factor. Experimental results are compared with available ones in literature and the ones calculated from conventional theory for macro flows, numerically. They observed

that the experimental friction factors in microchannels are 8 to 38% higher than theoretical predictions and depend on hydraulic diameter and  $Re$ . They attributed this difference to the effect of surface roughness. Later, Qu *et al.* [20] extended their work by experimentally investigating steady state heat transfer characteristics on those microchannels. The test channels are heated at the bottom wall with a film heater while other walls are insulated. Also, conjugate heat transfer simulations are conducted numerically to compare the experimental and numerical results. In simulations, the flow is assumed to be laminar and fully developed, and the fluid is considered to have constant properties. All the experimental  $Nu$  values are found to be much lower than the numerical ones in which the discrepancies are attributed to the surface roughness.

Another set of experiments are conducted by Wu and Cheng [21-22]. In [21] Wu and Cheng investigated the friction factors of laminar flow of deionized water in silicon microchannels having 28 different hydraulic diameters ranging from 25.9  $\mu\text{m}$  to 291  $\mu\text{m}$  and cross-sectional aspect ratios, which is defined as the ratio of base width to top width, ranging from 0 to 0.985 resulting in triangular and trapezoidal cross-sections. Channels are considered as smooth since the maximum relative roughness is 0.12%. They found that the cross-sectional shape of the channel affects the value of friction factor and friction constant increases with increasing cross-sectional aspect ratio. They also proposed a correlation for friction constant based on the experimental data set, which is a function of cross-sectional aspect ratio ( $W_b/W_t$ ), and given in Eq. (2.2):

$$(f Re) = 11.43 + (0.80) \exp\left(2.67 \frac{W_b}{W_t}\right) \quad (2.2)$$

Relative deviation of this equation from the experimental data is less than 9.7% and maximum uncertainty in determining  $(f Re)$  in experiments is 11%. Later, they investigated the laminar convective heat transfer and pressure drop characteristics in 13 different silicon microchannels having triangular and trapezoidal cross-sections [22]. The working fluid is chosen as deionized water and the channels are

heated at the bottom. The relative roughness ( $k/D_h$ ) of the channels are between  $3.26 \times 10^{-4}$  and  $1.09 \times 10^{-2}$ . Some of the microchannels' surface hydrophilic property is changed by depositing an oxide layer. Effects of geometric parameters, surface roughness, and surface hydrophilic properties on  $Nu$  and  $f$  are sought. They observed that geometric parameters of the channels have significant effect on both the  $Nu$  and  $f$ , and increasing surface roughness also increases the  $Nu$  and  $f$  values, which is more at larger  $Re$ .  $Nu$  increases almost linearly up to  $Re = 100$  and after that slowly. Moreover, increasing the surface hydrophilic character increases the  $Nu$  and pressure drop. Based on the experimental data, they proposed equations for  $Nu$  and  $f$ , which are functions of fluid and geometrical properties and given in Eqns. (2.3) to (2.5).

$$Nu = C_1 Re^{0.946} Pr^{0.488} \left(1 - \frac{W_b}{W_t}\right)^{3.547} \left(\frac{W_t}{H}\right)^{3.577} \left(\frac{k}{D_h}\right)^{0.041} \left(\frac{D_h}{L}\right)^{1.369} \quad (2.3)$$

Eq. (2.3) is valid for  $10 \leq Re \leq 100$ ,  $4.05 \leq Pr \leq 5.79$ ,  $0 \leq W_b/W_t \leq 0.934$ ,  $0.038 \leq H/W_t \leq 0.648$ ,  $3.26 \times 10^{-4} \leq k/D_h \leq 1.09 \times 10^{-2}$ , and  $191.77 \leq L/D_h \leq 453.79$ . The constant  $C_1$  depends on the surface material and takes the values of 6.7 and 6.6 for silicon and thermal oxide surfaces, respectively. Maximum deviation of Eq. (2.3) from experimental data is 20.3%.

$$Nu = C_2 Re^{0.148} Pr^{0.163} \left(1 - \frac{W_b}{W_t}\right)^{0.908} \left(\frac{W_t}{H}\right)^{1.001} \left(\frac{k}{D_h}\right)^{0.033} \left(\frac{D_h}{L}\right)^{0.798} \quad (2.4)$$

Eq. (2.4) is valid for  $100 \leq Re \leq 1500$ ,  $4.44 \leq Pr \leq 6.05$ ,  $0 \leq W_b/W_t \leq 0.934$ ,  $0.038 \leq H/W_t \leq 0.648$ ,  $3.26 \times 10^{-4} \leq k/D_h \leq 1.09 \times 10^{-2}$ , and  $191.77 \leq L/D_h \leq 453.79$ . Value of the constant  $C_2$  is 47.8 for silicon and 54.4 for thermal oxide surfaces. Maximum deviation of Eq. (2.4) from experimental data is 19.8%.

$$(f_{app} \cdot Re) = C_3 Re^{0.089} \left(1 - \frac{W_b}{W_t}\right)^{4.359} \left(\frac{W_t}{H}\right)^{4.444} \left(\frac{k}{D_h}\right)^{0.028} \left(\frac{D_h}{L}\right)^{1.023} \quad (2.5)$$

Eq. (2.5) is valid for  $10 \leq Re \leq 1500$ ,  $0 \leq W_b/W_t \leq 0.934$ ,  $0.038 \leq H/W_t \leq 0.648$ ,  $3.26 \times 10^{-4} \leq k/D_h \leq 1.09 \times 10^{-2}$ , and  $191.77 \leq L/D_h \leq 453.79$ . Value of the constant

$C_3$  is 508.7 for silicon and 540.5 for thermal oxide surfaces. Maximum deviation of Eq. (2.5) from experimental data is 19.3%.

Hao *et al.* [23] conducted experiments to observe the velocity field and pressure drop of water flowing in a trapezoidal microchannel. The channel has a hydraulic diameter of 237  $\mu\text{m}$  with base width, top width, height and side angle of 256  $\mu\text{m}$ , 523  $\mu\text{m}$ , 189  $\mu\text{m}$ , and 54.74°, respectively. The  $Re$  range of the experiments is 50 to 2800. The relative roughness of the channels are about 0.025% and are considered as smooth. They stated that the experimental results agreed well with the theoretical fully developed  $Po$  for  $Re < 1400$  when the entrance effects are included. Transition from laminar to turbulent flow occurred at  $Re$  between 1500 and 1800. The entrance length was found to be about  $L_e = (0.08\sim 0.09)Re D_h$  based on the centerline velocity distribution.

Renaud *et al.* [24] conducted experiments to investigate the microchannel fluidic resistances of liquid deionized water and ethanol for different flow rates and pressure drops of very low  $Re$  flows ( $Re < 1$ ) in trapezoidal silicon microchannels. Channels have depths of 21.5  $\mu\text{m}$ . Length and width of the channels varied between 200  $\mu\text{m}$  to 440  $\mu\text{m}$  and 58  $\mu\text{m}$  to 267  $\mu\text{m}$ , respectively. They also developed a simple 2D numerical procedure based on Navier-Stokes equations and no-slip wall boundary condition to compute the resistance of a complex 3D microchannel setup and published the results as diagrams for three different cross-sections. Wu *et al.* [25] also conducted experiments of ethanol-water solutions flowing in five different trapezoidal silicon microchannels with hydraulic diameters ranging between 141.7  $\mu\text{m}$  and 268.6  $\mu\text{m}$ , to investigate the effects of geometrical parameters and volume concentration friction and heat transfer. Depths and lengths of these channels are kept constant. The relative roughness of the channel surfaces are less than 0.02% and are considered as smooth. The considered ethanol volume concentrations in the solutions varied from 0 (pure water) to 0.8. They observed that volume concentration of ethanol on friction is ignorable. However,  $Nu$  increases with increasing volume concentration of ethanol due to increasing  $Pr$ . On the other hand, geometrical parameters of microchannels have important effects on both  $Po$  and  $Nu$ .

Microchannels with greater base width to top width ratio and smaller height to top width ratios exhibited higher friction factors and  $Nu$  values. They also proposed correlations for  $Po$  and  $Nu$  based on the experimental data, which are provided in Eq. (2.6) and Eq. (2.7), respectively.

$$(f \cdot Re) = 13.66 \left(\frac{W_b}{W_t}\right)^{0.148} \left(\frac{W_t}{H}\right)^{0.233} (L^+)^{-0.151} \quad (2.6)$$

Here  $L^+$  is the dimensionless hydrodynamic entrance length and defined as  $L^+ = L/(D_h Re)$ . Eq. (2.6) is valid for  $0.188 < W_b/W_t < 0.852$ ,  $1.802 < W_t/H < 10.101$ , and  $0.095 < L^+ < 0.67$ . Mean absolute error and mean relative error of this equation is 3.32% and 0.51%, respectively. Also, fully developed laminar flow is formed when  $L^+ = 0.0575$ .

$$Nu = (0.723)Re^{0.089}Pr^{0.209} \left(\frac{W_b}{W_t}\right)^{0.015} \left(\frac{W_t}{H}\right)^{0.106} (L_h^+)^{-0.105} (1 + X)^{0.342} \quad (2.7)$$

Here  $L_h^+$  is the dimensionless thermal entrance length and defined as  $L_h^+ = L/(D_h Re Pr)$ . Eq. (2.7) is valid for  $0.188 < W_b/W_t < 0.852$ ,  $1.802 < W_t/H < 10.101$ ,  $0.025 < L_h^+ < 0.175$ ,  $80 < Re < 1000$ ,  $5.6 < Pr < 23.6$ , and the concentration range of  $0 \leq X \leq 0.8$ . Mean absolute error and mean relative error of this equation is 8.67% and 1.05%, respectively. Also, fully developed thermal boundary layer is formed when  $L_h^+ = 0.05$ .

Wang *et al.* [26] conducted experiments and numerical simulations to investigate the laminar forced convection heat transfer characteristics of deionized water flowing in a trapezoidal microchannel having hydraulic diameter of 155  $\mu\text{m}$ , top width of 427  $\mu\text{m}$ , bottom width of 276  $\mu\text{m}$ , height of 107  $\mu\text{m}$ , length of 40 mm, and side angle of 54.7°. The channel was heated at the bottom with 15 microheaters each having 2 mm length and 200  $\mu\text{m}$  width. They conducted the experiments for various heat fluxes and inlet mass fluxes. In each case, inlet, exit, and microheater temperatures are measured and then, Nusselt numbers are evaluated from the measurements. They conducted 3D numerical simulations with the commercial

CFD program FLUENT with temperature dependent thermophysical properties. For partially heated cases, it is found that the  $Nu$  values increases with increasing mass flux without approaching a limit. However, heat flux had a little effect on  $Nu$  since the fluid properties vary with the temperature. For the fully heated cases, local  $Nu$  values gradually approached to a constant value for lower mass fluxes. However,  $Nu$  does not approach to a constant at the end of the heating section, which indicates that the thermal entrance length of the flow is larger than the heating length.

Chai *et al.* [27] experimentally and numerically investigated the laminar steady state flow of deionized water in a silicon heat sink that contains 10 parallel microchannels with trapezoidal cross-sections.  $Re$  range of the investigation is 350 to 755, and the applied heat flux is between 296 and 875 [kW/m<sup>2</sup>]. For the numerical part, they used FLUENT and considered two different models of the same problem. In the first model, simulations are conducted in a unit cell that contains a single microchannel and its surroundings, where the second model contains all the microchannels with the inlet and outlet buffers to investigate the inlet and exit effects. They compared the results obtained by these two models with the experimental results. The first model resulted in a slightly higher friction constant than the experimental one. On the other hand, the second model resulted in a slightly lower friction constant than the experimental one. Local  $Po$  value decreases along the flow direction and asymptotically reaches 13.736. Also, the average  $Nu$  for the experiments is calculated as the highest followed by first and second model, and all of them increased with increasing  $Re$ . Moreover, it is found that, for a given pumping power, increasing heating power reduces the thermal resistance.

Duryodhan *et al.* [28] numerically and experimentally investigated single phase deionized water flow and heat transfer in converging and diverging microchannels having trapezoidal cross-sections.  $Re$  range for the investigation is 30 to 274. Considered channels have a fixed depth of 86  $\mu\text{m}$ , hydraulic diameter of 156  $\mu\text{m}$  and divergence angle of 8°. Hydraulic diameter, aspect ratio, average velocity, and  $Re$  are calculated at characteristic locations, which are defined as  $L/3$  for the diverging microchannel and  $L/3.6$  for the converging microchannel from the narrow

end of the channels, where  $L$  is the channel length. For the numerical part of the investigation, steady state 3D conjugate heat transfer problem with constant thermophysical properties except viscosity is considered and solved by FLUENT. Deviation of numerically calculated average  $Nu$  values from the experimentally obtained ones is about 10% in average and 18% maximum. Diverging and converging microchannels exhibited better thermal and hydraulic performance than uniform cross-sectional microchannels. Also, conjugate effects,  $Nu$  value, and pressure drop are found to be larger in converging channels compared to diverging channels.

Sadasivam *et al.* [29] numerically investigated the effects of geometrical parameters, namely the aspect ratio and side angle, of trapezoidal and hexagonal channels on  $Po$  and  $Nu$  values for H1 and T thermal boundary conditions. They assumed hydrodynamically and thermally fully developed, laminar flow at steady state, and used coordinate transformation and finite difference method as numerical model. They considered sidewall angles of  $30^\circ$ ,  $45^\circ$ ,  $60^\circ$ , and  $75^\circ$  in their investigations and compared their results with [30]. They found excellent agreement. They also proposed equations for  $Po$  and  $Nu$  for the mentioned sidewall angles based on their findings, which are functions of aspect ratio and given in Eq. (2.8). The polynomial constants in Eq. (2.8) are tabulated for  $Po$ ,  $Nu_{H1}$ ,  $Nu_T$ , and considered sidewall angles in [29]. The difference between these equations and computed values are about  $\pm 2\%$ .

$$\begin{cases} fRe \\ Nu \end{cases} = b_0 + b_1\gamma + b_2\gamma^2 + b_3\gamma^3 + b_4\gamma^4 + b_5\gamma^5 + b_6\gamma^6 + b_7\gamma^7 \quad (2.8)$$

Zhuo *et al.* [31] numerically investigated the 3D conjugate heat transfer of incompressible laminar flow through a trapezoidal and a triangular silicon microchannel, which is heated at the bottom of the substrate with a constant heat flux. Thermophysical properties of water and silicon are taken constant except the viscosity of the water, which is a function of temperature. The  $Re$  range of the simulations is 30 to 400 based on the outlet conditions of the channels. They

compared their results with the experimental results of another study in literature, which match the geometrical and physical conditions of the simulations. The authors stated that the agreement of the findings are good and found that the fully developed  $Nu$  values increase sharply and linearly as the  $Re$  value increase when  $Re < 100$ . Above that  $Re$ , increase in  $Nu$  is lower.

Bahrami *et al.* [32] studied pressure drop and friction characteristics of fully developed, steady state, laminar flow for various geometries having constant cross-sectional area and perimeter. The fluid is assumed to be incompressible and has constant thermophysical properties. They proposed an approximate model to predict  $Po$  that is a function of cross-sectional area, perimeter, aspect ratio, and polar moment of inertia, and uses square root of area as characteristic length instead of hydraulic diameter. They compared the results of the model with existing analytical and experimental results for various geometries. Deviation is found to be in the 10% band, mostly less than 8% and in some cases a maximum of 14%. Later, the model proposed in [32] is extended to calculate  $Nu$  under H1 thermal boundary condition by Sadeghi *et al.* [33]. Maximum difference between the model and analytical solutions is about 10%.

Chen *et al.* [34] conducted 3D numerical conjugate heat transfer simulations of silicon heat sinks with rectangular, triangular, and trapezoidal microchannels on a unit cell basis. They applied constant heat flux at the bottom of the heat sink and assumed other walls as adiabatic. They considered the steady laminar flow of deionized water with constant thermophysical properties, and compared the calculated  $Nu$  and  $Po$  values of microchannels having different cross-sections. It is found that  $Nu$  values are higher at the entrance region and quickly approach the fully developed value at the exit, in which the rectangular channel has higher local  $Nu$  values than trapezoidal and triangular ones, and trapezoidal and triangular channels have nearly same local  $Nu$ .  $Po$  values for each cross-section remains nearly constant as the  $Re$  increases and  $Po$  for rectangular channel having the highest value. Moreover, they defined a thermal efficiency value, which is the ratio of heat transfer

rate to pumping power, and stated that the triangular microchannel has the highest thermal efficiency, followed by trapezoidal and then rectangular channel when the channel inlet and exit temperatures are fixed.

Another 3D conjugate heat transfer simulation in heat sinks having rectangular, trapezoidal, and triangular microchannels was conducted by Gunnasegaran *et al.* [35] with the assumptions of steady-state laminar, incompressible flow of single phase water with constant thermophysical properties in the  $100 < Re < 1000$  range. Each simulated heat sink has 25 microchannels of 10 mm length with the mentioned geometries. The length and the number of microchannels are fixed in each simulation while the other geometrical parameters such as width, height, and spacing of the microchannels inside the heat sink, the tip angle of triangular channels, and hydraulic diameters are changed. Effects of these geometrical changes on the pressure drop,  $Nu$ , and friction factor are investigated. Heat sink is heated from the top plate by applying a constant heat flux ranging from 100 to 1000 W/m<sup>2</sup>. Similar to [31], they found that the friction and heat transfer coefficients increase with increasing  $Re$ , which is highest at the rectangular microchannels and lowest at triangular microchannels. Moreover, pressure drop increases with increasing  $Re$  and/or decreasing hydraulic diameter, while decreases with increasing heat flux since increase in heat flux also increases the fluid temperature which yield reduction in fluid viscosity and thus reduces the pressure drop. From their study, it is understood that every geometrical parameter has a great effect on heat sink performance even when the flow conditions or the overall dimensions remain same, and the effect of each parameter should be examined and considered carefully on the design stage of such heat sinks.

Wang *et al.* [36] also investigated the effect of geometrical parameters on flow and heat transfer characteristics of microchannel heat sinks containing microchannels of rectangular, triangular, and trapezoidal cross-sectional shapes by 3D conjugate heat transfer simulations. All the considered microchannels have same cross-sectional area but different aspect ratios and hydraulic diameters. They assumed laminar,

steady flow of deionized water flowing in copper heat sinks where the properties of water and copper are taken constant except the viscosity of water, which is a function of temperature. They used FLUENT in their simulations and validated their results with experimental ones. They found that as the hydraulic diameter of the channels gets smaller, thermal resistance of the channels also reduces with increasing pressure drop. Also, thermal resistance reduces with increasing  $Re$  and increasing the number of channels in the heat sink whereas the pressure drop increases. For the same hydraulic diameter and cross-sectional area, rectangular channels are found to have the smallest thermal resistance and the triangular channels the highest, among the considered geometries.

McHale and Garimella [37] investigated the effects of aspect ratio and side angles of trapezoidal microchannels on heat transfer and friction factor, numerically in three dimensions by the finite volume method based commercial program FLUENT. The flow is assumed laminar, at steady state and the fluid is incompressible with constant thermophysical properties. They considered both the hydrodynamically fully developed thermally developing flow and simultaneously developing flow with H1 boundary condition where the microchannel is heated from all of the boundaries. Aspect ratios ( $\alpha$ ), which is defined as the ratio of the short base width to the height of the channel, of the simulated trapezoidal microchannels ranges from 0, which corresponds to triangle cross-section, to 100, and the sidewall angles of the channels are  $45^\circ$  and  $54.7^\circ$ . Channel height is fixed to  $250 \mu\text{m}$  and their length is fixed to 5 m while the short base of the trapezoidal channel varies from 0 (triangle) to 12.5 mm. They found that increasing aspect ratio also increases the local and average  $Nu$  and the  $Po$  value. They proposed separate correlations for each of the considered sidewall angles for friction constant, fully developed local and average  $Nu$ , and thermal entrance length for thermally developing flow with H1 boundary condition, which are based on aspect ratio. Proposed correlations for fully developed  $Po$  and  $Nu$  are presented in Eqns. (2.9) and (2.10) for the sidewall angle of  $54.7^\circ$ ,

respectively. They also stated that for the simultaneously developing flow, hydrodynamic boundary layer development provides an increase in local  $Nu$  values.

$$fRe = 13.35 + 10.74 \exp\{-\exp[-0.85(\ln(\alpha) - 1.25)]\} \quad (2.9)$$

$$Nu_{fd} = \begin{cases} 3.121 \\ 3.265 + 5.075 \exp\{-\exp[-0.9041(\ln(\alpha) - 1.3496)]\}, \\ 8.235 \end{cases} \quad (2.10)$$

$$\begin{aligned} 0 &\leq \alpha < 0.1 \\ 0.1 &\leq \alpha < 250 \\ 250 &\leq \alpha < \infty \end{aligned}$$

Lorenzini and Morini [38] numerically investigated the flow and heat transfer characteristics in rectangular and trapezoidal microchannels with sharp and rounded corners, which will be result of fabrication process in wet etching of microchannels and observed especially at the base corners. They considered steady, laminar, fully developed flow with constant thermophysical properties, and applied uniform heat flux either to four sides of the channels (H1) or to three sides. It is found that, for rectangular channels, the  $Po$  and  $Nu$  values increases up to about 20% with increase of radius of curvature of the rounded corners, and the rate of increase decreases as the aspect ratio decreases. However, for the trapezoidal channels, effect of rounded corners on  $Po$  and  $Nu$  are found to be minimal where the maximum increase is about 2%.

Sharma *et al.* [39] numerically investigated the conjugate heat transfer of liquid gallium and water flowing in silicon microchannels. Channels have three different cross-sectional geometries with same cross-sectional area and same total substrate volume, namely: A-type trapezoid where the longer side of the trapezoid is at the base, V-type trapezoid where the longer side of the trapezoid is at the top, and a rectangle. Flow is assumed to be at steady state and laminar. The working fluids and silicon substrate are assumed to have constant properties, and viscous dissipation is neglected. Constant and uniform heat flux is applied at the base of the microchannels and resulting governing equations are solved with FLUENT. They compared the

results on the basis of pumping power and heated surface maximum temperature at various flow rates, which correspond to  $Re = 230-805$  for water and  $Re = 251-879$  for liquid gallium. For the liquid gallium cases, they found that thermal performance of A- and V-type trapezoidal channels are better than rectangular one at all flow rates due to having smaller hydraulic diameters than the rectangular channel with same cross-sectional area and thus have more heat transfer surface area. Among the trapezoidal channels, A-type channel yield lower surface temperatures since it has larger heat transfer area close to the heating surface. However, pumping power for the trapezoidal channels are larger than the rectangular one. For the water cases, rectangular channel performs better both in temperature and pumping power at same flow rates.

Tran *et al.* [40] numerically investigated the effect of channel shapes of circle, square, trapezoid, two concave sides, and two convex sides in a microchannel heat sink on thermal performance where the hydraulic diameter of all channels are kept the same. For the simulations, they assumed steady state, single phase, and laminar developing flow of water in copper channels with constant thermophysical properties and solved the 3D conjugate problem with CFD-ACE+ program. Best thermal performance is achieved with microchannels produced with circular channels. It is found that when the aspect ratio is between 0.33 and 1, thermal performance of the heat sink with trapezoidal cross-section is better than the heat sink with square cross-section, but still lower than the circular ones.

Cao *et al.* [41] numerically investigated the effects of slip velocity, temperature jump, aspect ratio, and base angle on gas flow subjected to uniform heat flux thermal boundary condition through a trapezoidal microchannel in slip flow regime by coordinate transformation technique. Flow is considered as fully developed, laminar and at steady state while body forces and viscous dissipation are neglected. They found that the rarefaction effects reduce the friction and  $Nu$  values and the effects of aspect ratio and base angle become insignificant at high rarefactions. However, when  $Kn$  is constant, as the base angle increase up to about  $60-75^\circ$ ,  $Nu$  and friction

coefficient gradually increases when aspect ratio is below 1 and sharply increase when aspect ratio is larger than 1.

Niazmand *et al.* [42] also numerically investigated the effects of rarefaction, aspect ratio and the side angle on friction and heat transfer in three-dimensional trapezoidal microchannels. They considered simultaneously developing gas flows having low Reynolds numbers ( $0.1 \leq Re \leq 10$ ) in the continuum and slip flow region ( $0 \leq Kn \leq 0.1$ ) with constant wall temperature, velocity slip, and temperature jump boundary conditions. The studied side angles are  $30^\circ$ ,  $45^\circ$ ,  $60^\circ$ , and  $90^\circ$ , and the aspect ratio range is  $0.25 \leq \alpha \leq 2$  where the aspect ratio is defined as the ratio of channel height to the short base of the channel. They neglected the body forces and viscous dissipation in their model. They found great reduction in the friction and heat transfer coefficients in the entrance region of the channel of rarefied flow. Similarly, in the fully developed region,  $Nu$  and  $Po$  values decrease as the rarefaction and aspect ratio increase, and side angle decrease. Moreover, it is found that the rarefaction have more effect on  $Po$  value than the side angle, and as the channel aspect ratio increases,  $Nu$  become less affected from the rarefaction.

Kuddusi and Çetegen [43] numerically investigated the steady state, incompressible, hydrodynamically developed, thermally developing gaseous slip flow in trapezoidal silicon microchannels by transforming the geometry to a unit square and using finite difference method. In their simulations, they included the velocity slip and temperature jump conditions at the walls of the microchannel, but neglected the axial heat conduction. They used constant heat flux boundary condition on side and top walls, and considered the bottom wider wall as adiabatic. They investigated the effect of the aspect ratio ( $\gamma$ ) of the channel, which is defined as the ratio of the height to the wider side of trapezoidal cross-section and ranges from 0 to 0.707 (flat plate to triangular channel), and rarefaction in the range of  $0.001 < Kn < 0.1$ , on  $Nu$  and friction factor. They found that increasing rarefaction and/or aspect ratio reduces the friction in which the rate of decrease is less pronounced for aspect ratios greater than 0.5. Heat transfer rates are found to be very high at the entrance region for low

rarefied thermally developing flows and approaches to fully developed flow values quickly. However, at high rarefactions  $Nu$  does not change along the channel from inlet to outlet. In a following study, Kuddusi [44] extended the analysis of the same problem by considering viscous dissipation and entropy generation. The author found that the friction factor decreases with increasing rarefaction and with increasing aspect ratio up to 0.5. Further increasing the aspect ratio ( $\gamma > 0.5$ ) does not change the friction factor. In the  $\gamma < 0.5$  range,  $Nu$  starts decreasing. In addition,  $Nu$  decreases with increasing rarefaction effect. Moreover, viscous dissipation is found to be effective when  $Br > 0.005$  and increases heat transfer. Below this value, it can be neglected. Lastly, the author argued that the heat transfer from the walls of the microchannel is the main irreversibility source for the  $Br < 0.005$  flows. After that, fluid flow and viscous heating becomes dominant in the total irreversibility.

Among the reviewed experimental and numerical studies in trapezoidal microchannels, a common finding is the dependency of the values of  $Nu$  and  $f$  on  $Re$  in laminar liquid flow. As the  $Re$  increases, values of  $f$  and  $Nu$  also increase [22, 27, 31, 35]. However, in some studies this increase in  $f$  and  $Nu$  are found to be more pronounced in low  $Re$  regime [31], while in some studies it is found to be more in high  $Re$  flows [22]. Additionally, increase in surface hydrophobic character [22], increase in cross-sectional aspect ratio [21, 25], and reduction in microchannel height [37] have increasing effect on the values of  $Po$  and  $Nu$  of liquid flows in trapezoidal microchannels. For the laminar gas slip flows in smooth trapezoidal microchannels, increase in rarefaction and aspect ratio of the trapezoidal microchannel reduces the values of  $Nu$  and  $Po$ . However, at high rarefaction the effect of aspect ratio on  $Nu$  and  $Po$  diminishes [41-43].

In addition to the  $Re$  dependency of  $Nu$  and  $f$ , another common observation is the effect of geometrical parameters of the trapezoidal channels on the results. It is seen that variations in geometrical parameters, such as height, side angle, length of short or long base of trapezoidal channels, greatly changes the obtained  $Po$  or  $Nu$  values.

In some numerical simulations, constant thermophysical properties for the fluid is used. However, temperature variation between the inlet and exit of the microchannels could be great, especially in low velocity flows with heating. In such cases, increase of temperature cause increase or decrease in thermophysical properties, which also cause deviations from the experimental or theoretical results.

## 2.2 STUDIES IN ROUGH MICROCHANNELS

In addition to the previously mentioned experimental studies of [19, 20, 22], Mala and Li [45] also experimentally investigated water flow through rough fused silica and stainless steel microtubes with internal diameters ranging from 50  $\mu\text{m}$  to 254  $\mu\text{m}$ , and mean roughness heights of  $\pm 1.75 \mu\text{m}$ . Experiments were performed up to  $Re = 2500$ . They observed higher friction factor and pressure gradient with an early transition to turbulent flow which is around  $Re = 1000$ . Deviation from the conventional theories increased with increasing  $Re$  and reducing diameter, which is attributed to the effect of surface roughness. They proposed a roughness-viscosity model (RVM) to explain the effects of surface roughness that depends on the idea of increased momentum transfer around the roughness elements. This increased momentum is accounted for by additional viscosity, named roughness viscosity, which is maximum at the wall and gradually reduces towards the center of the channel. When the roughness viscosity is applied to conventional formulation, relatively good agreement is obtained between the theory and experimental results. However, proposed roughness viscosity formulation contains a coefficient, which could only be determined experimentally, makes the applicability of the model difficult.

Kleinstreuer and Koo [46] considered the roughness on the wall of microchannel as a porous medium and proposed the porous medium layer (PML). In this model, the effect of surface roughness on friction factor is simulated by the resistance of the porous layer. In a following study [47], they extend their model to heat transfer in

such conduits and found that the roughness effect on friction factor is more than that on heat transfer. Moreover, effect of  $Re$  on  $Nu$  is also found to be negligible.

Kandlikar and his group are actively working on the effect of surface roughness in microstructures. In [48] Kandlikar *et al.* experimentally investigated the effect of roughness in stainless steel tubes with 0.62 mm and 1.032 mm diameters on pressure drop and heat transfer. The  $Re$  range of the experiments is 500 – 3000. For the larger tube, effect of roughness on pressure drop and  $Nu$  are found to be negligible and experimental results were comparable to theoretical solutions. However, for the smaller tube, roughness increased the pressure drop and heat transfer, which is higher for increased relative roughness. Later, Kandlikar *et al.* [49] proposed new roughness characterization parameters to understand and define the rough surface, and constricted flow concept in which the hydraulic diameter of the rough tube is defined by the newly proposed parameters. They also modified the Moody's diagram with this new concept and extended its range up to 14% relative roughness. Taylor *et al.* [50] discussed the works and new definitions of [49] about the characterization of surface roughness with new parameters and constricted flow approach, by giving attention to the importance of defining and measuring the surface texture properties accurately, and stated the needed future work to understand this phenomenon. Rawool *et al.* [51] numerically investigated air flow in rough square serpentine microchannel for  $40 < Re < 200$  range with CFD-ACE+. Roughness is modeled by trapezoidal, rectangular, and triangular obstructions and sawtooth elements on the sidewalls. It is found that, friction factor and pressure drop increased with increasing roughness height, which is more pronounced with rectangular and triangular elements. Lin and Kandlikar [52] experimentally investigated the effect of geometrical parameters of sinusoidal roughness on heat transfer in rectangular minichannels. The channels are constructed with stainless steel plates in which the roughness patterns are generated laterally on these plates by wire EDM. Height and pitch of roughness structures are varied from 18  $\mu\text{m}$  to 96  $\mu\text{m}$ , and from 250  $\mu\text{m}$  to 400  $\mu\text{m}$ , respectively. Also, the channel is heated with silicon film heaters on back of these plates. Investigated geometrical parameters of

roughness elements are pitch and height of sinusoidal pattern, channel gap and relative roughness, which is defined as the roughness height to hydraulic diameter ratio. They observed that roughness causes early laminar to turbulent transition and significantly increases the heat transfer with increasing relative roughness but the pressure drop increases as well. However, the element pitch is found not to have any important effect on heat transfer among the tested values. Similar geometries are also studied experimentally by Wagner and Kandlikar [53]. This time, structured roughness's pitch and height varied between 150  $\mu\text{m}$  and 400  $\mu\text{m}$ , and 36  $\mu\text{m}$  and 131  $\mu\text{m}$ , respectively. They observed that as the aspect ratio of the channel decreases or the roughness increases with decreasing hydraulic diameter, friction factor increases which is more pronounced for dense and higher roughness. Also, while the roughness pitch is kept constant, increasing roughness height increases the friction. They were unable to find any systematic increase or decrease in friction factor with the change of pitch and height of the roughness. However, they found pitch to height ratios that result in consistently highest friction factors among the tested geometries, which indicates that the geometrical properties of the roughness elements such as height, spacing, height to pitch ratio, height to channel height ratio, etc. have great effect on flow parameters and each geometrical set should be investigated separately. In a later study, Dharaiya and Kandlikar [54] investigated the effects of sinusoidal roughness height, pitch, and channel gap on heat transfer and pressure drop numerically with FLUENT, in low aspect ratio rectangular channels. Steady, laminar, fully developed flow is considered with Kandlikar's constricted flow approach. Sinusoidal roughness is modeled on the opposing two walls of the channel where the fluid is also heated with constant heat flux from these walls. They found that the roughness effect and the fully developed  $Nu$  value reduced with the increase of the channel separation. However, considered roughness pitches were found to be ineffective on fully developed  $Nu$ .

Croce and D'Agaro [55] numerically investigated the heat transfer and pressure drop characteristics in rough microtubes and microchannels for laminar incompressible flow. Surface roughness is modeled as randomly generated rectangular and

triangular obstructions on the smooth surface. Rectangular roughness elements yield increase in  $Nu$ , however triangular roughness elements causes decrease. In a following work, Croce and D'Agaro [56] compared their results with the results of Mala and Li [45] and Kleinstreuer and Koo [46]. Croce *et al.* [57] extended their previous work [55] by defining the roughness elements as three-dimensional conical peaks on a plane microchannel. They found that the effect of roughness is more on pressure drop and less on heat transfer, and stated that geometrical properties of the roughness elements have great effect on the performance of microchannel. Mentioned numerical simulations of Croce and D'Agaro [55-57] are conducted with no-slip boundary conditions.

Croce *et al.* [58] also investigated the compressibility and rarefaction effect on pressure drop in rough parallel plate microchannels, numerically, where they modeled the roughness as triangular obstructions in a portion of the channel. In a following study, they investigated the heat transfer under same conditions [59]. Ji *et al.* [60] also numerically investigated the roughness effect on rarefied, compressible gas flow in microchannels. They modeled the roughness as uniformly placed rectangular slabs on the plates. They found that roughness effect was more pronounced for low  $Kn$  values and the reduction in average  $Nu$  for rarefied flow is more compared to compressible flow. Turgay and Yazıcıoğlu [61] numerically investigated the effect of surface roughness on heat transfer in 2D parallel plate microchannels for air flows having  $Re \leq 100$  by comparing the local and average  $Nu$  values obtained for smooth and rough channels. Roughness is simulated as triangular obstructions on the lower plate of the channel. They found that local  $Nu$  changes periodically over the roughness elements and takes maximum value over the tip of the triangular elements and minimum value at the base corners. Roughness seems to have great impact on heat transfer, compared to the smooth channel, especially at low  $Kn$ . Also it is found that increasing relative roughness increases local and average  $Nu$  when axial conduction and viscous dissipation effects are considered, which is more obvious at low  $Kn$ . On the other hand, when axial

conduction is neglected, surface roughness tends to decrease the average  $Nu$  at low  $Re$  since axial conduction is more dominant at low speed flows.

Zhang *et al.* [62] numerically investigated the effects of roughness shape, size, and spacing on pressure drop and heat transfer of a 2D steady laminar flow between parallel plates. In the analyses  $750 \leq Re \leq 1500$  range is considered. Roughness is modeled as triangle, rectangle, and semicircle obstructions on both plates as shown in Fig. (2.1). Channel height, length, and roughness elements base widths ( $s_o$ ) are  $100 \mu\text{m}$ ,  $5 \text{ mm}$ , and  $8 \mu\text{m}$ , respectively. Roughness heights varied up to  $4 \mu\text{m}$ , and spacing between the roughness elements varied between  $32 \mu\text{m}$  to  $128 \mu\text{m}$ . Liquid ammonia with constant properties is chosen as working fluid. Viscous dissipation and gravitational effects are neglected and uniform heat flux is applied on the walls. It is found that roughness increases the local  $Nu$  and pressure drop along the channel in which the increase is more for semicircle for both, followed by triangle and rectangle elements. Also, average  $Nu$  and  $Po$  values are found to be increasing with  $Re$  for semicircle and triangle elements, while average  $Nu$  decreases and  $Po$  increases very little with increasing  $Re$  for rectangular elements. Roughness height is found to have increasing effect on average  $Nu$  and  $Po$ , which is weaker for rectangle elements. Lastly, increasing the spacing between the roughness elements is found to decrease the average  $Nu$  and  $Po$  that is more obvious for semicircle and triangle elements.

Hossainpour and Khadem [63] numerically investigated the effect of roughness shape on heat transfer and friction factor of a pressure driven gas flow in a two dimensional parallel plate channel. For this purpose, they considered four separate cases, in which they modeled the roughness as uniformly and symmetrically placed rectangular, triangular, and trapezoidal elements, and randomly distributed triangular peaks, on both of the plates. Representative geometries of these channels are shown in Fig. (2.2).

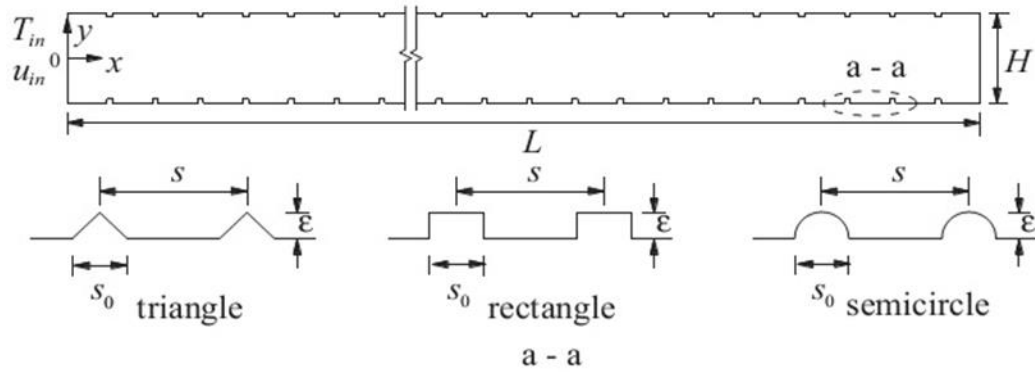


Figure 2.1: Schematic of the rough microchannel and roughness elements used in [62].

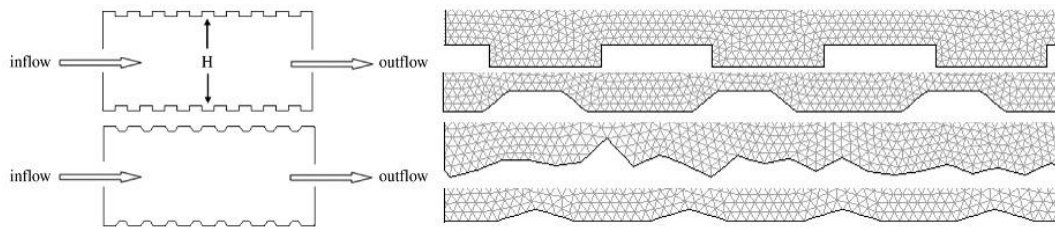


Figure 2.2: Representative channel geometries used in [63].

They assumed that the flow is steady, compressible, in slip flow regime, and the working fluid is the air with constant thermophysical properties. They considered four relative roughness height ( $\epsilon$ ) values, 1.25%, 2.5%, 3.75%, and 5.0%. They also defined a parameter called peak density,  $Pd$ , as the number of roughness elements in each 0.1 mm of channel length and considered the cases of  $Pd$  equal to 10, 20, and 50. They solved the governing equations with constant wall temperature, slip velocity and temperature jump boundary conditions by a finite volume CFD code. For the channels having rectangular and trapezoidal roughness elements, they found that the  $Po$  increases with increasing peak density or relative roughness, where the

effect of peak density on  $Po$  becomes more obvious as relative roughness increases. It should also be noted that the effect of the rectangular elements is greater than the trapezoidal elements since trapezoidal elements have smoother corners and disturb the flow less compared to the rectangular ones, resulting in lower friction and  $Po$  for trapezoidal geometry than rectangular geometry. When peak density is taken constant and relative roughness is between 1.25% and 3.75%, rectangular elements yield the highest  $Po$ , which is followed by trapezoidal and randomly distributed triangular elements, and the uniform triangular elements yield the lowest  $Po$  values. However, as the relative roughness increased further to 5.0%, randomly distributed triangular elements yield the highest  $Po$  while the order between the others do not change, which shows the distribution of the elements become more important after some degree of relative roughness value. For the heat transfer analysis, they found that  $Nu$  decreases as the relative roughness or peak density increases, and the decrease is more obvious at high peak density values for rectangular and trapezoidal elements. As the relative roughness increases, difference between the  $Nu$  values of trapezoidal, rectangular and triangular elements becomes more obvious and  $Nu$  of rectangular case drops more than the others. Hossainpour and Khadem [63] stated that the recirculation behind the roughness elements affect the heat transfer in a reducing manner. The channel with triangular roughness elements happens to have the greatest average  $Nu$  values than the others where the rectangular geometry yields the smallest for all peak densities and relative roughnesses. They also stated that the effect of roughness is more pronounced at higher  $Kn$  values with high relative roughness. However, the paper lacks convenient results. Moreover, nothing is stated about the inlet, average, or exit  $Kn$  value for any of the results of rough channels presented.

Liu *et al.* [64] investigated the effect of roughness and rarefaction on  $Po$  numerically by lattice Boltzmann method (LBM), where the rarefied gas is flowing in a 2D microchannel in the  $0.02 \leq Kn \leq 0.8$  range. Surface roughness is modeled by rectangular obstructions on the walls. The width and spacing of the obstructions are kept constant, while their height is varied, which yield a relative roughness range of

$0 \leq \varepsilon \leq 0.1$ . They found that roughness increases the friction factor while the rarefaction decreases. Another LBM simulation is done by Cui *et al.* [65] in which the effects of surface wettability and roughness characteristics on pressure drop in a 2D parallel plate channel is investigated. They defined the roughness as uniformly distributed rectangular peaks on both the plates, and numerically showed that the presence of surface roughness can reduce the pressure drop on hydrophobic surfaces while increases on hydrophilic surfaces, compared to smooth walls.

Ding *et al.* [66] investigated the flow patterns and drag coefficients of incompressible viscous flow over various non-smooth surfaces for  $Re = 2000$  numerically by Lattice Boltzmann method. Considered surfaces include roughness shapes of regular and irregular sinusoidal waves with different wave amplitudes, convex and concave circular elements, and convex and concave triangular elements. They found that the smallest drag coefficient is obtained with the circular concave surface, which is followed by the triangular concave surface. On the other hand, highest drag coefficients are obtained with circular and triangular convex surfaces, which are also higher than the theoretical value for a smooth plane. The reason for the drag reduction is attributed to the streamwise vortices, which are formed and settled inside the concave surfaces. These vortices behave like a fluid roller bearing and reduce the drag force. However, simulations are only carried out for  $Re = 2000$ , and it is not shown how the surfaces behave for flows having higher or lower  $Re$  values.

Chen *et al.* [67] numerically investigated the steady laminar heat transfer in 2D rough parallel plate channels where the roughness is defined by fractal rectangular shaped Cantor structures on both of the plates, by finite difference method. They applied the constant heat flux boundary condition at both walls, and assumed constant fluid properties. Investigation ranges of  $Re$  and relative roughness ( $\varepsilon$ ) are  $500 \leq Re \leq 1500$  and  $0.005 \leq \varepsilon \leq 0.020$ , respectively. They found that the heat transfer performance of the rough channel is better than the smooth one and the average  $Nu$  value increases linearly with increasing  $Re$ . According to the authors,

the enhancement in heat transfer is due to flow perturbation near the rough walls, which causes flow separation and boundary layer regeneration, and reduced cross-section at the rough peaks, which increases the local velocities.

Xiong [68] conducted 3D numerical simulations of water with constant hydrodynamic properties flowing in rough trapezoidal microchannels by using ANSYS-CFX software. Roughness is defined at the base wall of the channel randomly and other walls of the channel are considered as smooth. The author investigated the effect of relative roughness height,  $Re$ , aspect ratio, and sidewall angle of trapezoidal channel on  $Po$  value, and found that  $Po$  increases with  $Re$  in the developing flow region, while it remains independent in fully developed region. Additionally, existence of roughness increased  $Po$  in both regions, which is larger in developing flow region. Moreover, as the aspect ratio of the rough channel becomes smaller,  $Po$  values deviate more from the theoretical ones.

Liu *et al.* [69] numerically studied the heat transfer and liquid flow in microchannels having five different surface geometries, with (A) ridge-shaped grooves, (B) V-shaped grooves, (C) shield-shaped grooves, (D) straight slot grooves, and (E) smooth surface, as shown in Fig. (2.3). However, groove heights (or depths) are 1 mm, and channel length and widths are 60 mm and 20 mm, respectively. Therefore, the channels are actually in mini size rather than micro size. Simulations are conducted by using 10 roughness elements with constant wall temperature and periodic boundary conditions. They simulated the liquid water flow with constant density and temperature dependent viscosity, thermal conductivity, and specific heat in  $50 \leq Re \leq 500$  range by using FLUENT and lattice Boltzmann method (LBM) in the continuum regime. Then, they compared the results of each method. They found that maximum heat transfer enhancement is obtained by shield-shaped grooves among the investigated geometries, which is about 1.3 times the smooth channel value. They also stated that both CFD (FLUENT) and LBM gives similar results.

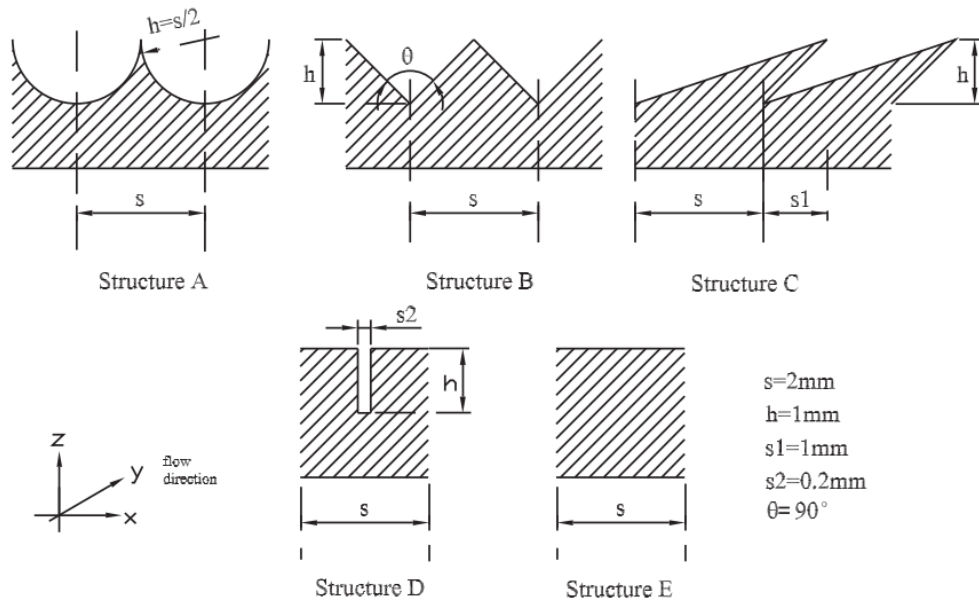


Figure 2.3: Representative channel geometries used in [69] (A) ridge-shaped grooves, (B) V-shaped grooves, (C) shield-shaped grooves, (D) straight slot grooves, and (E) smooth surface.

Cui and Fu [70] numerically investigated the pressure drop and drag reduction performance of four different biologically inspired grooved surfaces by Lattice Boltzmann Method (LBM). The considered surfaces are similar to those of [68] and consist of placoid-shaped grooves that resembles skin of sharks (a), V-shaped grooves that inspired from wing of jaegers (b), riblet-shaped grooves that inspired from skin of seals (c), and ridge-shaped grooves that resembles the outside surface of shells (d), which are shown in Fig. (2.4). Channels have 40 mm length, 8 mm height, and 20 grooves are evenly distributed on the bottom wall, which are  $s = 2$  mm apart from each other, and have the same height of  $h = 1$  mm. Additionally,  $s1$  and  $s2$  values in Fig. (2.4) are 1 mm and 0.2 mm, respectively. Water is chosen as the working fluid and the 2D numerical simulations are conducted for  $Re$  up to 200. They computed the friction factor and pressure drop along the channel for each geometry and compared them with those obtained for the smooth channel. They

stated that when the  $Re$  of the flow exceeds a critical value, which is different for each geometry, vortices are formed within the grooves and decrease the shear force between the fluid and wall, resulting in drag reduction. However, if the vortices cannot be formed, pressure loss and thus the drag increases. All the geometries resulted in reduced pressure drop, but ridge-shaped grooves performed better in drag reduction among the others. Moreover, the authors also recommended using smaller width-to-height ratio ridge-shaped grooves for low  $Re$  flows ( $Re < 100$ ) since these flows have low energy and produce smaller vortices, and higher width-to-height ratio ridge shaped grooves for the high  $Re$  flows ( $Re > 100$ ) which can form larger vortices.

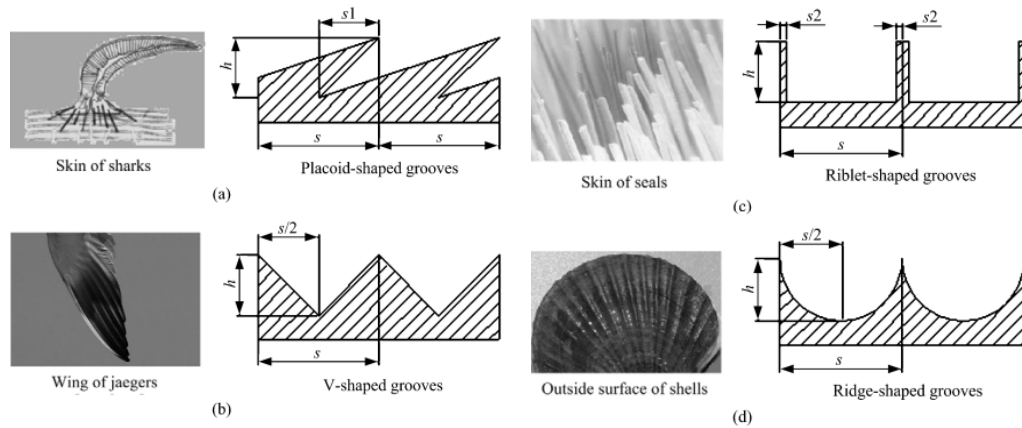


Figure 2.4: Bionic surface geometries considered in [70] (a) placoid-shaped grooves, (b) V-shaped grooves, (c) riblet-shaped grooves, and (d) ridge-shaped grooves.

Liu *et al.* [71] experimentally investigated the heat transfer and pressure drop of water flowing in rectangular microchannels with longitudinal vortex generators (LVG). For this purpose, they produced six silicon microchannels by etching. Five of the microchannels have different number of LVG pairs, configurations, and different attack angles, while one of the microchannels is kept smooth as a control channel. Length, width, and height of the produced channels are  $100 \mu m$ ,  $1500 \mu m$ ,

and 20,000  $\mu m$ , respectively. LVGs length and widths are 400  $\mu m$  and 50  $\mu m$ , respectively, and the attack angles of the LVGs are between 30° and 150°. Experimental  $Re$  range is  $170 \leq Re \leq 1200$ . Authors stated that early transition, from laminar to turbulent flow, occurred and the  $Re_{cr}$  values are between 600 and 730 for channels with different LVG configurations. They found that the channels having LVG pairs with attack angle of 45° and 135° have better heat transfer performance, lower  $Re_{cr}$ , higher friction factor and pressure drop than the channels having LVG pairs with attack angle of 30° and 150°. When  $Re < 600$ ,  $Nu$  values for channels with LVGs are slightly higher than the smooth channels, which indicate that the longitudinal vortices are not effective in laminar regime. However when  $Re \geq 600$ ,  $Nu$  values differ significantly than the smooth channel values and  $Nu$  increases more as  $Re$  increases, which indicates that the three-dimensional vortices enhance swirl flow and heat transfer, and cause early transition to turbulence. Similarly,  $Nu$  is not affected much in laminar regime when the number of LVG pairs is increased, but in turbulent regime, increasing the number of LVG pairs also increases the  $Nu$  value. Moreover, placing the angle of the LVG pairs does not affect the  $Nu$ , friction factor, and pressure drop much if the number of LVGs are constant. However, increasing the number of LVG pairs is found to increase the friction factor meanwhile increasing the  $Re$  reduces the friction factor.

Ahmed *et al.* [72] investigated the effect of copper-water nanofluid use on heat transfer and pressure drop in a 2D corrugated channel, numerically. Channel geometry is presented in Fig. (2.5). They solved the laminar incompressible flow governing equations by finite difference method for  $100 \leq Re \leq 1000$ , and nanoparticle volume fraction range of 0 to 0.05. They found that local  $Nu$  takes higher values over the converging section of the corrugations than the diverging section due to higher velocities in the converging section, and local and average  $Nu$  values increase with increasing volume fraction of nanoparticles up to  $Re = 200$ . Meanwhile, pressure drop also increases slightly. However, enhancement in  $Nu$  starts decreasing after  $Re = 200$ , which is more obvious for high volume fractions,

due to flow separation and increased thermal conductivity of the fluid being more effective than convection at low  $Re$  values.

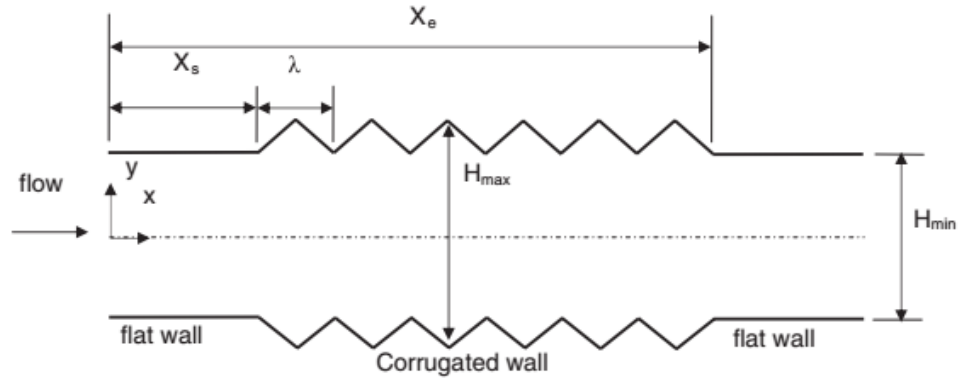


Figure 2.5: Schematics of the corrugated channel used in [72].

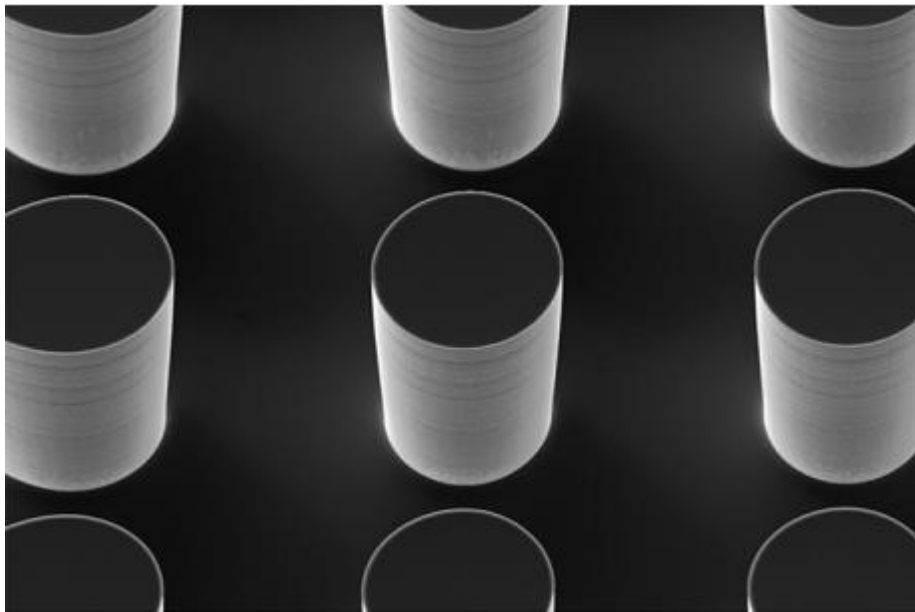


Figure 2.6: Image of the micro pin fins used in [73].

Ndao *et al.* [73] experimentally investigated single-phase jet impingement heat transfer on both a smooth surface and a surface containing 64 circular micro pin fins with diameters of 125  $\mu\text{m}$ , heights of 230  $\mu\text{m}$ , and pitches of 250  $\mu\text{m}$ , as shown in Fig. (2.6). They found no significant enhancement in heat transfer at low  $Re$  values, however  $Nu$  increases with increasing  $Re$  for both the smooth surface and the structure with pin fins. Experimental results for the smooth surface show that the  $Nu$  values are higher than those predicted by the correlations existing in the literature. Moreover, enhancement in heat transfer coefficient of micro pin fin structure is found to be up to 200% with respect to smooth cases. Authors attributed this enhancement to increase in the area, flow mixing, turbulence, and boundary layer interruption.

Tamayol *et al.* [74] experimentally and analytically investigated the steady creeping flow of nitrogen in silicon rectangular microchannels consisting of fin like cylindrical structures. The channels are manufactured by deep reactive ion etching (DRIE) method. Produced channels have 2 mm widths, 200  $\mu\text{m}$  heights, and 10 mm lengths, whereas the micro cylinders inside the channels have diameters varying between 15 to 210  $\mu\text{m}$  with spacing 40 to 400  $\mu\text{m}$ . An example of the produced channel is shown in Fig. (2.7). They compared the pressure drop and flow resistance results of two different analytical approaches, namely the porous medium approach where the problem is modelled as a channel filled with porous medium, and variable cross-section channel approach where the flow between cylinders is modelled as the flow along a variable cross-section microchannel, with the experimental ones. The results indicated that the former approach shows good agreement over a wide range of porosity and maximum deviation from the experiments is less than 25%, while the latter approach gives more accurate results for lower porosities. Results indicate that adding micro cylinders to micro/mini channels enhances the surface area to volume ratio, which will increase the heat transfer eventually, at the expense of an increase in overall pressure drop. However, there is no linear relation between pressure drop and surface area to volume ratio. Using small sized micro cylinders can yield high surface area to volume ratio with a lower pressure drop. On the other

hand, if small surface area is desired, using micro cylinders with larger diameters yield lower pressure drop.

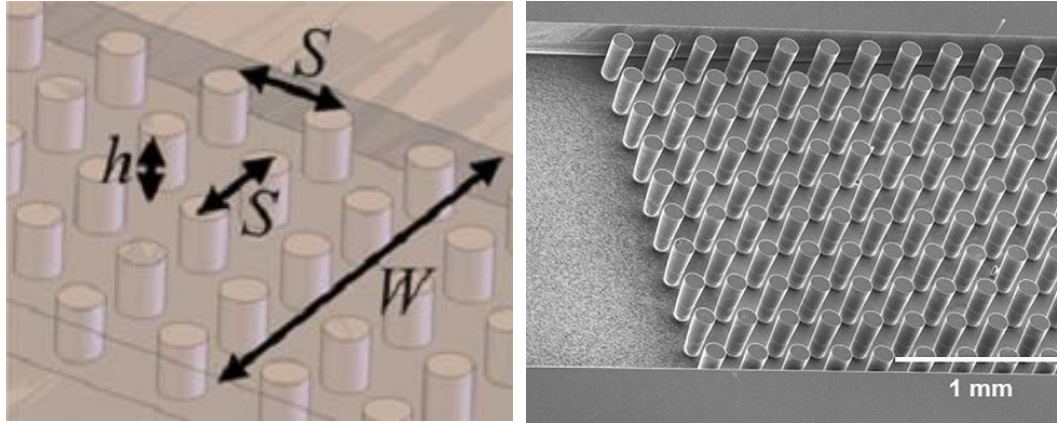


Figure 2.7: Schematic view of the channel with micro cylinders (left), and SEM image of a silicon micro cylinder array [74].

More recently, Kirsch and Thole [75] investigated the heat transfer and friction factor in microchannels with pin fin arrays, experimentally. Investigated pin fin arrays have four different spacing configurations and are produced by a 3D printing method, namely laser powder bed fusion method (LPBF). Produced arrays have noticeably higher surface roughness than the conventionally manufactured ones, due to production method. They observed that the surface roughness in the pin fin array structure manufactured by LPBF depends on pin spacing and shape of the pin since as the number of pins is increased, surface roughness also increases and more distorted pin shapes are obtained. They conducted experiments in the range  $500 < Re < 25,000$  and stated that friction factor is increased considerably compared to smooth pin fin arrays. However, heat transfer enhancement remained minimal.

Gong and Wei [76] numerically investigated effects of geometrical properties of waves and dimples in microchannel walls on heat transfer and pressure drop. The

simulated copper heat sink that cools a CPU contains square microchannels of 20 mm length. They applied constant heat flux at the middle of the channel to simulate the heat-dissipating chip of 10 mm length, and considered only the center microchannel of the heat sink. They compared the pressure drops and  $Nu$  values of microchannels with wavy walls, containing dimples at the bottom walls, and channels having both wavy walls and dimples with the smooth channel results. Schematics of the channels are given in Fig. (2.8). They found that wavy walls increase the heat transfer with an increase in the pressure drop. On the other hand, the dimples in the channel can reduce the flow resistance depending on the depth of the dimples and increase the heat transfer. Combination of both the wavy walls and dimples further increase the heat transfer with negligible additional pressure drop compared to wavy wall only microchannel.

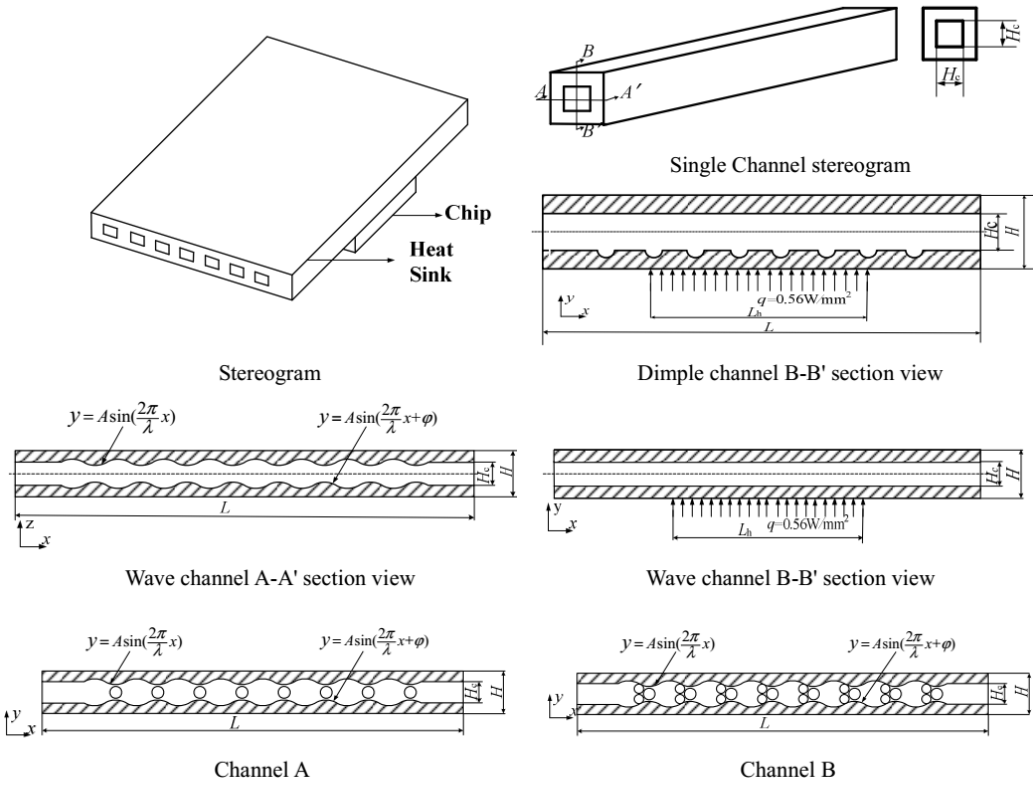


Figure 2.8: Schematic views of the channels considered in [76].

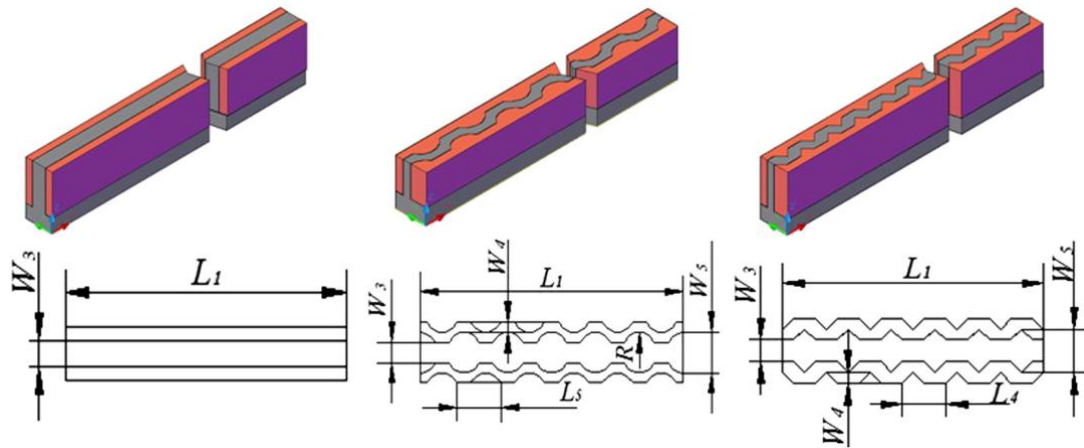


Figure 2.9: Schematics of simulated channels in [77], regular rectangular (left), with offset fan-shaped reentrant cavities (middle), and with triangular reentrant cavities (right).

Xia *et al.* [77] numerically investigated the effects of inlet/outlet locations, header shapes and channel shapes of silicon microchannel heat sinks on fluid flow and heat transfer. Considered microchannel shapes are shown in Fig. (2.9), and are regular rectangular channels, channels with offset fan shaped (semicircular) reentrant cavities, and channels with triangular cavities, where the cavities are placed at the sidewalls. They assumed single-phase laminar flow of water at steady state with temperature dependent piecewise-linear thermophysical properties, and solved the 3D conjugate problem with FLUENT by taking the entire heat sink as the computational domain, which is heated from the bottom with a constant heat flux. It is found that pressure drop is higher in channels with reentrant cavities than rectangular channels, and total pressure drop increases with increasing flow rate. On the other hand, average and maximum temperatures for channels with triangular reentrant cavities are lower than rectangular channels. Existence of reentrant cavities enhanced heat transfer by increasing heat transfer area, disturbing flow near the cavities that interrupts the laminar boundary layer and cause to redevelop, and

causing expansion / contraction in flow cross-section that increases mixing between the wall and core flow.

Li *et al.* [78] also numerically investigated effect of fin and cavity shapes on flow and heat transfer in 10 different microchannel heat sinks, in which the geometries of investigated microchannels are similar to those of [77], and shown in Fig. (2.10). They assumed steady laminar flow of water with temperature dependent thermal conductivity and dynamic viscosity. Other thermophysical properties of water and the silicon substrate are kept constant. They used FLUENT to solve the 3D conjugate problem. They found that channels with rectangular fins resulted in the lowest average heated surface temperatures, while the channels with triangular fins resulted in the highest. On the other hand, triangular fins caused smallest increase in friction while the rectangular fins caused the largest. In addition, it is observed that, different configurations of fins and cavities performed better for different  $Re$  ranges.

Kim *et al.* [79] experimentally showed the drag reduction capabilities of engineered surfaces with hierarchical micro and nanostructures. For this purpose, they produced a bare smooth metal surface, a metal surface with micro riblets, a metal surface with nanostructures, and a metal surface with nanostructures over micro riblets, where the micro riblet dimensions range between 35  $\mu\text{m}$  and 270  $\mu\text{m}$  with 20  $\mu\text{m}$  spacing between them, and nanostructure heights are 150 nm. They conducted the experiments in rectangular microchannels, where the bottom walls are the mentioned metal surfaces, and measured the pressure drop between the inlet and exit of the channels for  $1500 \leq Re \leq 7600$  range. It is found that the pressure drop in channels with smooth and engineered bottom surfaces in laminar regime and early transition regime is nearly same. However, as the  $Re$  of flow is increased, increase in pressure drop reduced with the complexity of the surfaces. For the upper  $Re$  limit of the experiments 20%, 28%, and 36% drag reduction ratios compared to bare metal surface are achieved for surfaces with micro riblets, nanostructures, and nanostructures over micro riblets, respectively.

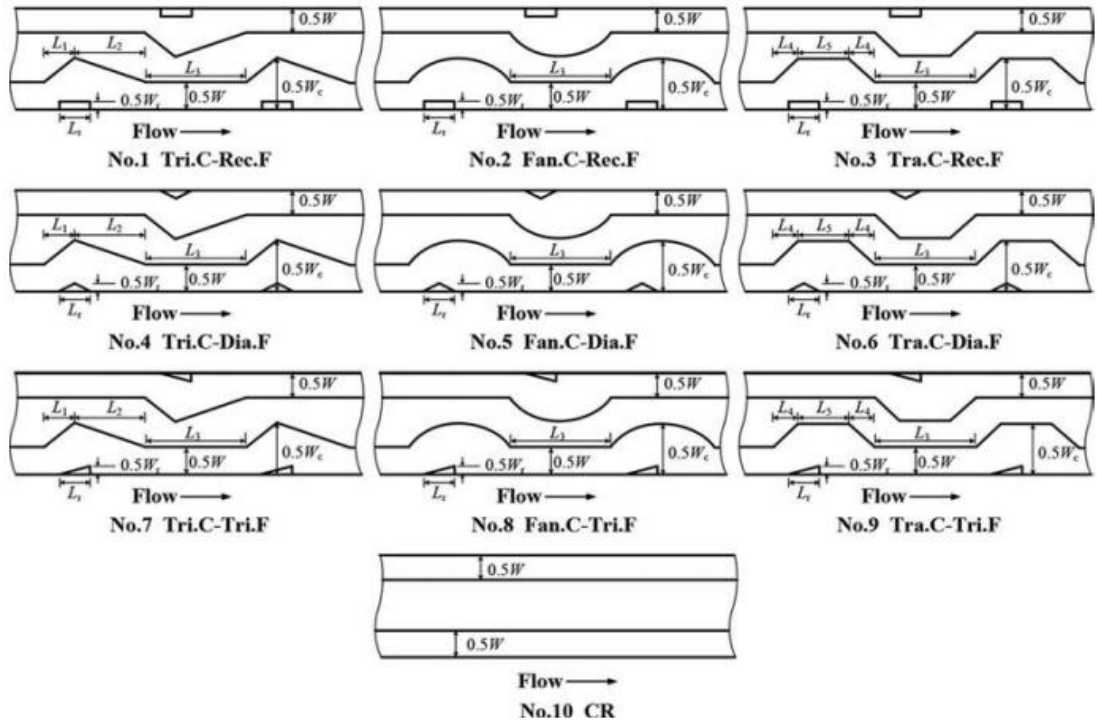


Figure 2.10: Schematics of channels used in [78] (*Rec*: Rectangular, *Tri*: Triangular, *Fan*: Fan shaped, *Tra*: Trapezoidal, *Dia*: Diamond, *C*: Cavity, *F*: Fin, *CR*: Conventional Rectangular).

Surface roughness, natural or engineered, is not only an important parameter for heat transfer and pressure drop, but also an important parameter for biomedical applications. Tsougenia *et al.* [80] investigated the mechanical stability of rough structures on microchannel surfaces and protein adsorption on these channels. Rough microchannels are produced via lithography and deep  $O_2$  plasma etching on PMMA (polymethyl methacrylate) substrates. They demonstrated controlled protein adsorption and extremely sensitive target protein detection by changing the roughness and wettability properties of the microchannels experimentally, which can be used in bioanalytical microfluidic and lab-on-a-chip devices. Surfaces of these microchannels are shown in Fig. (2.11).

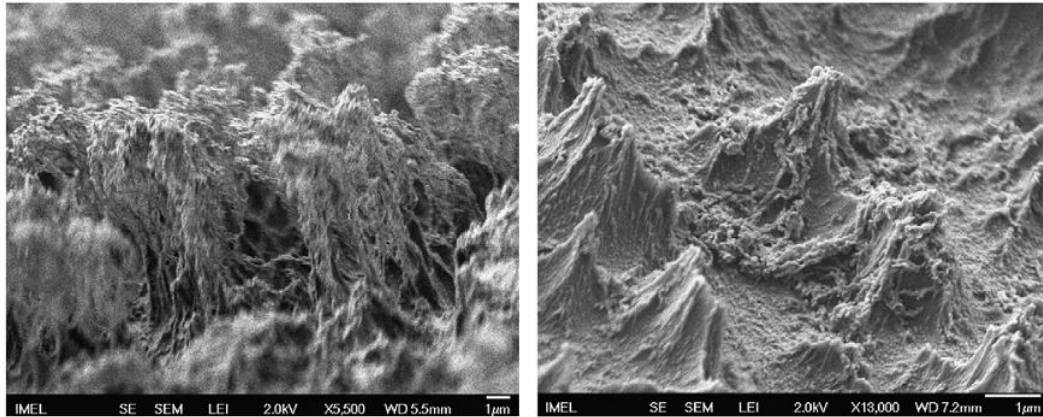


Figure 2.11: SEM images of PMMA surfaces at the bottom of microchannels formed by means of etching in  $O_2$  plasma prior to (left) and after (right) immersion in water and drying [80].

An interesting work studying natural roughness in shark's skin is presented by Oeffner and Lauder [81]. They experimentally investigated the hydrodynamic performance of both rigid and flexible membrane-like foils made of real shark skin where skin denticles are shown in Fig. (2.12), silicon riblet material with evenly spaced ridges that mimics shark's skin (Fig. (2.13)), and Speedo shark skin-like swimsuit fabric (Fig. (2.14)). In terms of swimming speed, they found 12.3% increase with flexible real shark skin and 7.2% increase with silicon riblet material, compared to that of a shark skin foil whose denticles are removed by sanding. However, they could not find any consistent speed increase with Speedo fabric. One interesting finding is when the denticles are removed from the shark's skin that is attached to the flexible foil; it slows down the swimming speed. However, if the shark's skin is attached to a rigid foil it increases the swimming speed, which indicates that the skin denticles are important and effective on moving flexible bodies. They also stated that the denticles and the riblets that mimic them alter the vortex formation and location, and reduces drag while increasing the thrust, lift, and maneuvering forces of the sharks. Lastly, for the riblets, they found that the

geometric properties of roughness elements are more important than their orientation with respect to flow direction.

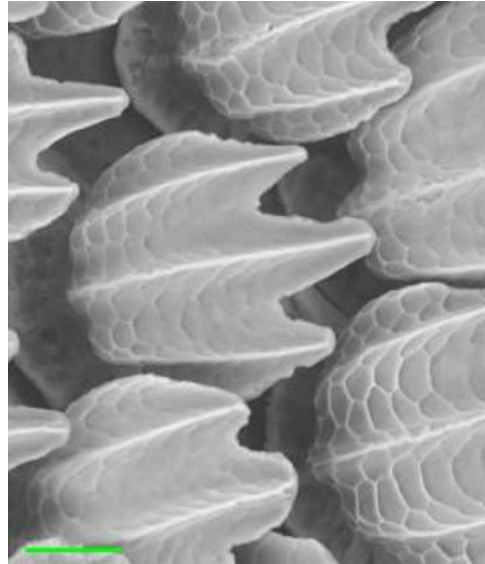


Figure 2.12: Image of denticles from the surface of the mid-body region in a bonnethead shark (Scale bar =  $50 \mu m$ ) [81].

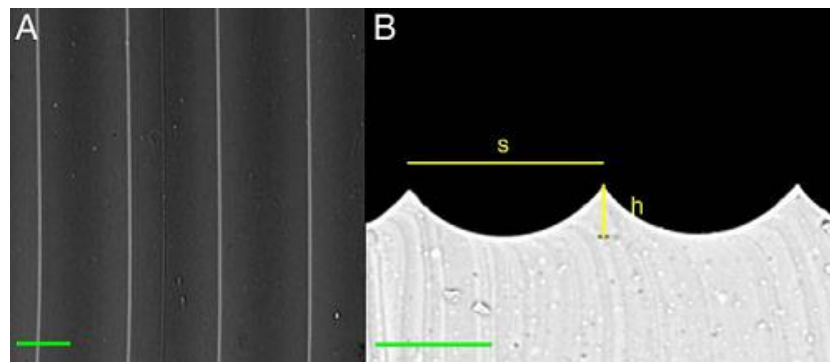


Figure 2.13: Images of the biomimetic riblet silicone material (Scale bars =  $200 \mu m$ ). (A) Front side. (B) Cross-section view,  $h = 87 \mu m$ ,  $s = 340 \mu m$  [81].

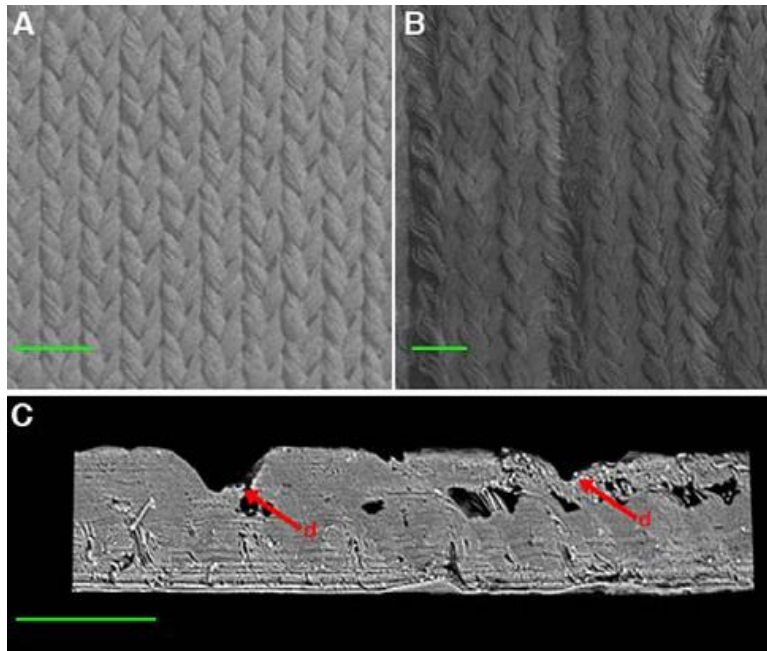


Figure 2.14: Images of Speedo shark skin-like swimsuit fabric (Fastskin FS II) (Scale bars =  $500 \mu m$ ). (A) Underside surface image (non-biomimetic), (B) Outside surface image (biomimetic), (C) Cross-section image showing the dents on the biomimetic side (red arrows) [81].

Another natural phenomenon where surface roughness plays an important role is the lotus effect. Samaha *et al.* [82] reviewed the works about lotus effect, superhydrophobic surfaces, alternative production methods, and probable use of these engineered surfaces in different areas from self-cleaning surfaces to submarines. In short, lotus effect is the superhydrophobicity of a surface in which the fluid exerts minimal skin friction drag on a surface and so the surface repels the fluid like in the lotus leaf. Lotus leaves consist of epidermal cells that look like microstructures and hair-like wax crystals in nanoscale. Combination of these micro and nanostructured roughness elements reduces the contact area between the fluid droplet and the leaf surface and increases the static contact angle above  $150^\circ$ , which results in a superhydrophobic surface. SEM images of a lotus leaf showing these micro and nanostructures is provided in Fig. (2.15).

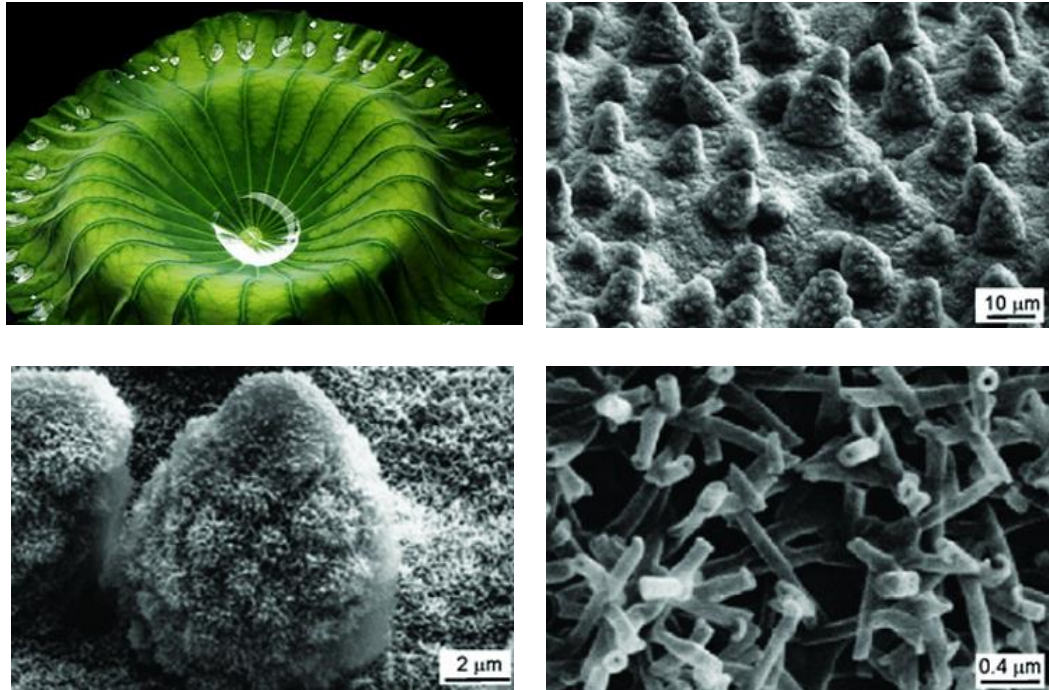


Figure 2.15: Images of a lotus leaf showing micro and nano structures [82].

Additionally, effects of natural or engineered surface features of biomedical materials and their use in biomedical applications for protein, blood, and bacterial adhesion and analysis is discussed by Luong-Van *et al.* [83]. It is seen that surfaces can be engineered to get the designed response and effectiveness from the biomedical device, but design criteria will be different for each biomaterial and the biological matter that interacts with these surface features. However, in general, by using natural random roughness of the surfaces or the engineered rough surfaces like pillars, protein adhesion or selection can be done effectively.

To understand the effect of surface roughness on flow and heat transfer, various geometries resembling roughness have been used by the researchers. Most commonly used geometries are randomly generated or orderly placed rectangular, triangular, trapezoidal, and cylindrical structures. It is observed from the literature that, not only the geometrical properties of the main channel but also the geometrical properties of the simulated roughness elements, such as height, cross-sectional

shape, spacing and density of used elements, affects the flow parameters and desired results considerably. Moreover, each roughness geometry yields different results for similar flow conditions in the same microchannel. Each geometry can increase or decrease pressure drop,  $P_o$ , and  $Nu$  in a different way, depending on the flow conditions and geometrical properties. A systematic formulation has not been proposed yet, due to the randomness character of roughness.

### 2.3 STUDIES CONDUCTED WITH COMSOL MULTIPHYSICS

From the reviewed literature, it is observed that use of simulation programs is increasing with time. Due to developments in computer hardware, increased computational power, and accessibility, efficiency, and cost advantage compared to experiments along with the ease of use of such programs, both the number of simulation programs and the published works that are performed with these programs are increasing in the literature. Since the current work is numerical and the commercial CFD program COMSOL Multiphysics is used for this purpose, knowing the capabilities, advantages, and disadvantages of this program, how well it solves various problems compared to other commercial CFD programs, and what kind of adjustments should be done for acceptable results, becomes a significant issue. Thus, in addition to the presented literature review about microscale flow and heat transfer in smooth and rough channels, studies done by using this specific program are also reviewed for further knowledge.

Other than the in-house codes, there are several commercial and open source CFD programs existing in the market, such as the widely used ANSYS Fluent, ANSYS-CFX, COMSOL Multiphysics, ADINA, and OpenFOAM. Among these programs ANSYS Fluent, ANSYS-CFX, and OpenFOAM use finite volume method (FVM) while COMSOL Multiphysics and ADINA use finite element method (FEM). Knowing their solution methodologies and performance on specific fields is

essential for the users. Additionally, comparing such programs in specific test cases gives users very valuable information about the details on the use of these programs.

Chang *et al.* [84] tested the commercial programs COMSOL Multiphysics v4.4 and ANSYS-CFX v14.5 and open source program OpenFOAM v2.3.1 with the benchmark problem of CANDU nuclear reactor. All the tested programs gave comparable results. Jeong and Seong [85] compared the commercial programs ANSYS-CFX v11, ANSYS Fluent v6.3 and ADINA v8.6 within a test geometry and by using the same mesh elements in each program. They stated that FEM solutions are sensitive to mesh type and mesh quality, and require approximately five times more calculation time than FVM codes.

Each CFD program has its advantages and disadvantages depending on the application field. COMSOL Multiphysics [86] is a powerful simulation program in which the user can model and solve various multiphysics problems easily, including fluid flow and heat transfer. Al-Waaly *et al.* [87] experimentally and numerically investigated the effectiveness of subchannels in microchannel heat sinks to reduce the temperature of hotspots on chips or circuits with non-uniform heat flux. They considered steady state, single phase, laminar flow of deionized water in the microchannel heat sink without subchannels, which has normal parallel channels, and with subchannels in which the main parallel channels are divided into two subchannels above the hotspots. For the numerical simulations, they used COMSOL v3.5a. They found that adding subchannels reduces the surface temperature and improves temperature distribution uniformity. Brinda *et al.* [88] used COMSOL to numerically investigate the effect of aspect ratio of parallel ladder shaped microchannels having rectangular cross-section that is used in integrated circuit cooling. They analyzed the variations in pressure drop,  $Po$  value, thermal resistance, and heat transfer coefficient of laminar single-phase water flow. They stated that high thermal performance is achieved by smaller aspect ratio with higher pumping power. Han *et al.* [89] numerically investigated the effects of geometrical properties, electrical potential, and driving pressure on thermal performance of trapezoidal and

rectangular microchannel heat sinks under pure pressure driven flow, pure electro-osmotic flow, and combined flow conditions with COMSOL. They considered steady laminar flow of water with temperature dependent thermophysical properties, joule heating, and viscous dissipation. They found that trapezoidal microchannel has better thermal performance and less thermal resistance than the rectangular one with the same bottom width and hydraulic diameter. Also, increased fluid motion has been achieved with combined flow especially in microchannels with small hydraulic diameter, compared to pure pressure driven flow. Another numerical heat sink investigation is done by Kim *et al.* [90] in which five stacked multistage heat sinks containing parallel square minichannels is investigated with COMSOL. The authors considered laminar, single-phase, steady state water flow. They analyzed the changes in local convection coefficient, coolant temperature, channel wall temperature, effectiveness, and pressure drop with varying mass flux, heat source temperature, and number of stacks. They found that the cooling rate increases with number of stacks. However, this increase gradually reduces as the number of stacks increased and the largest effectiveness is found to be with three stacks. On the other hand, pressure drop is higher in the multistage heat sink than the single stage due to additional corners and increased channel length. However, increase in pressure drop is small compared to increase in cooling rate.

Yu *et al.* [91] experimentally and numerically investigated fluid flow and heat transfer in a microscale heat sink having rectangular cross-section with Piranha Pin Fin (PPF) configuration, which is shown in Fig. (2.16), using COMSOL. It is found that PPFs increases the friction factor compared to the plain channel a little, but much smaller than normal pin fin heat sinks. Existence of PPFs also increases the heat transfer since they provide additional heat transfer area, disturb the velocity field, and enhance mixing. Moreover, fluid extraction through PPFs significantly increases the  $Nu$  and reduces the pressure drop.

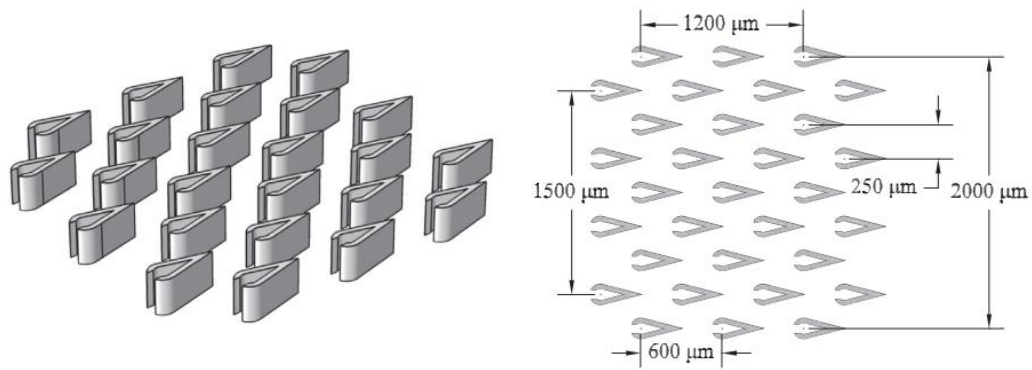


Figure 2.16: Piranha Pin Fin (PPF) array used in [91].

Lin *et al.* [92] experimentally and numerically investigated the effects of fins length, height, cross-sectional shape, and density on cooling of LED by natural convection with a finned heat sink. For the numerical part, 3D transient conjugate heat transfer is considered via COMSOL. Authors stated that trapezoid shaped fins performed better than rectangular fins on cooling. Yao *et al.* [93] experimentally and numerically investigated the junction temperature distribution of microchips of high voltage LEDs in different configurations. They used COMSOL for the 3D conjugate numerical simulation part and obtained good agreement with the experiments.

Rao *et al.* [94] demonstrated the modeling of fluid-structure interaction using ALE method in a 2D microchannel in which the deformed obstacles are circular, rectangular, and ellipse shaped, with COMSOL v4.2a. Bejan *et al.* [95] numerically compared different cross-sectional shapes of channels by means of pressure drop and flow resistance along the flow channel and thermal resistance in transverse direction by using COMSOL v4.3. Outside channel elements have square and triangle cross-sections while the inside flow cross-sections are circle, square with rounded corners, and square with 90° corners for square outside channel elements, and triangle and circle for triangle outside channel elements. For mesh independence tests, they sought the difference in average outlet temperature. They stated that, square flow channel with 90° corners exhibits best performance while the circular

is the worst for the square elements. For the triangular elements, triangular flow cross-section performed better than the circular one.

Luo *et al.* [96] numerically investigated heat and mass transfer characteristics of laminar flow of water with constant thermophysical properties for very low  $Re$  region ( $Re < 2.733 \times 10^{-3}$ ) in two circular and one square leaf-vein-inspired microchannels with COMSOL v4.3b, which are modeled with reticulate/pitted (Fig. (2.17a)), annular (Fig. (2.17b)), and helical wall thickening (Fig. (2.17c)) patterns inside the channels. Inner diameters of the channels varied between  $17 \mu\text{m}$  and  $25 \mu\text{m}$ . They used predefined normal mesh size with P1+P1 linear elements. They compared the obtained  $Po$  and  $Nu$  values with the smooth ones and found that the best heat transfer performance is achieved with reticulate/pitted wall thickening pattern. Furthermore, they extend their study by examining the effect of wall thickening pattern geometrical dimensions such as inner diameter, thickening width, height, spacing, aligned, and offset placement for reticulate/pitted thickening pattern. They found that offset patterning has better performance than aligned patterning. As the inner diameter and thickening width increases, reduction in  $Po$  and increase in  $Nu$  is observed. However, as the thickening height increased,  $Nu$  increases as well as  $Po$ . On the other hand, changing thickening spacing resulted in increased  $Po$  but variation in  $Nu$ .

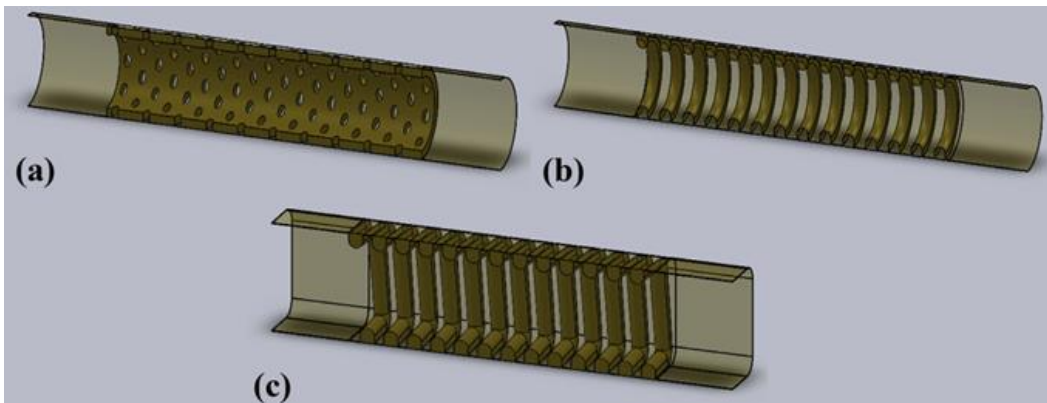


Fig. 2.17: Wall thickening patterns used in the simulations of [96].

Rajagopal and Das [97] numerically investigated the effects of inclination angles of villi structures, which exist in the intestinal surface of digestive systems, on drag and shear stress. Working fluid is a non-Newtonian fluid that mimics mucus. They used single-phase laminar flow and general form PDE interface of Comsol v4.4 in their simulations. For the meshing sequence, they used P2+P1 elements.

Ionescu and Neagu [98] numerically investigated the heat transfer characteristics of a MEMS-based counter flow heat exchanger having circular, rhombic, square, and octagonal fluid channel cross-sections. They used heat transfer in solids and heat transfer in fluids interfaces of Comsol v5.0, and the geometries are meshed with predefined normal mesh size. Working fluid is chosen as water whose thermophysical properties are temperature dependent. They presented their results as temperature and internal energy distributions, enthalpy variation, and effective volumetric heat capacities. They found that the heat exchanger with square channels removes heat more effectively than the other investigated channel geometries.

Yaici *et al.* [99] conducted 3D numerical simulations with COMSOL v5.0 to investigate the air side heat transfer and pressure drop characteristics for different inlet air flow distributions and different geometrical parameters, namely the longitudinal and transversal tube pitches and fin pitches, of staggered plate-fin-and-tube heat exchangers. They considered steady state, laminar air flow with constant inlet properties in the  $150 \leq Re \leq 2000$  range, and water flow inside the tubes with constant tube surface temperature. Mesh independence studies are carried with predefined mesh sizes of coarse, normal, fine, and finest, and the fine mesh size is chosen. They validated their simulations with experimental results.

Haertel and Nellis [100] conducted a density-based topology optimization study on an additively manufactured heat exchanger that is 3D printed with polymers, which includes thermally conductive metal filament, using COMSOL v5.2. Al-Neama *et al.* [101] experimentally and numerically investigated single phase laminar and turbulent water flow and heat transfer in serpentine microchannel heat sinks of four different configuration. Channels are stated as microchannels but actual geometries

are on the order of millimeter. The numerical part is conducted as 3D conjugate heat transfer by COMSOL v5.2. Agreement between the experimental and numerical results are good and the difference is between the experimental uncertainty margins. It is found that most effective heat transfer and smallest thermal resistance are achieved with triple-path multi-serpentine rectangular microchannel configuration with larger pressure drop than the other configurations.

Patel and Chhabra [102] numerically investigated the effect of angle of attack of a Bingham plastic fluid passing over a fixed aspect ratio elliptic cylinder, in two dimensions. Changes on flow and heat transfer characteristics are studied for various  $Re$ ,  $Pr$ ,  $Bn$ , and inclination angle values with constant wall temperature and constant heat flux boundary conditions applied to the elliptic cylinder. They used COMSOL and meshed the computational domain with structured quadrilateral elements. A direct solver is used with  $10^{-5}$  relative tolerance.

Amber and O'Donovan [103] conducted 2D time dependent simulations of natural convection caused by solar radiation in molten salt filled inclined enclosures. Inclination angle of the enclosure varied between 0 and 60, and used molten salt is  $KNO_3 - NaNO_3$  with temperature dependent thermophysical properties. Numerical simulations are done with COMSOL Multiphysics and P2+P1 element discretization is used with  $10^{-5}$  relative tolerance value. It is found that, natural convection reduces with the increase in inclination angle but increases with Rayleigh ( $Ra$ ) number.

Gerlich *et al.* [104] used COMSOL for benchmark calculations of heat transfer in buildings that exist in the standards. They compared the obtained results with available analytical models, measured data, and the results obtained by other programs. Authors stated that calculations would be in excellent agreement with the analytical solution when the solver is set properly. Also, a very fine mesh should be used to decrease the numerical error below 1% and solver error tolerance should be smaller than default value.

Stute *et al.* [105] discussed the performance and optimum settings of iterative solvers of COMSOL v3.5a and v4.1 via studying mass transfer by convection, diffusion, and adsorption in 3D sphere packings that are commonly used for separation of large molecules. They stated that meshing and iterative solvers failed to work with the default setting for the studied problem and used versions of the program.

As can be seen from the reviewed works, COMSOL Multiphysics is used in many research areas with different mesh and solver adjustments. In some cases linear P1+P1 elements (i.e.; first order elements for velocity and pressure fields) are used due to their computational cheapness [96]. However, some researchers [97, 103] prefer P2+P1 element discretization (i.e.; second order elements for velocity field and first order elements for pressure field) if enough computational sources are available. For the meshing part, some researchers [98, 99] preferred to use predefined meshing options. On the other hand, some researchers [105] preferred to use fine-tuned meshes due to the failure of predefined mesh profiles or to optimize the mesh for lower computational sources. Use of different levels of relative error tolerance than the default value of the program [102-104] can also be observed. In addition, it is seen that various versions of COMSOL are used by the researchers, from the oldest version 3.5a [87, 105] to the relatively newer one, 5.2 [100, 101]. With all these observations and suggestions of the authors from different fields, investigating and determining the effects of different types of element discretization, mesh construction, relative tolerance levels, and some options that are offered in different versions of the simulation programs become important for the accuracy and validity of the results.

## 2.4 SUMMARY OF LITERATURE REVIEW AND OBJECTIVES

From the literature reviewed for the flow and heat transfer in smooth and rough microchannels, following key conclusions can be drawn:

- Experiments give contradictory results about heat transfer and pressure drop, which will be the result of surface conditions, not knowing the actual channel geometries of the used microchannels, flow characteristics, and fluid properties, as well as the measurement errors.
- Numerical simulations yield different results than experimental results if simulations are oversimplified or the scaling effects are not considered.
- Cross-sectional geometry of the microchannel and microchannel's aspect ratio have great impact on the flow field and heat transfer.
- The material and the manufacturing methods used for manufacturing of the microchannels and microfluidic devices are important, and yield different surface conditions, which affect flow and heat transfer characteristics.
- Roughness geometry, the density, spacing, and height of the roughness elements have great impact on the flow and heat transfer characteristics.
- Different roughness shapes (random or ordered square, rectangular, triangular elements in two-dimensions or conical, cubical, cylindrical elements in three-dimensions) and spacing of these elements yield different results under similar flow conditions with the same fluid.
- Efforts to obtain a general formula for pressure drop, friction factor, or  $Nu$  for rough surface conditions yield no result due to random characteristics of roughness and different responses obtained for various geometries for the flow and heat transfer.
- Roughness of the surfaces of the microchannels can be arranged to obtain specific desired results. Depending on the flow condition and geometrical configuration of the roughness elements, heat transfer, pressure drop, and friction factor can be higher or lower than the smooth one.

Changing the geometrical properties of the roughness elements can increase or decrease the heat transfer and/or pressure drop for example, even if the other parameters of the microchannel are kept constant. These different properties of roughness elements directed the researchers to work with the engineered surfaces in which the shape of roughness elements is changed deliberately as needed. Since every change in a geometrical parameter, in a flow parameter, or in a thermophysical property of the fluid yield different results, great amount of data concerning these parameters is needed to actually understand the phenomena. Thus, the main objective of this study is to numerically investigate the effect of surface roughness, which is constructed with conical elements to resemble the surface of silicon microchannels or a lotus leaf, on flow and heat transfer in microchannels and obtain data. The other objectives of this study can be given as follows:

- Verification of usability of COMSOL Multiphysics in microchannel flow and heat transfer simulations.
- Comparison of macroscale and microscale flow in trapezoidal channels.
- Evaluation of the effect of different roughness configurations on flow and heat transfer parameters in microchannels.
- Evaluation of the effect of roughness geometrical properties on flow and heat transfer parameters in microchannels.



## CHAPTER 3

### GOVERNING EQUATIONS

Throughout this study, various channel geometries are used. In two-dimensional cases, which are performed as an extension of a previous work [106], smooth and rough parallel plate microchannels are considered. In three-dimensional cases, smooth macroscale, and smooth and rough microscale trapezoidal channels are considered. During the simulations, the flow is assumed to be at steady state in the laminar regime and single-phase water is chosen as the working fluid. Body forces and radiative heat transfer are neglected. Then, governing Navier-Stokes and energy equations, which are given in Eqns. (3.1), (3.2), and (3.3), are solved with the commercial CFD program COMSOL Multiphysics.

$$\rho \nabla \cdot \vec{u} = 0 \quad (3.1)$$

$$\rho(\vec{u} \cdot \nabla \vec{u}) = \nabla \cdot [-p \underline{I} + \mu(\nabla \vec{u} + (\nabla \vec{u})^T)] \quad (3.2)$$

$$\rho C_p \vec{u} \cdot \nabla T = \nabla \cdot (k \nabla T) + Q_{vh} \quad (3.3)$$

Here,  $\rho$  is the density,  $\vec{u}$  is the velocity field,  $p$  is the pressure,  $\mu$  is the viscosity,  $C_p$  is the specific heat,  $T$  is the temperature,  $k$  is the thermal conductivity, and  $Q_{vh}$  is the viscous heating term defined as:

$$Q_{vh} = \mu \left( \nabla \vec{u} + (\nabla \vec{u})^T - \frac{2}{3} (\nabla \cdot \vec{u}) \underline{I} \right) : \nabla \vec{u} \quad (3.4)$$

When viscous dissipation is considered,  $Q_{vh}$  term is added to energy equation. Otherwise, it is neglected. Two-dimensional parallel plate simulations are carried

out by both considering and neglecting the viscous dissipation. However, in three-dimensional simulations, viscous dissipation term is neglected.

Experimental studies of liquid flows that are conducted at microscale revealed that Navier-Stokes equations with no-slip velocity wall boundary condition are applicable down to hydraulic diameters of about  $1 \mu\text{m}$  with acceptable deviation. For that reason, no-slip velocity wall boundary condition is used in the current simulations.

For 2D simulations, representative schematics of the parallel plate microchannel is given in Fig. (3.1). Uniform velocity and temperature is used as the inlet boundary conditions. Also, constant wall temperature and no-slip velocity boundary conditions are used at the walls. Boundary conditions for the 2D cases can be summarized as follows:

$$\text{Walls: } u = 0, \quad v = 0, \quad T = T_w$$

$$\text{Inlet: } u = U_i, \quad v = 0, \quad T = T_i$$

$$\text{Outlet: } \textit{outflow}, \quad p = 0$$

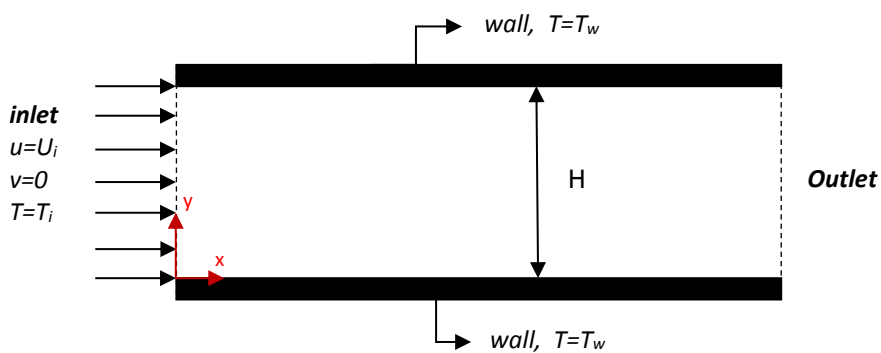


Figure 3.1: Schematics of 2D parallel plate microchannel and boundary conditions.

Uniform inlet velocity is controlled by  $Re$  and calculated with Eq. (3.5) as:

$$U_i = \frac{Re \mu}{\rho D_h} \quad (3.5)$$

Here,  $D_h$  is the hydraulic diameter of the channel. The local Nusselt number is defined as,

$$Nu_x = \frac{h_x D_h}{k} \quad (3.6)$$

where  $h_x$  is the local heat transfer coefficient and written as,

$$h_x = \frac{k}{(T_m - T_w)} \left( \frac{\partial T}{\partial n} \right)_w \quad (3.7)$$

Here,  $T_w$  is the wall temperature and  $T_m$  is the mean temperature of the fluid and calculated by the following.

$$T_m = \frac{\int_{\Gamma} \rho u C_p T d\Gamma}{\int_{\Gamma} \rho u C_p d\Gamma} \quad (3.8)$$

Here,  $\Gamma$  represents the cross-sectional line that the integrals are performed over.

For 3D simulations, various macro and microscale trapezoidal channels are used. A representative schematic for trapezoidal cross-section is presented in Fig. (3.2). For the flow part of the 3D simulations, uniform inlet velocity boundary condition is used, which is either controlled by  $Re$  as in Eq. (3.5) or by inlet mass flux ( $G$ ) as:

$$U_i = \frac{G}{\rho} \quad (3.9)$$

Zero pressure is imposed at the outlet and no-slip condition is used at walls. Due to the symmetry about the  $yz$ -plane, symmetry boundary condition is applied to this plane and only half of the channel is used as the computational domain. For the heat transfer part of the 3D simulations, constant temperature is used as the inlet

boundary condition. Symmetry boundary condition is applied to the  $yz$ -plane. Thermal insulation boundary condition is applied at walls except the heater surface. On the heater surface, uniform inward heat flux is applied. Boundary conditions for the 3D cases can be summarized as follows:

$$\text{Walls: } \vec{u} = 0, \quad -\hat{n} \cdot (-k\nabla T) = 0$$

$$\text{Inlet: } \vec{u} = -U_0\hat{n}, \quad U_0 = U_{in}, \quad T = T_{in}$$

$$\text{Outlet: } \textit{outflow}, \quad p = 0$$

$$\text{Heater Surface: } q_0 = q_{eff}$$

$$\text{Symmetry: } \textit{at } yz\text{-plane}$$

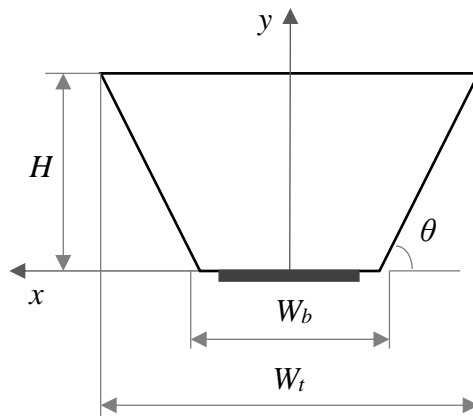


Figure 3.2: Representative schematic for channels having trapezoidal cross-section.

Local  $Nu$  values in relevant 3D simulations are calculated by the following formula.

$$Nu = \frac{q_{eff} D_h}{k \Delta T} \quad (3.10)$$

Here,  $q_{eff}$  is the effective heat transfer,  $\Delta T$  is the difference between the wall mean temperature  $T_w$  and bulk mean temperature  $T_m$  at the cross-section at interest which are calculated by,

$$T_w = \frac{1}{L_\Gamma} \int_{\Gamma} T_w d\Gamma \quad (3.11)$$

$$T_m = \frac{\int_{A_c} \rho w C_p T dA_c}{\int_{A_c} \rho w C_p dA_c} \quad (3.12)$$

Here,  $w$  is the velocity component in the  $z$  direction,  $L$  is the length, and  $\Gamma$  and  $A_c$  represent the boundary line and cross-sectional area where the integrals are effective.

Additionally, the friction constant  $f$ ,  $Re$  and  $Po$  values are calculated by:

$$f = \frac{\Delta p D_h}{2 \rho U_m^2 L_z} \quad (3.13)$$

$$Re = \frac{\rho U_m D_h}{\mu} \quad (3.14)$$

$$Po = f Re \quad (3.15)$$

Here,  $U_m$ ,  $\Delta p$ , and  $L_z$  are the mean velocity, pressure drop, and distance between the considered two locations in the flow direction.

Two-dimensional simulations are carried out with both constant and variable thermophysical properties of water that are functions of temperature. On the other hand, three-dimensional simulations are carried out with variable thermophysical properties of water. In COMSOL Multiphysics, values of temperature dependent  $\mu$ ,

$C_p$ ,  $\rho$ , and  $k$  for water are obtained with polynomial functions given by Eqs. (3.16) to (3.19).

$$\begin{aligned} \mu(T) = & 1.3799566804 - 0.021224019151 \times T \\ & + 1.3604562827E - 4 \times T^2 - 4.6454090319E - 7 \\ & \times T^3 + 8.9042735735E - 10 \times T^4 \\ & - 9.0790692686E - 13 \times T^5 + 3.8457331488E \\ & - 16 \times T^6 \end{aligned} \quad (3.16)$$

$$\begin{aligned} C_p(T) = & 12010.1471 - 80.4072879 \times T + 0.309866854 \times T^2 \\ & - 5.38186884E - 4 \times T^3 + 3.62536437E - 7 \times T^4 \end{aligned} \quad (3.17)$$

$$\begin{aligned} \rho(T) = & 838.466135 + 1.40050603 \times T - 0.0030112376 \times T^2 \\ & + 3.71822313E - 7 \times T^3 \end{aligned} \quad (3.18)$$

$$\begin{aligned} k(T) = & -0.869083936 + 0.00894880345 \times T - 1.58366345E - 5 \\ & \times T^2 + 7.97543259E - 9 \times T^3 \end{aligned} \quad (3.19)$$

Eq. (3.16) is valid for the temperature range of  $273.15 \text{ [K]} < T < 413.15 \text{ [K]}$ . Eqs. (3.17) to (3.19) are valid for the temperature range of  $273.15 \text{ [K]} < T < 553.75 \text{ [K]}$ .

## CHAPTER 4

### 2D FLOW AND HEAT TRANSFER SIMULATIONS BETWEEN PARALLEL PLATES

Effect of triangular surface roughness in two dimensional parallel plate channels has been investigated numerically in [61,106-107] considering gas flows. In those works, the flow was assumed to be incompressible and in the slip flow regime at steady state. Air was chosen as the working fluid with constant thermophysical properties. Triangular roughness elements were placed on one of the plates. Relative roughness was defined as  $\varepsilon = e/D_h$ . Three different relative roughness values in the same channel were considered, namely 1.325%, 2.00%, and 2.65%, which yield 30, 20, and 15 roughness elements along the channel, respectively. Schematics of the channel with the boundary conditions and geometrical properties of the triangular elements are shown in Fig. (4.1). Governing Navier-Stokes and energy equations were solved with slip velocity and temperature jump wall boundary conditions for  $5 \leq Re \leq 100$  and  $0 \leq Kn \leq 0.10$  range with a finite element code written by the author in non-dimensional sense. Then, obtained  $Nu$  values were compared with the smooth ones. It was found that, tested roughness geometries reduce the  $Nu$  in the continuum case ( $Kn = 0$ ) while they cause an increase in the slip flow regime ( $Kn > 0$ ), especially at low  $Kn$  values. The increase was more obvious due to the increase of molecular interactions with the solid surface.

As an extension of [106], first, simulations of water flowing between parallel plates are conducted in the current work. Dimensions of channels, boundary conditions and roughness geometries are chosen similar to the previously investigated cases, but all dimensional this time, as  $L = 1000 \mu\text{m}$ ,  $H = 100 \mu\text{m}$ ,  $T_{in} = 340 \text{ K}$ , and  $T_w =$

300 K, where  $L$  is the channel length,  $H$  is the channel height,  $T_{in}$  is the inlet temperature of water, and  $T_w$  is the constant wall temperature of the microchannel. Triangular roughness element heights ( $e$ ) are  $2.75 \mu\text{m}$ ,  $4 \mu\text{m}$ , and  $5.3 \mu\text{m}$ , for relative roughness values of 1.325%, 2.00%, and 2.65%, respectively. Effect of surface roughness is investigated with the combined effect of variable thermophysical properties of water and viscous dissipation.

Simulations are carried out with commercial program COMSOL Multiphysics for uniform inlet velocities that are controlled by  $Re$  values of 5, 10, 20, 50, and 100. The computer used in the simulations has two Intel Xeon X5660 CPU and 48 GB of physical memory with Windows 7 Enterprise Edition operating system. Test geometries with the test cases are summarized in Table – (4.1).

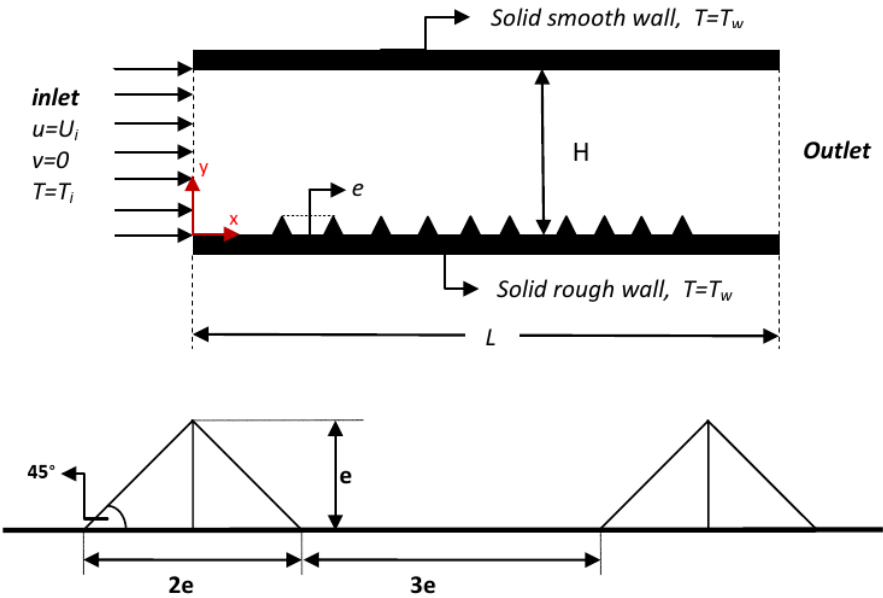


Figure 4.1: Schematics of the rough parallel-plate channels and geometrical properties of roughness elements [106].

Table 4.1: Test cases for 2D water flow simulations.

		<i>Water Properties</i>		<i>Viscous Dissipation</i>	
<i>Geometry</i>	Case #	<i>Constant</i>	<i>Variable</i>	<i>Not Included</i>	<i>Included</i>
<i>Geometry (a) (smooth)</i> <i>Geometry (b) (1.325%)</i> <i>Geometry (c) (2.000%)</i> <i>Geometry (d) (2.650%)</i>	01	++	--	++	--
	02	++	--	--	++
	03	--	++	++	--
	04	--	++	--	++

Extensive mesh independence studies are carried out for each case and geometry with parametric sweep of all  $Re$  values considered in this study. Triangular elements are used during the 2D simulations. Since the element numbers and related degrees of freedom (DOFs) were relatively low, direct solvers are used with  $10^{-6}$  relative tolerance. Distribution of local  $Nu$  and the change in its value, cell  $Re$ , cell  $Pe$  numbers are used as control parameters for the mesh independence studies, as well as the tests for computational cost.

In COMSOL Multiphysics reference manual [108], it is advised that for numerically stable simulations without any need of a numerical stabilization method, cell  $Re$  and cell  $Pe$  values should be below one. Cell  $Re$  and cell  $Pe$  numbers are calculated in the mesh elements, thus as the element sizes reduced, their values also reduce. However, this means more elements in the computational domain and more memory are needed. For small-scale simulations, it is not a problem, but when the problem size increases, memory need could become unfeasible.

One example for the mesh independence study is given for the *Case-04* of *Geometry (b)* where variable fluid properties and viscous dissipation were considered with 1.325% relative roughness. Properties of the used meshes are given in Table – (4.2), with solution times, and resulting maximum cell  $Re$ , and cell  $Pe$  numbers.

Corresponding cell  $Re$ , and cell  $Pe$  of the meshes are shown graphically for selected meshes in Fig. (4.2) and Fig. (4.3), respectively.

Throughout the mesh independence tests, both first order and second order elements are used. Their effect on the results are observed as well as the computational costs. It is observed that similar accuracy of second order elements could be achieved with small enough linear elements with reduced memory cost in the expense of solution times. Additionally, effect of using or not using boundary layer mesh on the results is also investigated. Details on the use of boundary layer mesh in 2D test geometries can be found in App. (A.1).

Table 4.2: Properties of meshes used in the mesh independence studies of *Geometry (b) Case-04*.

<i>Mesh #</i>	<i># of Elements</i>	<i>Element Order</i>	<i>Run Time</i>	<i>Cell <math>Re_{max}</math></i>	<i>Cell <math>Pe_{max}</math></i>
1	269,250	N-S: P2+P1 T: Quadratic	00h:25m:40s	0.31	2.79
2	236,244	N-S: P2+P1 T: Quadratic	00h:22m:50s	0.32	2.76
3	789,007	N-S: P1+P1 T: Linear	00h:26m:23s	0.17	1.53
4	993,202	N-S: P1+P1 T: Linear	00h:34m:17s	0.16	1.46
5	1,370,712	N-S: P1+P1 T: Linear	00h:49m:44s	0.13	1.13
6	1,252,176	N-S: P1+P1 T: Linear	00h:50m:24s	0.14	1.14
7	1,971,353	N-S: P1+P1 T: Linear	01h:12m:49s	0.11	0.89
8	3,148,147	N-S: P1+P1 T: Linear	02h:00m:06s	0.08	0.71
9	1,069,436	N-S: P2+P1 T: Quadratic	02h:55m:45s	0.12	1.15
10	5,184,929	N-S: P1+P1 T: Linear	05h:39m:00s	0.06	0.55

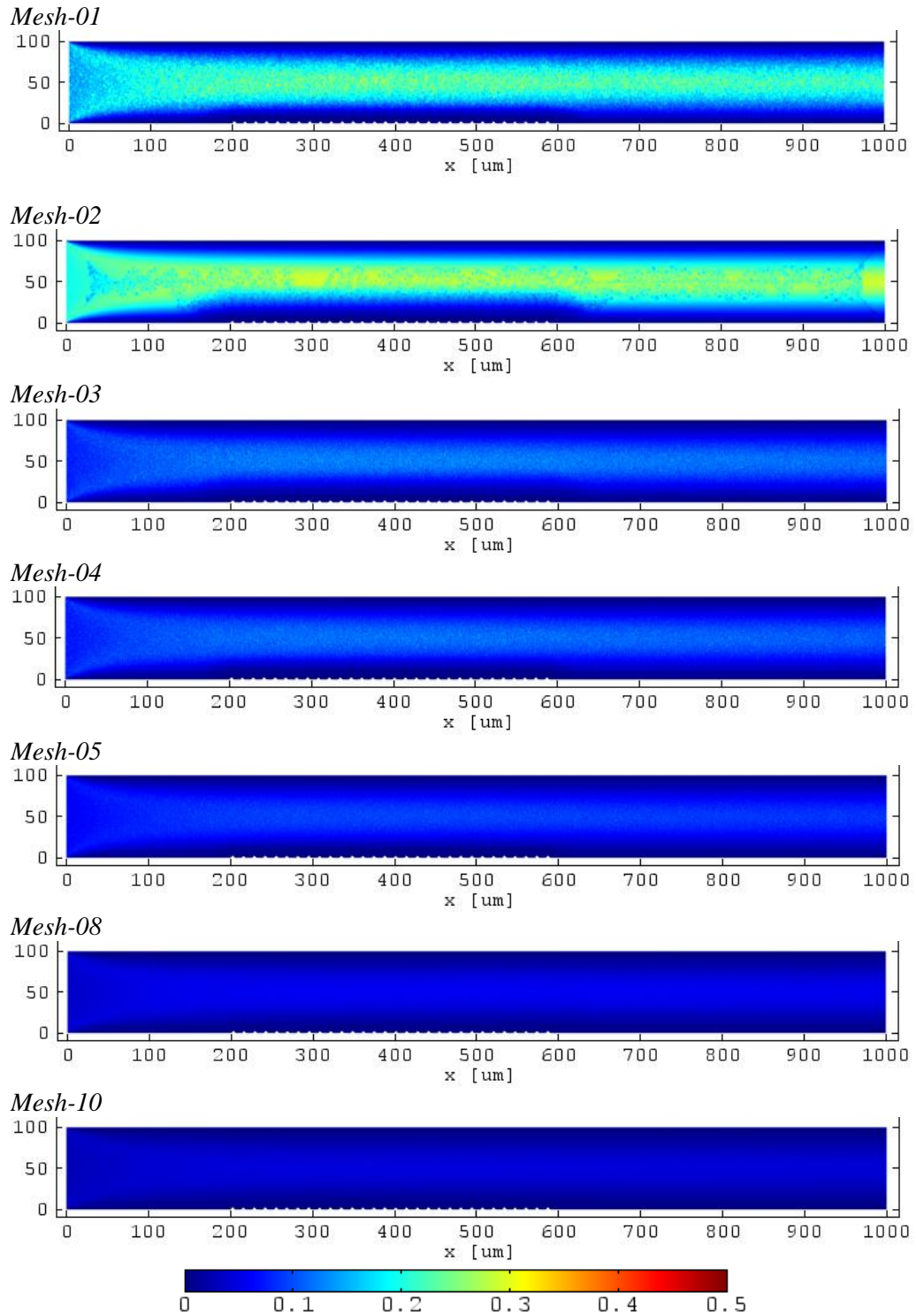


Figure 4.2: Selected cell  $Re$  plots for mesh independence studies of *Geometry (b)* *Case-04* (with 1.325% relative roughness).

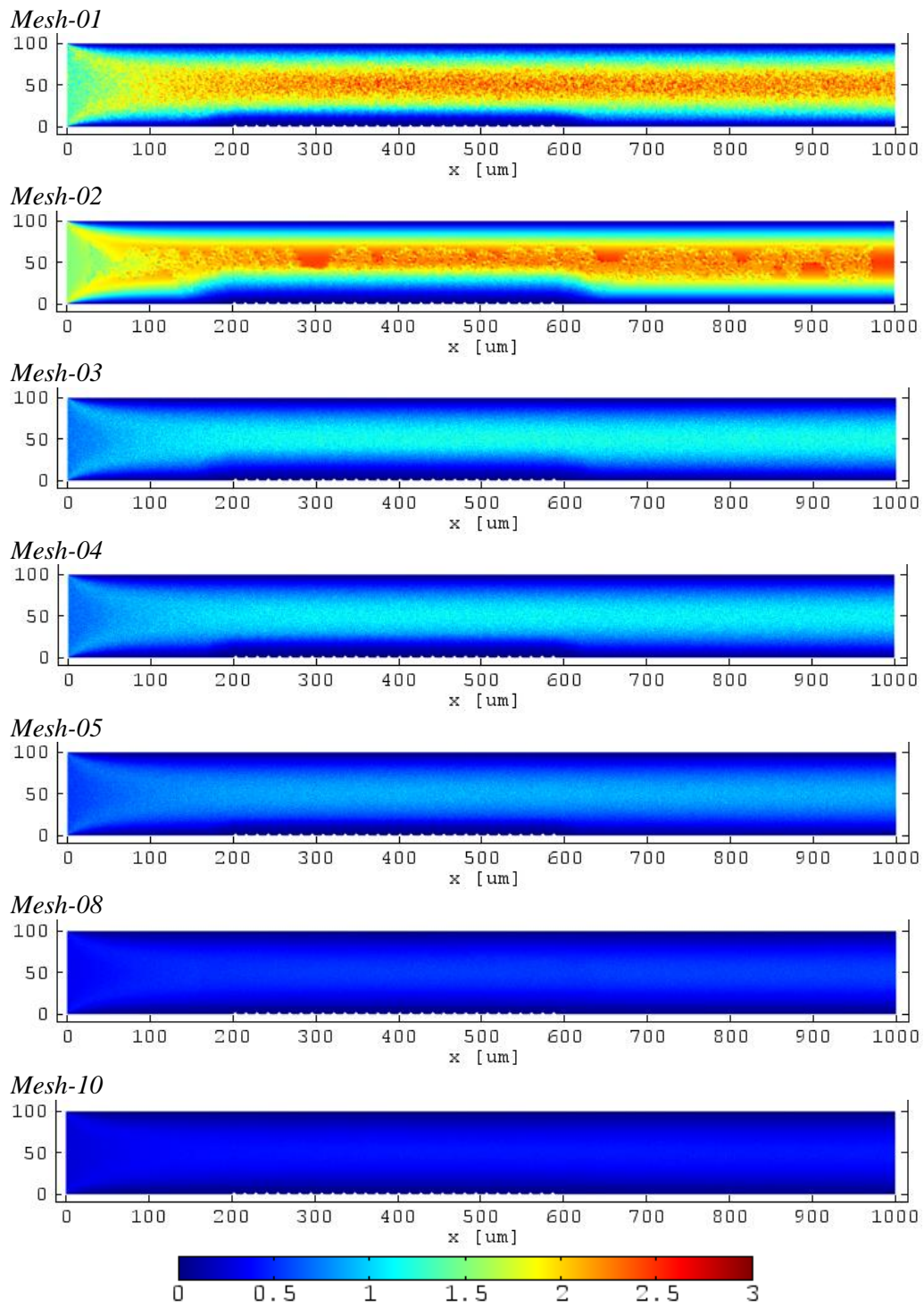


Figure 4.3: Selected cell  $Pe$  plots for mesh independence studies of *Geometry (b)* *Case-04* (with 1.325% relative roughness).

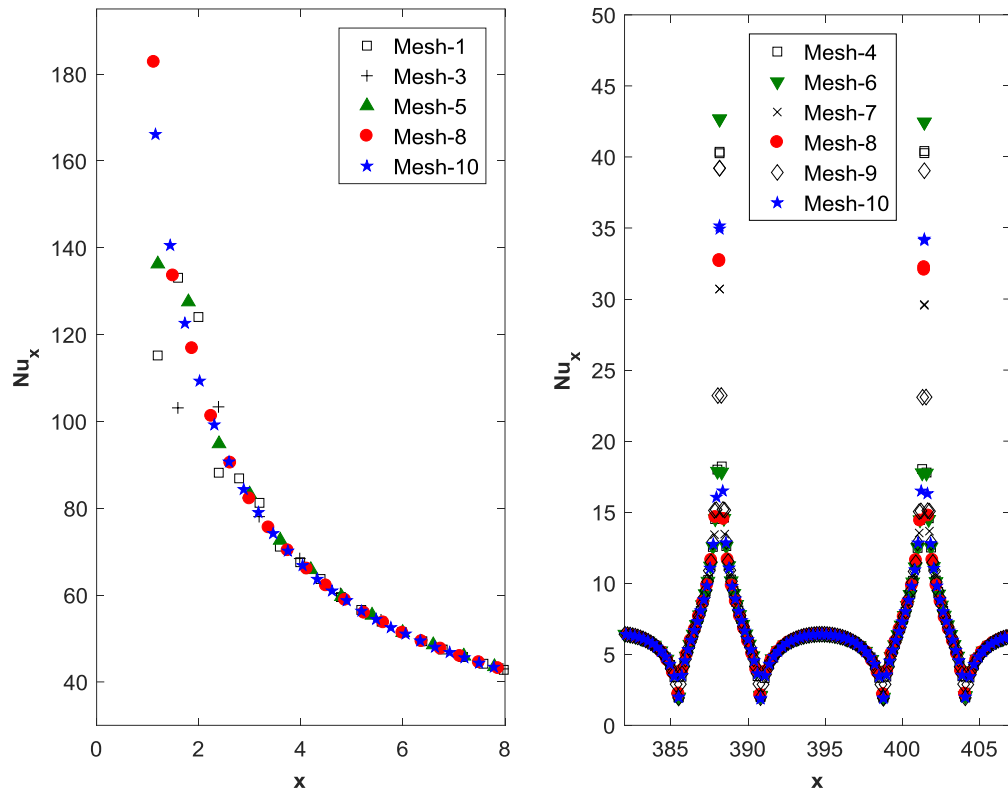


Figure 4.4: Local  $Nu$  distribution at the inlet of the channel and at the middle of the rough section for *Case-04* of *Geometry (b)* and  $Re = 100$ .

Figure (4.4) shows the local  $Nu$  distribution at the inlet of the channel and at the middle of the rough section for  $Re = 100$  of *Case-04* of *Geometry (b)*. Maximum deviations between the results of different meshes occur at the inlet of the channel and at the tip of the roughness elements, since maximum disturbance in the flow field occurs at these points. In other locations, the difference become miniscule as the element numbers increase.

Considering all the control parameters and computational cost, mesh number 8 is chosen for the later calculations for *Geometry (b)*. A similar procedure is applied to all other geometries and cases, and appropriate meshes are chosen. Properties of the chosen meshes for all geometries are given in Table – (4.3). In addition, distribution

of elements for the chosen meshes around the first two consecutive roughness elements for rough geometries is shown in Fig. (4.5). All the chosen meshes have average element qualities of over 0.9.

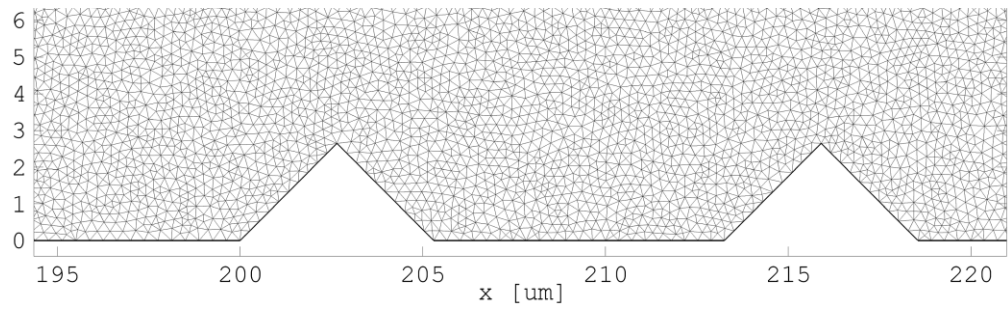
Streamlines around the middle section of the rough channels for *Case-03* of each geometry is shown in Fig. (4.6) for  $Re = 100$ . Also, velocity contour plots, which are drawn with 0.005 m/s level, around the middle roughness elements for *Case-03* of 2D smooth and rough channel geometries for  $Re = 100$  are shown in Fig. (4.7). Recirculation or any vortex formation between the roughness elements or after the roughness elements are not observed.

To see the effect of rough geometries' heat transfer and pressure drop performances, average temperature and average pressures are calculated at  $x = 200 \mu\text{m}$ , where the roughness starts, and  $x = 600 \mu\text{m}$ , where the roughness ends. Then, differences in temperature and pressure drop of rough channels are compared with the ones obtained from the smooth channel for each case, which is provided in Table – (4.4).

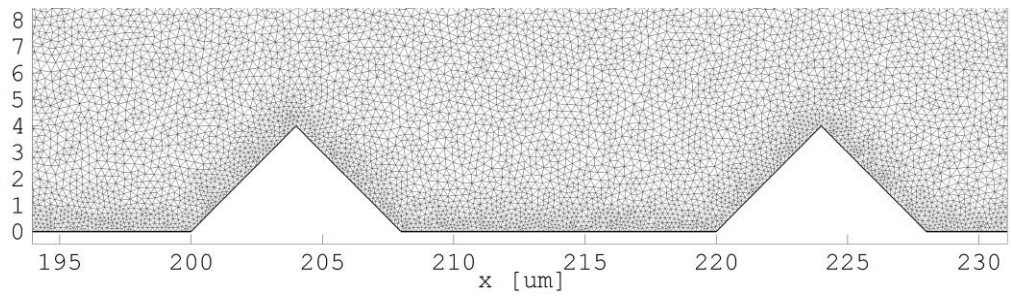
Table 4.3: Properties of selected meshes for each 2D rough geometry.

<i>Geometry</i>	<i># of elements</i>	<i>Element Order</i>	<i>Cell <math>Re_{max}</math></i>	<i>Cell <math>Pe_{max}</math></i>
<i>a (smooth)</i>	3,200,000	N-S: P1+P1 T: Linear	0.04 – 0.06	0.89 – 0.90
<i>b (<math>\epsilon=1.325\%</math>)</i>	3,148,147	N-S: P1+P1 T: Linear	0.05 – 0.08	0.70 – 0.71
<i>c (<math>\epsilon=2.00\%</math>)</i>	2,790,457	N-S: P1+P1 T: Linear	0.05 – 0.09	0.77 – 0.79
<i>d (<math>\epsilon=2.65\%</math>)</i>	2,781,218	N-S: P1+P1 T: Linear	0.05 – 0.09	0.77 – 0.78

*Geometry (b) (1.325%):*



*Geometry (c) (2.00%):*



*Geometry (d) (2.65%):*

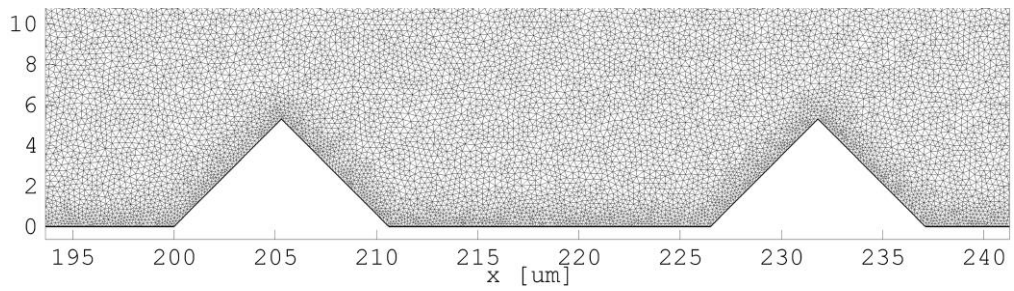
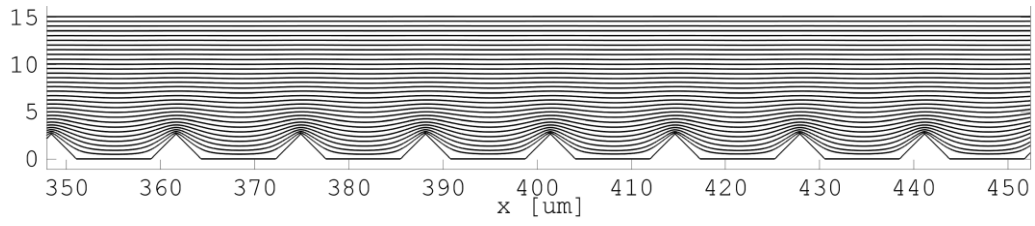
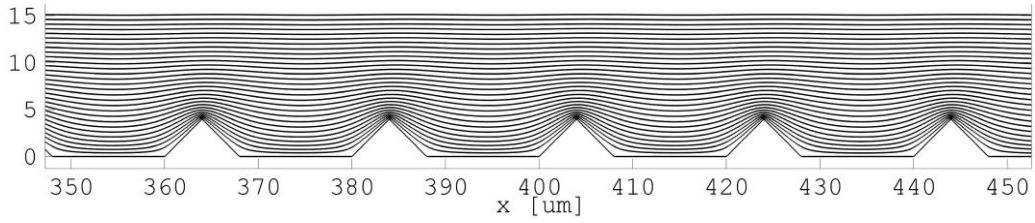


Figure 4.5: Distribution of chosen meshes around the first two roughness elements of 2D parallel plate channels.

*Geometry (b) (1.325%):*



*Geometry (c) (2.00%):*



*Geometry (d) (2.65%):*

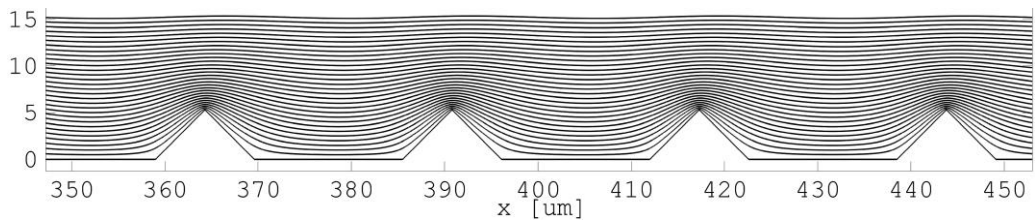
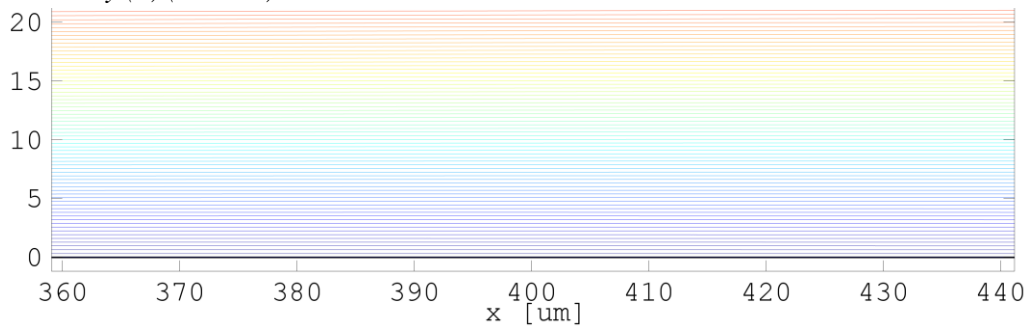
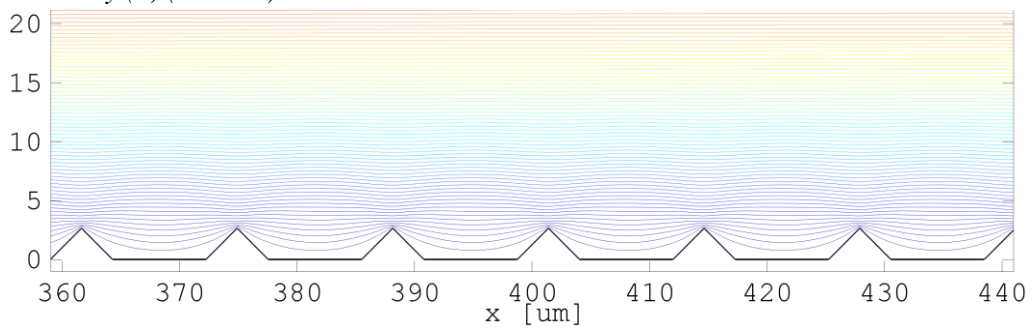


Figure 4.6: Streamlines around the middle roughness elements for *Case-03* of 2D rough channel geometries for  $Re = 100$ .

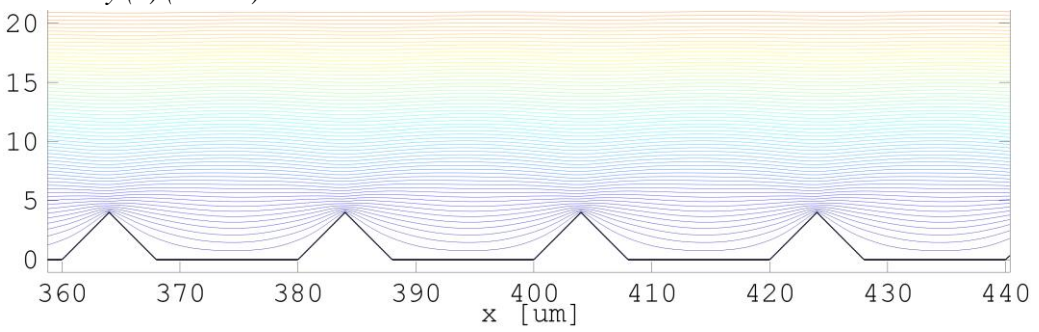
*Geometry (a) (Smooth):*



*Geometry (b) (1.325%):*



*Geometry (c) (2.00%):*



*Geometry (d) (2.65%):*

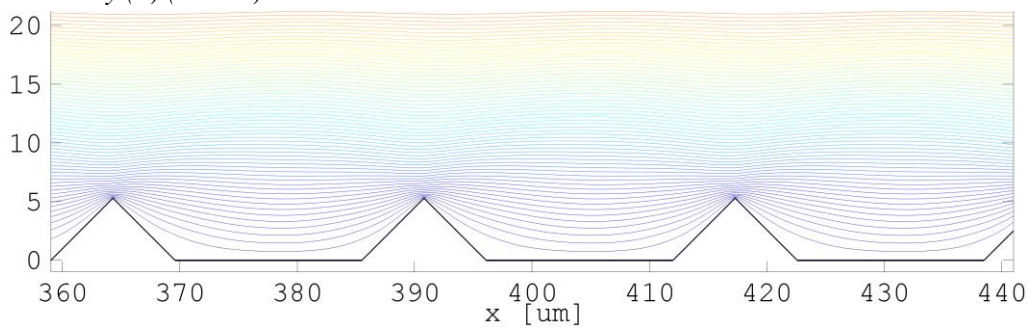


Figure 4.7: Velocity contour plots around the middle roughness elements for *Case-03* of 2D smooth and rough channel geometries for  $Re = 100$ .

Table 4.4: Percent differences in temperature and pressure compared to the smooth channel between  $x = 200 \mu\text{m}$  and  $x = 600 \mu\text{m}$  locations.

		% difference in $\Delta T$					% difference in $\Delta P$		
	<i>Re</i>	1.325%	2.00%	2.65%		<i>Re</i>	1.325%	2.00%	2.65%
<b>Case 1</b> ( <i>cfp</i> , <i>nvd</i> )	<b>5</b>	-0.868	-1.328	-1.889	<b>Case 1</b> ( <i>cfp</i> , <i>nvd</i> )	<b>5</b>	5.351	7.933	10.085
	<b>10</b>	-0.850	-1.393	-2.036		<b>10</b>	5.336	7.906	10.024
	<b>20</b>	-1.037	-1.773	-2.745		<b>20</b>	5.344	7.909	9.980
	<b>50</b>	-1.460	-2.513	-4.215		<b>50</b>	5.529	8.172	10.224
	<b>100</b>	-1.490	-2.486	-4.441		<b>100</b>	5.982	8.855	11.031
<b>Case 2</b> ( <i>cfp</i> , <i>vd</i> )	<b>5</b>	-0.868	-1.328	-1.889	<b>Case 2</b> ( <i>cfp</i> , <i>vd</i> )	<b>5</b>	5.351	7.933	10.085
	<b>10</b>	-0.850	-1.393	-2.036		<b>10</b>	5.336	7.906	10.024
	<b>20</b>	-1.037	-1.773	-2.745		<b>20</b>	5.344	7.909	9.980
	<b>50</b>	-1.460	-2.513	-4.215		<b>50</b>	5.529	8.172	10.224
	<b>100</b>	-1.490	-2.486	-4.441		<b>100</b>	5.982	8.855	11.031
<b>Case 3</b> ( <i>vfp</i> , <i>nvd</i> )	<b>5</b>	-0.855	-1.311	-1.867	<b>Case 3</b> ( <i>vfp</i> , <i>nvd</i> )	<b>5</b>	5.257	7.792	9.906
	<b>10</b>	-0.820	-1.352	-1.986		<b>10</b>	5.148	7.622	9.658
	<b>20</b>	-0.955	-1.653	-2.598		<b>20</b>	5.068	7.491	9.433
	<b>50</b>	-1.206	-2.138	-3.703		<b>50</b>	5.280	7.782	9.696
	<b>100</b>	-1.089	-1.886	-3.524		<b>100</b>	5.792	8.544	10.608
<b>Case 4</b> ( <i>vfp</i> , <i>vd</i> )	<b>5</b>	-0.855	-1.311	-1.867	<b>Case 4</b> ( <i>vfp</i> , <i>vd</i> )	<b>5</b>	5.257	7.792	9.906
	<b>10</b>	-0.820	-1.352	-1.986		<b>10</b>	5.148	7.622	9.658
	<b>20</b>	-0.955	-1.653	-2.598		<b>20</b>	5.068	7.491	9.433
	<b>50</b>	-1.206	-2.138	-3.703		<b>50</b>	5.280	7.782	9.696
	<b>100</b>	-1.089	-1.886	-3.524		<b>100</b>	5.792	8.544	10.608
<i>cfp</i> : constant fluid properties		<i>vfp</i> : variable fluid properties							
<i>vd</i> : viscous dissipation included		<i>nvd</i> : viscous dissipation not included							

Results showed that tested roughness elements reduce the heat transfer performance and this reduction increases with increasing relative roughness, which should be the result of formation of low velocity regions behind the roughness peaks and between the roughness elements. Temperature difference between the inlet and exit of the rough section drops to approximately between 0.8% and 4.5%. Effect of roughness is found to be much higher on pressure drop than on heat transfer. Increase in pressure drop is found to be between 5% and 11%, and increases with the relative

roughness height. Moreover, the increase is nearly on the same level for the flows having  $Re$  values between 5 and 50. However, when the  $Re$  reaches 100, a jump in pressure drop is observed which indicates investigation of flows with higher velocities is necessary for better understanding of this phenomenon. On the other hand, among the tested geometries and considered flow conditions, effect of viscous dissipation is found to be negligible. Comparing *Case-1* and *Case-3*, and *Case-2* and *Case-4*, it is seen that the effect of using constant or variable fluid properties on temperature difference and pressure drop is less than 1%. However, as the  $Re$  of the flow increases, difference becomes noticeable.

Local  $Nu$  distribution along the smooth channel is given in Fig. (4.8) with the close-up view of the entrance section of the channel and analytical  $Nu$  value of 7.54 for the parallel plate channels. It is observed that using variable or constant fluid properties showed little effect on the local  $Nu$  for the considered simulation ranges. Local  $Nu$  values are higher at the entrance of the channel and approach the analytical value through the end of the channel. As the  $Re$  increases, local  $Nu$  gains higher value at the entry region and the length scale where it reaches the analytical value also increases.

Local  $Nu$  distribution along the *Geometry (b)*, where the relative roughness is 1.325%, and close-up view between the two consecutive roughness elements between  $x = 395 \mu\text{m}$  and  $x = 420 \mu\text{m}$  is given in Fig. (4.9) for  $Re = 5$  and  $Re = 100$ . Roughness elements suppress and slows down the flow near the boundaries, which is more at the bottom corners of the triangular elements. Since there is no vortex formation occurring between the roughness elements, flows with slow velocity result in lower  $Nu$  values. However, in the vicinity of the tip of the roughness elements, velocity is much higher and results in higher  $Nu$  values.

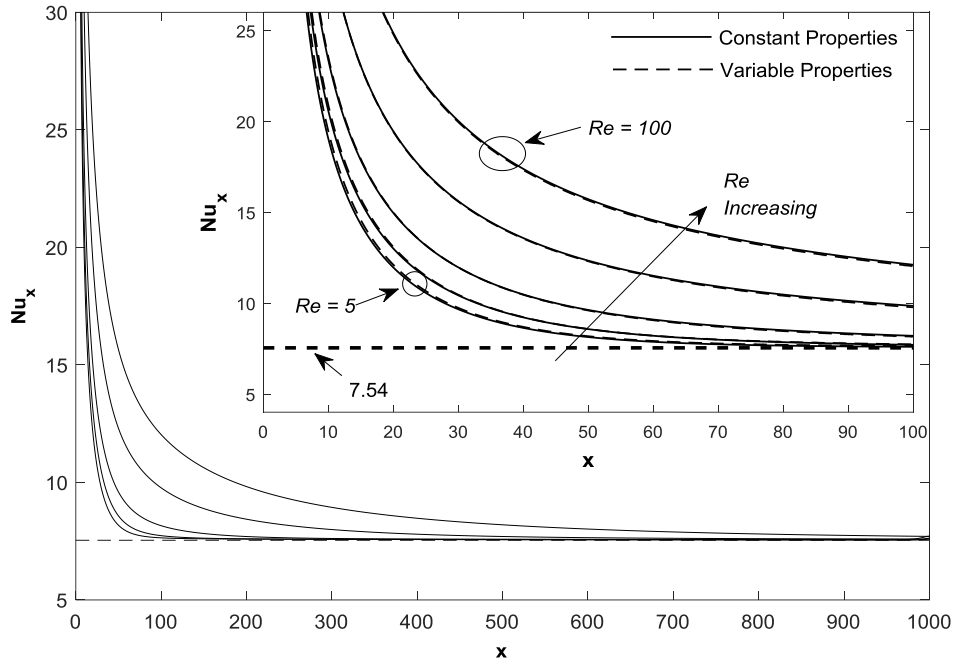


Figure 4.8: Local  $Nu$  distribution along the 2D Geometry (a) (smooth) and close-up view of entrance section.

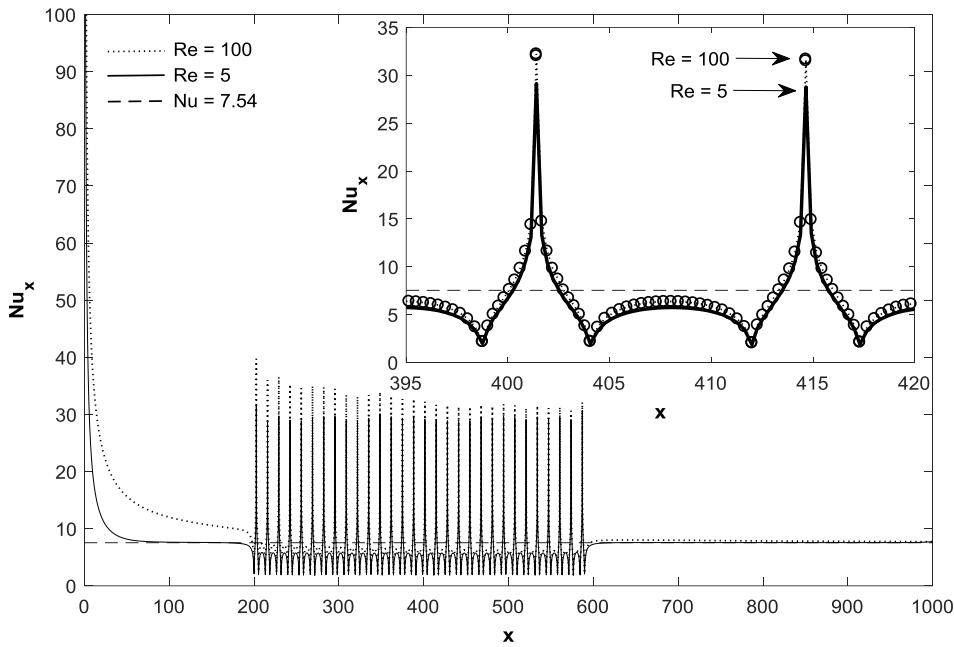


Figure 4.9: Local  $Nu$  distribution along the 2D Geometry (b) ( $\epsilon = 1.325\%$ ) and close-up view between the two consecutive roughness elements.

Local  $Nu$  distribution along the *Geometry (c)*, where the relative roughness is 2.00%, and close-up view between the two consecutive roughness elements between  $x = 375 \mu\text{m}$  and  $x = 415 \mu\text{m}$  is given in Fig. (4.10) for  $Re = 5$  and  $Re = 100$ . Similar behavior of 1.325% case is observed for the 2.00% relative roughness. The only difference this time is that the local  $Nu$  values are higher in the vicinity of the tip of the roughness elements, since the height of the roughness elements are greater and exposed to higher velocities of the core flow.

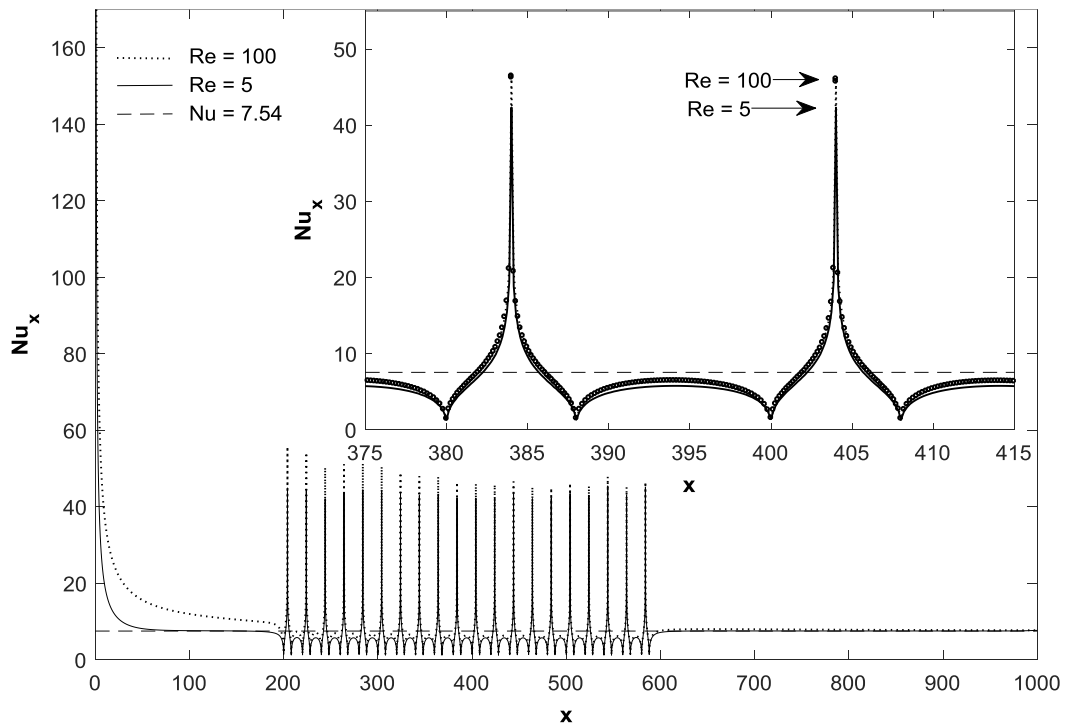


Figure 4.10: Local  $Nu$  distribution along the 2D *Geometry (c)* ( $\epsilon = 2.00\%$ ) and close-up view between the two consecutive roughness elements.

When the relative roughness is increased to 2.65%, general behavior of local  $Nu$  remained similar with the previous cases, which is shown in Fig. (4.11). Local  $Nu$  near the tip of the triangular elements take higher values than the cases with lower relative roughness, due to increasing height and become closer to the high velocity core flow. However, between the roughness elements, local  $Nu$  values are still lower than the smooth case and the difference between the  $Nu$  values of minimum and maximum  $Re$  cases considered in this study is miniscule, similar to the previous cases.

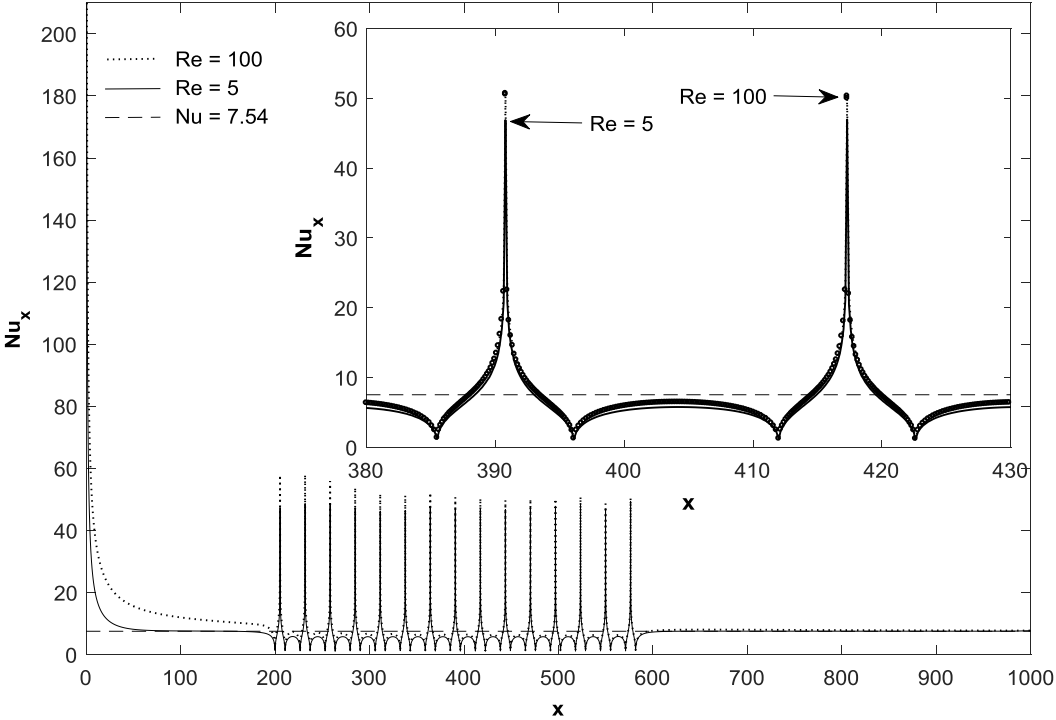


Figure 4.11: Local  $Nu$  distribution along the 2D Geometry ( $d$ ) ( $\epsilon = 2.65\%$ ) and close-up view between the two consecutive roughness elements.

## CHAPTER 5

### 3D FLOW SIMULATIONS IN TRAPEZOIDAL CHANNELS

In this chapter, conducted three-dimensional isothermal fluid flow simulations in channels with trapezoidal cross-sections are described separately. At the beginning, four macroscale smooth channels are considered, which have widely used fully developed  $Po$  solutions and documented in Ref. [109], to test the modeling procedure and accuracy. Then, four smooth microchannels with the same aspect ratios and side angles of macrochannels, and one smooth microchannel whose geometrical properties are different from the former ones and taken from Ref. [26] are considered, and compared with the macro counterparts. Lastly, three different rough channels are considered, where the roughness is modeled by conical obstructions at the base of the smooth microchannel with different patterns. Results obtained from the rough channel simulations are compared with the results obtained from the smooth channel simulations to determine the effect of designed roughness on  $Po$  values. Also, mesh independence studies for each case are described. Laminar flow module of COMSOL Multiphysics program is used in all of the simulations.

#### 5.1 FLOW SIMULATIONS IN MACROSCALE SMOOTH CHANNELS

Macroscale flow simulations are conducted to test the modelling procedure and accuracy in the used commercial software, COMSOL Multiphysics, by comparing the calculated  $Po$  values with the analytical ones. Fully developed  $Po$  values of macrochannels are tabulated in [109] for specific aspect ratios  $\alpha$ , which is defined as the ratio of height to the short base width, and trapezoid side angles  $\theta$ . From these

tabulated data, two different aspect ratios, namely 0.25 and 0.50, and two different side angles,  $45^\circ$  and  $60^\circ$  are chosen. By this way, specific aspect ratio of 0.3876 and side angle of  $54.79^\circ$  of the microchannel taken from Ref. [26] is enclosed for further comparison purposes, since its value is not specified in the tabulated data of [109].

Schematics of the used trapezoidal macroscale channels are presented in Fig. (5.1) and geometrical properties are summarized in Table – (5.1) with the corresponding analytical values of  $Po$ . Base width and length of the channels are taken as 20 mm and 400 mm, respectively. Other dimensions are calculated using aspect ratio and side angles.  $Po$  is calculated in the midsection of the channel after the flow develops to compare the results with the analytical fully developed ones.

Table 5.1: Geometrical properties of the smooth macro trapezoidal channels used in simulations.

<b><i>Geometry</i></b>	<b><i><math>\alpha</math></i></b>	<b><i><math>\theta</math></i></b>	<b><i><math>W_b</math> [mm]</i></b>	<b><i><math>W_t</math> [mm]</i></b>	<b><i><math>H</math> [mm]</i></b>	<b><i><math>L</math> [mm]</i></b>	<b><i><math>Po</math></i></b>
Macro_G01	0.25	$45^\circ$	20	30	5	400	17.397
Macro_G02	0.50	$45^\circ$	20	40	10	400	15.206
Macro_G03	0.25	$60^\circ$	20	25.77	5	400	18.053
Macro_G04	0.50	$60^\circ$	20	31.55	10	400	15.693

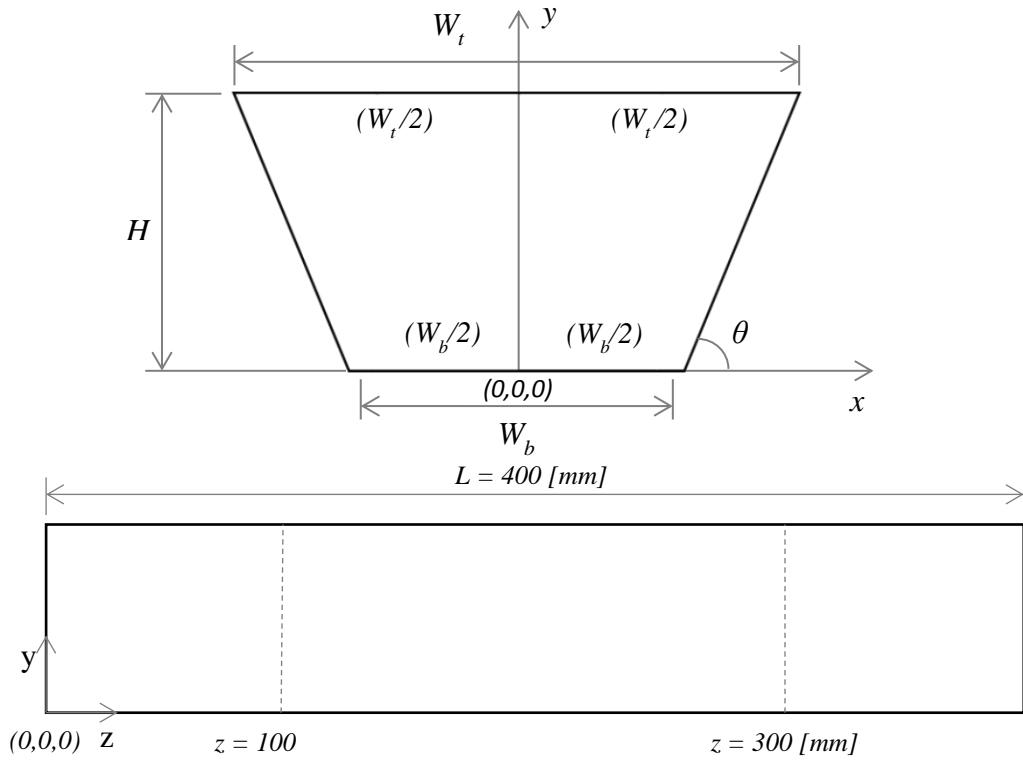


Figure 5.1: Schematics of the cross-sections of trapezoidal channel used in macroscale flow simulations.

Mesh independence runs are carried out for  $Re = 100$  for each channel separately. Mesh element sizes gradually reduced, thus increasing the mesh element number and degrees of freedom (DOFs), resulting in approximately  $2 \times 10^6$  to  $14 \times 10^6$  elements. During the simulations, iterative multigrid is used with  $10^{-6}$  relative tolerance.

Generally, the difference between the numerically calculated  $Po$  values and the analytical values drops below 1% after about  $5 \times 10^6$  elements are used. One example of changing of  $Po$  with element number for mesh independence runs of *Macro\_G01* case is shown graphically in Fig. (5.2a), and corresponding memory use and solution times are shown in Fig. (5.2b). Considering the computational cost and accuracy

balance, chosen element numbers are tabulated in Table – (5.2) with corresponding  $Po$  values. For the chosen meshes, difference from the analytical solutions are less than 0.7%.

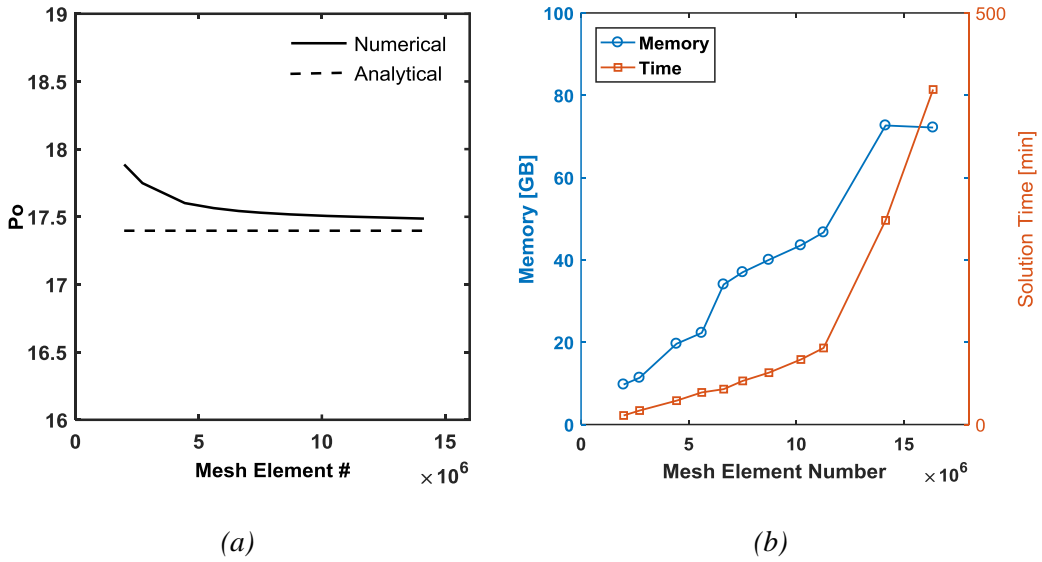


Figure 5.2: (a) Change of  $Po$  values with respect to element number for mesh independence runs of *Macro\_G01* case, (b) Solution time and memory use with respect to element numbers.

Table 5.2: Accepted mesh element numbers for each case with corresponding  $Po$  values and percentage differences from analytical values.

<i>Geometry</i>	<i>Mesh Element Number</i>	<i>Po (Numerical)</i>	<i>Po (Analytical)</i>	<i><math>\Delta Po</math> [%]</i>
Macro_G01	8,723,400	17.517	17.397	0.6928
Macro_G02	8,546,380	15.311	15.206	0.6911
Macro_G03	6,216,943	18.173	18.053	0.6667
Macro_G04	7,293,062	15.777	15.693	0.5358

## 5.2 FLOW SIMULATIONS IN MICROSCALE SMOOTH CHANNELS

Microscale flow simulations contain five different geometries. Four of them have the same aspect ratio ( $\alpha$ ) and side angle ( $\theta$ ) values with the channels previously mentioned in macroscale flow simulations. However, total length ( $L$ ) and base width ( $W_b$ ) of these channels are taken from the fifth geometry, which is adopted from the experimental and numerical work of Wang et al. [26], and constructs the basis of rough microchannels. By this way, one can compare the calculated  $Po$  values for microchannels with the analytical values of macrochannels and can estimate the effect of roughness in microchannels, which is going to be added to this channel. Schematics of the microchannel geometry along the flow direction used in smooth microscale flow simulations is given in Fig. (5.3) and geometrical properties of these channels are summarized in Table – (5.3).

Mesh independence studies are conducted by using approximately  $4.3 \times 10^6$  to  $12.9 \times 10^6$  elements for  $Re = 100$ . Average element qualities were above 0.76 for all the test cases. Iterative multigrid solver is used in the simulations and relative tolerance is set to  $10^{-6}$ . During the mesh independence study,  $Po$  values are calculated in the midsection,  $z = 10$  mm and  $z = 30$  mm planes, similar to the macro flow simulations, and the difference between the consecutive calculated values are considered. Generally, after  $8 \times 10^6$  elements, the change between the consecutive steps becomes less than 0.4%. Change in  $Po$  with respect to mesh element number is shown in Fig. (5.4) for *Micro\_G03* and *Micro\_G04* geometries as an example, and selected meshes with corresponding  $Po$  values are tabulated in Table – (5.4).

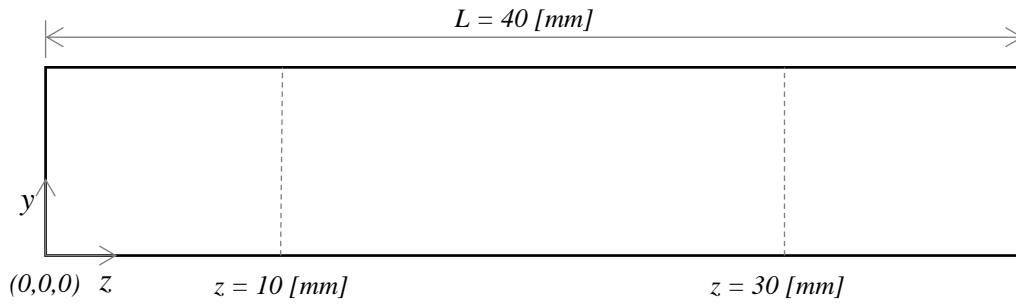


Figure 5.3: Schematics of the side view of microchannel geometry along the flow direction used in smooth microscale flow simulations.

Table 5.3: Geometrical properties of smooth microchannels used in simulations.

<b>Geometry</b>	<b><math>\alpha</math></b>	<b><math>\theta</math></b>	<b><math>W_b</math> [<math>\mu\text{m}</math>]</b>	<b><math>W_t</math> [<math>\mu\text{m}</math>]</b>	<b><math>H</math> [<math>\mu\text{m}</math>]</b>	<b><math>L</math> [mm]</b>
Micro_G01	0.25	45°	276	414	69	40
Micro_G02	0.50	45°	276	552	138	40
Micro_G03	0.25	60°	276	355.674	69	40
Micro_G04	0.50	60°	276	435.349	138	40
Micro_G05	0.3876	54.79°	276	427	107	40

Table 5.4: Accepted mesh element numbers for each case with corresponding  $Po$  values.

<b>Geometry</b>	<b>Mesh Element Number</b>	<b><math>Po</math> (Numerical)</b>
Micro_G01	10,192,806	17.846
Micro_G02	10,032,703	15.382
Micro_G03	10,229,101	18.439
Micro_G04	10,358,107	15.836
Micro_G05	11,377,065	16.559

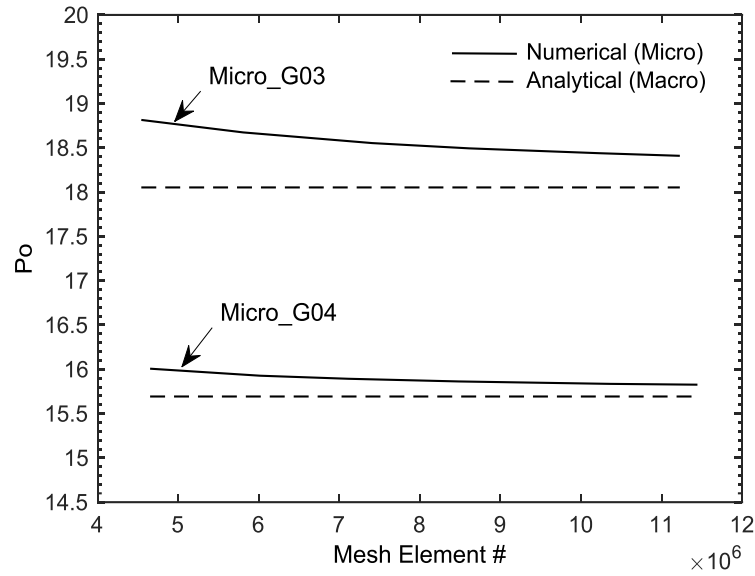


Figure 5.4: Change in  $Po$  with respect to mesh element number for *Micro\_G03* and *Micro\_G04* cases.

### 5.3 FLOW SIMULATIONS IN MICROSCALE ROUGH CHANNELS

Microflow simulations in rough channels are carried out by considering three different roughness configurations. Roughness is simulated as placing cones on the base of the *Micro\_G05* case geometry. Mesh independence runs are conducted for  $Re = 100$  by using approximately  $5 \times 10^6$  to  $17 \times 10^6$  elements for each case and change in  $Po$  value between two consecutive runs are considered. Similar to previous simulations, iterative multigrid solver is used with  $10^{-6}$  relative tolerance. Apart from the previously mentioned smooth cases,  $Po$  values are calculated between the  $z = 5,000 \mu\text{m}$  and  $z = 35,000 \mu\text{m}$  planes instead of  $z = 10 \text{ mm}$  and  $z = 30 \text{ mm}$  planes, which covers the inlet and exit of the rough section completely.

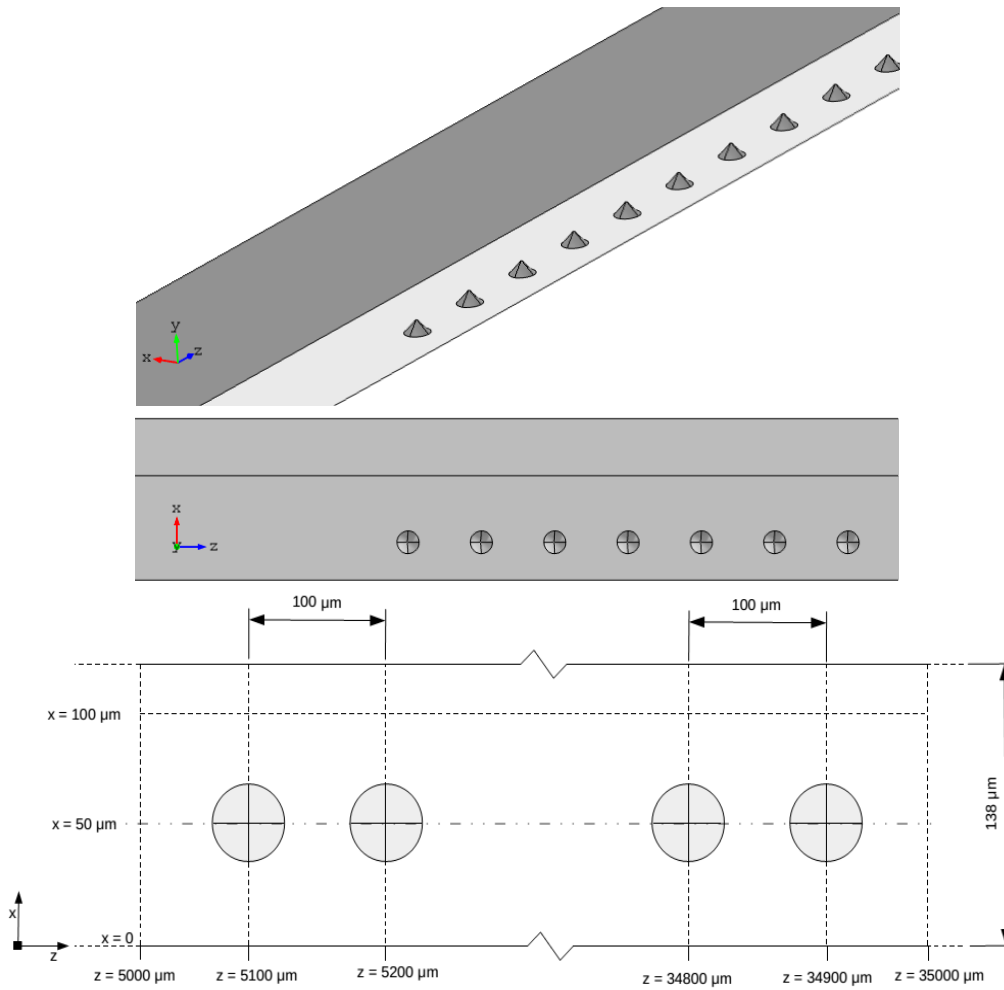


Figure 5.5: Model of *Micro\_G06 (1LineCone)* case and geometrical properties of its roughness elements.

In the first rough case, named as *Micro\_G06 (1LineCone)*, 299 cones are placed along a line on the base of the channel, between  $z = 5,000 \mu\text{m}$  and  $z = 35,000 \mu\text{m}$  planes, which have height and base radius of  $15 \mu\text{m}$ . Model picture and placing dimensions of these roughness elements are given in Fig. (5.5).

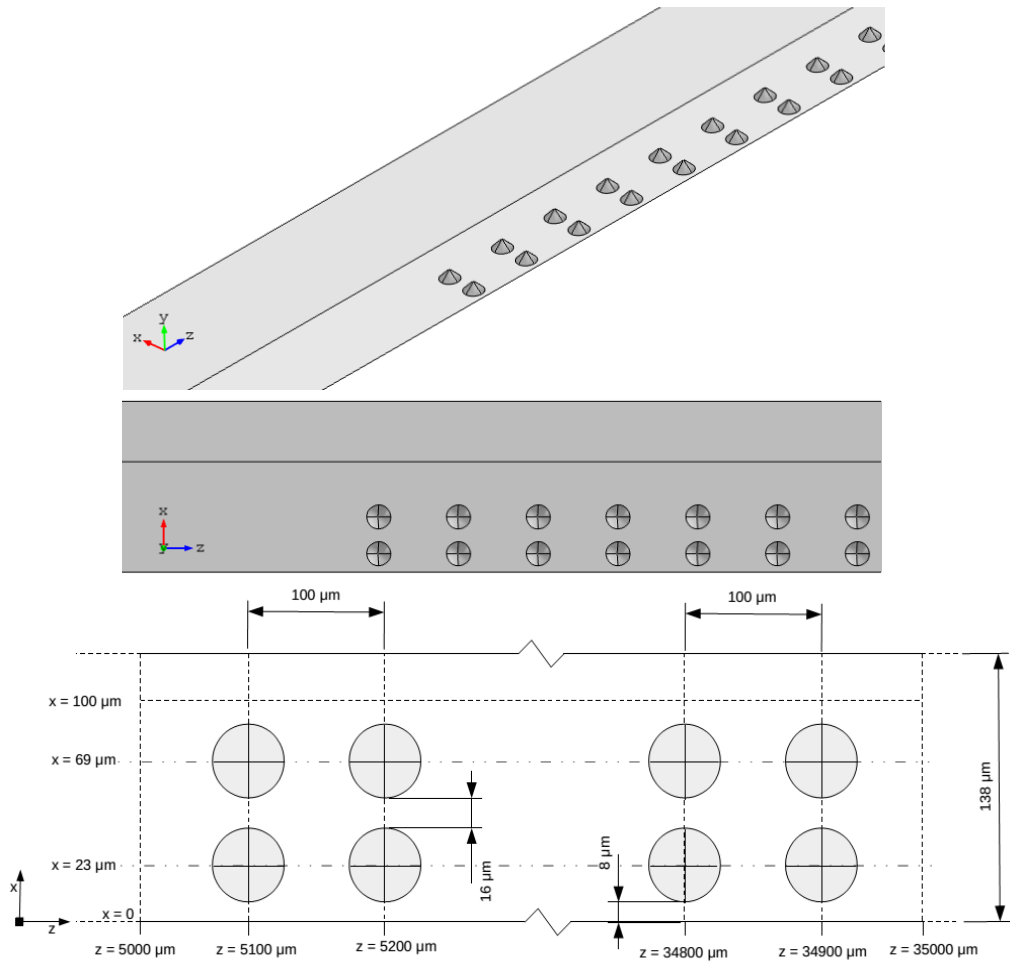


Figure 5.6: Model of *Micro\_G07 (2LineCone)* case and geometrical properties of its roughness elements.

The second rough case, named as *Micro\_G07 (2LineCone)*, has 598 cones placed along two lines on the base of the channel, between  $z = 5,000 \mu\text{m}$  and  $z = 35,000 \mu\text{m}$  planes. Its configuration is practically doubling of the first rough geometry. In this case, cones also have height and base radius of  $15 \mu\text{m}$ . Model picture and placing dimensions of this geometry are given in Fig. (5.6)

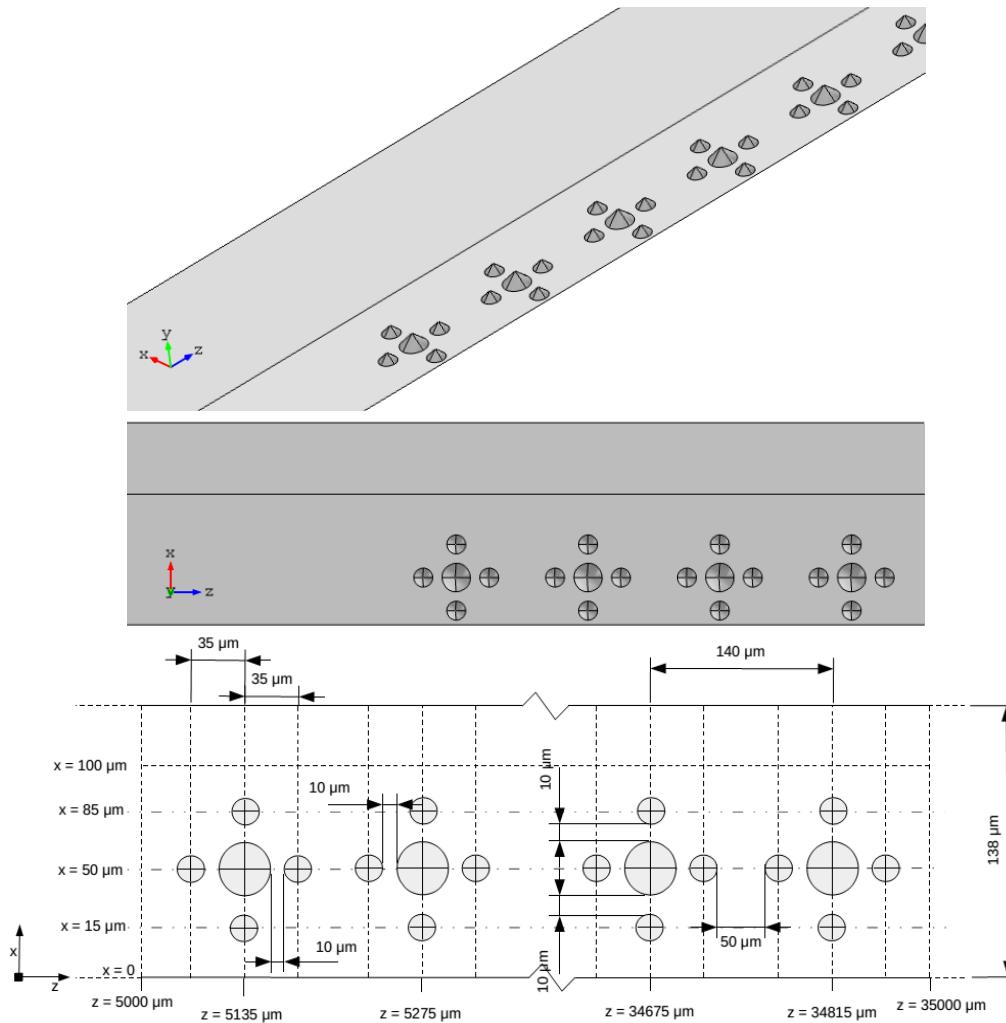


Figure 5.7: Model of *Micro\_G08 (DaisyCone)* case and geometrical properties of its roughness elements.

The third rough case, named as *Micro\_G08 (DaisyCone)*, has 852 small cones which have 10  $\mu\text{m}$  height and base radius, 213 big cones which have 15  $\mu\text{m}$  height and base radius, placed in a pattern on the base of the channel, between  $z = 5,000 \mu\text{m}$  and  $z = 35,000 \mu\text{m}$  planes which is shown in Fig. (5.7).

Calculated  $Po$  values with respect to mesh element numbers are shown in Fig. (5.8) with the smooth *Micro\_G05* case. After using about  $10 \times 10^6$  mesh elements for *Micro\_G06* and *Micro\_G07* cases, and about  $15 \times 10^6$  mesh elements for *Micro\_G08* case, percentage difference between the two consecutive runs reduces to below 0.5%. Chosen meshes for rough cases are given in Table – (5.5).

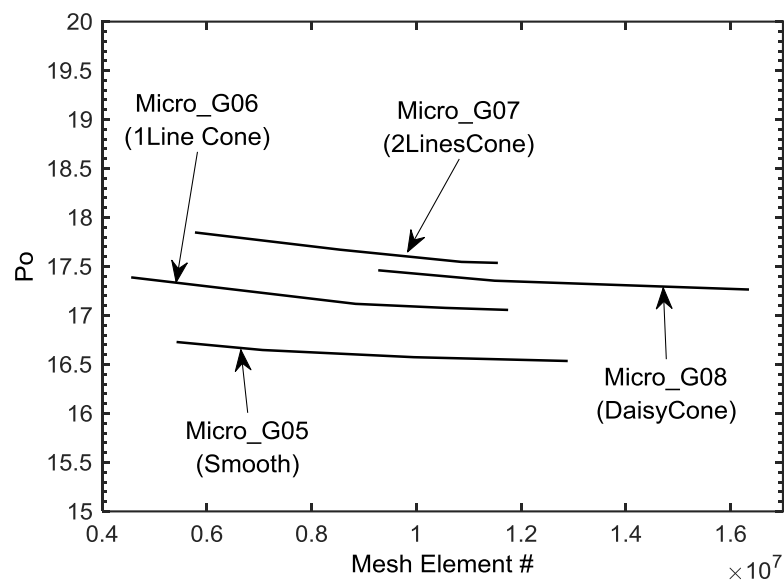


Figure 5.8: Calculated  $Po$  values with respect to mesh element numbers for mesh independence studies of micro smooth and rough geometries.

Table 5.5: Accepted mesh element numbers for each micro case with corresponding  $Po$  values.

<i>Geometry</i>	<i>Mesh Element Number</i>	<i>Po (Numerical)</i>
Micro_G05 ( <i>Smooth</i> )	11,377,065	16.559
Micro_G06 ( <i>1LineCone</i> )	11,751,285	17.057
Micro_G07 ( <i>2LineCone</i> )	11,555,372	17.537
Micro_G08 ( <i>DaisyCone</i> )	16,351,465	17.265

#### 5.4 DISCUSSIONS

Calculated  $Po$  values for macro and microscale smooth channels having aspect ratios of 0.25 and 0.50, and trapezoid side angles of  $45^\circ$  and  $60^\circ$  are summarized in Table – (5.6) with the percent difference between the counterparts. Percentage difference is calculated by

$$\Delta Po = abs\left(\frac{Po_{Macro} - Po_{Micro}}{Po_{Macro}}\right) \times 100 \quad (5.1)$$

When the channel sizes reduced to micro level, a small increase in  $Po$  values is observed. This increase is below 0.5% for higher aspect ratio channels, and about 1.5-2% for the lower aspect ratio channels. Effect of side angle is found to be even smaller for the higher aspect ratio channels. As the side angle reduced, the difference between them slightly increases. As a conclusion, it can be stated that, difference between the macro and microscale  $Po$  values is more pronounced for smaller aspect ratio channels. However, it should be noted here, since the mesh independence studies are truncated after the difference between consecutive runs drops below 0.5%, not to 0%, some portion of the difference between the values of macro and

microscale  $Po$  should belong to numerical error. Thus, the difference between the macro and microscale  $Po$  values of higher aspect ratio trapezoidal channels could be considered as negligible.

Table 5.6: Comparison of calculated  $Po$  values for macro and microscale smooth channels.

$\alpha$	$\theta$		$Po$ (num.)	$\Delta Po$ [%]	$Po$ (num.)		$\alpha$	$\theta$
0.25	45°	Macro_G01	17.517	1.878	17.846	Micro_G01	0.25	45°
0.50	45°	Macro_G02	15.311	0.464	15.382	Micro_G02	0.50	45°
0.25	60°	Macro_G03	18.173	1.464	18.439	Micro_G03	0.25	60°
0.50	60°	Macro_G04	15.777	0.374	15.836	Micro_G04	0.50	60°

Calculated  $Po$  values for considered smooth and rough microchannels are summarized and rough channel values are compared with the smooth  $Micro\_G05$  case values in Table – (5.7). Percentage difference is calculated by

$$\Delta Po = abs\left(\frac{Po_{G05} - Po_{rough}}{Po_{G05}}\right) \times 100 \quad (5.2)$$

It is found that existence of roughness in conical forms increases the  $Po$  value with respect to the smooth channel value. This increase is found to be between 3% and 6%, depending on the roughness pattern. Doubling the number of cones in an ordered way like in  $Micro\_G07$  case doubles the percentage difference with respect to smooth value. However, increase in  $Micro\_G08$  (*DaisyCone*) configuration, which has more conical obstructions with a more complex pattern, is less than the  $Micro\_G07$  two line cone configuration. Similar behavior of less increase in  $Po$  value with complex patterns in engineered surfaces is also reported in literature previously for different geometries.

Table 5.7: Comparison of calculated  $Po$  values for microscale smooth and rough channels.

	<b><math>Po</math> (num.)</b>	<b><math>\Delta Po</math> [%]</b>
Micro_G05 ( <i>Smooth</i> )	16.559	-
Micro_G06 ( <i>1LineCone</i> )	17.057	3.007
Micro_G07 ( <i>2LineCone</i> )	17.537	5.906
Micro_G08 ( <i>DaisyCone</i> )	17.265	4.264

## CHAPTER 6

### 3D FLOW AND HEAT TRANSFER SIMULATIONS IN TRAPEZOIDAL MICROCHANNELS

In this chapter, three dimensional fluid flow and heat transfer simulations in smooth and rough microchannels are described. First, the reference smooth problem that constitutes the basis for the rough channel simulations is described. Then, simulation procedure and results of the reference problem are presented with comparisons of reference results. Later, simulations in rough microchannels with *1LineCone*, *2LineCone*, and *DaisyCone* configurations are described and results are presented. Lastly, some flow and heat transfer parameters obtained from smooth and rough microchannel simulations are compared and summarized.

#### 6.1 REFERENCE PROBLEM DEFINITION

In this study, as briefly explained in Chapter 5 – Section 2, the channel geometry, and main simulation conditions for the heat transfer and fluid flow simulations in smooth microchannels are adopted from the experimental and numerical work of Wang *et al.* [26]. Published results of [26] for  $T_w$  and  $Nu$  are used as reference for mesh independence studies and validation of the obtained results. After smooth microchannel flow and heat transfer simulations, investigations are extended to rough microchannel geometries, which are presented in Chapter 5 – Section 3 and briefly explained here again.

In their numerical and experimental study Wang *et al.* [26] investigated the laminar forced convection heat transfer characteristics of degassed and deionized water flowing in a trapezoidal microchannel having hydraulic diameter of 155  $\mu\text{m}$ , top width of 427  $\mu\text{m}$ , bottom width of 276  $\mu\text{m}$ , and height of 107  $\mu\text{m}$ , which results in a sidewall angle of 54.7°. The microchannel used in the experiments are made by etching <100> silicon substrate, which constructs the channel sidewalls and then bonded by two Pyrex glass plates from top and bottom. The channel has a total of 40 mm length. Fifteen platinum microheaters, each having 2 mm length and 200  $\mu\text{m}$  width, are placed in the bottom Pyrex wall. Thus, a total of 200  $\mu\text{m} \times 30$  mm heating section obtained and placed starting 5 mm away from the inlet and ending 5 mm before the exit. Placement and sizes of microheaters resulted in an unheated section of 38  $\mu\text{m} \times 30$  mm at each side of the microheaters on the bottom surface. Each microheater is also used as a temperature sensor in which the average temperatures of heaters are calculated using electrical resistance. Schematic of the used microchannel and heater placement is given in Fig. (6.1).

The authors conducted the experiments in two parts. In the first part of the experiments, the channel is heated with the first microheater only with heat fluxes of 986.3  $\text{kW}/\text{m}^2$ , 1481.6  $\text{kW}/\text{m}^2$ , and 1974.9  $\text{kW}/\text{m}^2$ , and for inlet mass fluxes of about 300  $\text{kg}/(\text{m}^2\text{s})$  to 5000  $\text{kg}/(\text{m}^2\text{s})$ , resulting in Reynolds numbers of 45 to 815. For the second part of the experiments, the channel is heated with all of the microheaters supplying 300  $\text{kW}/\text{m}^2$  effective heat flux to the working fluid with inlet mass fluxes from 200  $\text{kg}/(\text{m}^2\text{s})$  to 3450  $\text{kg}/(\text{m}^2\text{s})$ , yielding Reynolds numbers of 33 to 565.

During the experiments, inlet, exit, and microheater temperatures are measured and then, Nusselt numbers are evaluated. Measurement error of  $D_h$ , effective heat flux, fluid temperature, and thermal conductivity are given as 1.8%, 2.6%, 2.9%, and 1.0%, respectively, which yield a maximum uncertainty of 8.3% in the calculation of  $Nu$ .

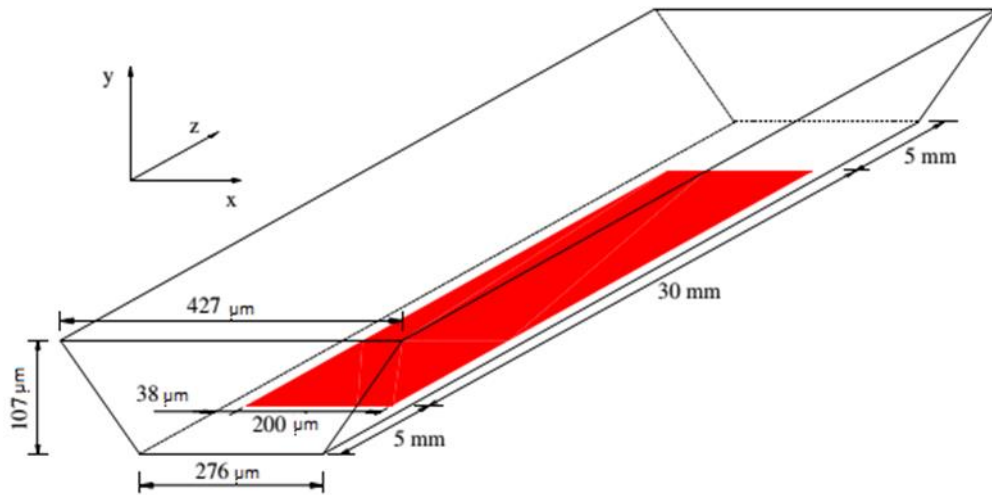


Figure 6.1: Schematic of trapezoidal microchannel and placement of heated section in the reference work [26].

After the experiments, the authors conducted 3D numerical simulations with the commercial CFD program FLUENT by mimicking the experimental conditions as much as possible with the assumptions of incompressible steady laminar flow of liquid water with temperature dependent thermophysical properties and negligible radiation, viscous dissipation, and gravity effects. Effective heat fluxes from the experiments are imposed as uniform heat fluxes over the heated section. They compared the experimentally and numerically obtained temperatures and  $Nu$  values for partially and fully heated channel cases, and presented them graphically.

For partially heated cases, it is found that the wall temperature decreases with increasing mass flux and decreasing heat flux, as expected.  $Nu$  values increase with increasing mass flux without approaching a limit in the test section. However, it is also found that heat flux has a small effect on  $Nu$  since the fluid properties vary with temperature. For the fully heated cases, local  $Nu$  values gradually approached to a constant value for lower mass fluxes. However,  $Nu$  does not approach to a constant

at the end of the heating section, which indicates that the thermal entrance length of the flow is longer than the heating length.

Among the experimental conditions of [26], cases with effective heat flux of 300 kW/m<sup>2</sup> and inlet mass fluxes of 200 kg/(m<sup>2</sup>s), 294 kg/(m<sup>2</sup>s), 368 kg/(m<sup>2</sup>s), 736 kg/(m<sup>2</sup>s), and 1016 kg/(m<sup>2</sup>s), which result in inlet  $Re$  values of approximately 31, 45, 57, 114, and 157, are selected for this study. Uniform inlet velocity that is based on the inlet mass fluxes and constant temperature of 293.15 K are used as inlet boundary conditions. Zero pressure is imposed at the outlet and no-slip velocity condition is used at walls. Also, effective heat flux is applied as uniform inward heat flux over the heated section. Due to the symmetry about the  $yz$ -plane, symmetry boundary condition is applied to this plane and only half of the channel is used as the computational domain.

Simulations are carried out by COMSOL Multiphysics. Wall mean temperatures, bulk mean temperatures, and local  $Nu$  values over the microheater locations are calculated by using COMSOL's LiveLink for MATLAB module with the equations described in Chapter 3. In addition to the change in  $T_w$ ,  $T_m$ , and  $Nu$ , the change in heated surface maximum and average temperatures, domain average temperatures, and  $Po$  values between the inlet and exit of heated section are examined.

As stated before, rough channels are constructed by replacing cones over the heated section of reference smooth channel. Three different roughness patterns are considered in this work, namely *1LineCone (RILC)*, *2LineCone (R2LC)*, and *DaisyCone (RDC)* configurations. For graphical representation of cone patterns, placement and spacing dimensions, see Figs. (5.5), (5.6), and (5.7). Cone heights ( $h$ ), base radii ( $r$ ), and total number of cones used in each geometry are summarized in Table – (6.1).

In *1LineCone* configuration (*RILC*), 299 cones, which have height and base radius of 15  $\mu\text{m}$  with 45° of side angle, are placed along the line passing through  $x = 50$   $\mu\text{m}$  and starting from  $z = 5,100$   $\mu\text{m}$ , over the heated section with 100  $\mu\text{m}$  tip-to-tip

spacing in  $z$  direction. This configuration yields 2.92% increase in surface area of the heater compared to the smooth heater surface. The *2LineCone* configuration (*R2LC*) is practically the doubling of the *1LineCone* configuration in which the 2 lines of cones with same geometrical properties are placed through the lines at  $x = 23 \mu\text{m}$  and  $x = 69 \mu\text{m}$  starting from  $z = 5,100 \mu\text{m}$ , and resulted in 5.84% increase in surface area. In *DaisyCone* configuration (*RDC*), two different sized cones are used. Bigger cones with  $15 \mu\text{m}$  height and base radius are placed at the middle of the pattern and surrounded by 4 smaller cones having  $10 \mu\text{m}$  height and base radius with  $90^\circ$  rotation angles. Center of the bigger cone of the first pattern is at  $x = 50 \mu\text{m}$  and  $z = 5,135 \mu\text{m}$  location. Tip-to-tip distance of the bigger and smaller cones in  $x$  and  $z$  directions is  $35 \mu\text{m}$ , and the distance between tips of bigger cones in  $z$  direction is  $140 \mu\text{m}$ . Surface area increase for this configuration is 5.77%.

Table 6.1: Cone heights ( $h$ ), base radii ( $r$ ), and total number of cones used in each geometry.

<i>Geometry</i>	<i>h</i>	<i>r</i>	<i># of Cones</i>
<i>1LineCone (RILC)</i>	$15 \mu\text{m}$	$15 \mu\text{m}$	299
<i>2LineCone (R2LC)</i>	$15 \mu\text{m}$	$15 \mu\text{m}$	598
<i>DaisyCone (RDC)</i>	<b>(Big)</b>	$15 \mu\text{m}$	213
	<b>(Small)</b>	$10 \mu\text{m}$	852

## 6.2 SMOOTH MICROCHANNEL SIMULATIONS

### 6.2.1 MESH INDEPENDENCE STUDIES

Mesh independence studies for the smooth microchannel are carried out for an effective heat flux of  $300 \text{ kW/m}^2$  and an inlet mass flux of  $1016 \text{ kg/(m}^2\text{s)}$ , with

several meshes consisting of about  $435 \times 10^3$  DOFs for the coarsest one to  $17.6 \times 10^6$  DOFs for the densest one. Direct and iterative multigrid solvers are both used to assess the RAM use and run times. Linear elements, which are computationally inexpensive, are used and the relative tolerance is set to  $10^{-3}$ . Additional information about the effects of element discretization and relative tolerance level can be found in Appendix (B) with some other numerical considerations in COMSOL. Element numbers and DOFs of used meshes, solver types, CPU times, used physical memory (PM) and virtual memory (VM) are summarized in Table – (6.2) with the calculated  $Po$  values over the heated region, and average and maximum heated surface temperatures. All the simulations are conducted with a workstation having two Intel Xeon X5660 CPU and 48 GB of physical RAM with Microsoft Windows 7 operating system. For the cases where physical memory is not enough, a partition in the hard disk is used as temporary RAM with a penalty of much longer computational times.

COMSOL offers users various ways of constructing the mesh for the computational domain [108]. One way is to use the predefined physics controlled meshes which are named as *extremely coarse*, *extra coarse*, *coarser*, *coarse*, *normal*, *fine*, *finer*, *extra fine*, and *extremely fine*. By choosing one of these options, the program constructs the mesh automatically with predefined mesh size parameters. Meshes of *Case 1*, *3*, *5*, and *7* are constructed by using the *coarse*, *normal*, *fine*, and *finer* predefined options, respectively. Another way of constructing the mesh is by manually defining the element numbers along the edges, and other size related parameters such as element growth rates, minimum and maximum element sizes on the boundaries and inside the domains. Advantage of this way of creating the mesh is to have more control on the mesh. The user can produce a much denser mesh where fine resolution is needed, and make other regions, where fine resolution is not needed, coarser to reduce the total element number and thus the solution time and RAM need. However, the user also must carefully watch the element qualities of constructed mesh. Meshes of *Case 2*, *4*, *6*, *8-11* in this part is constructed by this way, increasing the element number around the heated surface more than other parts

of the channel meanwhile ensuring high quality of elements as much as possible and smooth transition between the regions of different densities.

It is observed that direct solvers are much faster than iterative solvers. However, as the DOFs of the problem increases, memory requirement increases drastically. After *Case-8*, percentage difference of calculated  $Po$  values between the densest case (*Case-11*) and the other cases drops to below 1%. Also, percentage difference of  $Po$  between the consecutive runs drops to below 1% with *Case-8*.

Table 6.2: Summary of mesh properties and calculated values used in mesh independence tests of smooth channel simulations (*S*: Solver, *I*: Iterative, *D*: Direct, *PM*: Physical Memory, *VM*: Virtual Memory, *HS*: Heated Surface).

<i>Case</i>	<i>ELEM #</i>	<i>DOFs</i>	<i>S</i>	<i>CPU Time [s]</i>	<i>PM [GB]</i>	<i>VM [GB]</i>	<i>Po</i>	<i>T<sub>ave,HS</sub> [K]</i>	<i>T<sub>max,HS</sub> [K]</i>
<b>1</b>	259,970	435,980	<i>I</i>	274	2.92	7.95	17.342	312.899	323.825
<b>2</b>	441,579	484,480	<i>D</i>	136	3.70	3.94	19.252	314.794	327.746
<b>3</b>	490,677	742,735	<i>I</i>	441	4.28	9.29	18.034	313.174	323.897
<b>4</b>	947,086	1,000,330	<i>D</i>	271	7.32	7.68	17.694	314.584	326.755
<b>5</b>	1,287,106	1,716,650	<i>I</i>	968	7.98	13.03	17.397	313.630	324.402
<b>6</b>	2,156,329	2,150,445	<i>D</i>	813	17.87	18.53	16.707	314.452	326.021
<b>7</b>	4,536,646	5,400,180	<i>I</i>	3,553	24.71	30.35	16.403	314.019	325.272
<b>8</b>	4,625,585	4,440,570	<i>D</i>	2,431	45.65	47.02	16.227	314.471	325.597
<b>9</b>	7,559,401	7,289,865	<i>I</i>	8,913	25.70	26.04	16.136	314.347	325.238
<b>10</b>	12,176,164	11,554,880	<i>I</i>	17,560	45.26	53.41	16.046	314.392	325.102
<b>11</b>	18,765,917	17,636,260	<i>I</i>	32,541	45.65	64.63	15.999	314.420	325.076

Calculated wall mean temperatures over the microheaters for cases with predefined meshes and with manually adjusted meshes are shown in Figs. (6.2a) and (6.2b), respectively, with the experimental and numerical results of Wang *et al.* [26] for an effective heat flux of 300 kW/m<sup>2</sup> and an inlet mass flux of 1016 kg/(m<sup>2</sup>s). Predefined coarser mesh (*Case-1*) resulted in the lowest temperature profile. Results obtained by predefined meshes become closer to the reference results as the DOFs increase.

On the other hand, manually constructed meshes showed two different trends. Up to the fifth microheater, meshes yield lower temperatures than the reference result, and after that, higher, which is more obvious for the coarsest manual mesh (*Case-2*). However, as the DOFs increased and resolution of the mesh became good enough, obtained temperature distribution approached to reference values. With *Case-8*, calculated values nearly coincided with each other and the numerical results of [26].

Local  $Nu$  distribution for the mesh independence test cases is shown in Fig. (6.3) with the experimental uncertainty band of  $\pm 8.3\%$  of [26] in calculating  $Nu$ . After *Case-6* the difference between calculated  $Nu$  values becomes very small, and with *Case-9* values nearly coincide. For *Case-10* and *Case-11*, maximum difference between the reference and calculated values of  $Nu$  occurred over the first heater, which is about 3.5%. At the other locations, calculated  $Nu$  values are about 2% higher, in a constant manner, which will be the result of small differences in values of thermophysical properties of the fluid that are used by the CFD programs. Since thermophysical properties of water both in this work and in the reference, are temperature dependent, and the simulation programs will use different functions and databases to calculate the appropriate values, such small differences should be expected.

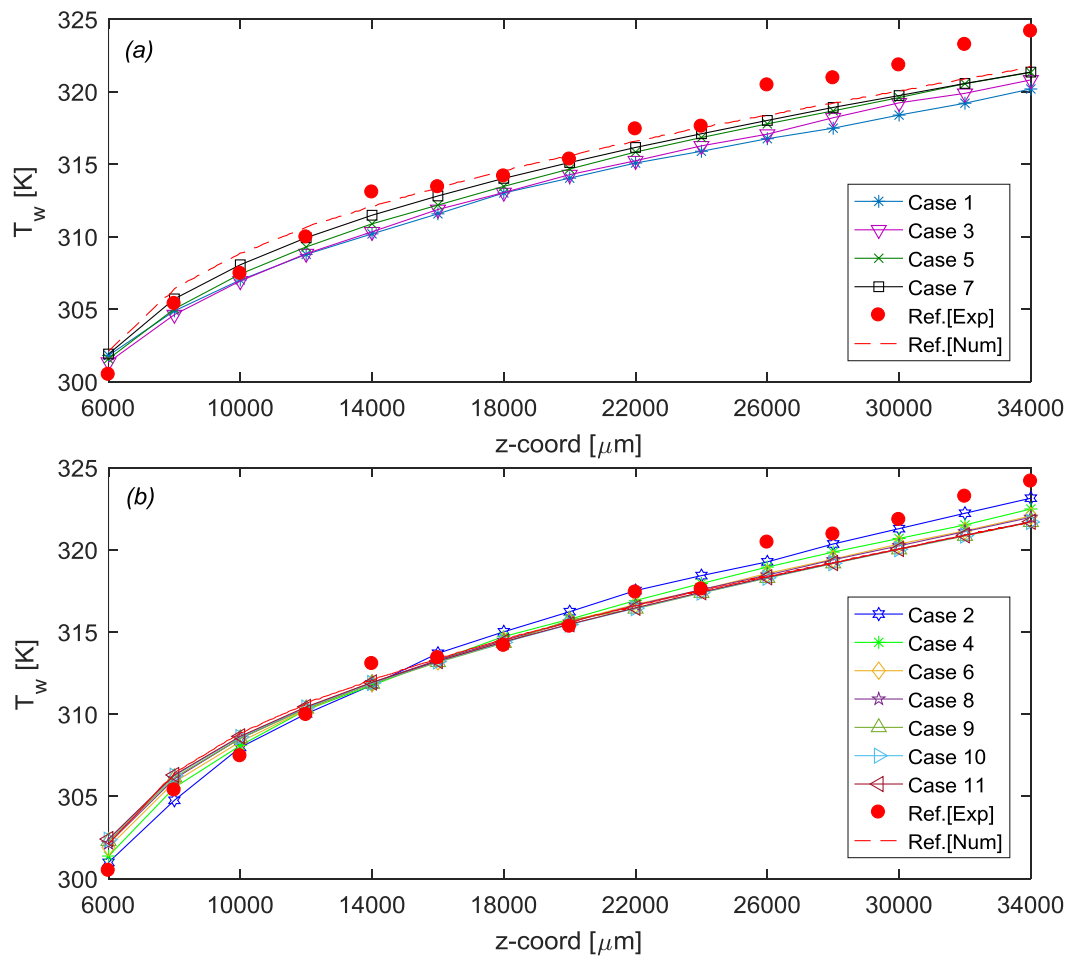


Figure 6.2: Wall mean temperatures over the microheaters for the mesh independence tests cases (a) Cases with predefined meshes, (b) Cases with manually adjusted meshes ( $q_{eff} = 300 \text{ kW/m}^2$ ,  $G = 1016 \text{ kg/(m}^2\text{s)}$ ).

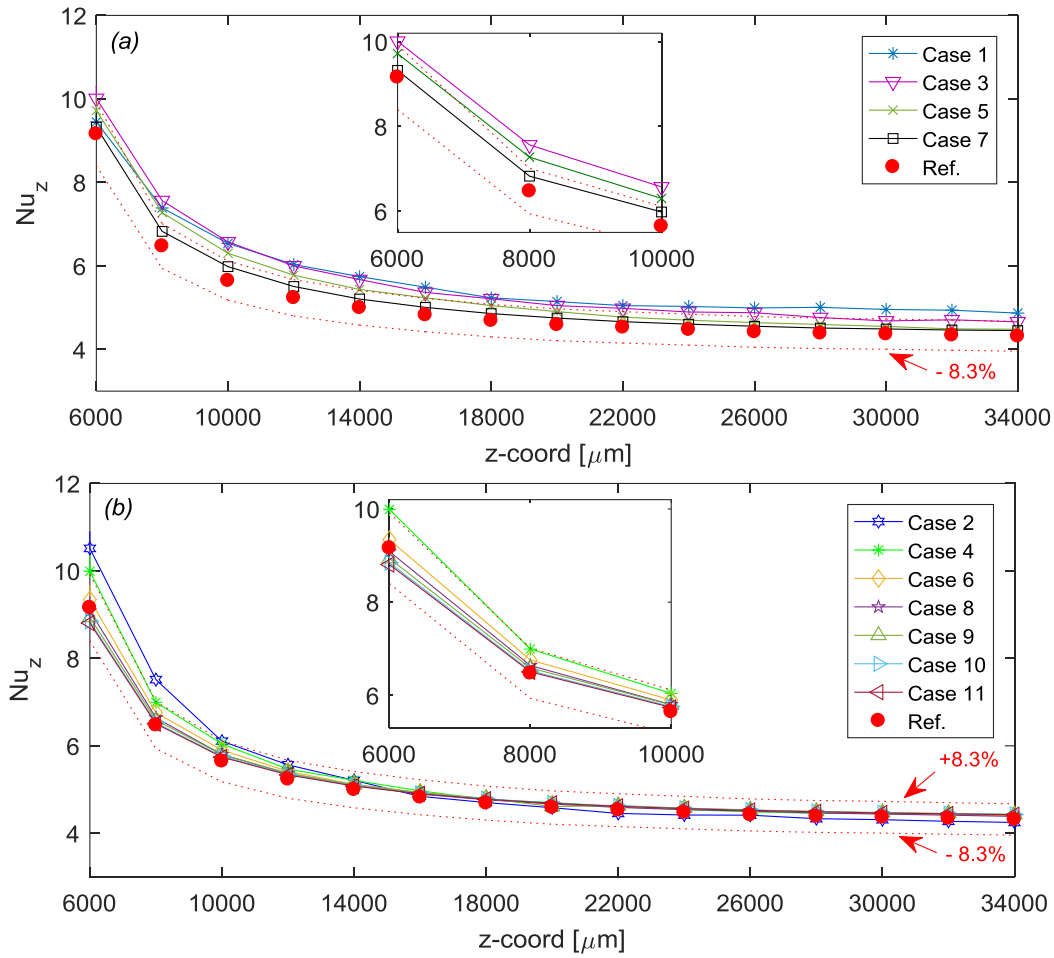


Figure 6.3: Local Nusselt numbers over the microheaters for the mesh independence test cases (a) Cases with predefined meshes, (b) Cases with manually adjusted meshes ( $q_{eff} = 300 \text{ kW/m}^2$ ,  $G = 1016 \text{ kg/(m}^2\text{s)}$ ).

Considering calculated values of  $Po$ ,  $T_w$ ,  $Nu$ , and the difference between the reference values with computational cost, mesh of *Case-10* is selected for good accuracy and affordable computational cost.

## 6.2.2 RESULTS AND DISCUSSIONS

Simulations for each inlet mass flux of 200 kg/(m<sup>2</sup>s) to 1016 kg/(m<sup>2</sup>s) are run by using the mesh of *Case-10* (with 11.55x10<sup>6</sup> DOFs) and setting the relative tolerance to 10<sup>-6</sup>.

Wall temperatures over the first two microheaters (at  $z = 6,000 \mu\text{m}$  and  $z = 8,000 \mu\text{m}$  positions) and last two microheaters (at  $z = 32,000 \mu\text{m}$  and  $z = 34,000 \mu\text{m}$ ) along the  $x$ -direction (from symmetry plane to the side of the microheater, perpendicular to flow direction) for various inlet mass fluxes are shown in Figs. (6.4) and (6.5), respectively. Also, wall temperatures along  $x$ -direction for various  $z$  locations for inlet mass fluxes of 200 kg/(m<sup>2</sup>s) and 1016 kg/(m<sup>2</sup>s) are shown in Fig. (6.6). The temperature of the wall increases along the flow direction since the fluid temperature increases. For the lowest inlet mass flux considered in this study, wall temperature nearly reaches the boiling point of water at the exit of the heated section. As the inlet mass flux increased, wall temperatures in all sections of the channel and difference between the inlet and exit temperatures drops accordingly.

Wall mean temperatures and  $Nu$  values that are calculated over the microheater locations along the  $x$ -direction, for various inlet mass fluxes are shown in Figs. (6.7) and (6.8), respectively, along with the reference results. Good agreement with the numerical results of the reference work is obtained.

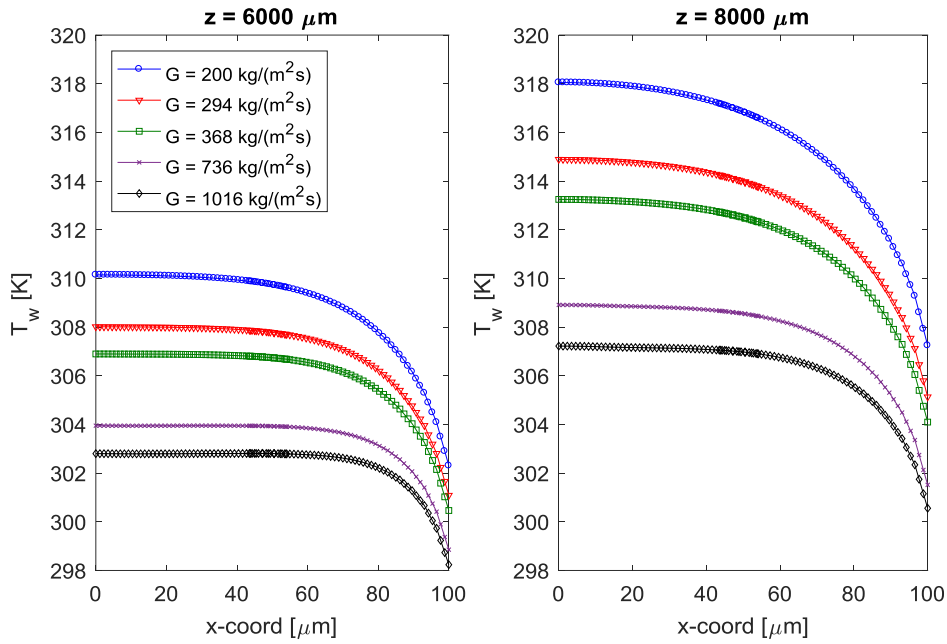


Figure 6.4: Wall temperatures over the first two microheaters (at  $z = 6000 \mu\text{m}$  and  $z = 8000 \mu\text{m}$ ) along  $x$ -direction for various inlet mass fluxes.

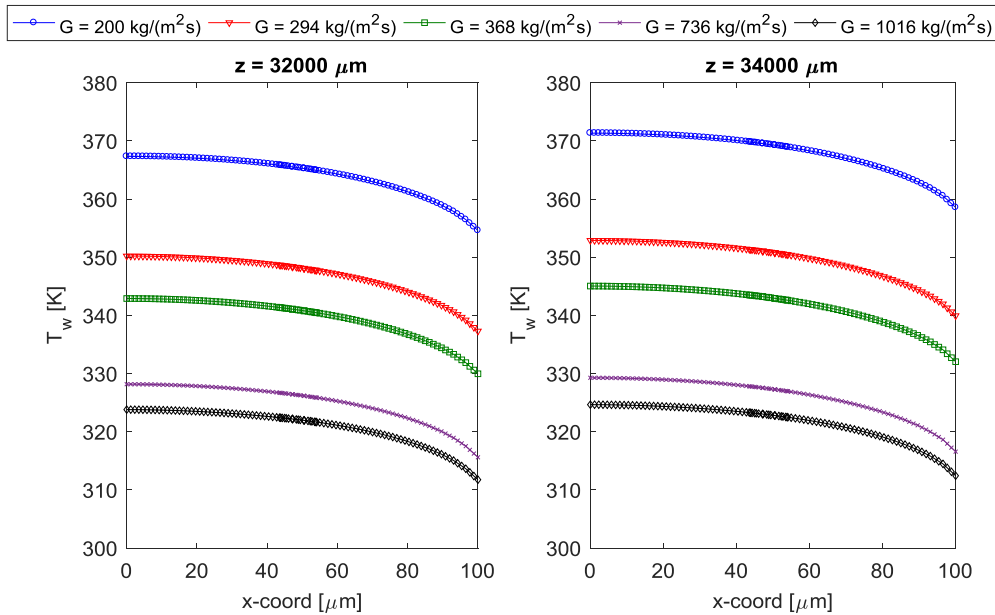


Figure 6.5: Wall temperatures over the last two microheaters (at  $z = 32000 \mu\text{m}$  and  $z = 34000 \mu\text{m}$ ) along  $x$ -direction for various inlet mass fluxes.

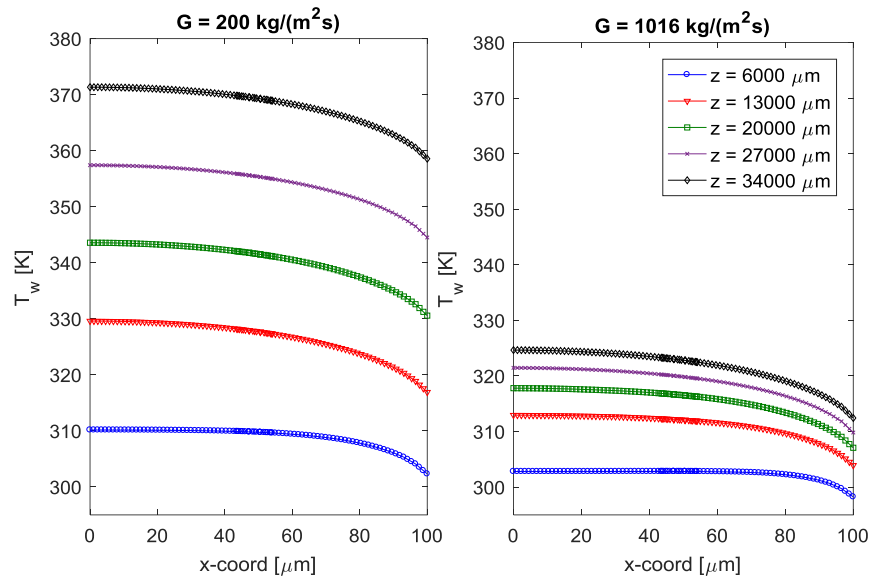


Figure 6.6: Wall temperatures along  $x$ -direction for various  $z$ -locations for inlet mass fluxes of  $200 \text{ kg}/(\text{m}^2\text{s})$  and  $1016 \text{ kg}/(\text{m}^2\text{s})$ .

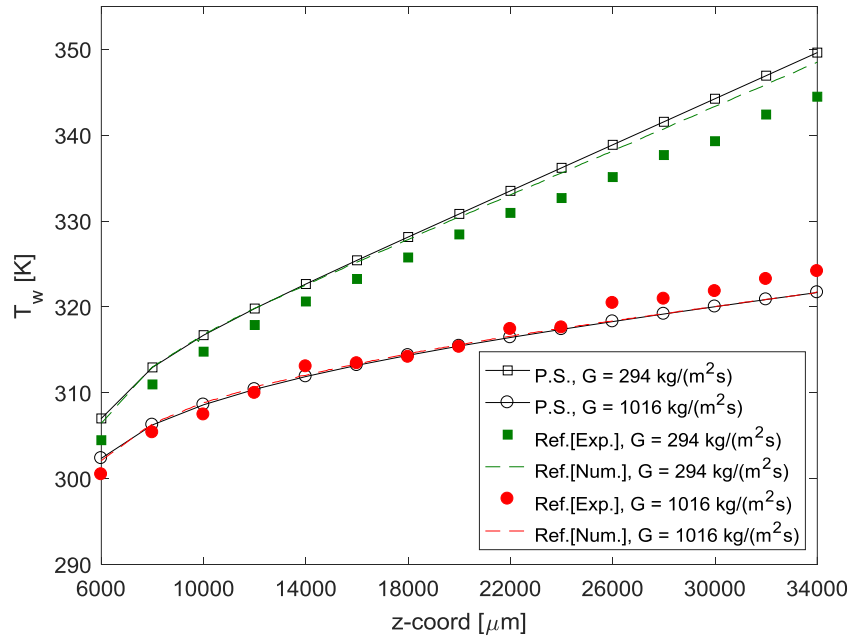


Figure 6.7: Wall mean temperatures for inlet mass fluxes of  $294 \text{ kg}/(\text{m}^2\text{s})$  and  $1016 \text{ kg}/(\text{m}^2\text{s})$  with reference results (*P.S.*: Present Study, *Ref.*: Reference Work, *Exp.*: Experimental, *Num.*: Numerical).

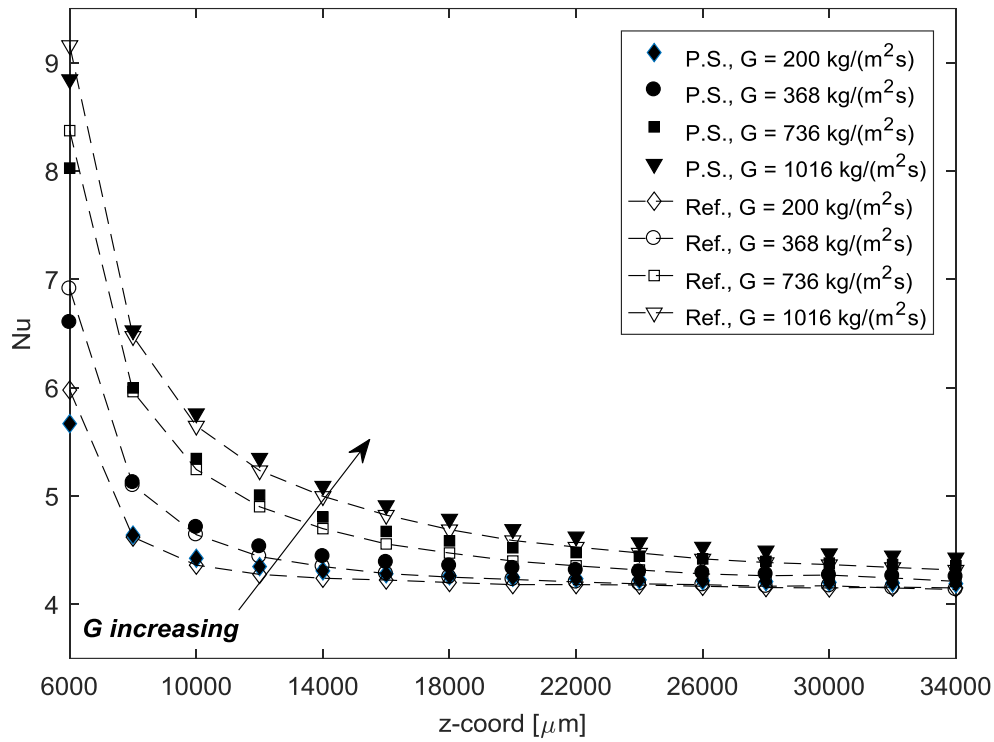


Figure 6.8: Calculated  $Nu$  values for various inlet mass fluxes along with the reference results (*P.S.*: Present Study, *Ref.*: Reference Work).

Calculated  $Po$  and  $Nu$  values are compared with the ones that are obtained from the equations proposed in the literature and reviewed in Chapter – 2 of this study. Since the analyzed problem has a unique heating geometry and heating conditions, there is not any equation that directly applies to this specific problem. Additionally, proposed equations are mostly for fully developed condition and standard boundary conditions of constant wall temperatures or constant heat flux with completely heated three or four walls. Other equations are experiment specific curve fitted equations with at least 10% experimental uncertainty. Moreover, some proposed equations only depend on geometrical properties of channels, while some of them also consider the flow parameters. Thus, wide range of  $Po$  and  $Nu$  values can be

found for flows in similar geometries. Figure (6.9) shows the obtained  $Po$  values for this study and the ones obtained from the equations proposed in literature. Calculated  $Po$  values are in close proximity of Eq. (2.1) (Morini [18]), Eq. (2.2) (Wu and Cheng [21]), and Eq. (2.9) (McHale and Garimella [37]). In addition,  $Nu$  values are compared in Fig. (6.10). Since the fully developed values are not reached, local values of  $Nu$  that are calculated over the last microheater (MH.15) is used for comparison. Obtained results are close to the results of McHale and Garimella [37] that is represented by Eq. (2.10).

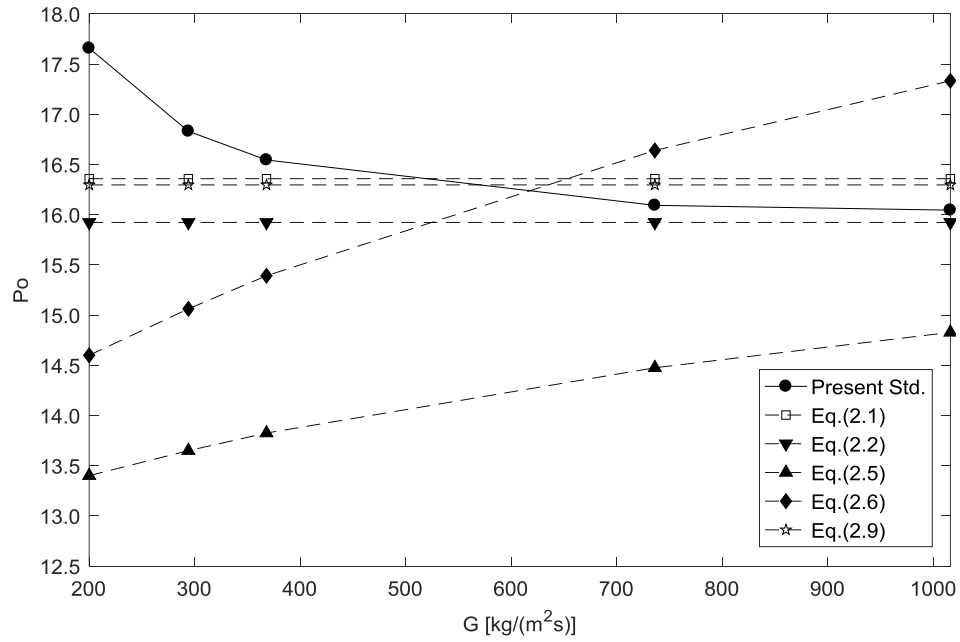


Figure 6.9: Comparison of  $Po$  values obtained from the equations proposed in literature.

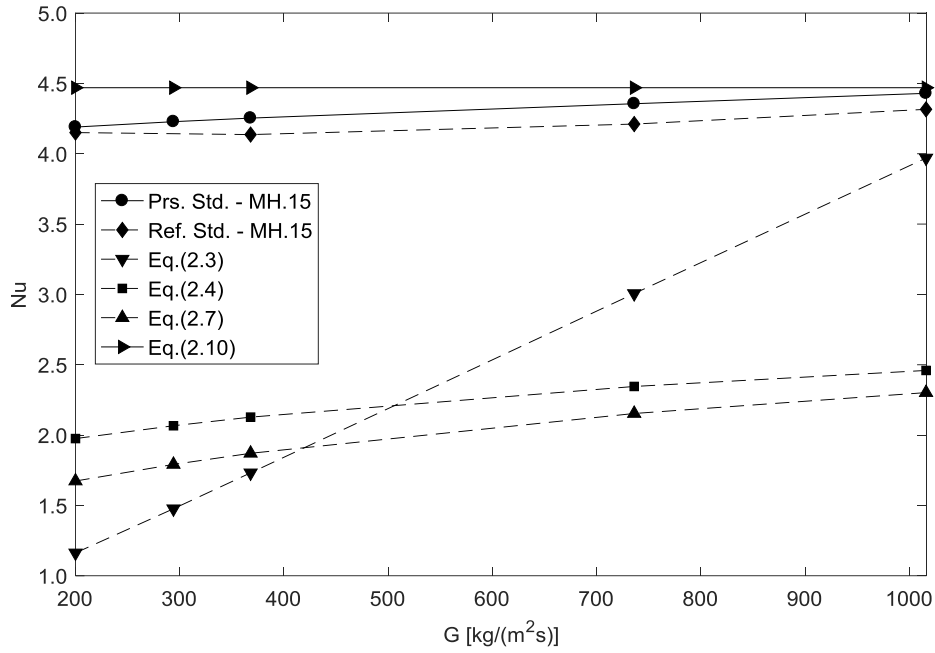


Figure 6.10: Comparison of  $Nu$  values obtained from the equations proposed in literature (*Prs. Std.*: Present Study, *Ref. Std.*: Reference Study [26], *MH.15*: 15<sup>th</sup> microheater).

### 6.3 ROUGH MICROCHANNEL SIMULATIONS WITH *ILineCone* (*RILC*) CONFIGURATION

#### 6.3.1 MESH INDEPENDENCE STUDIES

Mesh independence studies for the simulations in the microchannel having *ILineCone* roughness configuration (*RILC*) are carried out for an effective heat flux of 300 kW/m<sup>2</sup> and an inlet mass flux of 1016 kg/(m<sup>2</sup>s) case, with 8 different meshes consisting of about 2.51x10<sup>6</sup> DOFs for the coarsest one to 22.17x10<sup>6</sup> DOFs for the densest one. Iterative multigrid solver is used with linear mesh elements, and the relative tolerance is set to 10<sup>-3</sup>. Element numbers and DOFs of used meshes, CPU

times, used physical memory (PM) and virtual memory (VM) are summarized in Table – (6.3) with the calculated  $Po$  values over the heated region, and average and maximum heated surface temperatures. All the simulations are conducted with the same workstation used in smooth microchannel simulations. Again, for the cases where physical memory is not enough, a partition in the hard disk is used as temporary RAM with a penalty of longer computational times.

Among the test cases, meshes of *Case-1*, *Case-2*, and *Case-5* are constructed with predefined *coarse*, *normal*, and *fine* meshing schemes, respectively. Meshes of remaining cases are constructed manually by gradually increasing the element numbers on the edges of the geometry and reducing the element sizes inside the domain. Surface meshes around a conical roughness element of *Case-1*, *Case-6*, and *Case-8* are shown in Fig. (6.11), as an example.

Table 6.3: Summary of mesh properties and calculated values used in mesh independence tests of R1LC configuration (*PM*: Physical Memory, *VM*: Virtual Memory, *HS*: Heated Surface).

<i>Case</i>	<i>ELEM #</i>	<i>DOFs</i>	<i>CPU Time [s]</i>	<i>PM [GB]</i>	<i>VM [GB]</i>	<i>Po</i>	<i>T<sub>ave,HS</sub> [K]</i>	<i>T<sub>max,HS</sub> [K]</i>
<b>1</b>	1,957,312	2,513,200	1973	17.89	18.55	17.609	314.684	326.179
<b>2</b>	2,495,192	2,865,700	2570	19.85	20.59	17.241	314.870	326.437
<b>3</b>	6,155,356	5,929,560	10827	23.06	23.45	16.802	315.081	326.646
<b>4</b>	9,265,045	8,747,640	11648	30.32	30.77	16.635	315.143	326.659
<b>5</b>	11,696,345	11,994,300	23140	45.94	51.94	16.531	314.893	326.251
<b>6</b>	15,572,382	14,715,425	30195	44.3	50.81	16.465	315.099	326.480
<b>7</b>	18,986,064	17,720,375	40864	45.95	59.2	16.435	315.075	326.424
<b>8</b>	23,559,575	22,170,085	85333	46.86	65.08	16.348	315.097	326.431

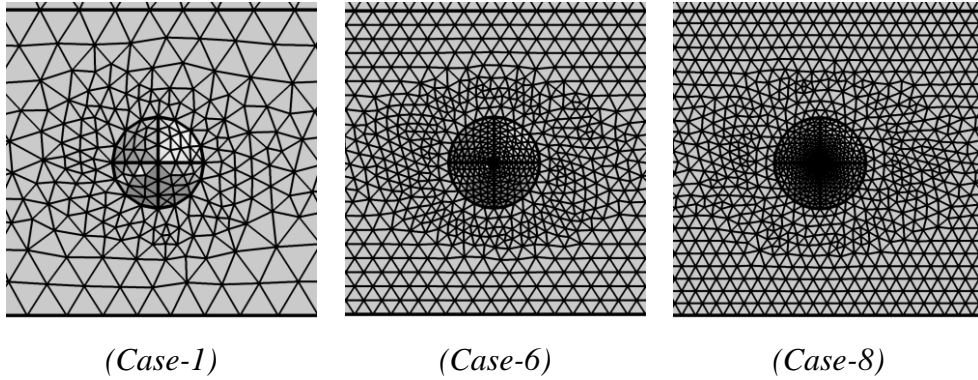


Figure 6.11: Surface meshes around the conical elements of RILC configuration for *Case-1* (coarsest), *Case-6*, and *Case-8* (densest).

The percentage difference of calculated  $Po$  values between two consecutive runs drops to below 1% with about  $6 \times 10^6$  DOFs (*Case-3*). The percentage difference of  $Po$  between the densest case (*Case-8*) and the other cases drops to below 1% about  $12 \times 10^6$  DOFs (*Case-5*). Also, average and maximum temperatures of heated surface remains nearly constant after *Case-5*.

Fluid bulk mean temperatures for mesh independence cases are calculated in cross-sectional planes that are  $5 \mu\text{m}$  apart from each other around the conical elements and  $10 \mu\text{m}$  apart between the conical elements in the flow direction. At the beginning of rough section, difference between the mean values for each test case is miniscule. At the end of the rough section, test meshes resulted in a maximum of 0.5 K difference. Results of the densest three meshes happened to be in the 0.1 K band. Fluid bulk mean temperature distributions around the first two and last two roughness elements for the mesh independence test cases are shown in Figs. (6.12) and (6.13), respectively.

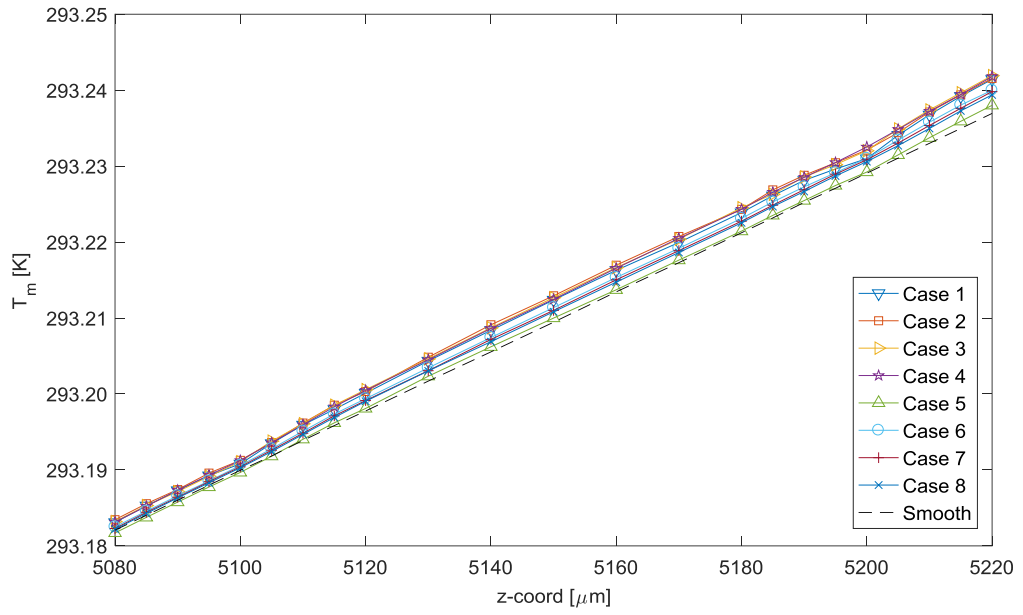


Figure 6.12: Fluid bulk mean temperature distribution for mesh independence test cases of R1LC configuration around the first two roughness elements.

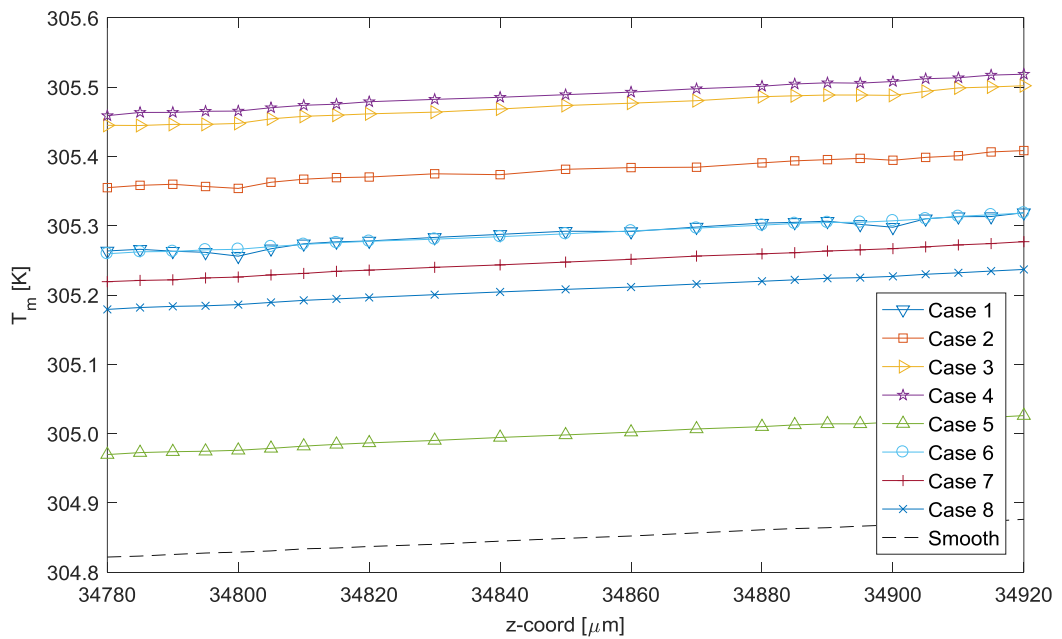


Figure 6.13: Fluid bulk mean temperature distribution for mesh independence test cases of R1LC configuration around the last two roughness elements.

Wall temperature distributions along the  $x$ -direction for  $z = 20,000 \mu\text{m}$  and  $z = 20,015 \mu\text{m}$  locations are shown in Fig. (6.14). Test meshes resulted in close temperature distribution, except the coarsest meshes, which are unable to represent the geometry correctly and resolve the flow field.

Additionally, wall mean temperature distributions around the first and the last two roughness elements for the mesh independence test cases are shown in Figs. (6.15) and (6.16), respectively. In each case, maximum difference is about 0.5 K. Except the coarsest meshes, all test cases showed similar distribution along the flow direction and yield close results.

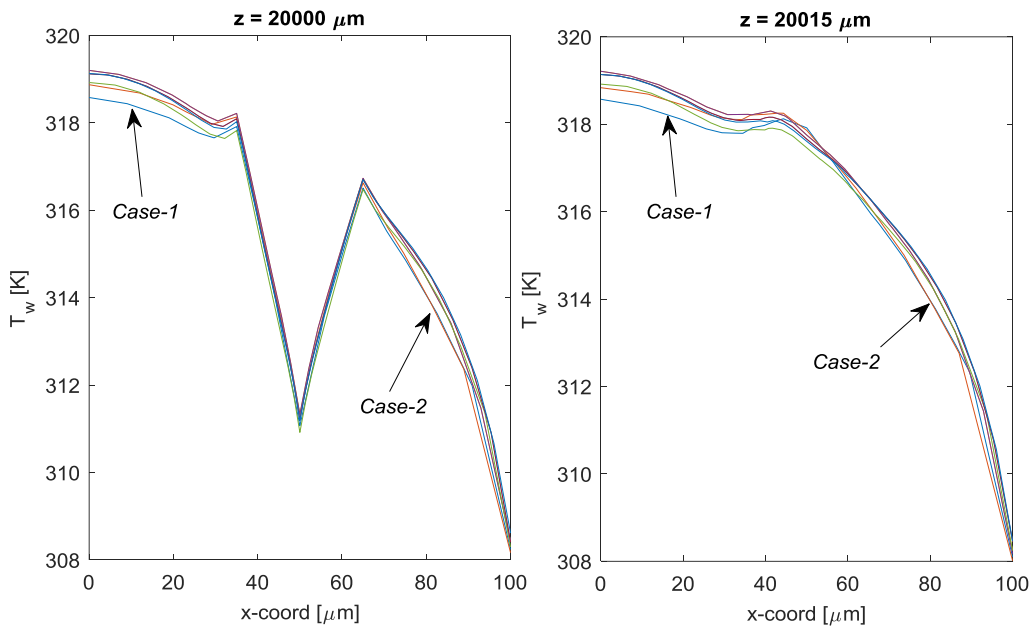


Figure 6.14: Wall temperature distributions for mesh independence test cases of R1LC configuration along the  $x$ -direction at  $z = 20000 \mu\text{m}$  and  $z = 20015 \mu\text{m}$  locations.

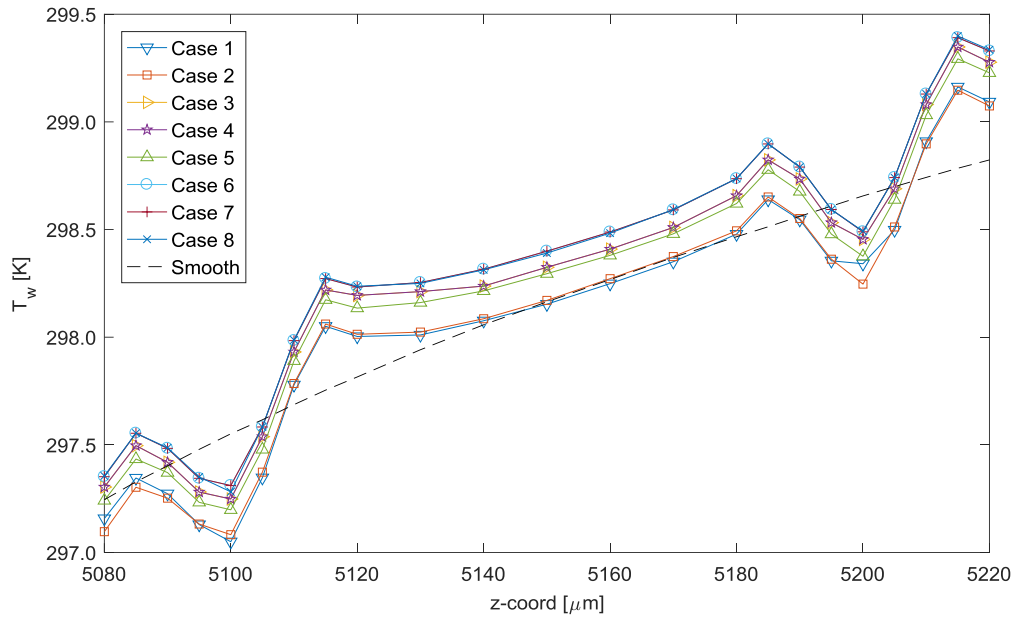


Figure 6.15: Wall mean temperature distribution for mesh independence test cases of R1LC configuration around the first two roughness elements.

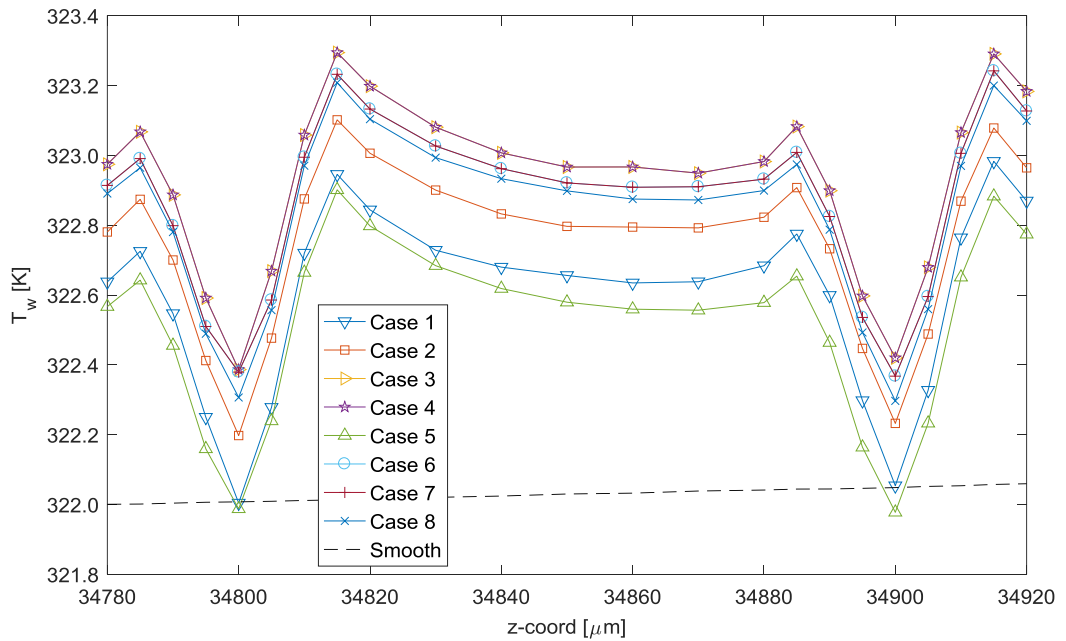


Figure 6.16: Wall mean temperature distribution for mesh independence test cases of R1LC configuration around the last two roughness elements.

Local Nusselt distributions for the mesh independence test cases are shown in the Figs. (6.17), (6.18), and (6.19) around the first two, middle, and the last roughness elements, respectively. As the number of DOFs increases, the difference between the results of each considered case reduces. With *Case-6*, the difference becomes miniscule, and the results over the conical peaks nearly coincide.

Considering the distribution of sought parameters and difference in calculated results with computational costs, mesh of *Case-6* is chosen for further simulations.

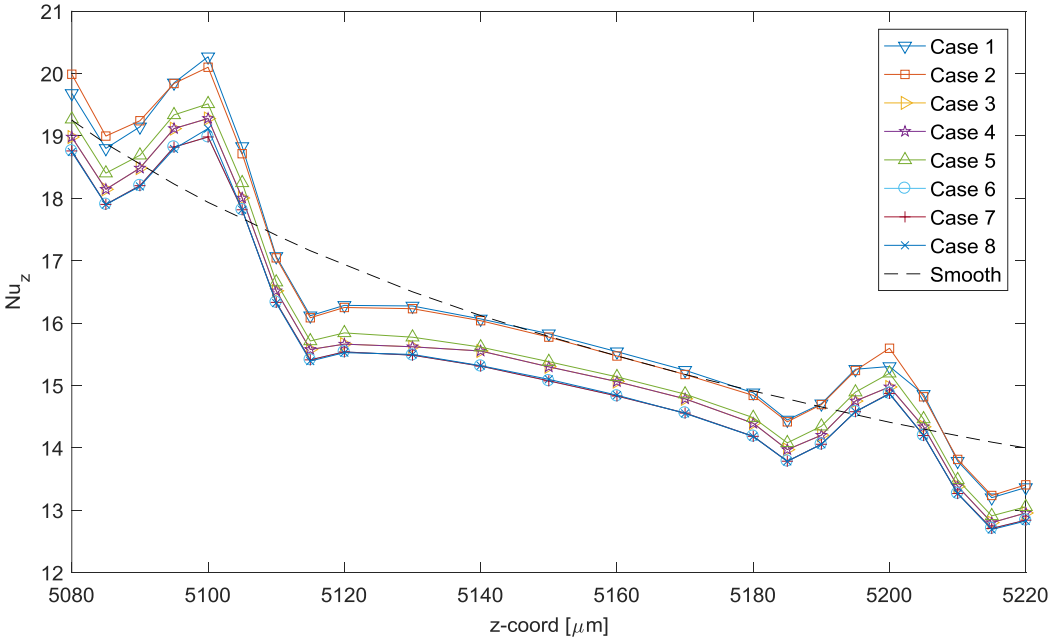


Figure 6.17: Local Nusselt distribution for mesh independence test cases of R1LC configuration around the first two roughness elements.

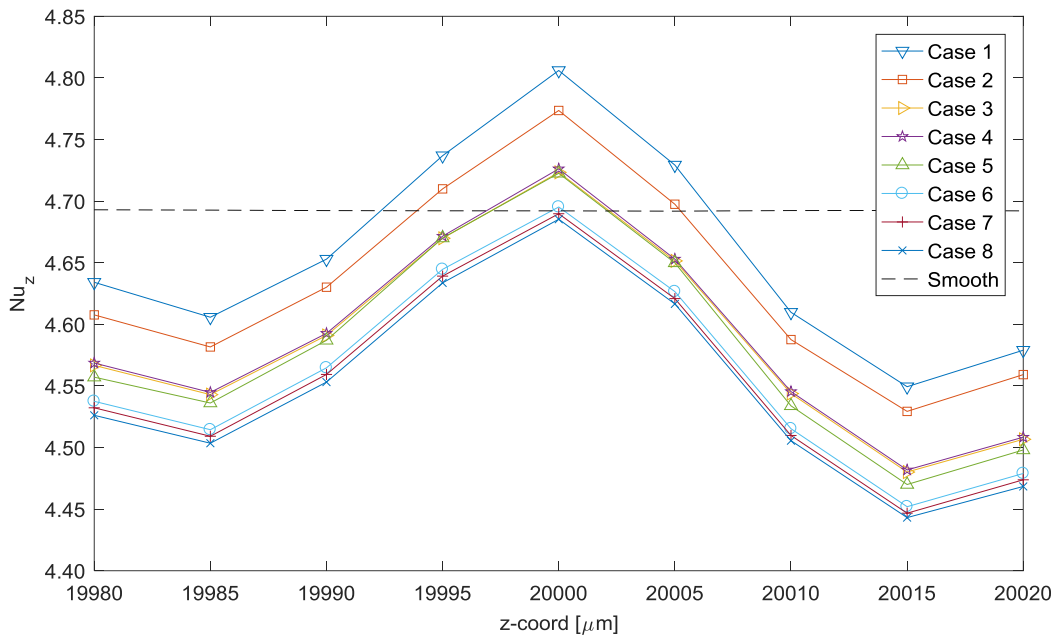


Figure 6.18: Local Nusselt distribution for mesh independence test cases of R1LC configuration around the middle roughness elements.

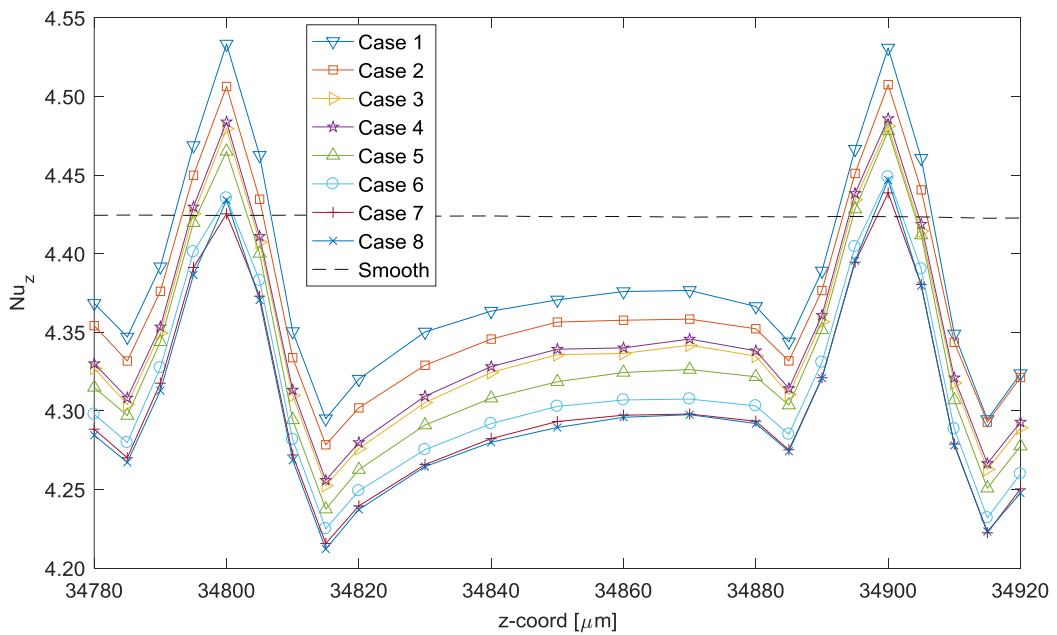


Figure 6.19: Local Nusselt distribution for mesh independence test cases of R1LC configuration around the last two roughness elements.

### 6.3.2 RESULTS AND DISCUSSIONS

Simulations for each inlet mass fluxes of 200 kg/(m<sup>2</sup>s) to 1016 kg/(m<sup>2</sup>s) are run by using the mesh of *Case-6* (with 14.71x10<sup>6</sup> DOFs) and setting the relative tolerance to 10<sup>-6</sup>.

Velocity magnitude profiles for inlet mass flux of 1016 kg/(m<sup>2</sup>s) along the  $y$ -direction (channel height) before and after the conical elements at  $x = 50 \mu\text{m}$  (mid-line of the cone) and various  $z$  locations are shown in Figs. (6.20) and (6.21) for the first and last conical element, respectively, with the corresponding smooth channel values. In addition, velocity magnitude profiles along the  $x$ -direction at  $y = 5 \mu\text{m}$  height from the base are given in Figs. (6.22) and (6.23) for the first and last conical elements, respectively. In each subplot, velocity magnitude plots are shown in a way that the  $z$  locations are symmetrical to the tip of the corresponding cone. Also, change of velocity in various cross-sections that are 5  $\mu\text{m}$  apart from each other in the flow direction around the middle roughness element is shown in Fig. (6.24) as surface plots.

Compared to the smooth channel, velocity reduces around the conical elements and obtains similar values away from the cones. Velocity after the cones are lower than the velocity in the symmetrical position before the cones. Existence of conical elements resulted in low velocity regions around the conical elements, which is more for the downstream locations, for the tested inlet mass fluxes.

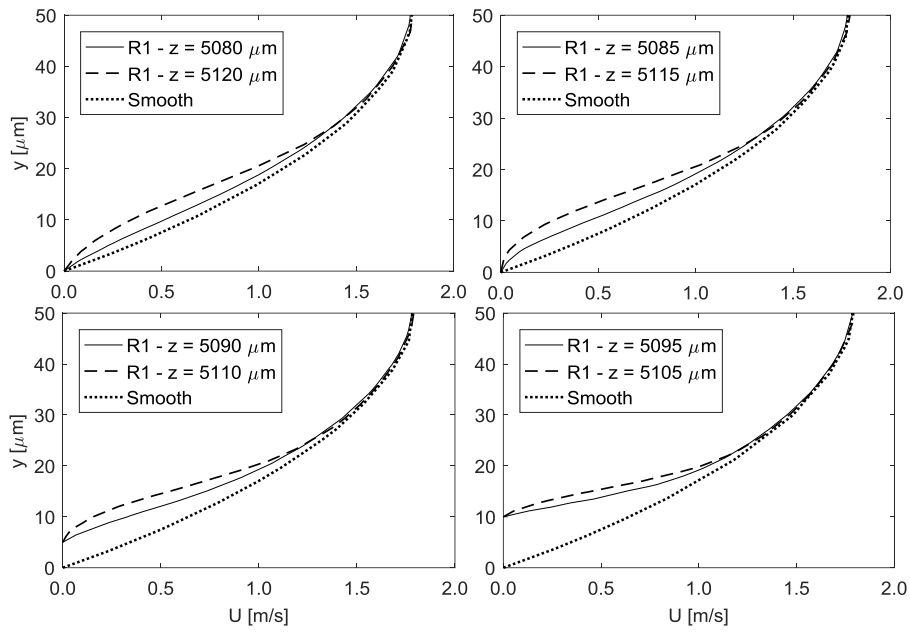


Figure 6.20: Velocity magnitude profiles along  $y$ -direction at  $x = 50 \mu\text{m}$  and various  $z$  locations for the first conical element of R1LC configuration.

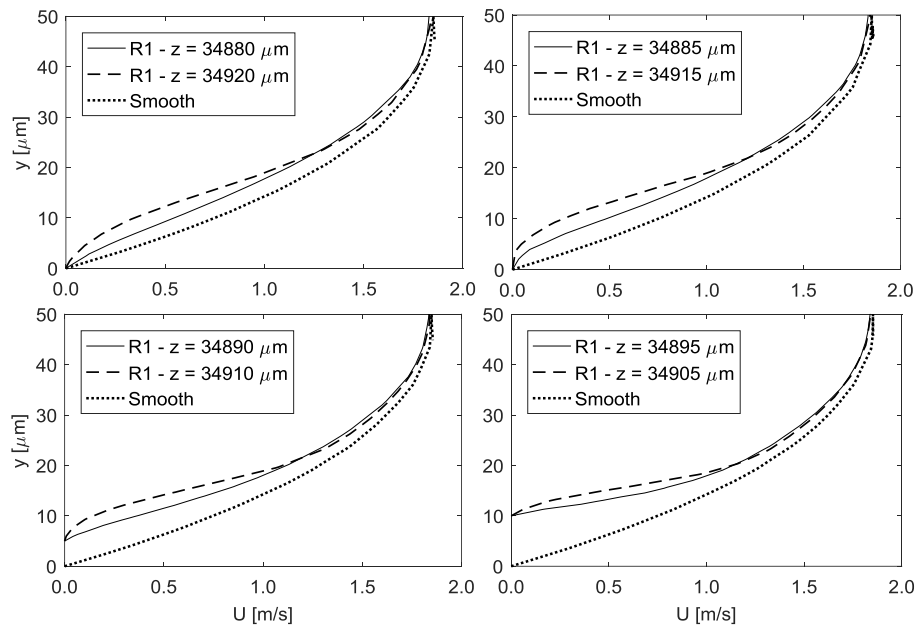


Figure 6.21: Velocity magnitude profiles along  $y$ -direction at  $x = 50 \mu\text{m}$  and various  $z$  locations for the last conical element of R1LC configuration.

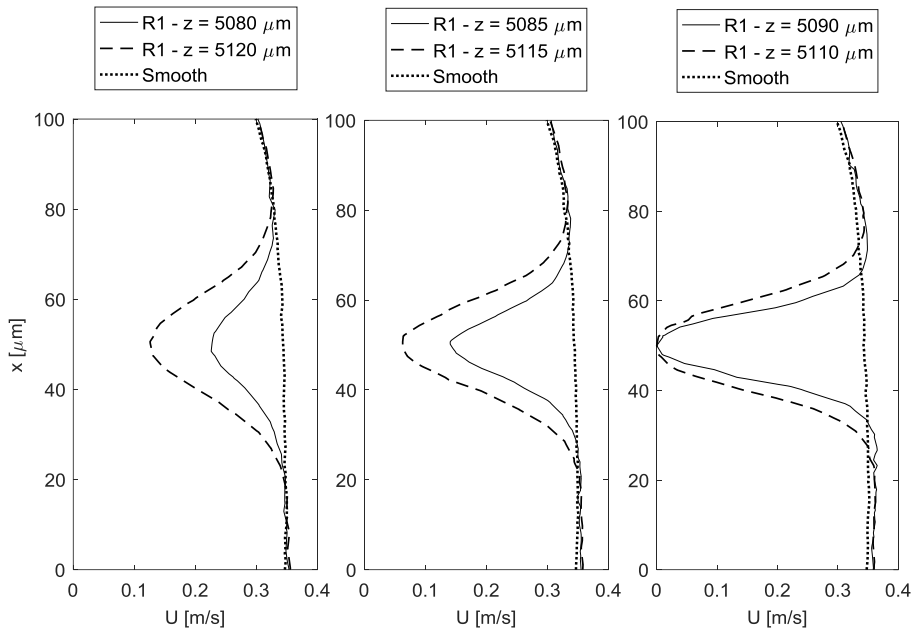


Figure 6.22: Velocity magnitude profiles along  $x$ -direction at  $y = 5 \mu\text{m}$  and various  $z$  locations for the first conical element of R1LC configuration.

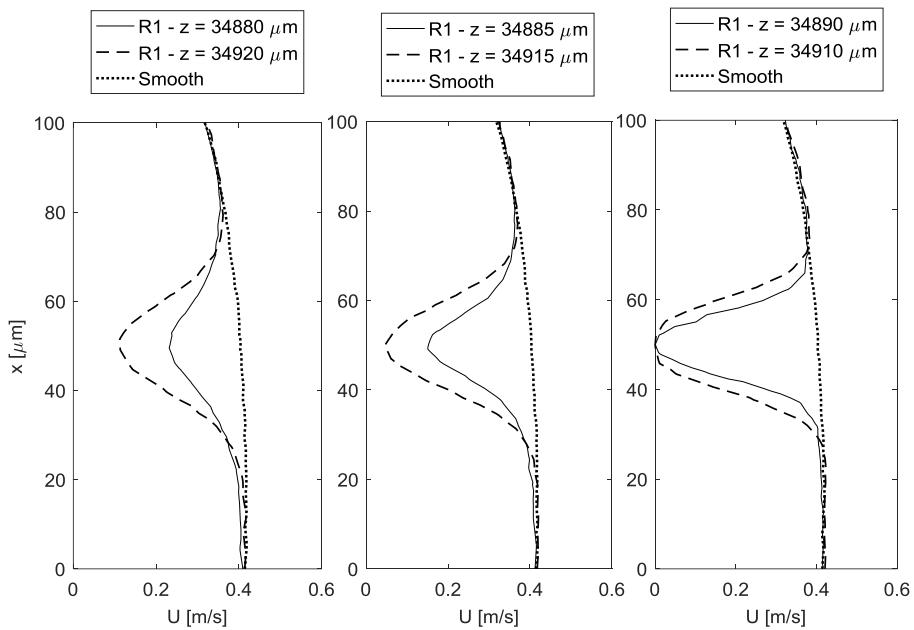


Figure 6.23: Velocity magnitude profiles along  $x$ -direction at  $y = 5 \mu\text{m}$  and various  $z$  locations for the last conical element of R1LC configuration.

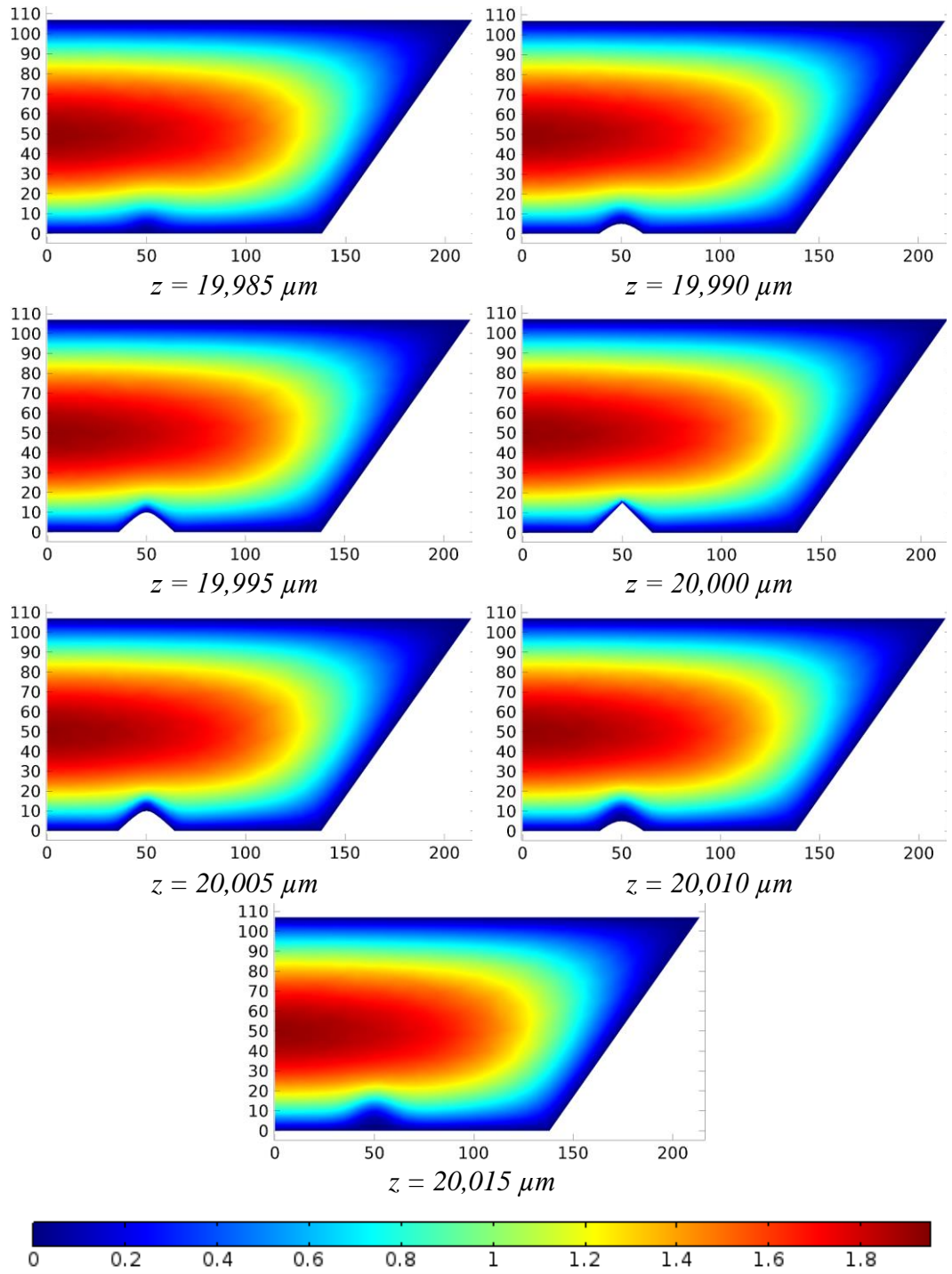


Figure 6.24: Velocity distribution at various cross-sections around the middle cone of R1LC configuration in the flow direction ( $G = 1016$  [kg/(m<sup>2</sup>s)]).

Wall temperatures at  $z = 6,000 \mu\text{m}$  and  $z = 34,000 \mu\text{m}$  along the  $x$ -direction (from symmetry plane through the side of the microheater, perpendicular to flow direction) for various inlet mass fluxes is shown in Figs. (6.25) and (6.26), respectively, with the corresponding smooth channel values. Wall temperatures become higher than the smooth channel at the base of the channel due to the increase in heating area and existence of low velocity regions around the conical elements, which reduces convective heat transfer and more obvious at the base circumference of the cones. On the other hand, through the tip of the conical element, cone surface is exposed to flow with higher velocity, thus the wall temperatures reduce significantly and obtain lower values than the smooth channel. As the inlet mass flux increases, wall temperature reduces. The difference between the smooth channel's wall temperature values and the temperature of the tip of the conical elements increases through the end of the heated section as the inlet mass flux increases.

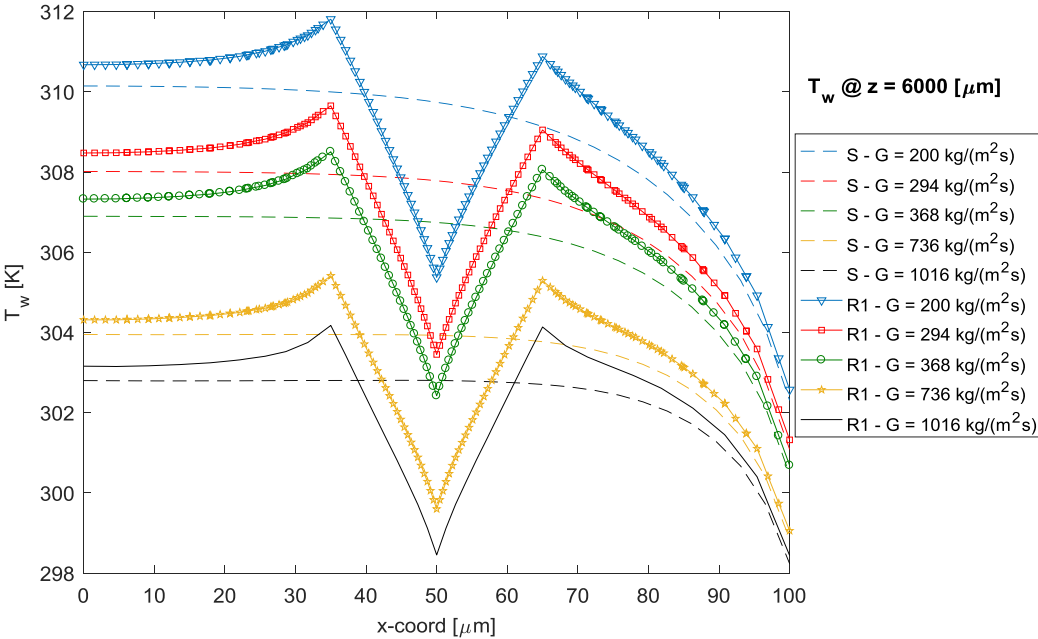


Figure 6.25: Wall temperature distribution at  $z = 6000 \mu\text{m}$  location for various inlet mass fluxes for R1LC configuration with corresponding smooth values.

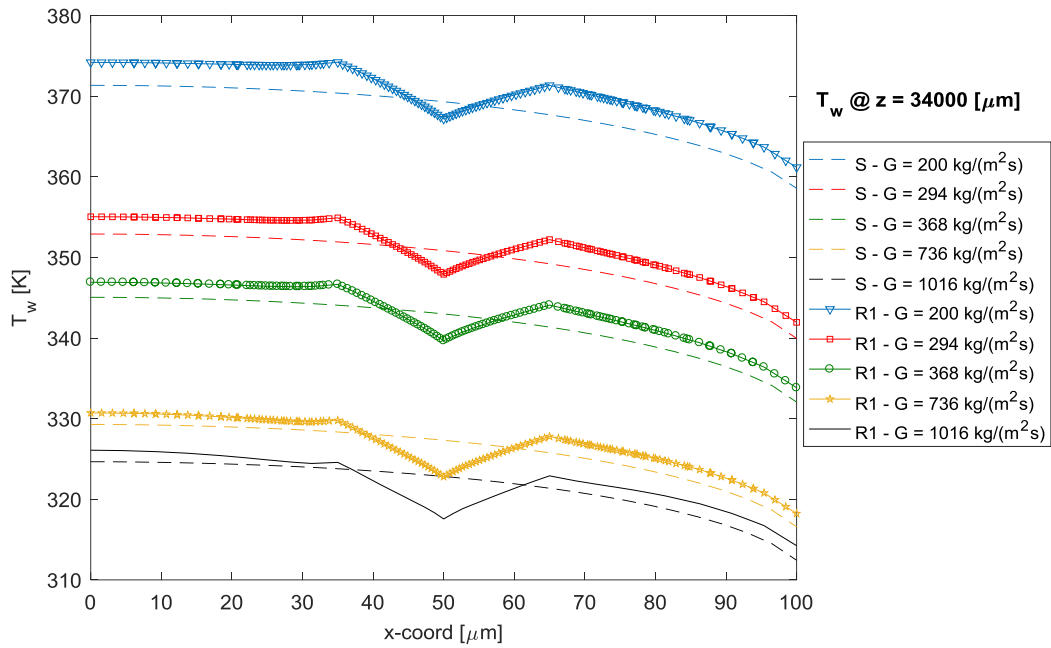


Figure 6.26: Wall temperature distribution at  $z = 34000 \mu\text{m}$  location for various inlet mass fluxes for R1LC configuration with corresponding smooth values.

Wall temperature distribution around the middle cone of R1LC configuration for inlet mass fluxes of  $200 \text{ kg}/(\text{m}^2\text{s})$  and  $1016 \text{ kg}/(\text{m}^2\text{s})$  is shown in Fig. (6.27). Also, change of temperature in various cross-sections that are  $5 \mu\text{m}$  apart from each other in the flow direction around the middle roughness element is shown in Fig. (6.28) as surface plots for an inlet mass flux of  $1016 \text{ kg}/(\text{m}^2\text{s})$ . Wall temperature of the downstream side of the cone is slightly higher than the upstream side of the cone due to reduced velocity zones and increased bulk fluid temperature.

Fluid bulk mean temperature distribution over the 10<sup>th</sup> roughness element, and over the last two roughness elements of R1LC configuration are shown in Figs. (6.29) and (6.30), respectively. Bulk mean temperatures are calculated in cross-sectional planes  $1 \mu\text{m}$  apart over the conical elements, and  $5 \mu\text{m}$  apart between the conical elements in  $z$ -direction. Mean temperatures for rough channel are slightly higher

than the smooth channel and the difference between them reduces as the inlet mass flux increases.

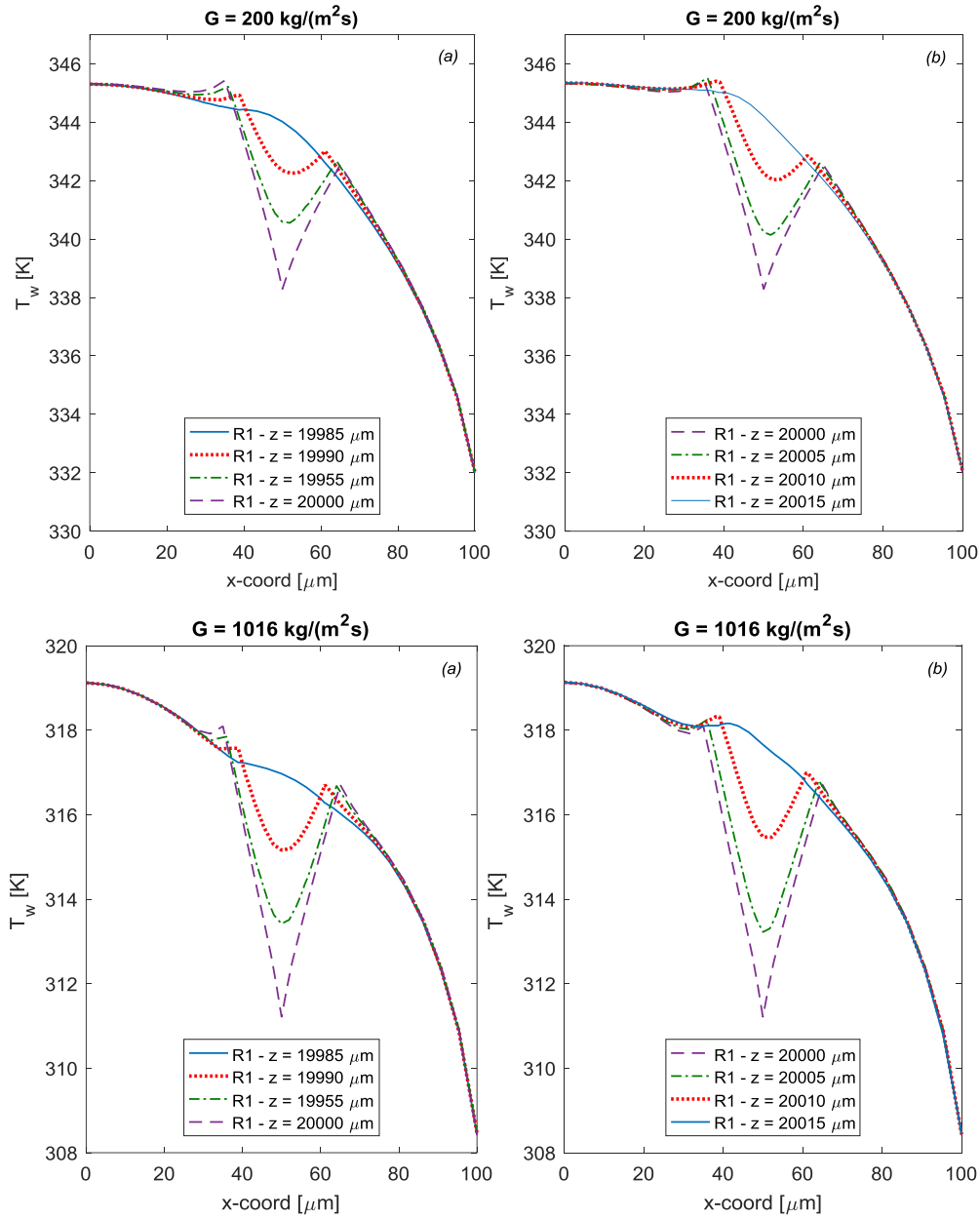


Figure 6.27: Wall temperature distribution around the middle cone of R1LC configuration for inlet mass fluxes of  $200 \text{ kg/(m}^2\text{s)}$  and  $1016 \text{ kg/(m}^2\text{s)}$  for (a) flow facing side of the cone, (b) back side of the cone.

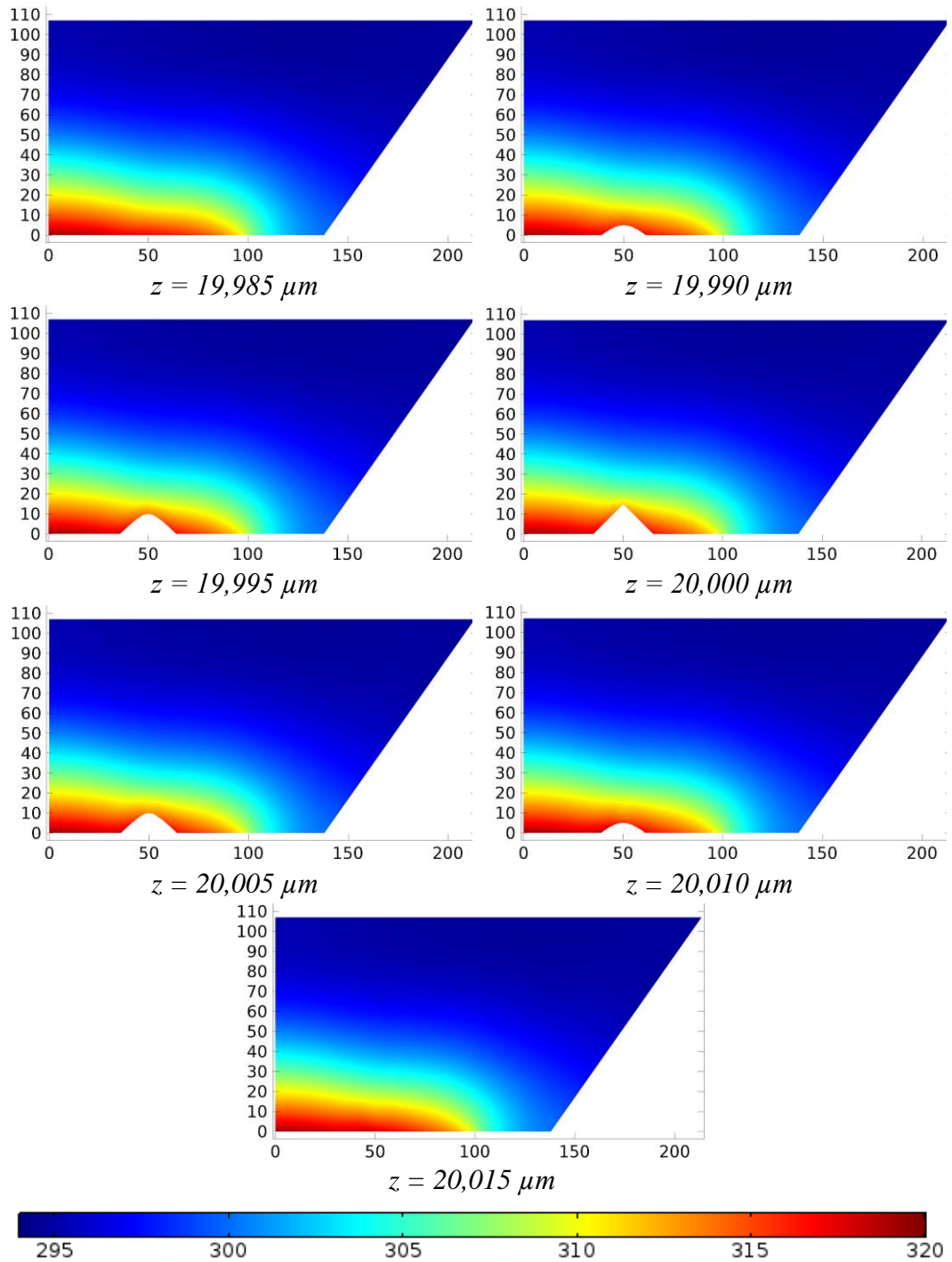


Figure 6.28: Temperature distribution at various cross-sections around the middle cone of RILC configuration in the flow direction ( $G = 1016 \text{ [kg/(m}^2\text{s)]}$ ).

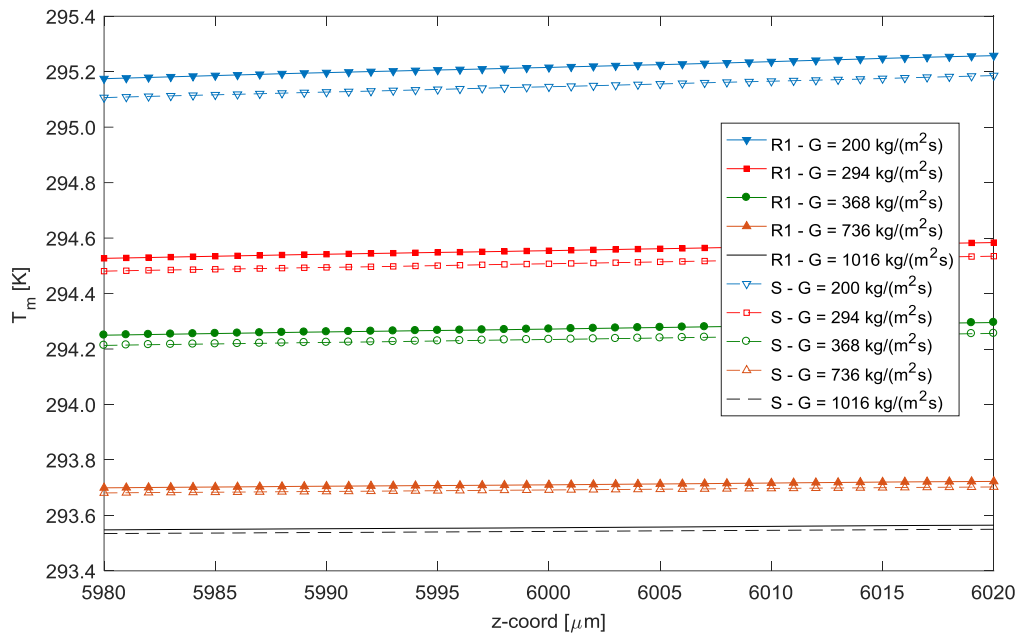


Figure 6.29: Fluid bulk mean temperature distribution over the 10<sup>th</sup> roughness element of R1LC configuration.

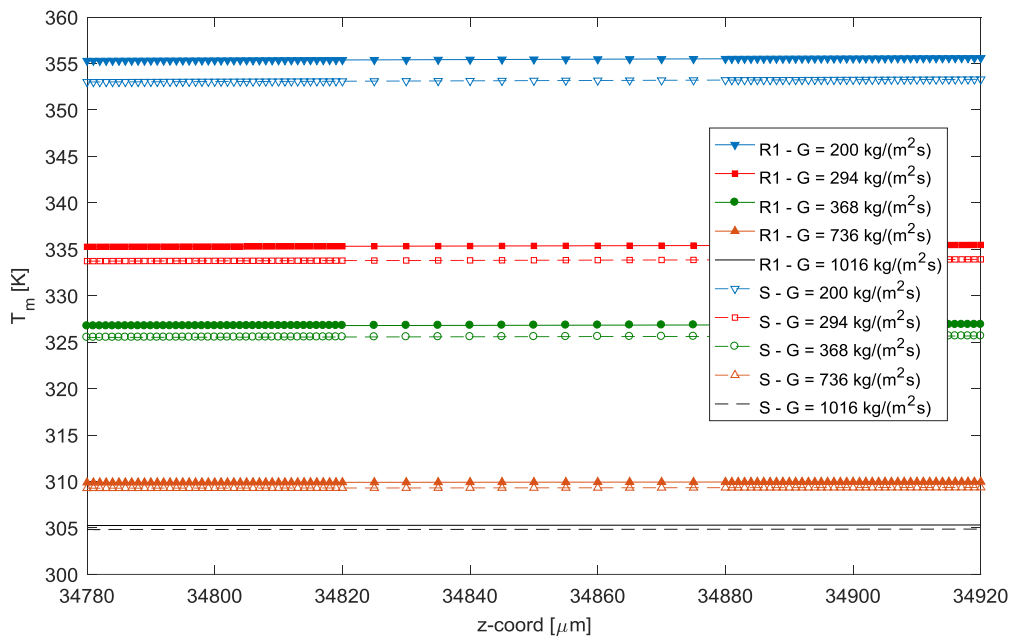


Figure 6.30: Fluid bulk mean temperature distribution over the last two roughness elements of R1LC configuration.

Wall mean temperature distribution over the first two roughness elements, around the middle roughness element, and over the last two roughness elements of R1LC configuration are shown in Figs. (6.31), (6.32), and (6.33) respectively. Wall mean temperatures are calculated 1  $\mu\text{m}$  apart over the conical elements and over the regions 5  $\mu\text{m}$  before and after the cones, and 5  $\mu\text{m}$  apart between the conical elements in  $z$ -direction. Wall mean temperatures for the rough channel are higher than the smooth channel and the difference between them reduces over the cones as the inlet mass flux increases.

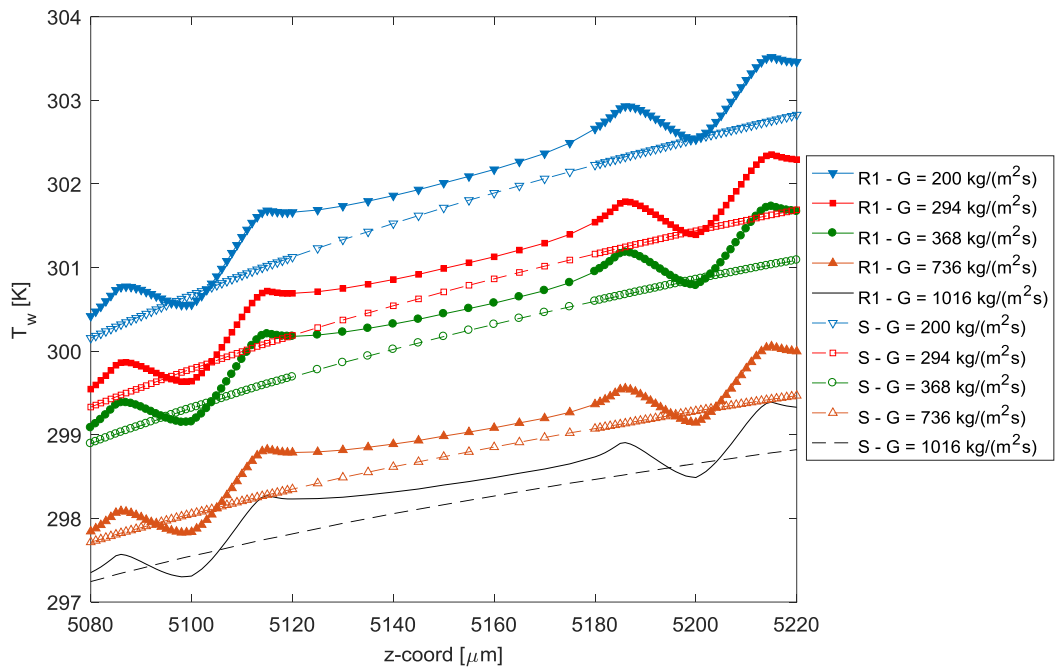


Figure 6.31: Wall mean temperature distribution over the first two roughness elements of R1LC configuration.

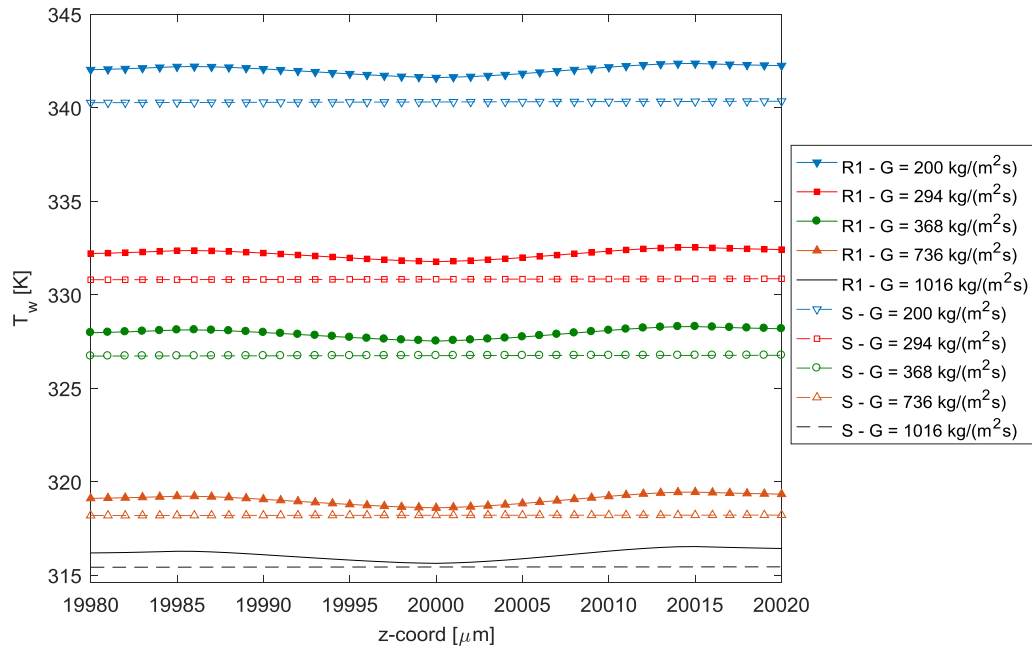


Figure 6.32: Wall mean temperature distribution near the middle roughness element of R1LC configuration.

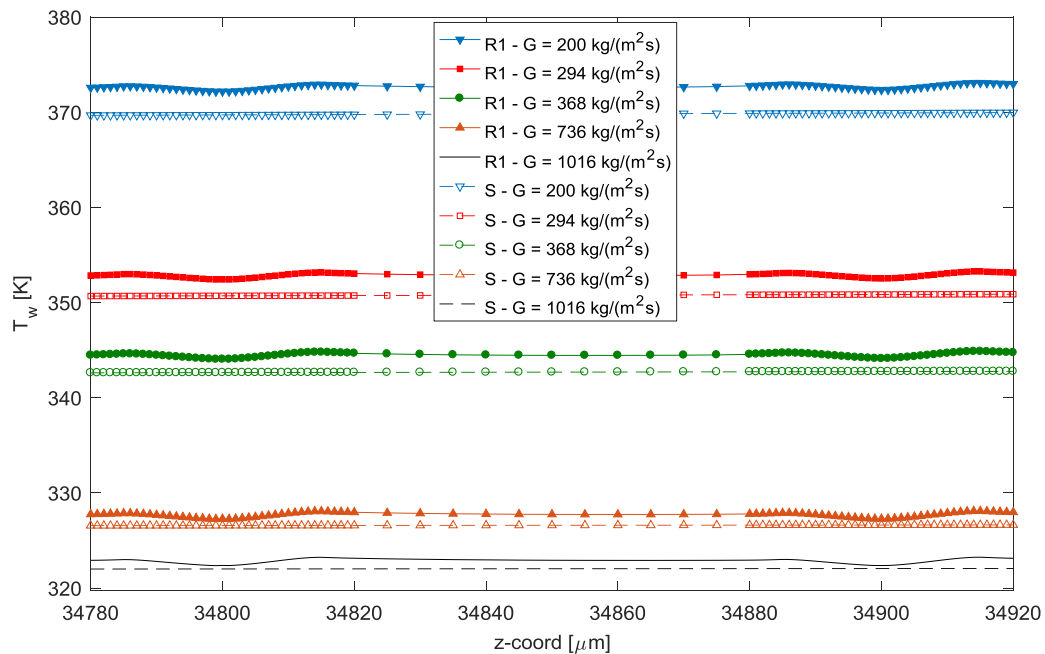


Figure 6.33: Wall mean temperature distribution over the last two roughness elements of R1LC configuration.

Due to the formation of reduced velocity regions around the conical elements, which is shown in Figs (6.20) to (6.24), convective heat transfer in the fluid reduces in these regions as shown in Fig. (6.34) for the middle cone of R1LC configuration for inlet mass flux of  $1016 \text{ kg}/(\text{m}^2\text{s})$ . In these figures, arrow sizes are scaled to the magnitude of convective heat flux in the fluid and the color scale bar shows the value of surface temperature. In the upper plot of Fig. (6.34) arrows that are representing the convective heat flux are drawn in a way that they are covering half of the cone. In the lower plot of Fig (6.34) arrows are drawn at  $y = 7.5 \text{ }\mu\text{m}$  plane, which levels to half of the cone height.

In this study, thermophysical properties of the working fluid, water, were considered as temperature dependent. Due to constant heating of the microchannel, wall temperatures and fluid temperature increase from inlet to outlet of the heated section, which is shown through Figs. (6.25) and (6.33). Increase in temperature also causes slight decrease in density, which is more between the conical elements and shown in Fig. (6.35) at  $x = 50 \text{ }\mu\text{m}$  plane of inlet, mid-section, and outlet of heated section for inlet mass flux of  $1016 \text{ kg}/(\text{m}^2\text{s})$ . Reduction of viscosity due to the increase in temperature over the heated section is more pronounced compared to density and shown in Fig. (6.36) for the same location and conditions. On the other hand, thermal conductivity of the fluid increases considerably with increasing temperature as shown in Fig. (6.37) at inlet, mid-section, and outlet of heated section at  $x = 50 \text{ }\mu\text{m}$  plane for inlet mass flux of  $1016 \text{ kg}/(\text{m}^2\text{s})$ .

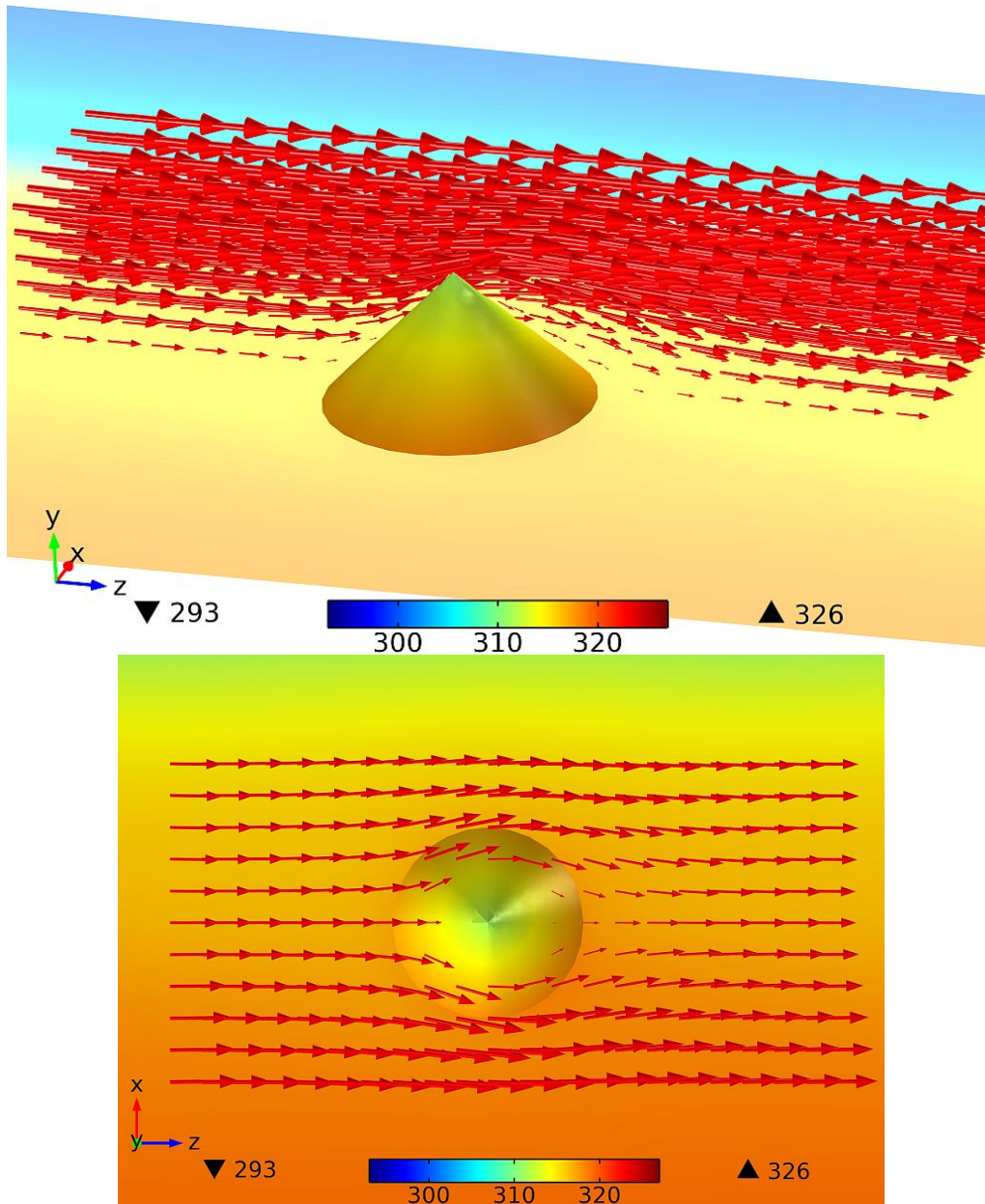


Figure 6.34: Surface temperature and convective heat flux around the middle cone of R1LC configuration for  $G = 1016 \text{ [kg/(m}^2\text{s)]}$  (*Top*: heat flux around the half of the cone, *Bottom*: heat flux at  $y = 7.5 \mu\text{m}$  plane).

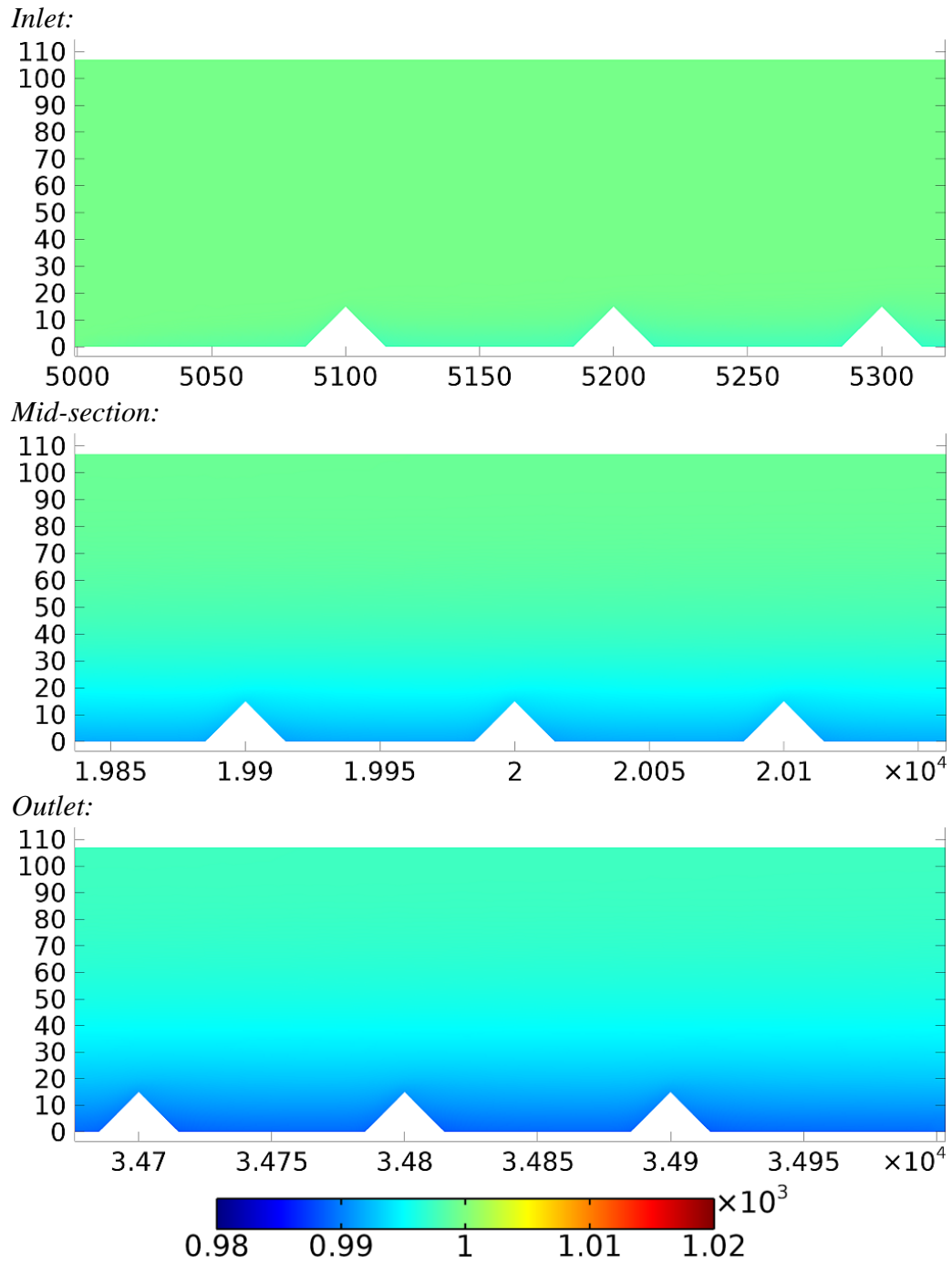


Figure 6.35: Change of density at  $x = 50 \mu\text{m}$  plane through the inlet to outlet of the rough section of R1LC configuration ( $G = 1016 \text{ [kg/(m}^2\text{s)]}$ ).

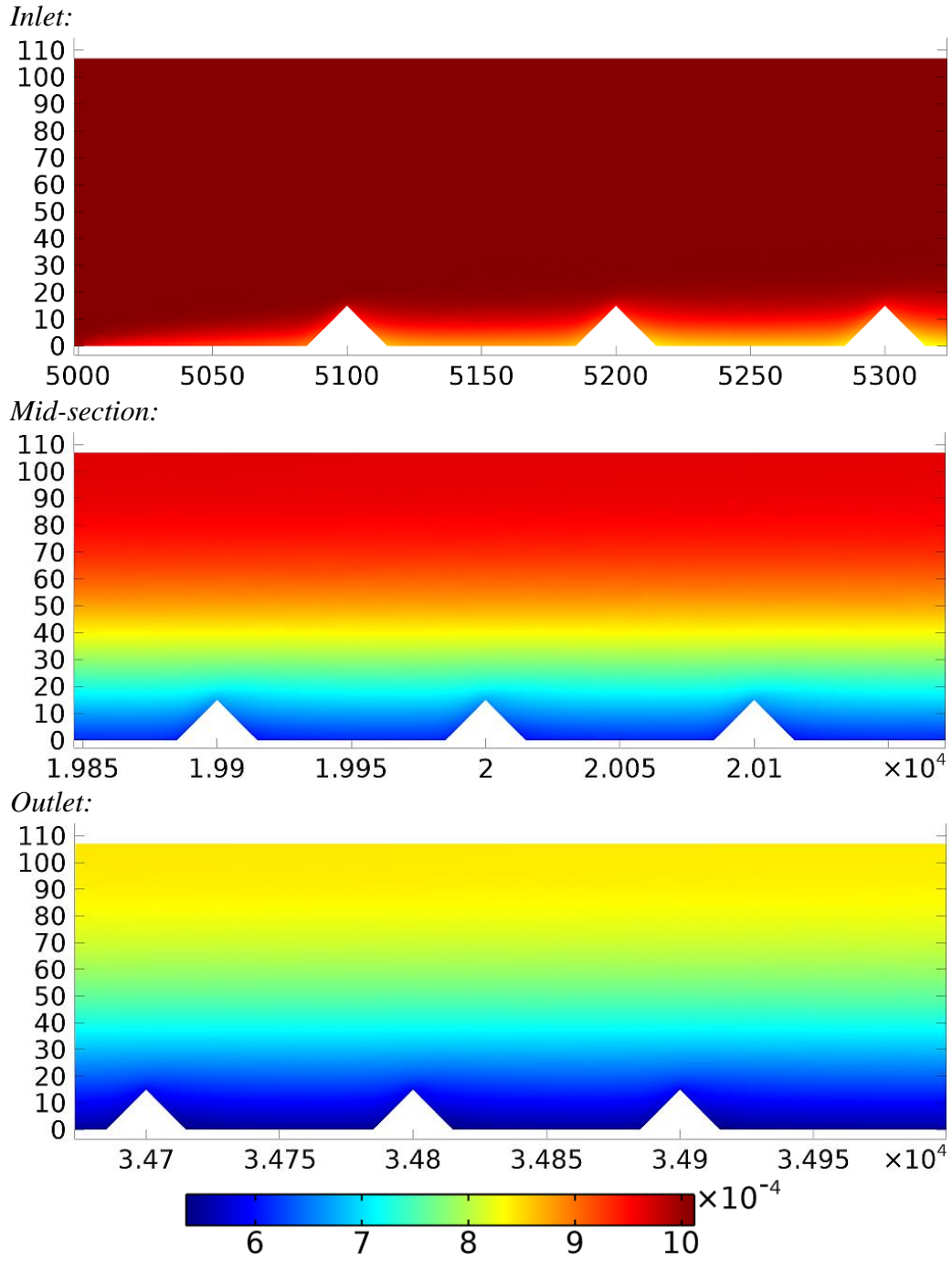


Figure 6.36: Change of viscosity at  $x = 50 \mu\text{m}$  plane through the inlet to outlet of the rough section of R1LC configuration ( $G = 1016 \text{ [kg/(m}^2\text{s)]}$ ).

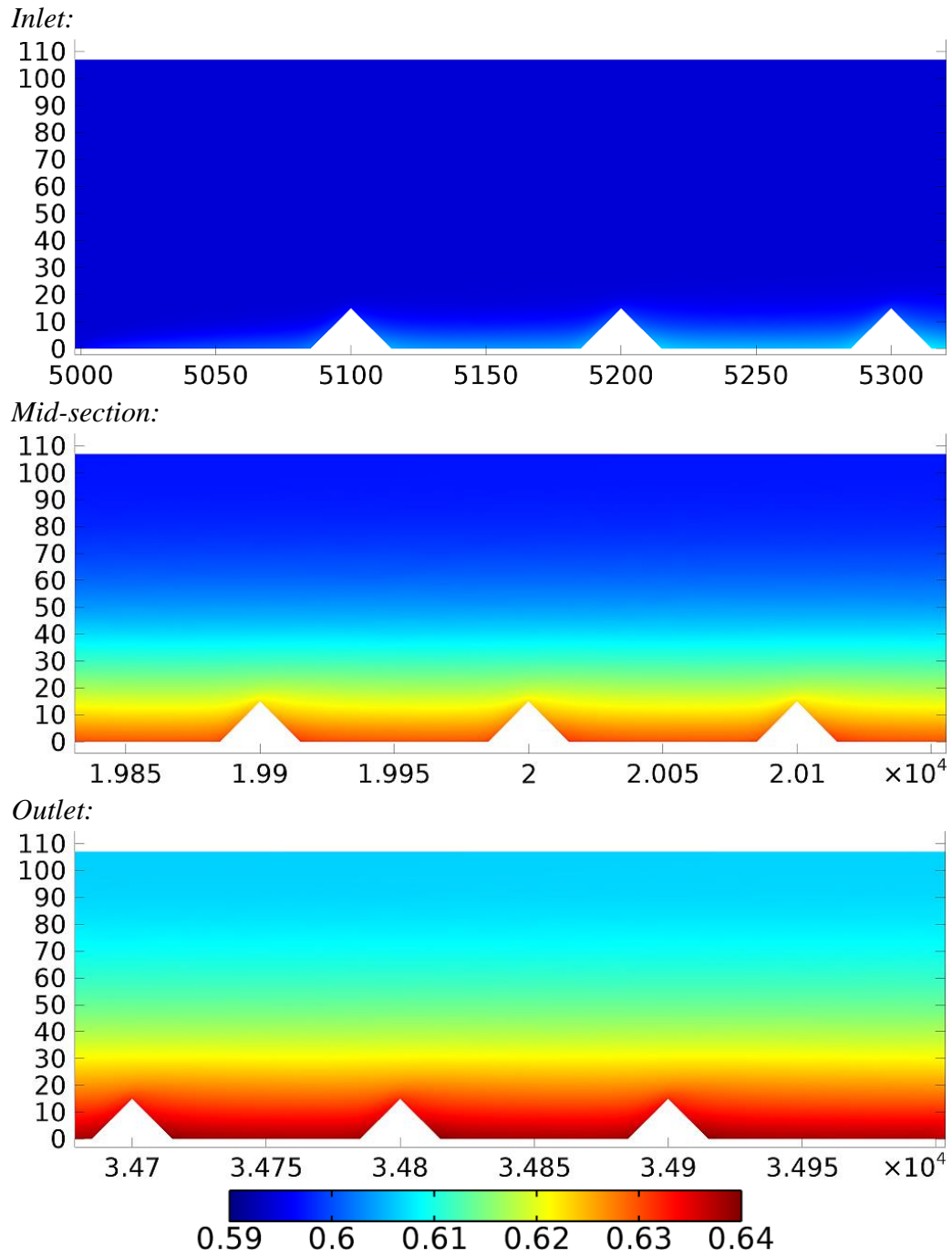


Figure 6.37: Change of thermal conductivity at  $x = 50 \mu\text{m}$  plane through the inlet to outlet of the rough section of R1LC configuration ( $G = 1016 \text{ [kg/(m}^2\text{s)]}$ ).

Local  $Nu$  distribution over the first two roughness elements, around the middle roughness element, and over the last two roughness elements of R1LC configuration are also shown in Figs. (6.38), (6.39), and (6.40) respectively. Local  $Nu$  takes the minimum value at the base of the cone due to reduced velocity zones and convective heat transfer, and increased thermal conductivity of the fluid. Local  $Nu$  increases towards the next cone, and when it reaches the next cone, starts to reduce again. Local  $Nu$  increases along the tip of the cone. However, except the inlet section, only for the highest limit of inlet mass flux of this study, local  $Nu$  at the tip of the cones takes higher value than the smooth channel counterpart.

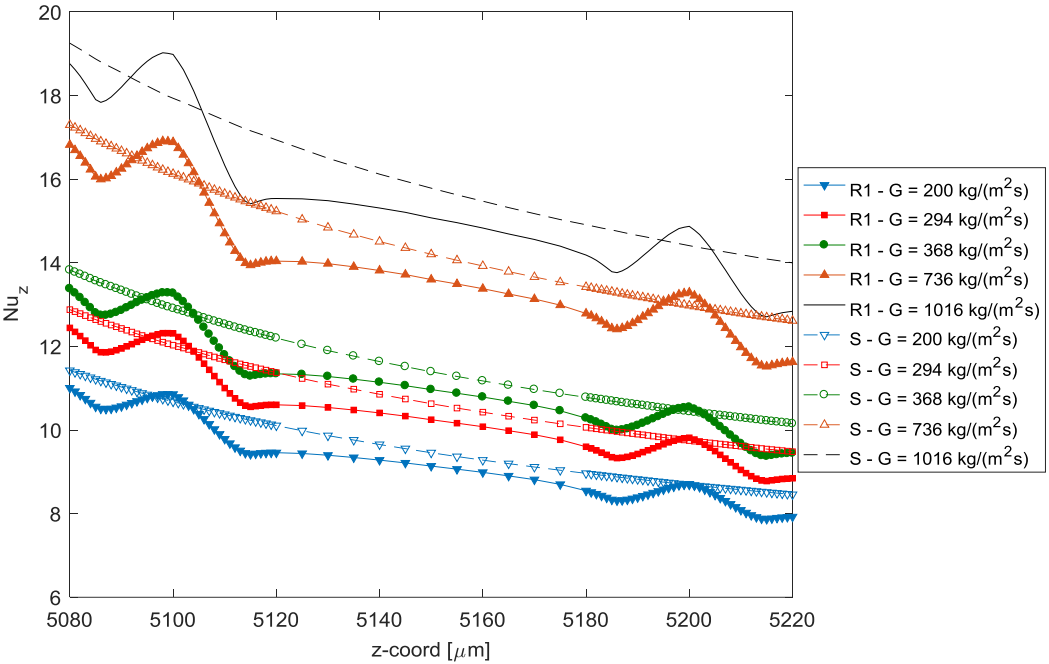


Figure 6.38: Local Nusselt distribution over the first two roughness elements of R1LC configuration.

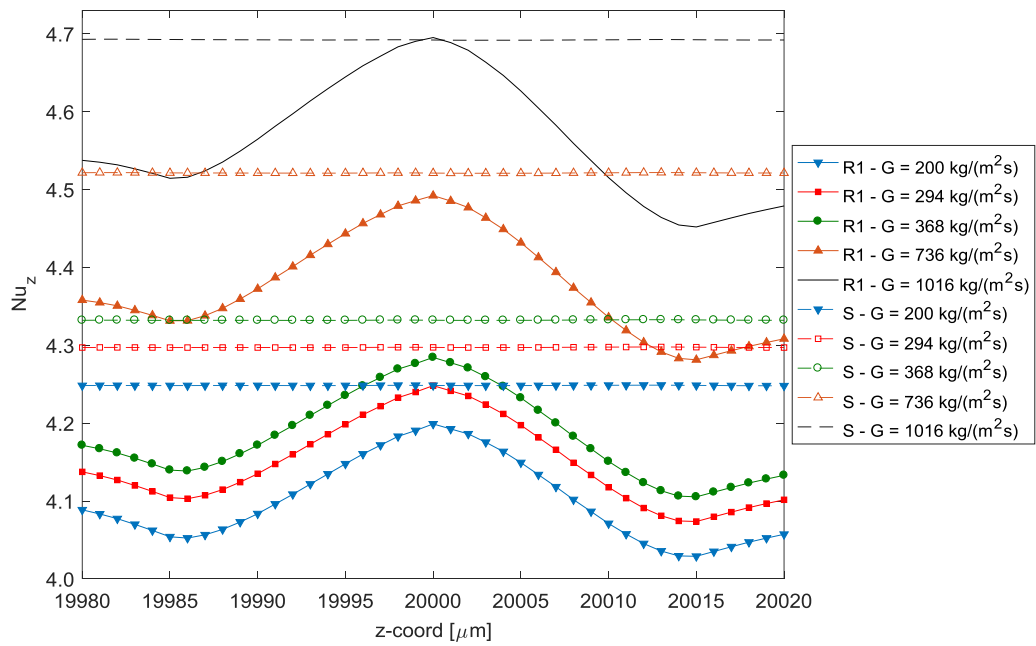


Figure 6.39: Local Nusselt distribution near the middle roughness element of R1LC configuration.

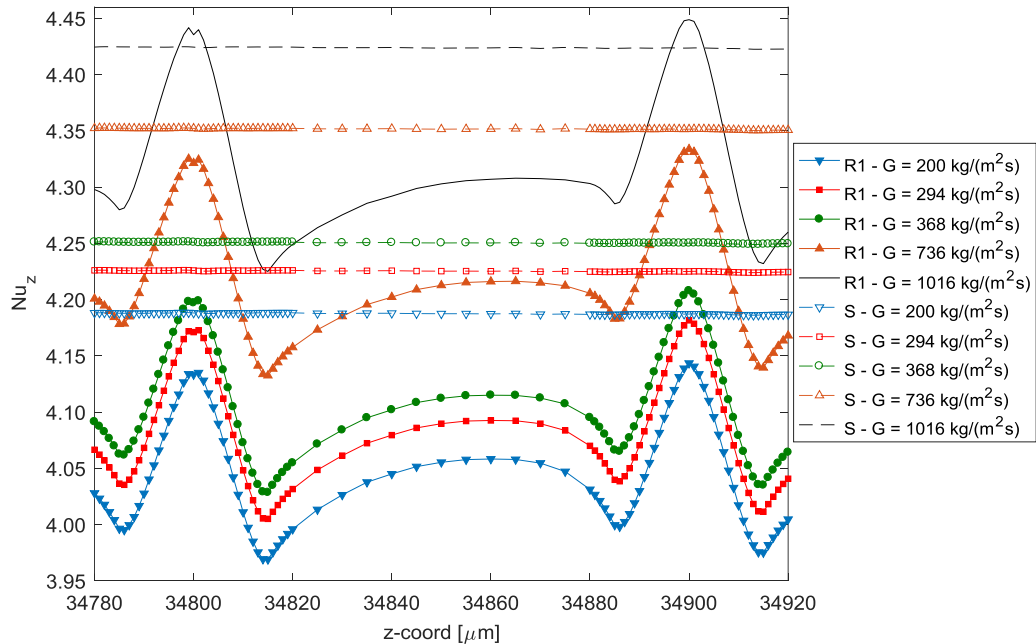


Figure 6.40: Local Nusselt distribution over the last two roughness elements of R1LC configuration.

## 6.4 ROUGH MICROCHANNEL SIMULATIONS WITH *2LineCone* (R2LC) CONFIGURATION

### 6.4.1 MESH INDEPENDENCE STUDIES

Similar to R1LC configuration case, mesh independence studies for the simulations in microchannel having *2LineCone* roughness configuration (R2LC) are carried out for effective heat flux of 300 kW/m<sup>2</sup> and inlet mass flux of 1016 kg/(m<sup>2</sup>s) case, considering 10 meshes having about 3.34x10<sup>6</sup> DOFs for the coarsest one to 21.79x10<sup>6</sup> DOFs for the densest one. Iterative multigrid solver is used with linear mesh elements, and the relative tolerance is set to 10<sup>-3</sup>. Element numbers and DOFs of used meshes, CPU times, used physical memory (PM) and virtual memory (VM) are summarized in Table – (6.4) with the calculated *Po* values over the heated region, and average and maximum heated surface temperatures. All the simulations are conducted with the same workstation used in smooth and R1LC microchannel simulations. Again, for the cases where physical memory is not enough, a partition in the hard disk is used as temporary RAM with a penalty of longer computational times.

The meshes of test cases *Case-1*, *Case-2*, and *Case-7* are constructed with predefined *coarse*, *normal*, and *fine* meshing schemes, respectively. Meshes of remaining cases are constructed manually by gradually increasing the element numbers on the edges of the geometry and reducing the element sizes inside the domain. Surface meshes around the conical roughness elements of *Case-1*, *Case-8*, and *Case-10* are shown in Fig. (6.41), as an example.

Table 6.4: Summary of mesh properties and calculated values used in mesh independence tests of *2LineCone* configuration (*PM*: Physical Memory, *VM*: Virtual Memory, *HS*: Heated Surface).

<i>Case</i>	<i>ELEM #</i>	<i>DOFs</i>	<i>CPU Time [s]</i>	<i>PM [GB]</i>	<i>VM [GB]</i>	<i>Po</i>	<i>T<sub>ave,HS</sub> [K]</i>	<i>T<sub>max,HS</sub> [K]</i>
<b>1</b>	2,577,250	3,342,290	2,999	24.85	25.65	18.227	315.524	328.028
<b>2</b>	4,045,655	4,780,690	5,360	37.69	38.71	17.526	315.642	327.872
<b>3</b>	7,142,061	6,942,655	7,954	24.99	25.43	17.330	315.863	328.394
<b>4</b>	11,411,171	10,899,210	28,252	44.96	47.66	17.119	315.916	328.244
<b>5</b>	14,342,020	13,621,420	29,530	45.14	48.16	17.012	315.922	328.203
<b>6</b>	16,025,817	15,191,880	34,796	45.97	52.15	16.979	315.928	328.194
<b>7</b>	17,226,694	17,470,925	177,390	47.08	72.61	16.961	315.746	327.781
<b>8</b>	18,850,881	17,769,015	47,219	45.31	57.61	16.941	315.938	328.196
<b>9</b>	21,428,219	20,120,245	133,993	45.17	63.92	16.904	315.951	328.203
<b>10</b>	23,202,800	21,792,870	503,045	47.01	67.14	16.896	315.957	328.204

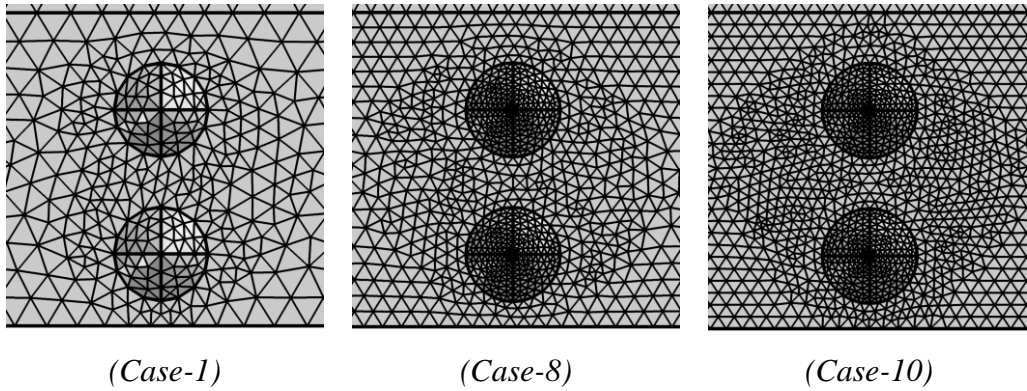


Figure 6.41: Surface meshes around the conical elements of R2LC configuration for *Case-1* (coarsest), *Case-8*, and *Case-10* (densest).

The percentage difference of calculated  $Po$  values between two consecutive runs drops to below 0.7% at about  $10.9 \times 10^6$  DOFs (*Case-4*) The percentage difference of  $Po$  between the densest case (*Case-10*) and the other cases drops to below 0.7% at about  $13.6 \times 10^6$  DOFs (*Case-5*). Also, average and maximum temperatures of heated surface remains nearly constant after *Case-4*.

Fluid bulk mean temperatures for mesh independence cases of R2LC configuration are calculated in cross-sectional planes that are 5  $\mu\text{m}$  apart from each other around the conical elements and 10  $\mu\text{m}$  apart between the conical elements in the flow direction. Test meshes resulted in a maximum of about 0.45 K difference at the end of the heated section, which is shown in Fig. (6.42).

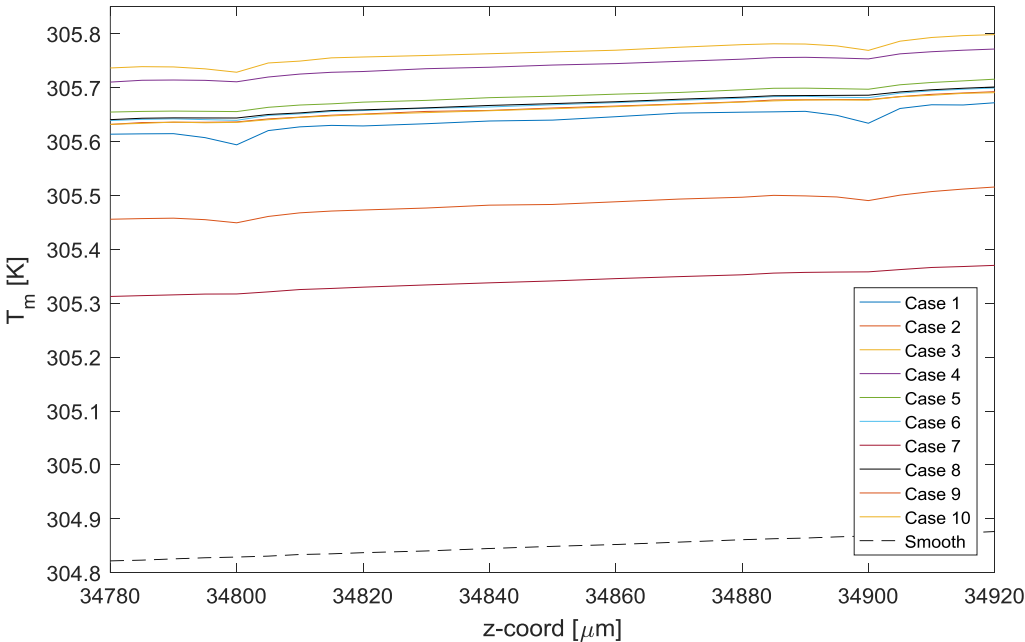


Figure 6.42: Fluid bulk mean temperature distribution for mesh independence test cases of R2LC configuration around the last two roughness elements.

Wall temperature distributions along the  $x$ -direction for  $z = 20,000 \mu\text{m}$  and  $z = 20,015 \mu\text{m}$ , and for  $z = 34,890 \mu\text{m}$  and  $z = 34,910 \mu\text{m}$  locations are shown in Figs. (6.43) and (6.44), respectively. Except the coarsest meshes, test meshes resulted in close temperature distribution.

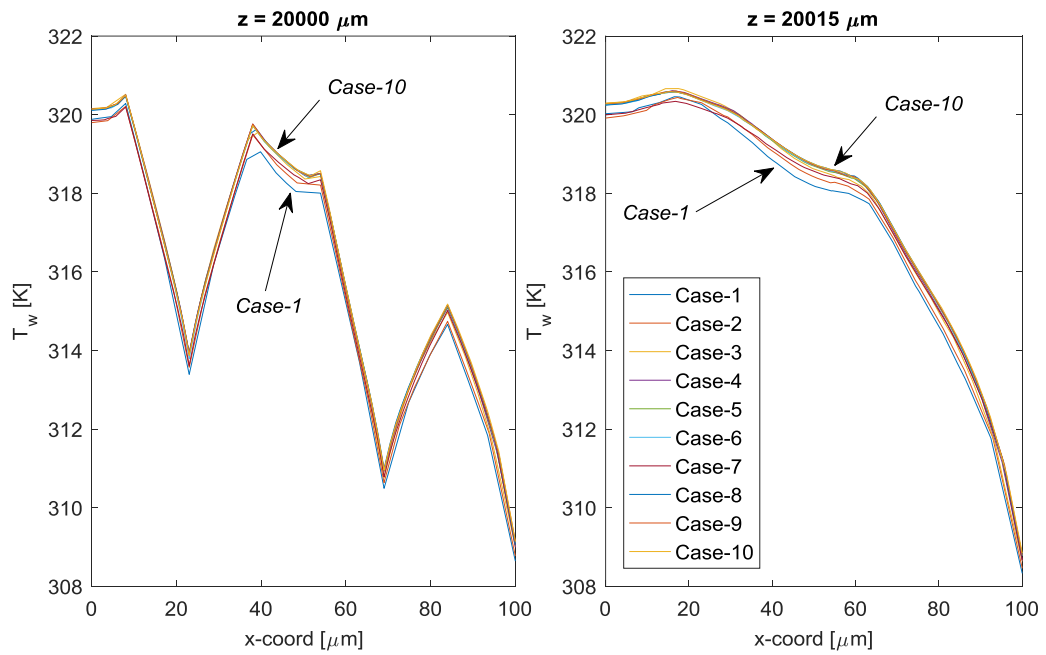


Figure 6.43: Wall temperature distributions for mesh independence test cases of R2LC configuration along the  $x$ -direction at  $z = 20000 \mu\text{m}$  and  $z = 20015 \mu\text{m}$  locations.

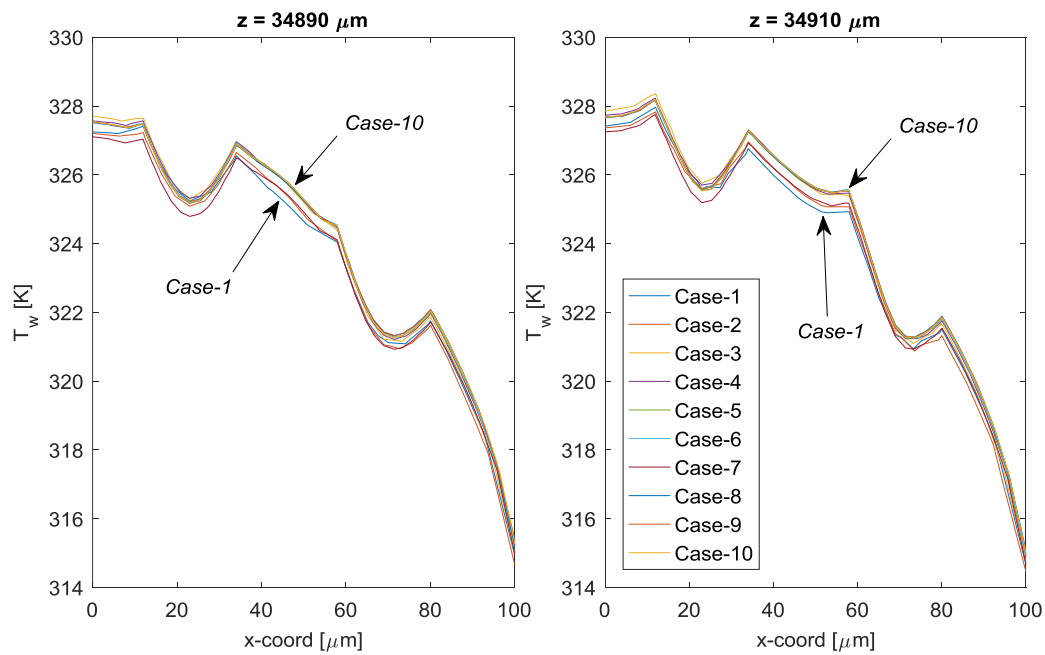


Figure 6.44: Wall temperature distributions for mesh independence test cases of R2LC configuration along the  $x$ -direction at  $z = 34890 \mu\text{m}$  and  $z = 34910 \mu\text{m}$  locations.

Wall mean temperature distributions around the first two and the middle roughness elements for the mesh independence test cases of R2LC configuration are shown in Figs. (6.45) and (6.46), respectively. In each case, the maximum difference is about 0.4 K. Except the coarsest meshes, all test cases showed similar distribution along the flow direction and yield close results.

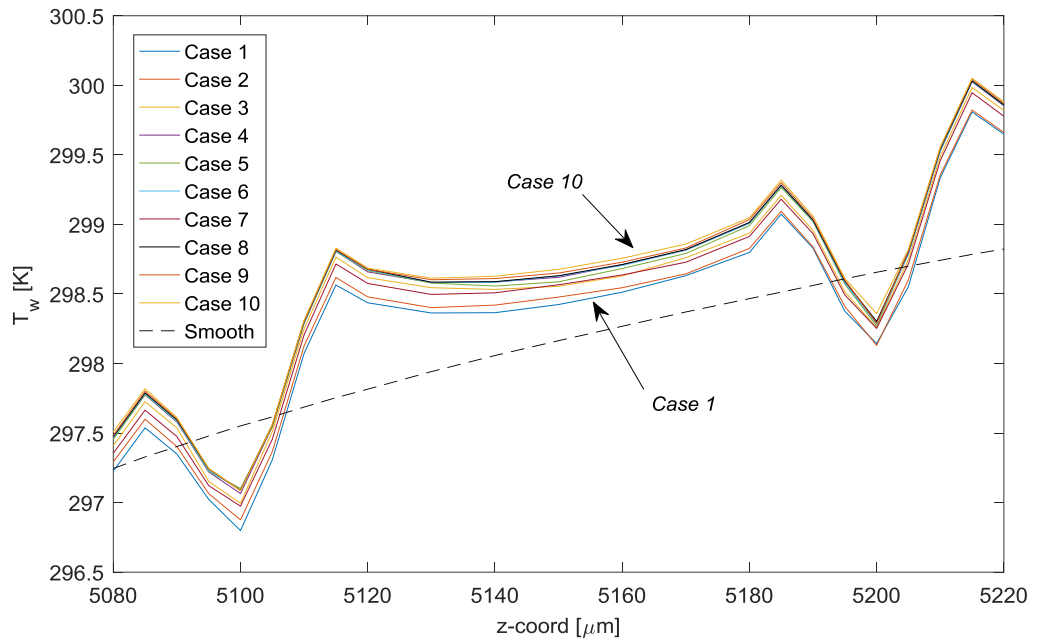


Figure 6.45: Wall mean temperature distribution for mesh independence test cases of R2LC configuration around the first two roughness elements.

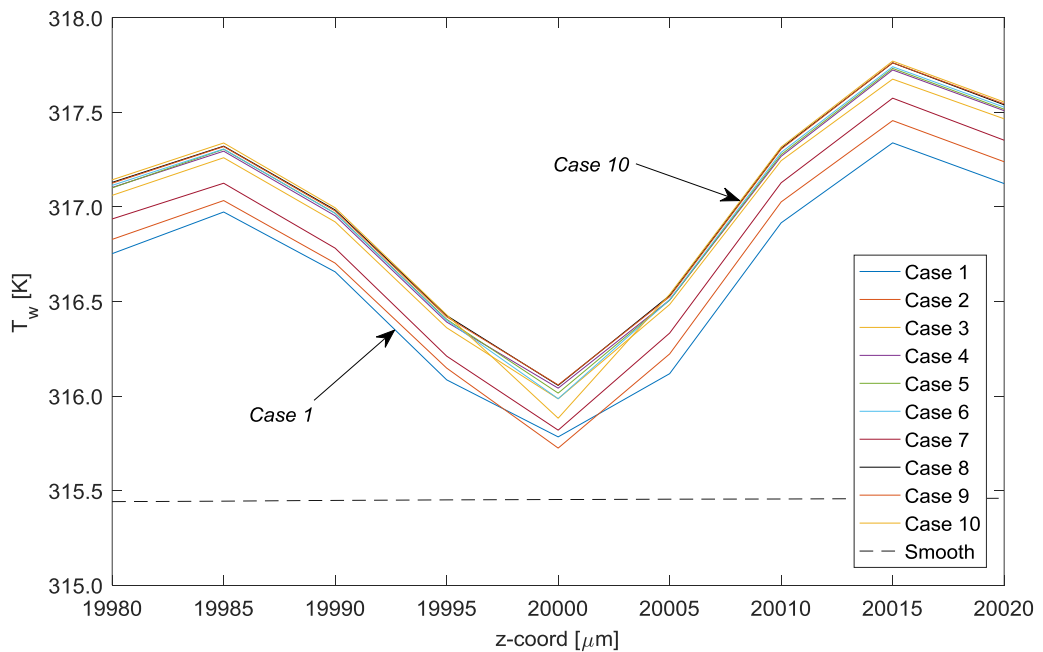


Figure 6.46: Wall mean temperature distribution for mesh independence test cases of R2LC configuration around the middle roughness element.

Local Nusselt distributions for the mesh independence test cases of R2LC configuration are shown in Figs. (6.47), (6.48), and (6.49) around the first two, middle, and the last two roughness elements, respectively. As the number of DOFs increases, difference between the results of each considered case reduces. After *Case-4*, the difference becomes very small, and the results over the conical peaks nearly coincide.

Considering the distribution of sought parameters and difference in calculated results with computational costs, mesh of *Case-8* is chosen for further simulations.

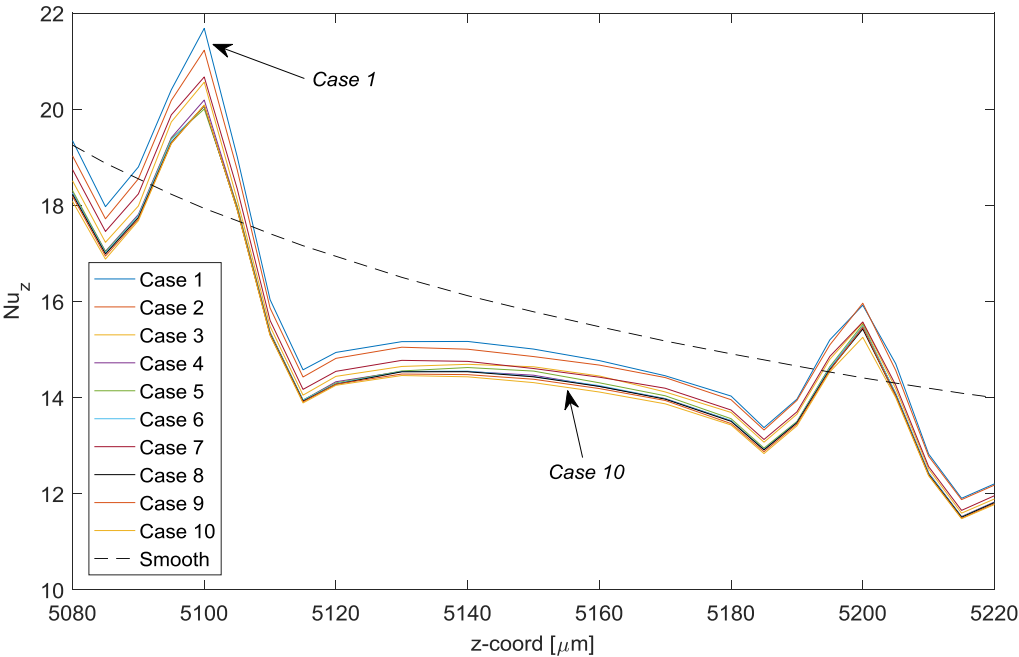


Figure 6.47: Local Nusselt distribution for mesh independence test cases of R2LC configuration around the first two roughness elements.

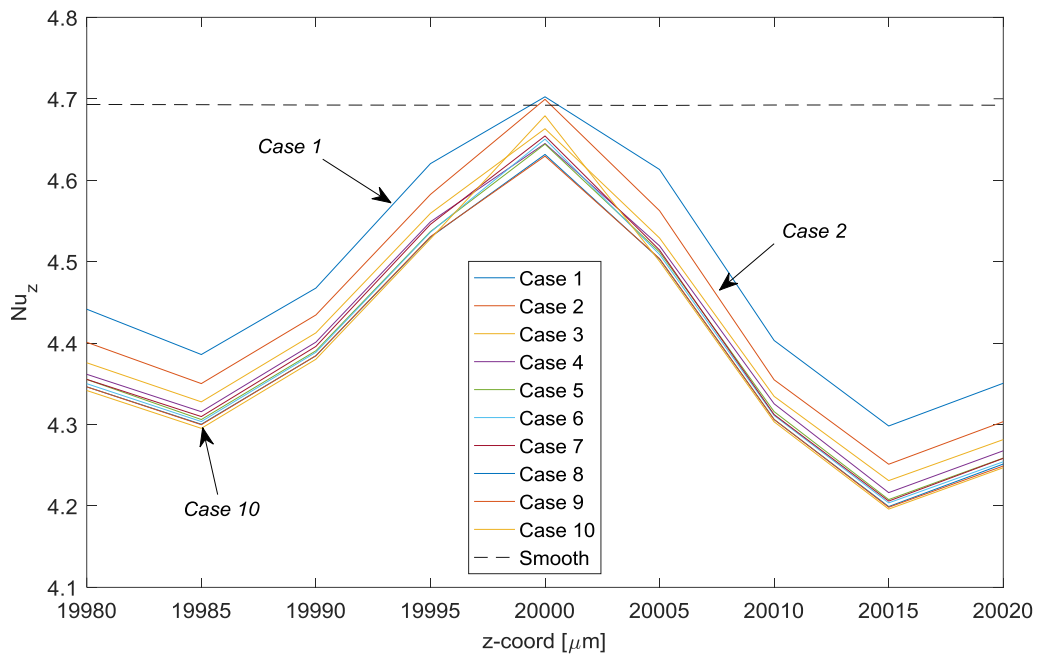


Figure 6.48: Local Nusselt distribution for mesh independence test cases of R2LC configuration around the middle roughness elements.

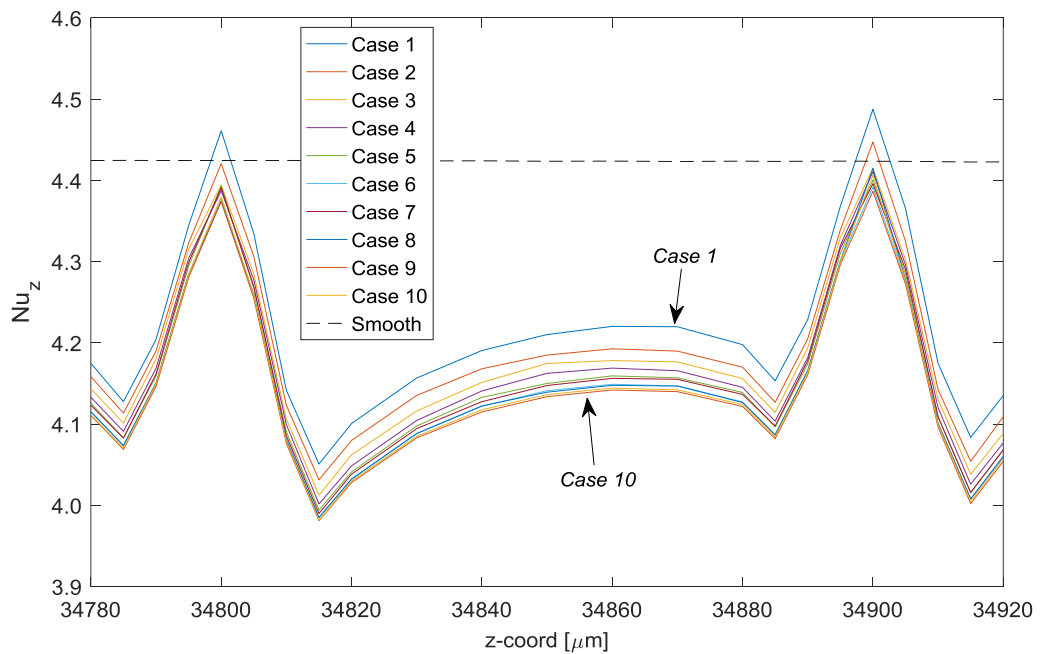


Figure 6.49: Local Nusselt distribution for mesh independence test cases of R2LC configuration around the last two roughness elements.

## 6.4.2 RESULTS AND DISCUSSIONS

Simulations for inlet mass fluxes of  $200 \text{ kg}/(\text{m}^2\text{s})$  to  $1016 \text{ kg}/(\text{m}^2\text{s})$  are conducted by using the mesh of *Case-8* (with  $17.76 \times 10^6$  DOFs) and setting the relative tolerance to  $10^{-6}$ .

Velocity magnitude profiles for inlet mass flux of  $1016 \text{ kg}/(\text{m}^2\text{s})$  along the  $y$ -direction (channel height) before and after the conical elements in the flow direction for various  $z$  locations are shown in Figs. (6.50) and (6.51) for the first conical element over the  $x = 23 \text{ }\mu\text{m}$  line, and last conical elements over the  $x = 69 \text{ }\mu\text{m}$  line, respectively, with the corresponding smooth channel values. In addition, velocity magnitude profiles along the  $x$ -direction at  $y = 5 \text{ }\mu\text{m}$  height from the base are given in Figs. (6.52) and (6.53) for the first and last conical elements, respectively. In each subplot, velocity magnitude plots are shown in such a way that the  $z$  locations are symmetrical to the tip of the corresponding cone. Also, change of velocity in various cross-sections that are  $5 \text{ }\mu\text{m}$  apart from each other in the flow direction around the middle roughness element is shown in Fig. (6.54) as surface plots.

Compared to the smooth channel, velocity reduces around the conical elements and obtains similar values away from the cones. Velocity at the downstream part of the cones are lower than the velocity in the symmetrical position upstream part of the cones. Similar to R1LC configuration, existence of conical elements resulted in low velocity regions around the conical elements, which is more for the downstream locations, for the tested inlet mass fluxes and also more than the R1LC configuration.

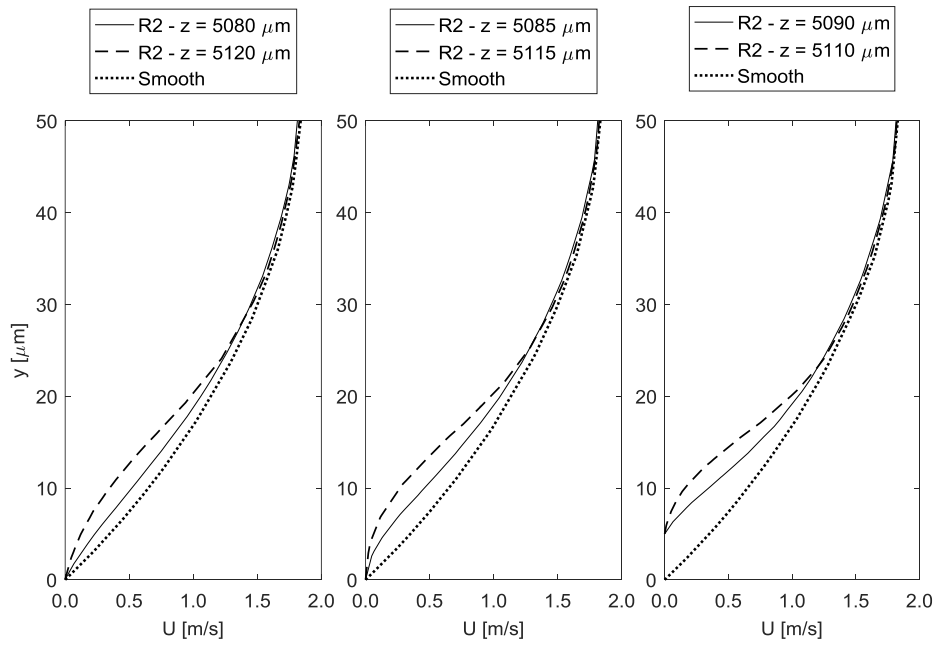


Figure 6.50: Velocity magnitude profiles along  $y$ -direction at  $x = 23 \mu\text{m}$  and various  $z$  locations for the first conical element of R2LC configuration.

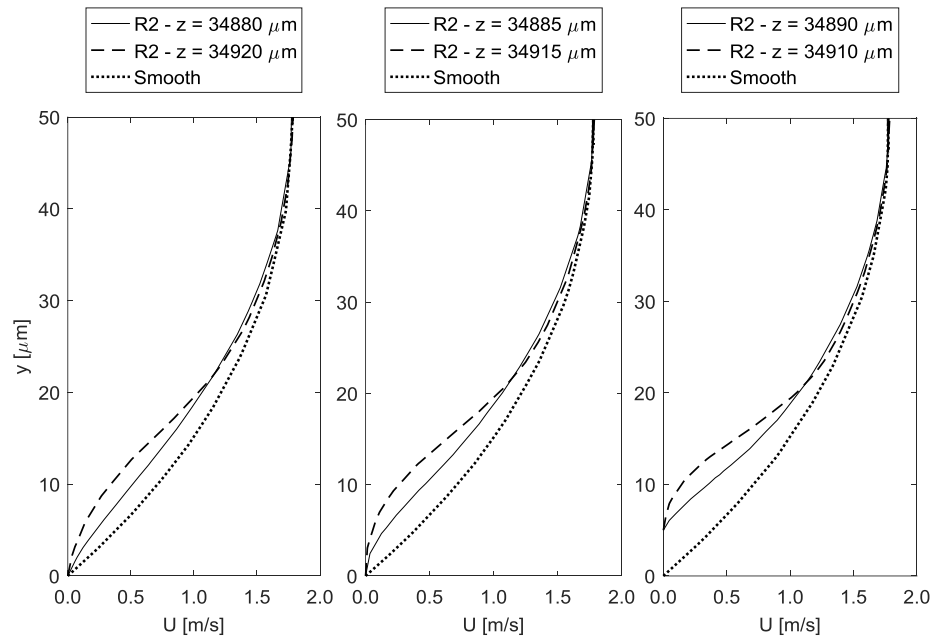


Figure 6.51: Velocity magnitude profiles along  $y$ -direction at  $x = 69 \mu\text{m}$  and various  $z$  locations for the last conical element of R2LC configuration.

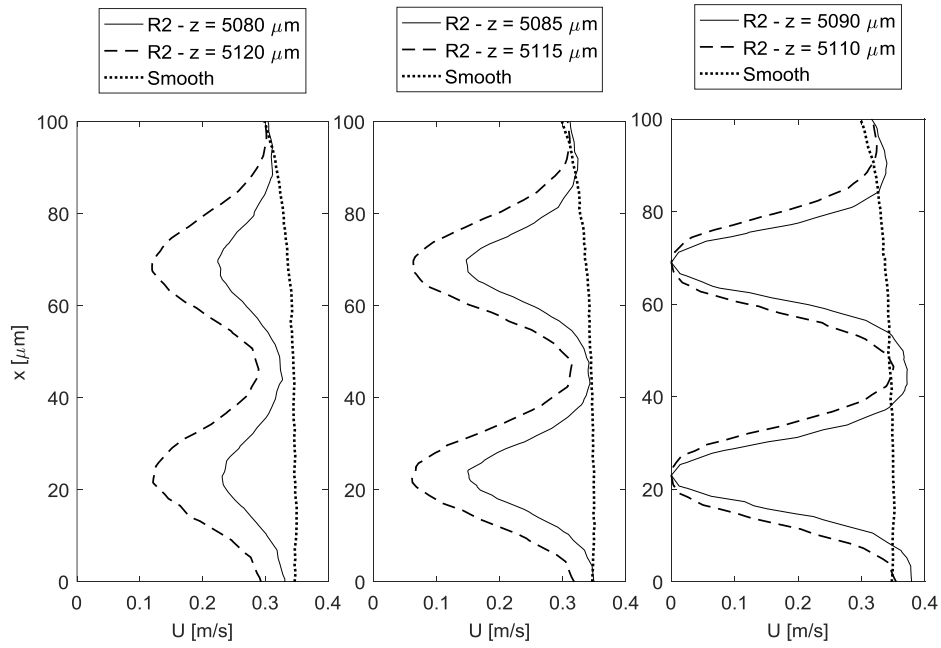


Figure 6.52: Velocity magnitude profiles along  $x$ -direction at  $y = 5 \mu\text{m}$  and various  $z$  locations for the first conical element of R2LC configuration.

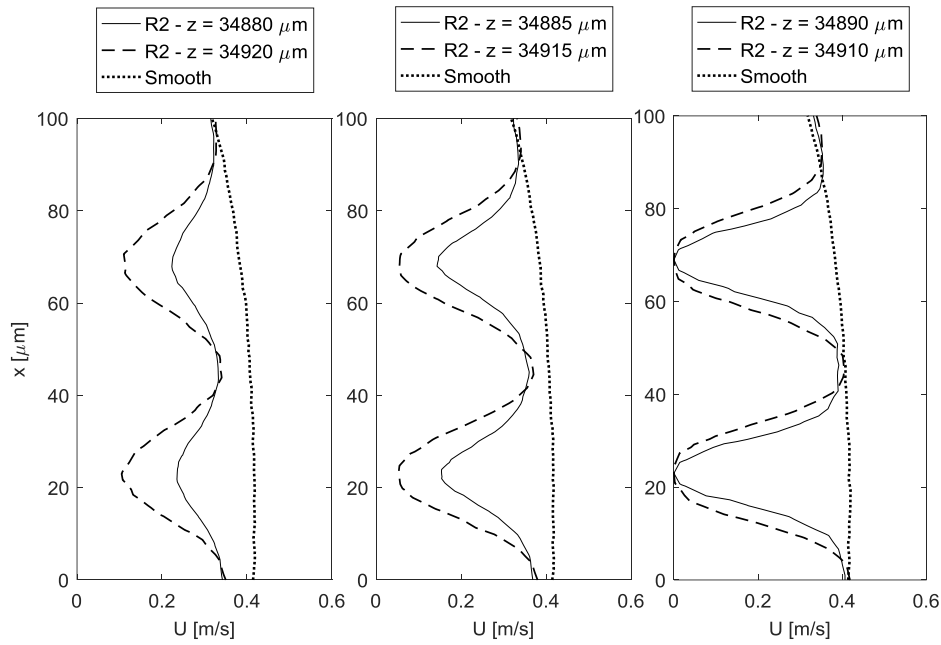


Figure 6.53: Velocity magnitude profiles along  $x$ -direction at  $y = 5 \mu\text{m}$  and various  $z$  locations for the last conical element of R2LC configuration.

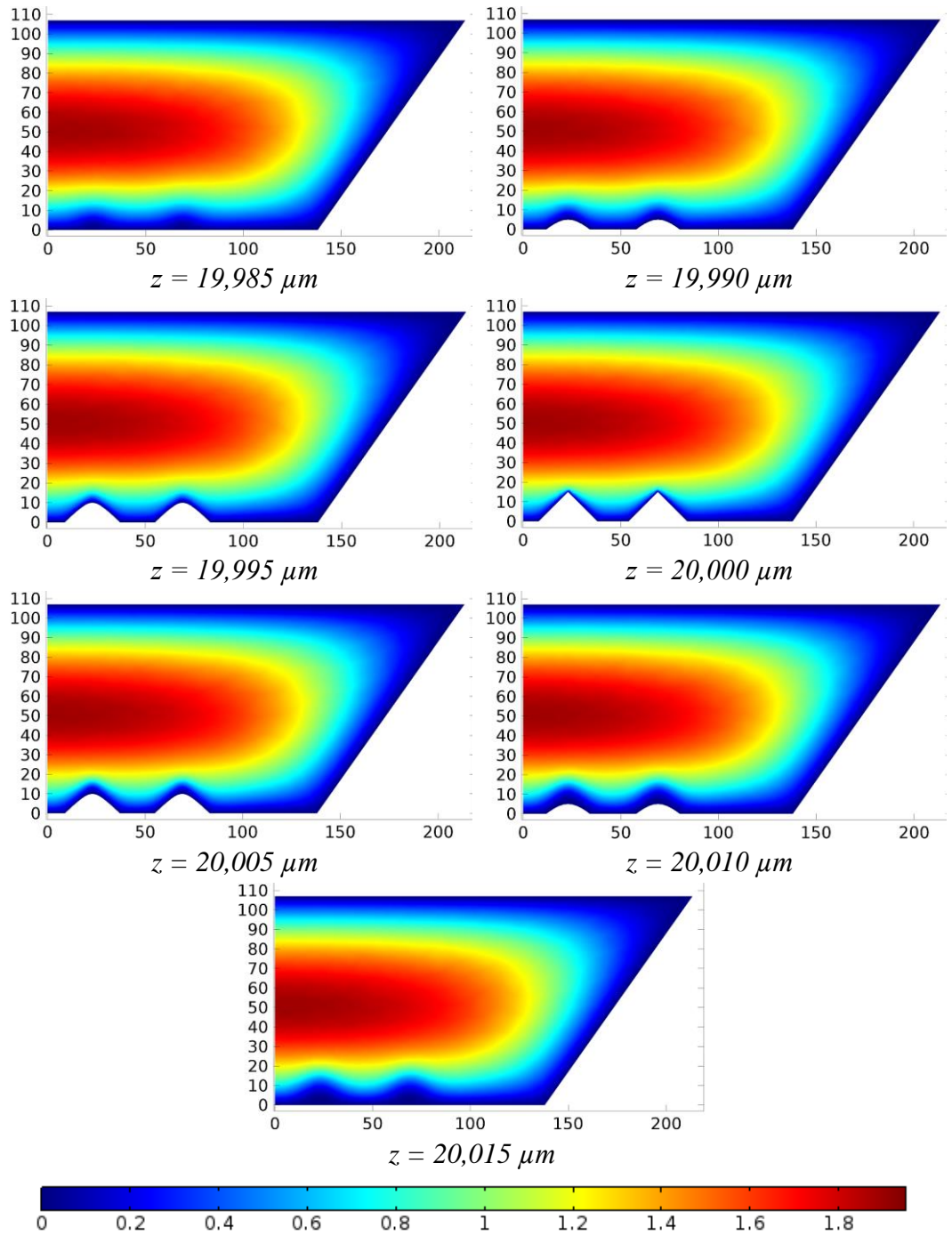


Figure 6.54: Velocity distribution at various cross-sections around the middle cone of R2LC configuration in the flow direction ( $G = 1016 \text{ [kg/(m}^2\text{s)]}$ ).

Wall temperatures at  $z = 6,000 \mu\text{m}$  and  $z = 34,000 \mu\text{m}$  the along  $x$ -direction, from symmetry plane through the side of the microheater and perpendicular to flow direction, for various inlet mass fluxes is shown in Figs. (6.55) and (6.56), respectively, along with the corresponding smooth channel values. Wall temperatures become higher than the smooth channel and R1LC configuration in locations where there is no cone, due to increase in heating area and increase of low velocity regions around the conical elements, which reduces convective heat transfer and more obvious at the base circumference of the cones. Similar to R1LC configuration, wall temperatures reduces through the tip of the cones. However, temperatures of the tip points of the cones increased with respect to R1LC configuration.

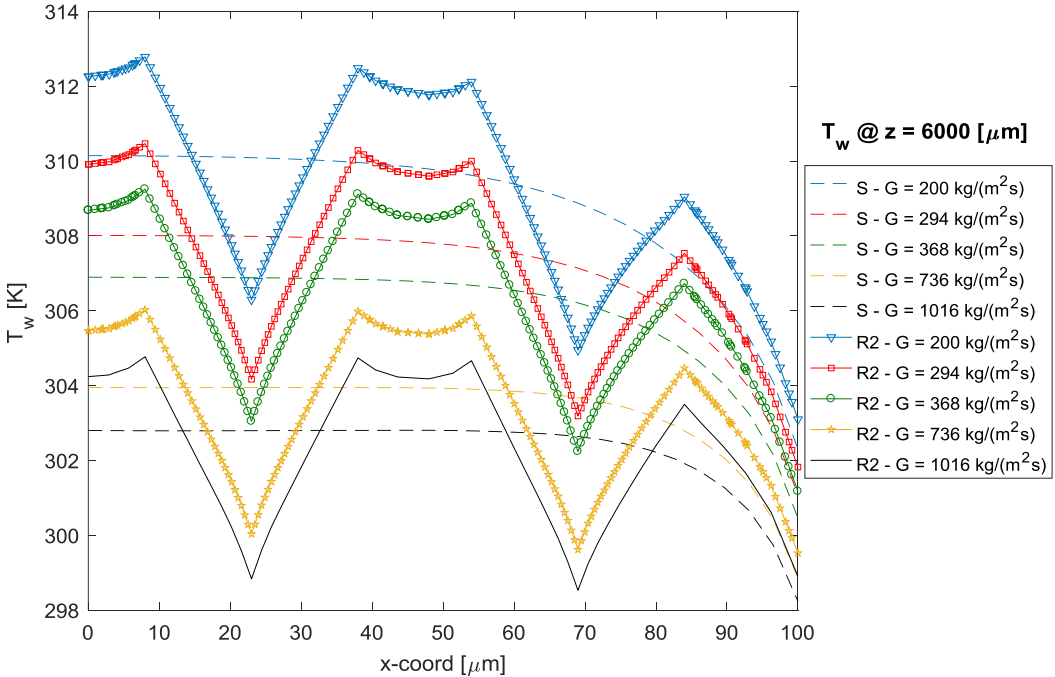


Figure 6.55: Wall temperature distribution at  $z = 6000 \mu\text{m}$  location for various inlet mass fluxes for R2LC configuration with corresponding smooth values.

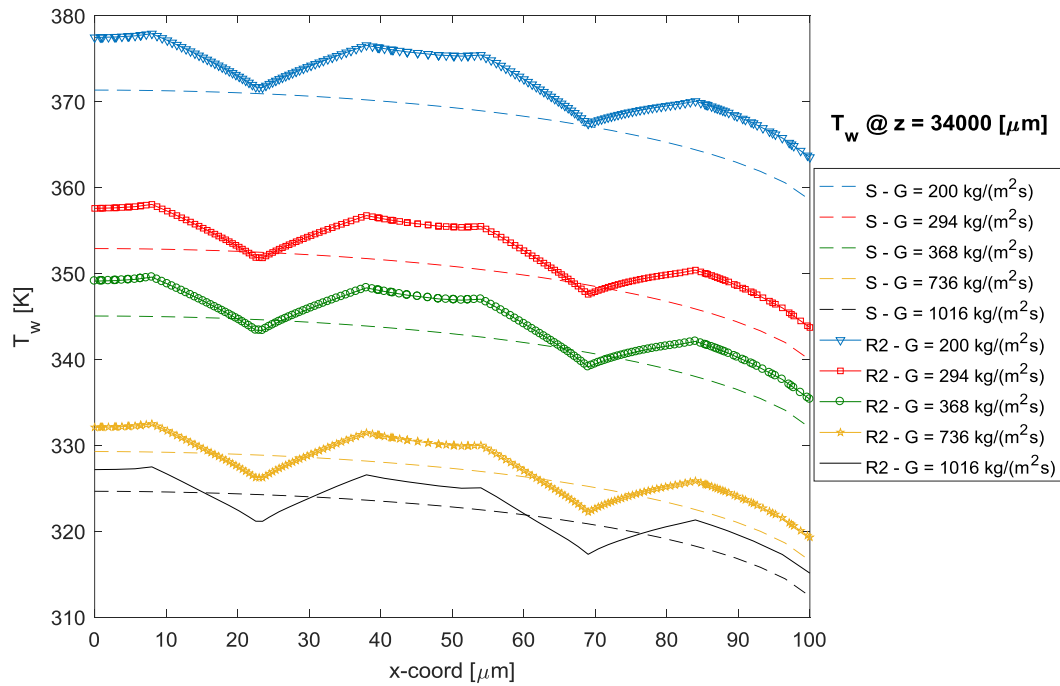


Figure 6.56: Wall temperature distribution at  $z = 34000 \mu\text{m}$  location for various inlet mass fluxes for R2LC configuration with corresponding smooth values.

Wall temperature distribution around the middle cone of R2LC configuration for inlet mass fluxes of  $200 \text{ kg}/(\text{m}^2\text{s})$  and  $1016 \text{ kg}/(\text{m}^2\text{s})$  is shown in Fig. (6.57). In addition, change of temperature in various cross-sections that are  $5 \mu\text{m}$  apart from each other in the flow direction around the middle roughness elements is shown in Fig. (6.58) as surface plots for an inlet mass flux of  $1016 \text{ kg}/(\text{m}^2\text{s})$ . Similar behavior of R1LC configuration is also observed with R2LC configuration with increased temperature values. Wall temperature of the downstream part of the cone is slightly higher than the flow facing side of the channel due to reduced velocity zones and increased bulk fluid temperature.

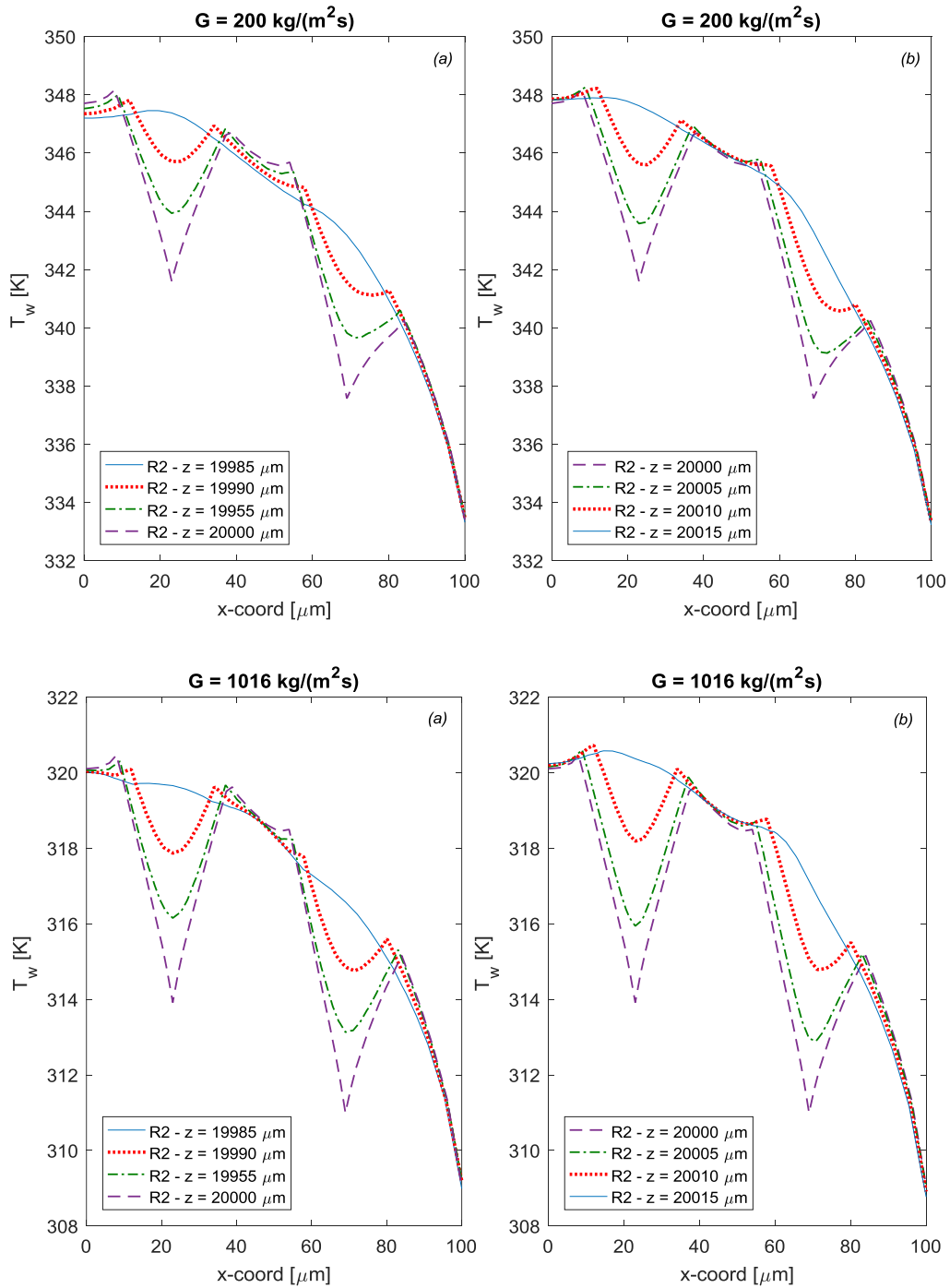


Figure 6.57: Wall temperature distribution around the middle cone of R2LC configuration for inlet mass fluxes of  $200 \text{ kg}/(\text{m}^2\text{s})$  and  $1016 \text{ kg}/(\text{m}^2\text{s})$  for (a) flow facing side of the cone, (b) back side of the cone.

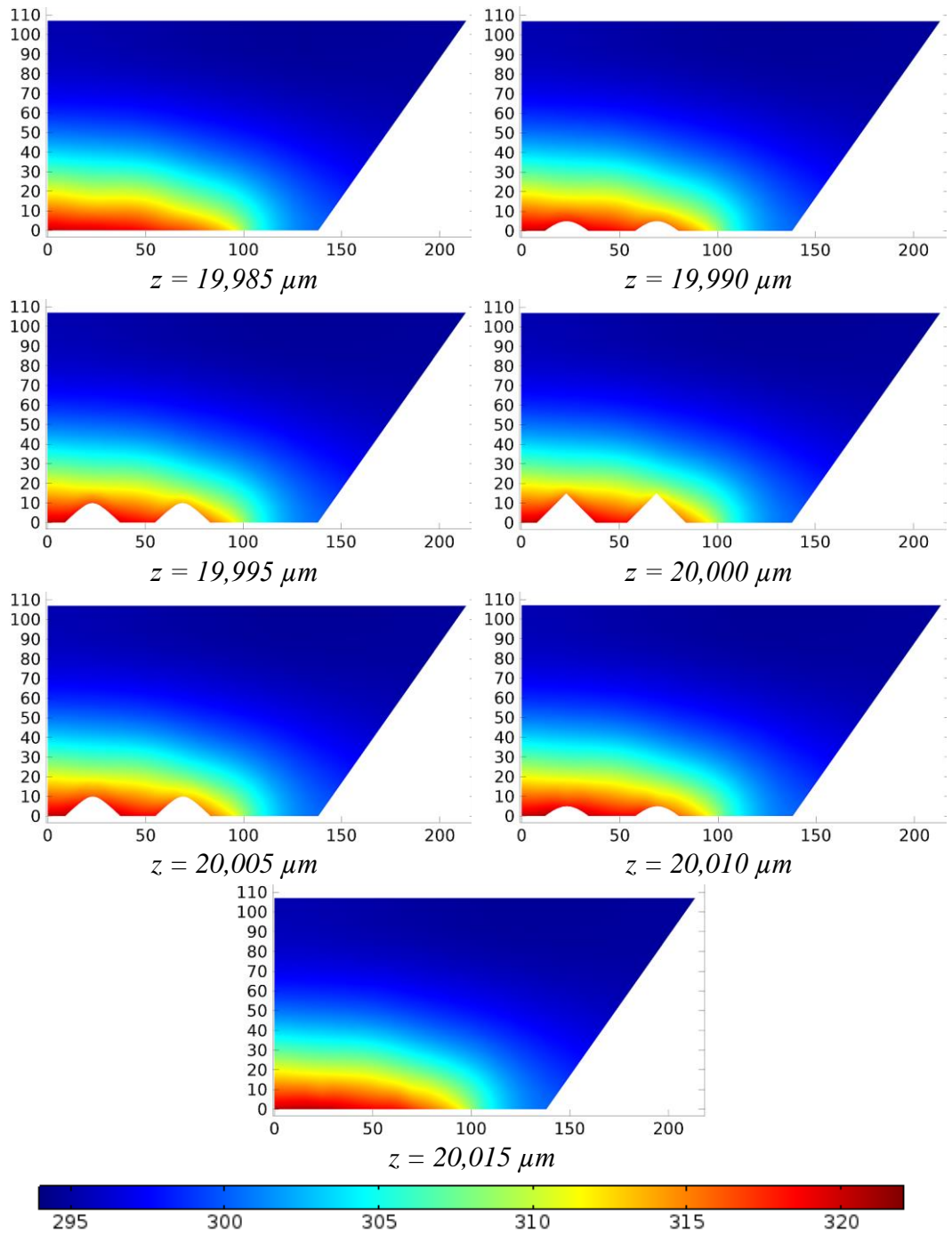


Figure 6.58: Temperature distribution at various cross-sections around the middle cone of R2LC configuration in the flow direction ( $G = 1016 \text{ [kg/(m}^2\text{s)]}$ ).

Fluid bulk mean temperature distribution over the 10<sup>th</sup> roughness element, and over the last two roughness elements of R2LC configuration are shown in Figs. (6.59) and (6.60), respectively. Similar to the previous geometry, bulk mean temperatures are calculated in cross-sectional planes 1  $\mu\text{m}$  apart over the conical elements, and 5  $\mu\text{m}$  apart between the conical elements in  $z$ -direction. Calculated fluid bulk mean temperatures for R2LC configuration are higher than the smooth channel and slightly higher than the R1LC configuration values. The maximum difference between R1LC and R2LC bulk mean temperatures are at the exit of the heated section and about 2.5 K for inlet mass flux of 200  $\text{kg}/(\text{m}^2\text{s})$ . Difference between them reduces as the inlet mass flux increases.

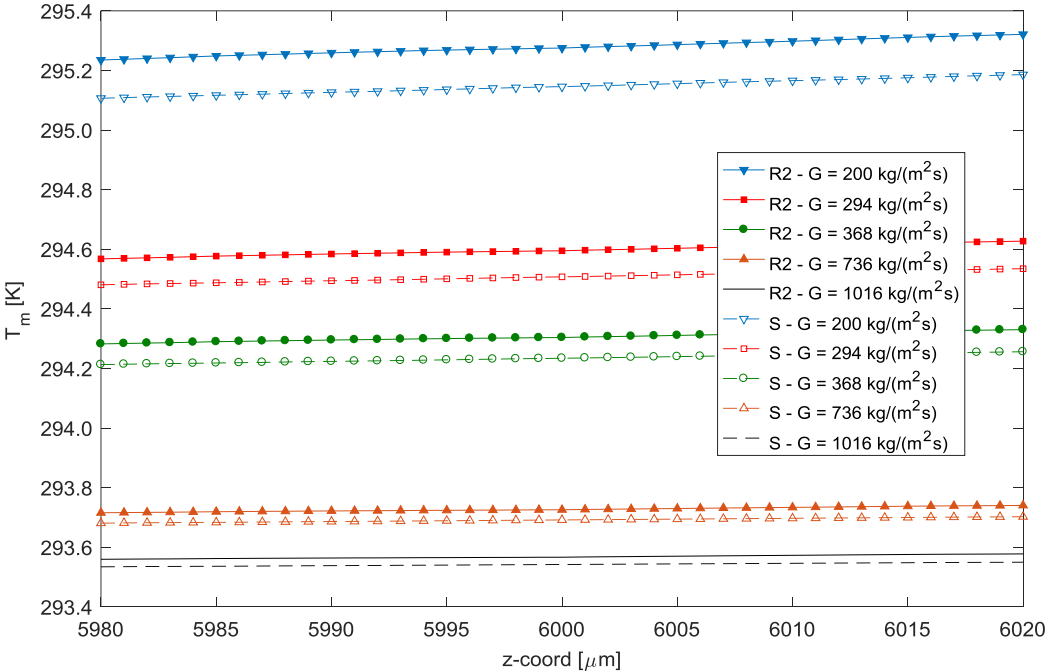


Figure 6.59: Fluid bulk mean temperature distribution over the 10<sup>th</sup> roughness elements of R2LC configuration.

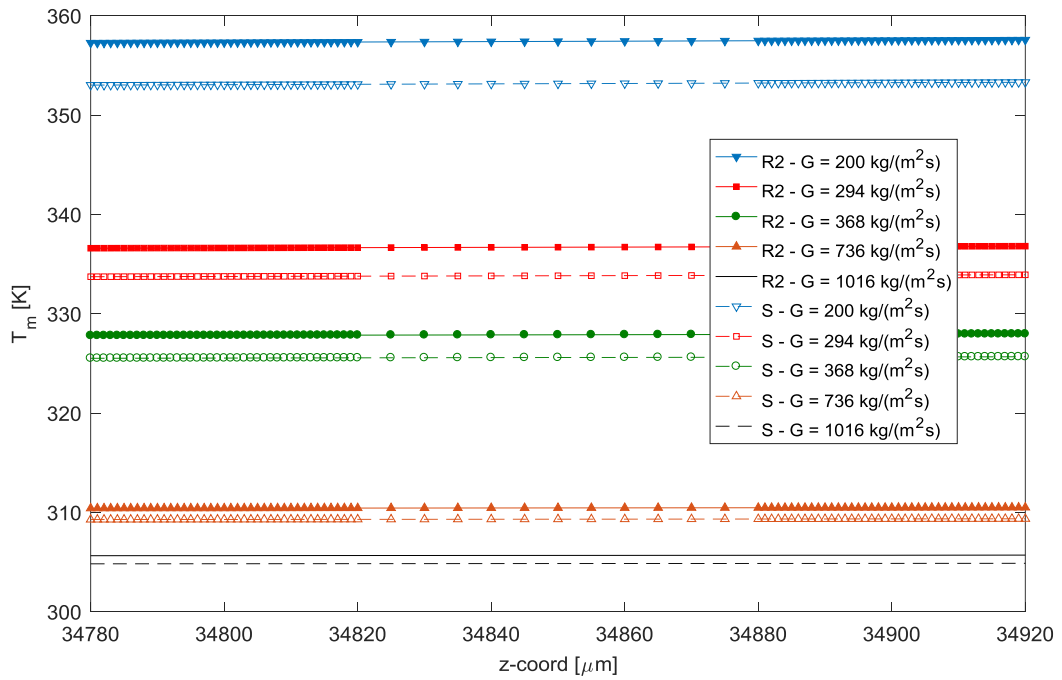


Figure 6.60: Fluid bulk mean temperature distribution over the last two roughness elements of R2LC configuration.

Wall mean temperature distribution over the first two roughness elements, around the middle roughness element, and over the last two roughness elements of R2LC configuration are shown in Figs. (6.61), (6.62), and (6.63) respectively. Wall mean temperatures are calculated  $1 \mu\text{m}$  apart over the conical elements and over the regions  $5 \mu\text{m}$  before and after the cones, and  $5 \mu\text{m}$  apart between the conical elements in the  $z$ -direction. Wall mean temperatures for R2LC configuration exhibit a similar pattern with the R1LC configuration and take higher values than R1LC configuration and the smooth channel values. Difference between the smooth and R2LC configuration wall mean temperatures reduces around the tip of the cones as the inlet mass flux increases.

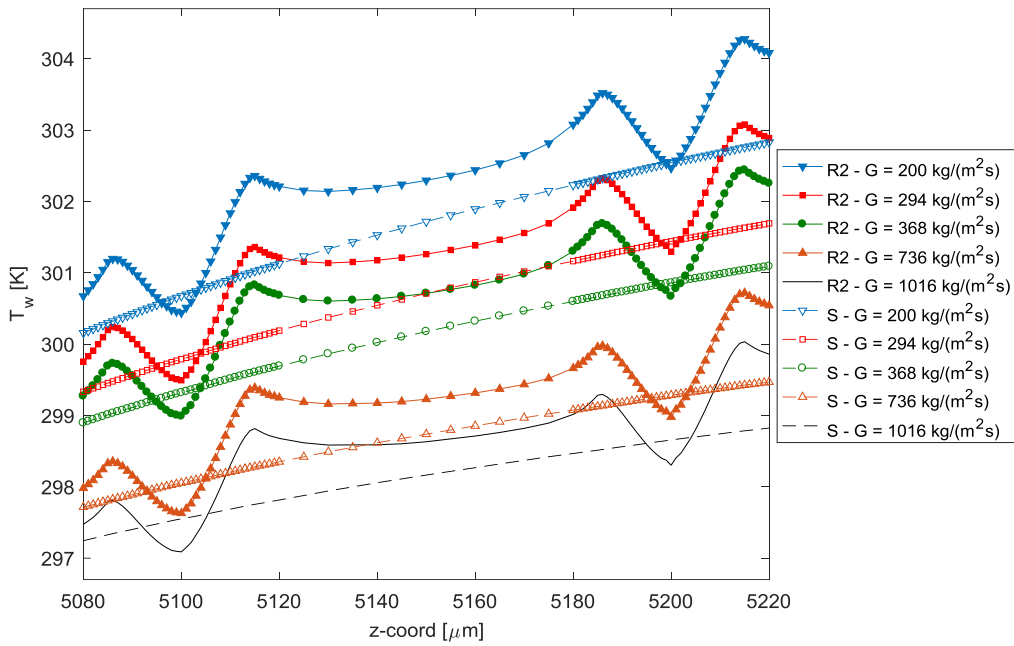


Figure 6.61: Wall mean temperature distribution over the first two roughness elements of R2LC configuration.

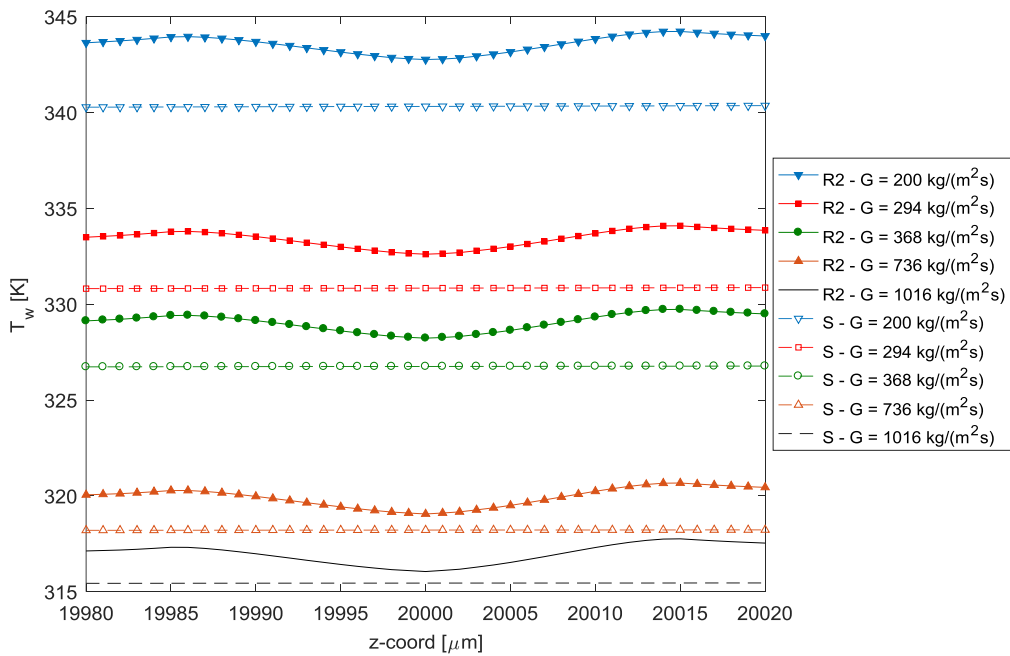


Figure 6.62: Wall mean temperature distribution near the middle roughness elements of R2LC configuration.

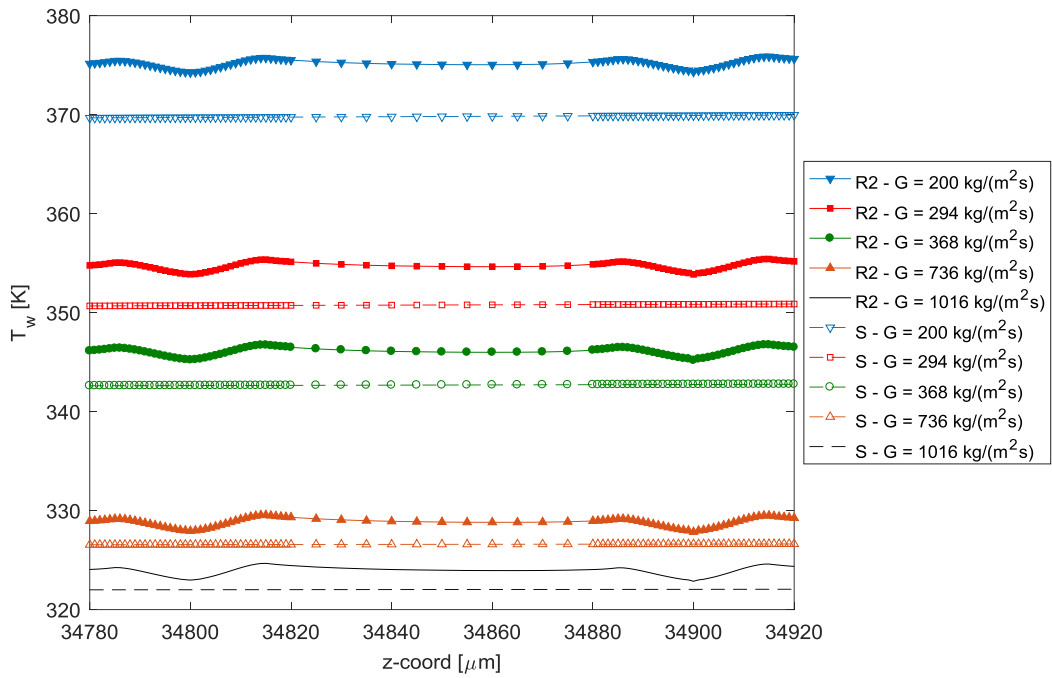


Figure 6.63: Wall mean temperature distribution over the last two roughness elements of R2LC configuration.

Surface temperature around the middle conical elements of R2LC configuration is shown in Fig. (6.64) for inlet mass flux of  $1016 \text{ kg}/(\text{m}^2\text{s})$ . In this figure, convective heat flux in the fluid at  $y = 7.5 \text{ } \mu\text{m}$  plane is also represented with arrows. Similar to R1LC configuration, convective heat flux is reduced at downstream side of the cones due to reduced velocity regions.

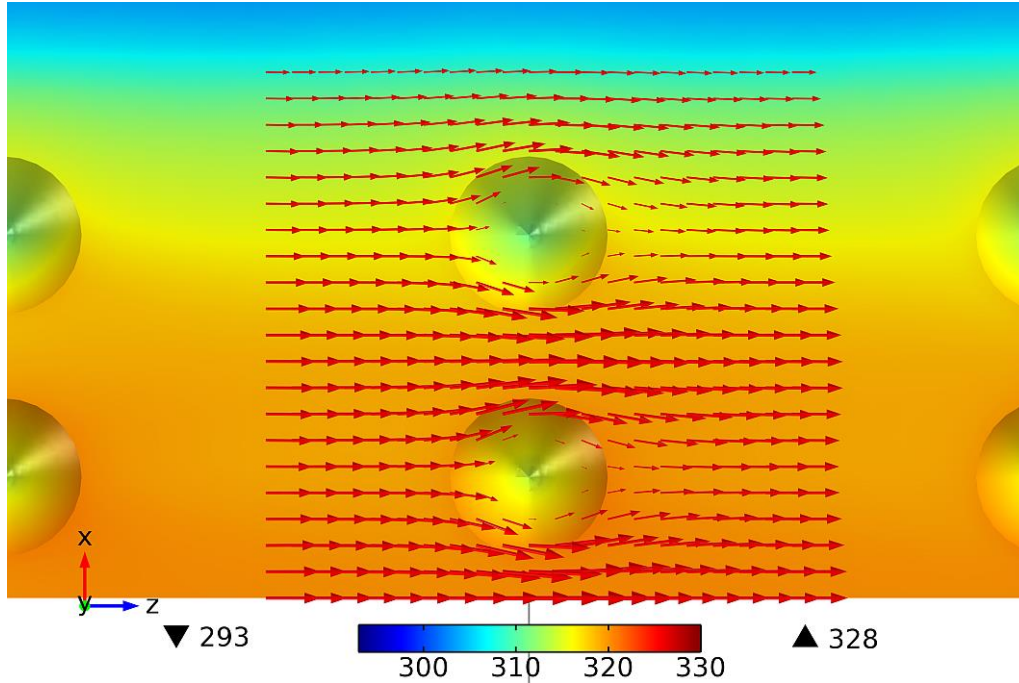


Figure 6.64: Surface temperature around the middle conical elements of R2LC configuration and convective heat flux in the fluid at  $y = 7.5 \mu\text{m}$  plane ( $G = 1016 \text{ [kg/(m}^2\text{s)]}$ ).

Local  $Nu$  distribution over the first two roughness elements, around the middle roughness element, and over the last two roughness elements of R2LC configuration are also shown in Figs. (6.65), (6.66), and (6.67) respectively. Similar to R1LC configuration, local  $Nu$  takes the minimum value at the base of the cone due to reduced velocity zones and reduced convective heat transfer around these zones, and increased thermal conductivity of the fluid between the conical elements due to rise in temperature, which is shown in Figs. (6.68) and (6.69). Then,  $Nu$  increases towards the next cone and when it becomes closer to the next cone, starts to reduce again. Local  $Nu$  increases towards the tip of the cone, since over the tip, the cone is subjected to high velocity flow. However, except the inlet section, local  $Nu$  takes lower value than the smooth channel and R1LC values.

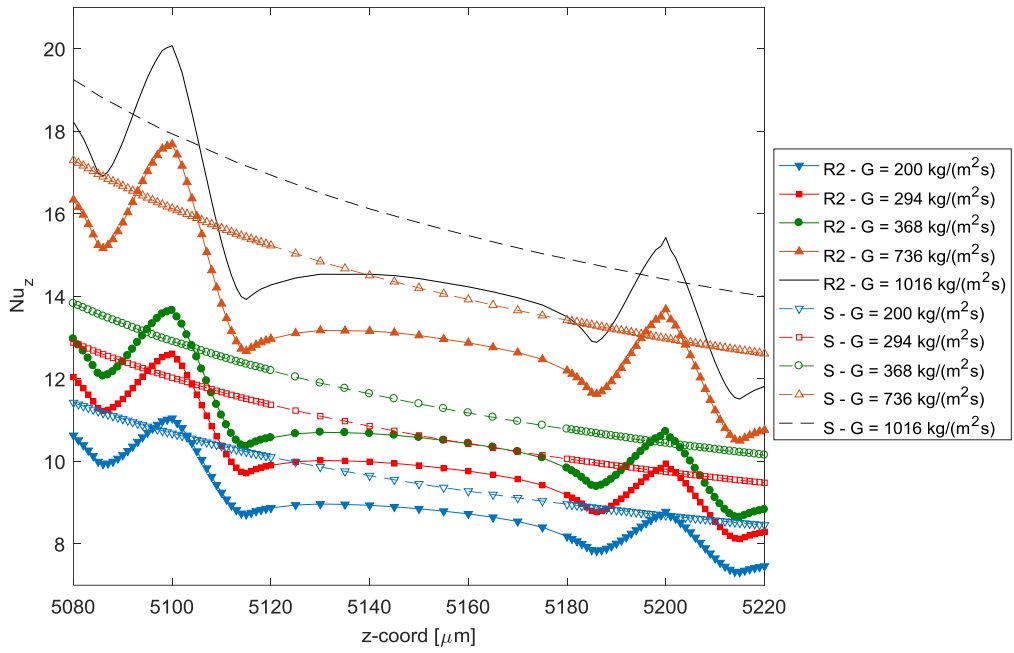


Figure 6.65: Local Nusselt distribution over the first two roughness elements of R2LC configuration.

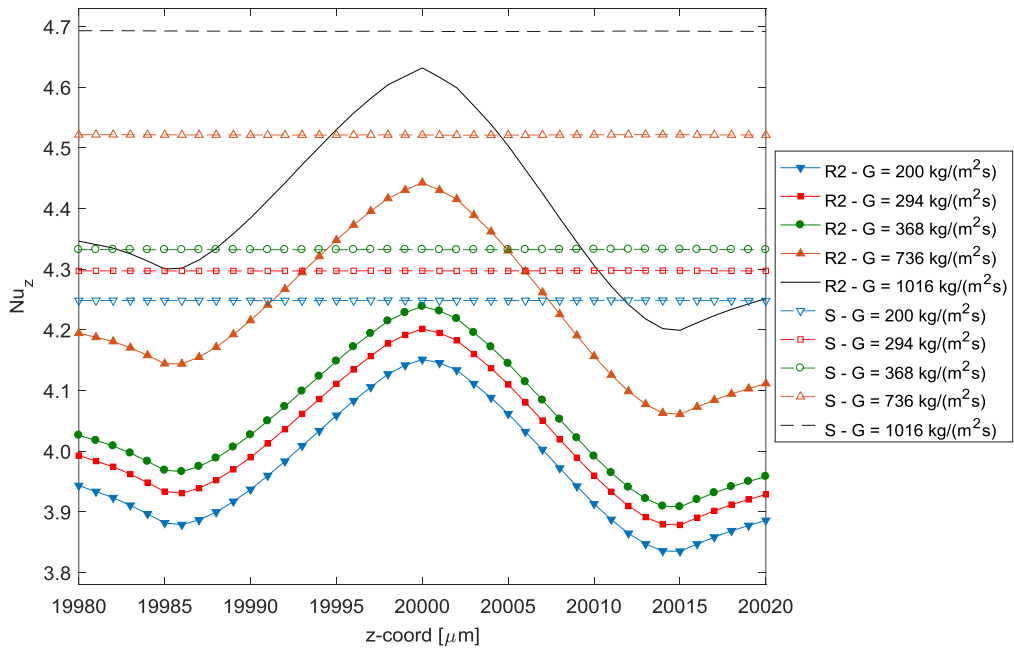


Figure 6.66: Local Nusselt distribution near the middle roughness element of R2LC configuration.

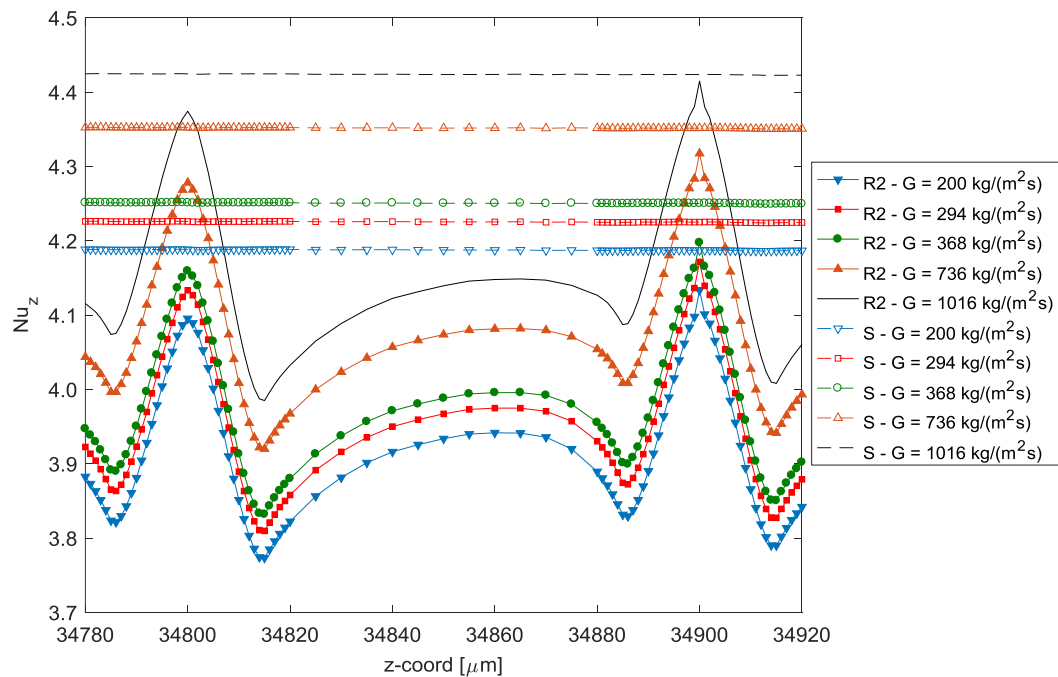


Figure 6.67: Local Nusselt distribution over the last two roughness elements of R2LC configuration.

In Fig. (6.68) the change of thermal conductivity is presented through the inlet to the outlet of the rough section of R2LC configuration, for an inlet mass flux of 1016  $\text{kg}/(\text{m}^2\text{s})$  at a plane passing through  $x = 23 \mu\text{m}$ , that is the tip point of inside cones. In Fig. (6.69) change of thermal conductivity is shown at a plane passing through  $x = 69 \mu\text{m}$ , which is the plane passing through the tip of outside cones, for the same conditions. Due to the unheated flow near the outside wall, temperature around the outside cone line is lower than the inside cone line, which results in lower thermal conductivity around the outside line of cone, and uneven change from the symmetry plane to the outside wall.

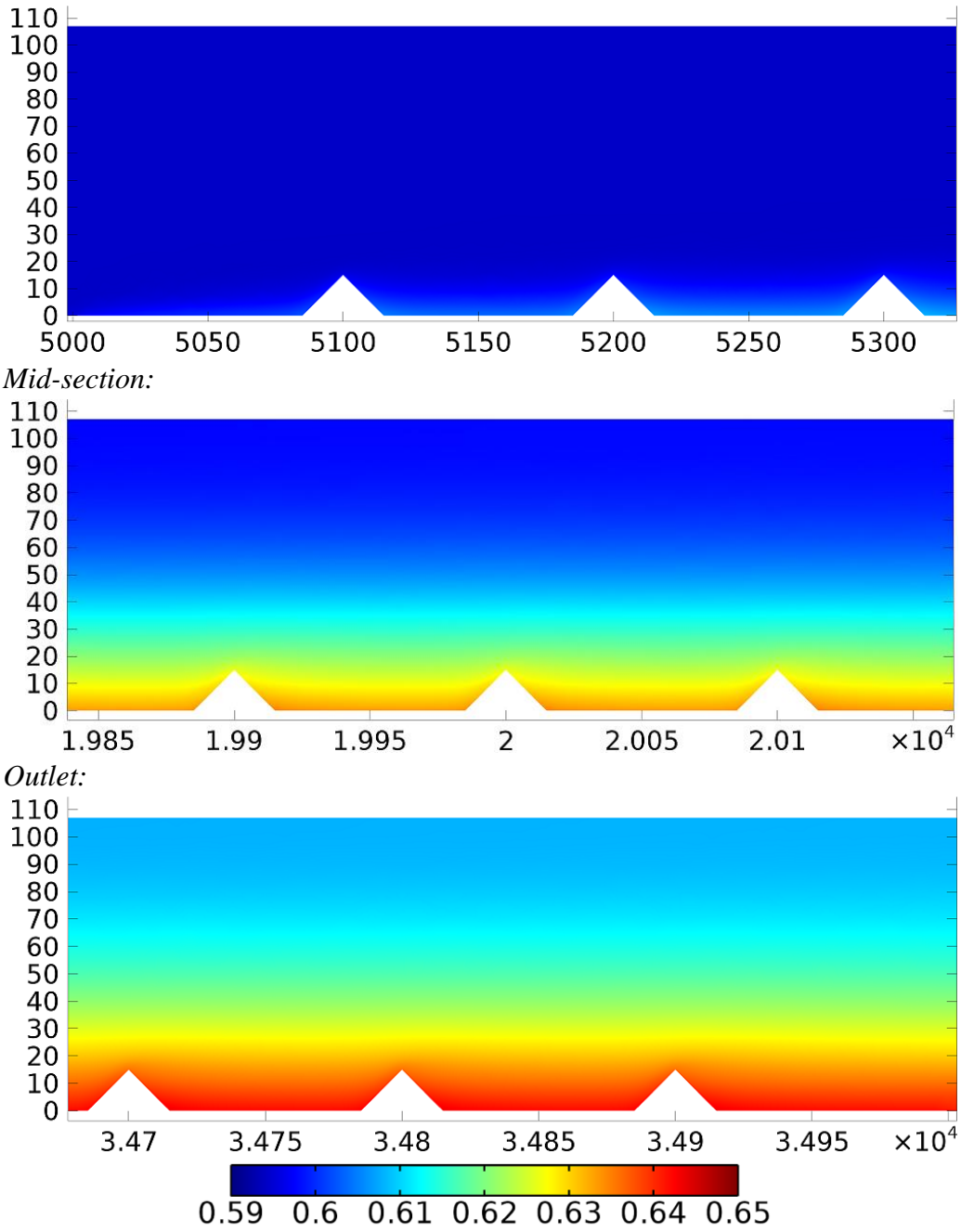


Figure 6.68: Change of thermal conductivity at  $x = 23 \mu\text{m}$  plane through the inlet to the outlet of the rough section of R2LC configuration ( $G = 1016 \text{ [kg/(m}^2\text{s)]}$ ).

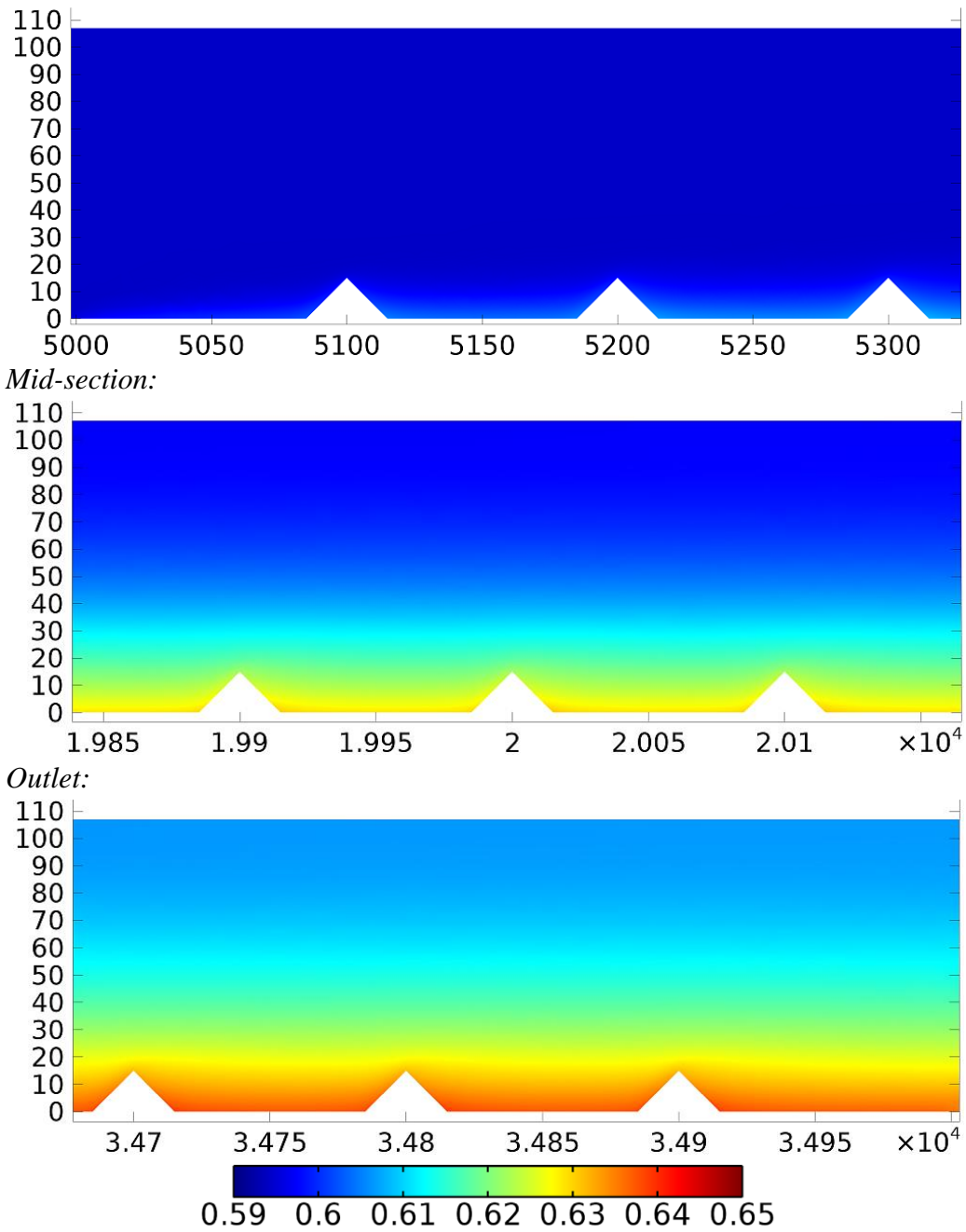


Figure 6.69: Change of thermal conductivity at  $x = 69 \mu\text{m}$  plane through the inlet to the outlet of the rough section of R2LC configuration ( $G = 1016 \text{ [kg/(m}^2\text{s)]}$ ).

## 6.5 ROUGH MICROCHANNEL SIMULATIONS WITH *DaisyCone* (RDC) CONFIGURATION

### 6.5.1 MESH INDEPENDENCE STUDIES

Similar to the previous cases, mesh independence studies for the simulations in the microchannel having *DaisyCone* roughness configuration (RDC) are carried out for an effective heat flux of  $300 \text{ kW/m}^2$  and an inlet mass flux of  $1016 \text{ kg/(m}^2\text{s)}$ , considering 8 different meshes containing about  $5.27 \times 10^6$  DOFs for the coarsest one to  $31.43 \times 10^6$  DOFs for the densest one. Iterative multigrid solver is used with linear elements. The relative tolerance is set to  $10^{-3}$ . Element numbers and DOFs of used meshes, CPU times, used physical memory (PM) and virtual memory (VM) are summarized in Table – (6.5) with the calculated  $Po$  values over the heated region, and average and maximum heated surface temperatures. All the simulations are conducted with the same workstation and operating system used in previous microchannel simulations, except *Case-8*. Again, for the cases where physical memory is not enough, a partition in the hard disk is used as temporary RAM with a penalty of longer computational times. *Case-8* simulation is done with the same workstation but using Linux operating system with 100 GB of swap partition that is used as temporary RAM.

The meshes of test cases *Case-1* and *Case-2* are constructed with predefined *coarse* and *normal* meshing schemes, respectively. Meshes of remaining cases are constructed manually by gradually increasing the element numbers on the edges of the geometry and reducing the element sizes inside the domain. Surface meshes around the cones of roughness pattern of *Case-1*, *Case-6*, and *Case-8* are shown in Fig. (6.70), as an example.

Table 6.5: Summary of mesh properties and calculated values used in mesh independence tests of *DaisyCone* configuration (*PM*: Physical Memory, *VM*: Virtual Memory, *HS*: Heated Surface).

<i>Case</i>	<i>ELEM #</i>	<i>DOFs</i>	<i>CPU Time [s]</i>	<i>PM [GB]</i>	<i>VM [GB]</i>	<i>Po</i>	<i>T<sub>ave,HS</sub> [K]</i>	<i>T<sub>max,HS</sub> [K]</i>
1	4,204,031	5,270,740	7,248	46.19	47.76	17.551	315.526	327.912
2	8,378,391	9,662,330	65,193	46.92	65.09	17.050	315.623	327.780
3	14,756,423	13,926,435	16,080	45.69	53.93	16.713	315.726	327.896
4	16,814,811	15,870,975	29,974	44.88	53.42	16.661	315.731	327.894
5	18,912,499	17,947,045	37,739	45.75	58.00	16.642	315.738	327.878
6	20,345,123	19,253,050	40,624	46.71	60.24	16.635	315.738	327.918
7	22,973,741	21,603,205	87,270	46.77	67.66	16.618	315.741	327.897
8	33,832,230	31,437,745	612,525	47.43	142.78	16.570	315.753	327.879

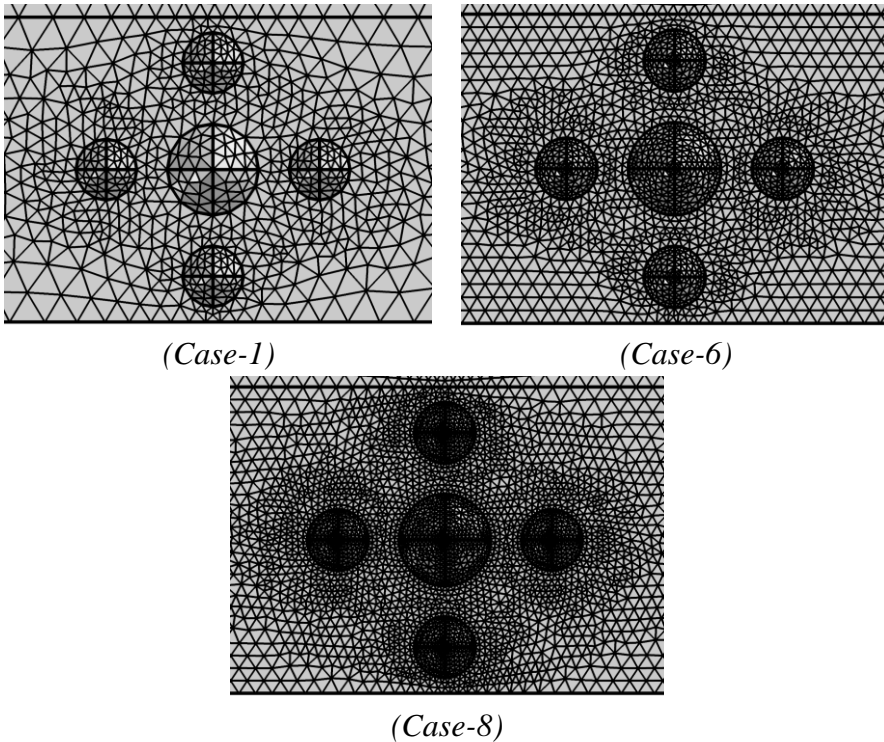


Figure 6.70: Surface meshes around the conical elements of RDC configuration for *Case-1* (coarsest), *Case-6*, and *Case-8* (densest).

The percentage difference of calculated  $Po$  values between two consecutive runs drops to below 0.3% after about  $13.9 \times 10^6$  DOFs (*Case-3*), and the percentage difference of  $Po$  between the densest case (*Case-8*) and the other cases drops to below 0.6% at about  $15.8 \times 10^6$  DOFs (*Case-4*). Also, average and maximum temperatures of the heated surface remain nearly constant after *Case-4*.

Fluid bulk mean temperatures for mesh independence cases of RDC configuration are calculated in cross-sectional planes that are 5  $\mu\text{m}$  apart from each other around the conical element set in the flow direction. Test meshes resulted in a maximum of about 0.2 K difference in bulk mean temperature at the end of the heated section and after *Case-4* the results nearly coincided, which is shown in Fig. (6.71).

Wall temperature distributions for mesh independence test cases of RDC configuration along the  $x$ -direction at  $z = 5135 \mu\text{m}$  and  $z = 5170 \mu\text{m}$  locations are shown in Fig. (6.72). Additionally, wall temperature distributions along  $x$ -direction at  $z = 19940 \mu\text{m}$  and  $z = 19975 \mu\text{m}$  locations, and  $z = 34815 \mu\text{m}$  and  $z = 34850 \mu\text{m}$  locations are shown in Figs. (6.73) and (6.74), respectively. Except the coarsest meshes, that are *Case-1* and *Case-2*, tested meshes resulted very close temperature distribution.

Wall mean temperature distributions around the first and the middle roughness element sets for the mesh independence test cases of RDC configuration are shown graphically in Figs. (6.75) and (6.76), respectively. Except the coarsest first two case meshes, all the other test cases showed similar distribution along the flow direction and yield close results in the 0.2 K band.

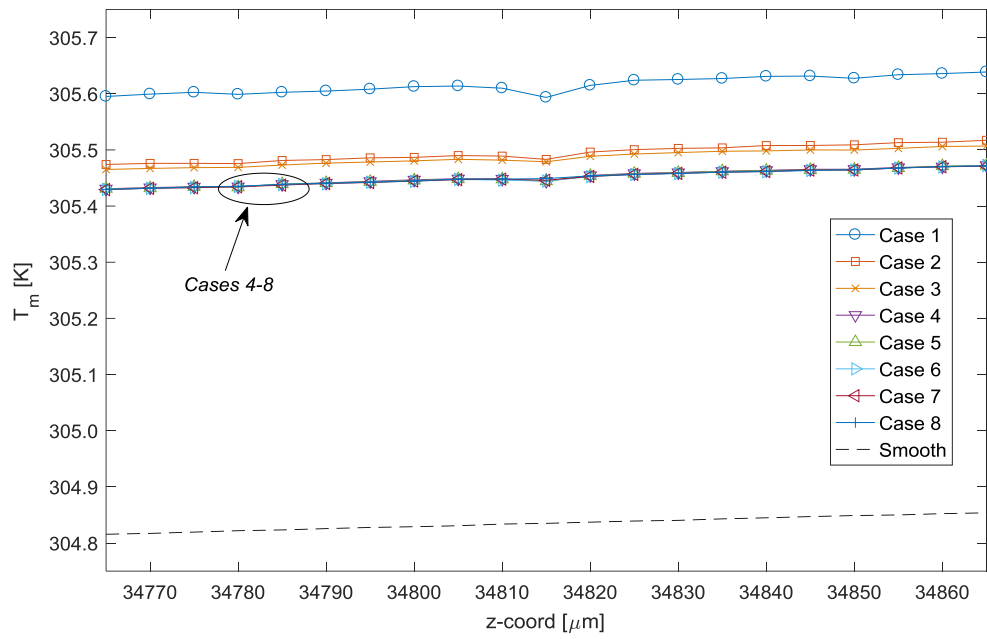


Figure 6.71: Fluid bulk mean temperature distribution for mesh independence test cases of RDC configuration over the last roughness element set.

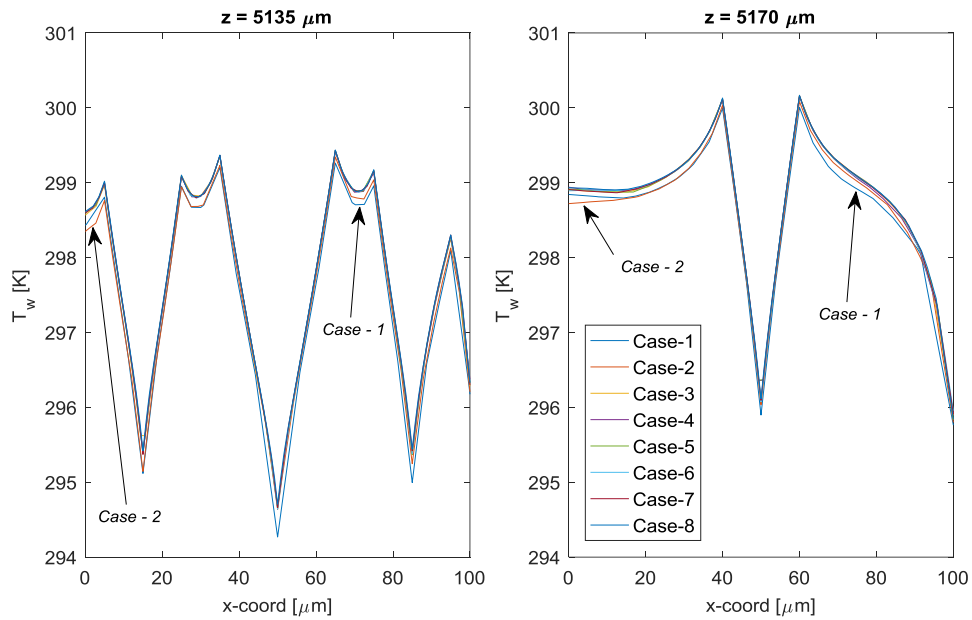


Figure 6.72: Wall temperature distributions for mesh independence test cases of RDC configuration along the  $x$ -direction at  $z = 5135 \mu\text{m}$  and  $z = 5170 \mu\text{m}$  locations.

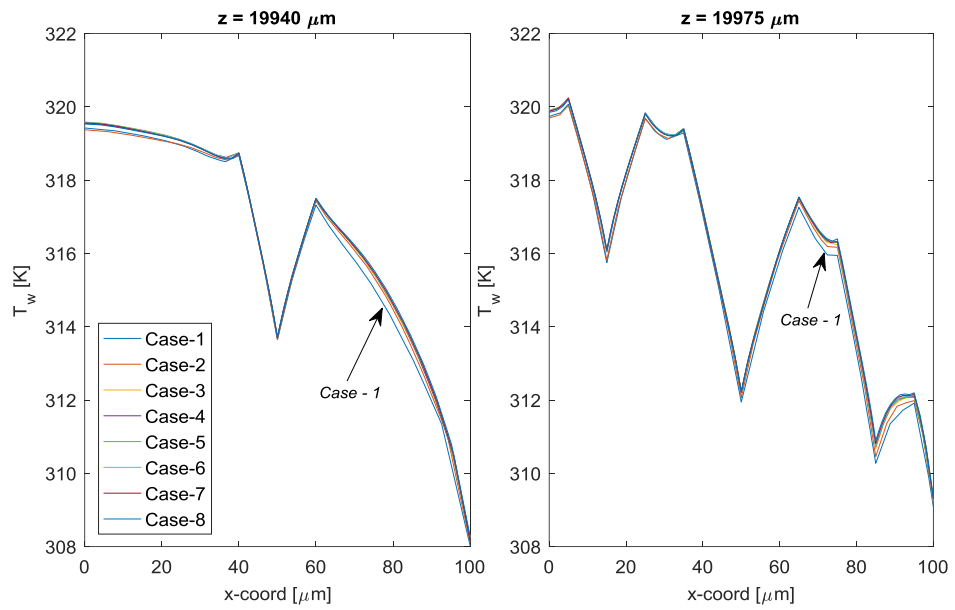


Figure 6.73: Wall temperature distributions for mesh independence test cases of RDC configuration along the  $x$ -direction at  $z = 19940 \mu\text{m}$  and  $z = 19975 \mu\text{m}$  locations.

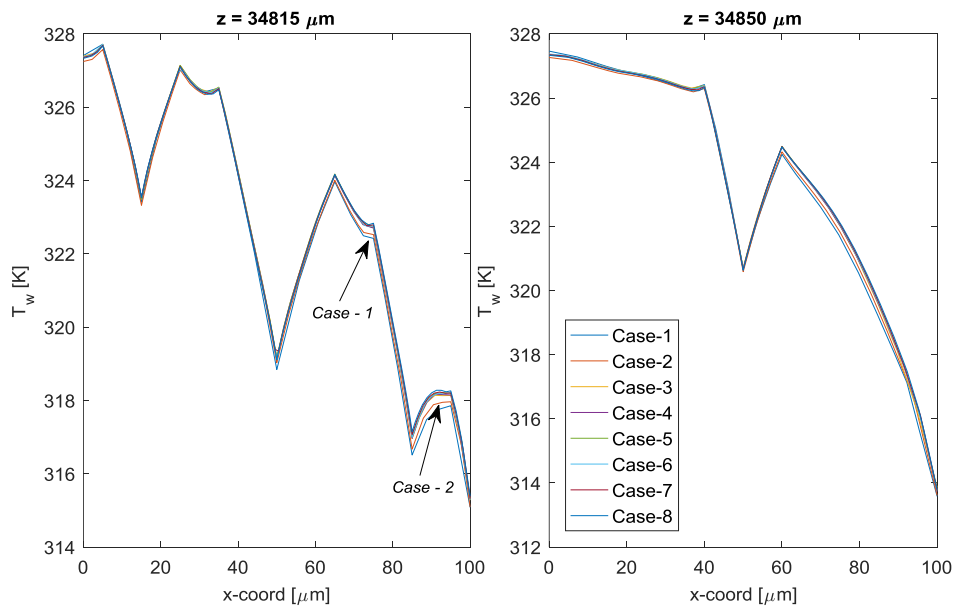


Figure 6.74: Wall temperature distributions for mesh independence test cases of RDC configuration along the  $x$ -direction at  $z = 34815 \mu\text{m}$  and  $z = 34850 \mu\text{m}$  locations.

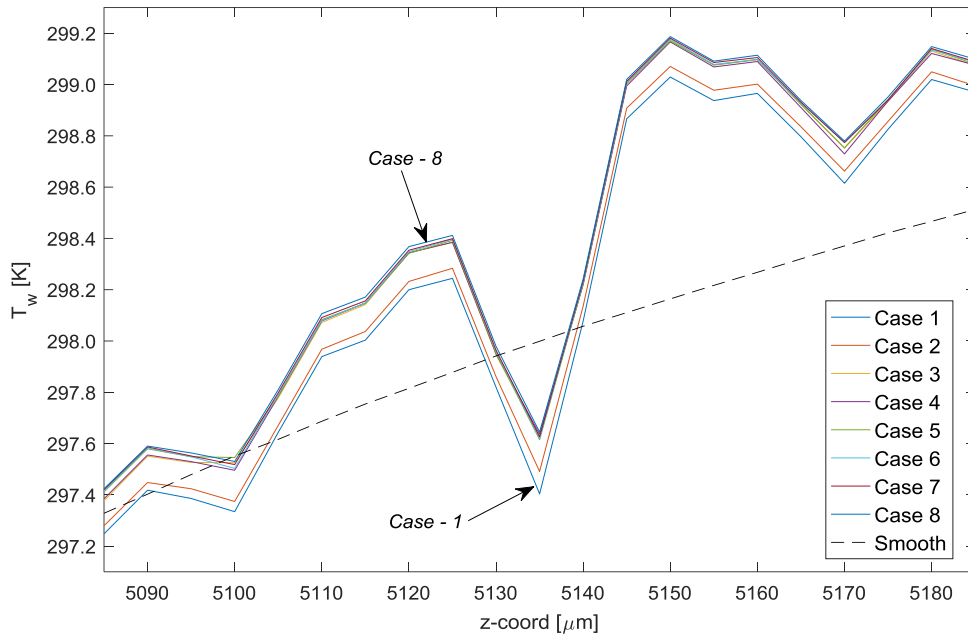


Figure 6.75: Wall mean temperature distribution for mesh independence test cases of RDC configuration around the first roughness element set.

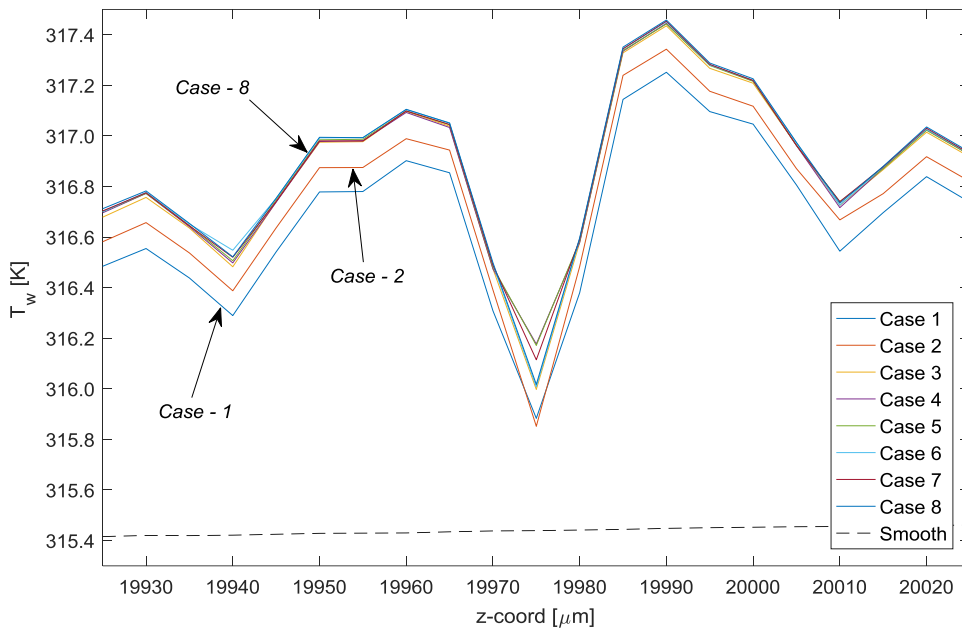


Figure 6.76: Wall mean temperature distribution for mesh independence test cases of RDC configuration around the middle roughness element set.

Local  $Nu$  distributions for the mesh independence test cases of RDC configuration are shown in Figs. (6.77), (6.78), and (6.79) around the first, middle, and the last roughness element sets, respectively. As the number of DOFs increases, difference between the results of each considered case reduces. With *Case-4*, difference becomes very small, and the results nearly coincide.

Considering the distribution of sought parameters and difference in calculated results with computational costs, mesh of *Case-6* is chosen for further simulations.

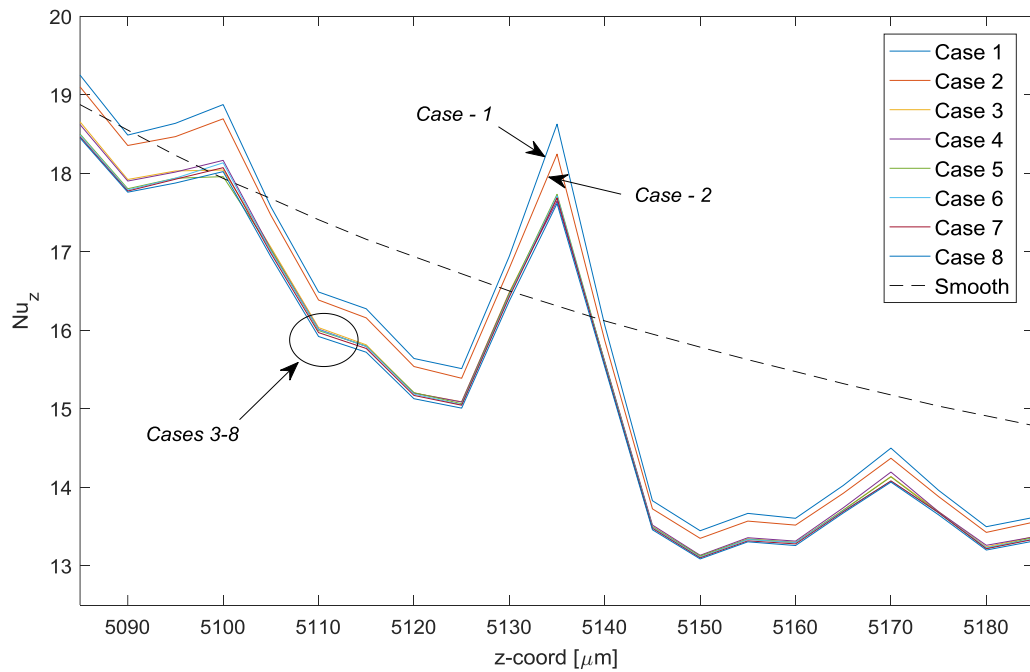


Figure 6.77: Local Nusselt distribution for mesh independence test cases of RDC configuration around the first roughness element set.

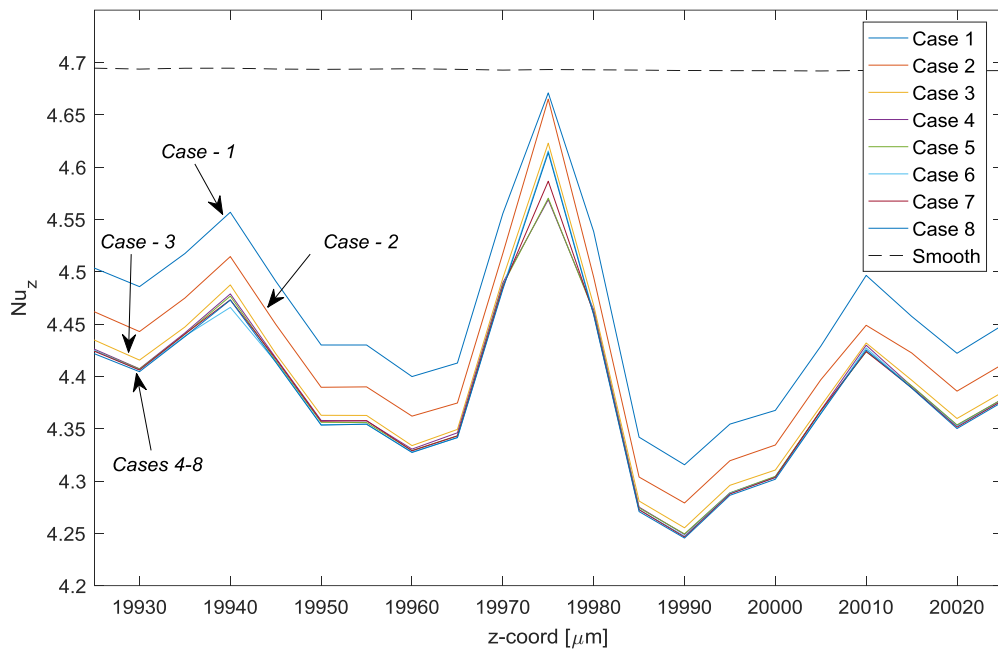


Figure 6.78: Local Nusselt distribution for mesh independence test cases of RDC configuration around the middle roughness element set.

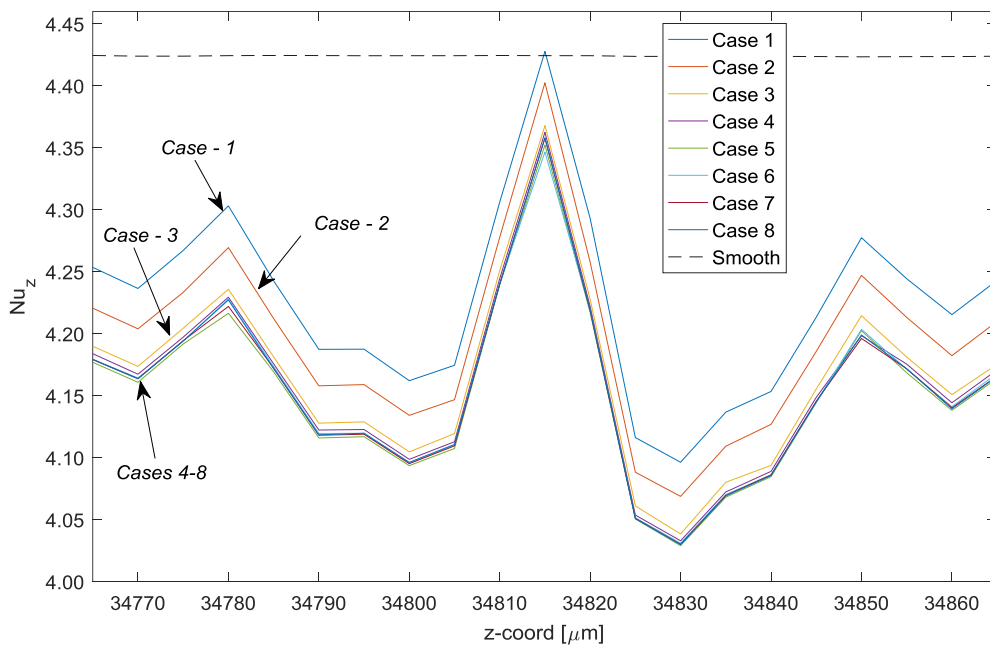


Figure 6.79: Local Nusselt distribution for mesh independence test cases of RDC configuration around the last roughness element set.

## 6.5.2 RESULTS AND DISCUSSIONS

Simulations for inlet mass fluxes of 200 kg/(m<sup>2</sup>s) to 1016 kg/(m<sup>2</sup>s) are conducted by using the mesh of *Case-6* (with 19.25x10<sup>6</sup> DOFs) and setting the relative tolerance to 10<sup>-6</sup>.

Velocity magnitude profiles for inlet mass flux of 1016 kg/(m<sup>2</sup>s) around the small side cones of the first and last roughness element sets of RDC configuration along the  $y$ -direction at  $x = 15 \mu\text{m}$  and  $x = 85 \mu\text{m}$  for various  $z$  locations are given in Fig. (6.80). Additionally, velocity magnitude profiles along the  $y$ -direction at  $x = 50 \mu\text{m}$  and various  $z$  locations, and velocity magnitude profiles along the  $x$ -direction at  $y = 5 \mu\text{m}$  and various  $z$  locations for the first and last roughness element set of RDC configuration are presented in Figs. (6.81) and (6.82), respectively. Change of velocity in various cross-sections that are 5  $\mu\text{m}$  apart from each other in the flow direction through the middle roughness element set is also shown in Fig. (6.83) for an inlet mass flux of 1016 kg/(m<sup>2</sup>s) as surface plots. Similar to previous geometries, velocity reduces around the cones and low velocity flow regions occur, and the flow is directed to the sides and upward. When the fluid leaves the patterned rough section, velocity profile gradually approaches the smooth profile.

Wall temperatures at  $z = 5,975 \mu\text{m}$  and  $z = 33,975 \mu\text{m}$  the along  $x$ -direction, from symmetry plane through the side of the microheater, for various inlet mass fluxes is shown in Figs. (6.84) and (6.85), respectively, with the corresponding smooth channel values. Wall temperatures become higher than the smooth channel values in locations where there is no cone due to increase in heating area and increase of low velocity regions around the conical elements, which reduces convective heat transfer and is more obvious at the base circumference of the cones. On the other hand, wall temperatures are slightly lower than the R2LC configuration, which could be the result of better mixing of the fluid due to pattern complexity. Similar to R1LC and R2LC configurations, wall temperatures reduce through the tip of the cones.

Wall temperature distribution in the  $x$ -direction around the bigger cone of middle roughness element set of RDC configuration for inlet mass fluxes of  $200 \text{ kg}/(\text{m}^2\text{s})$  and  $1016 \text{ kg}/(\text{m}^2\text{s})$  is shown in Fig. (6.86). In addition, change of temperature through various cross-sections that are  $5 \mu\text{m}$  apart from each other in the flow direction around the middle roughness element set is shown in Fig. (6.87) as surface plots for inlet mass flux of  $1016 \text{ kg}/(\text{m}^2\text{s})$ . Similar behavior of R1LC and R2LC configuration is also observed with RDC configuration. Wall temperature of the downstream sides of the cones is slightly higher than the flow facing sides of the cones due to reduced velocity zones and increased bulk fluid temperature.

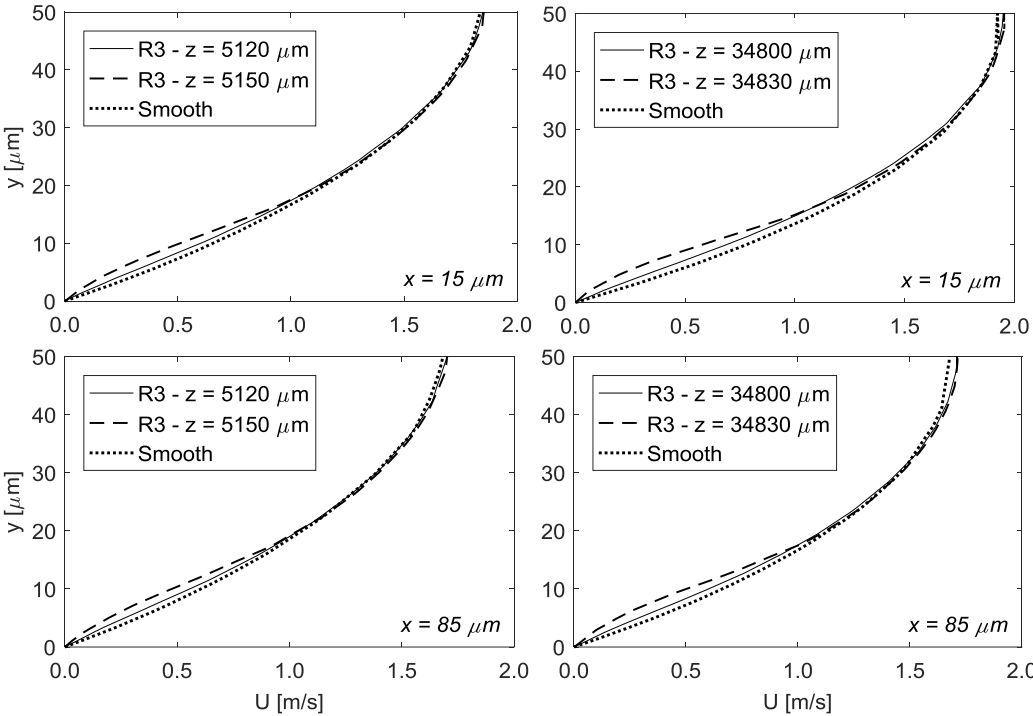


Figure 6.80: Velocity magnitude profiles around the small side cones of first and last roughness element set of RDC configuration along the  $y$ -direction at  $x = 15 \mu\text{m}$  and  $x = 85 \mu\text{m}$  for various  $z$  locations.

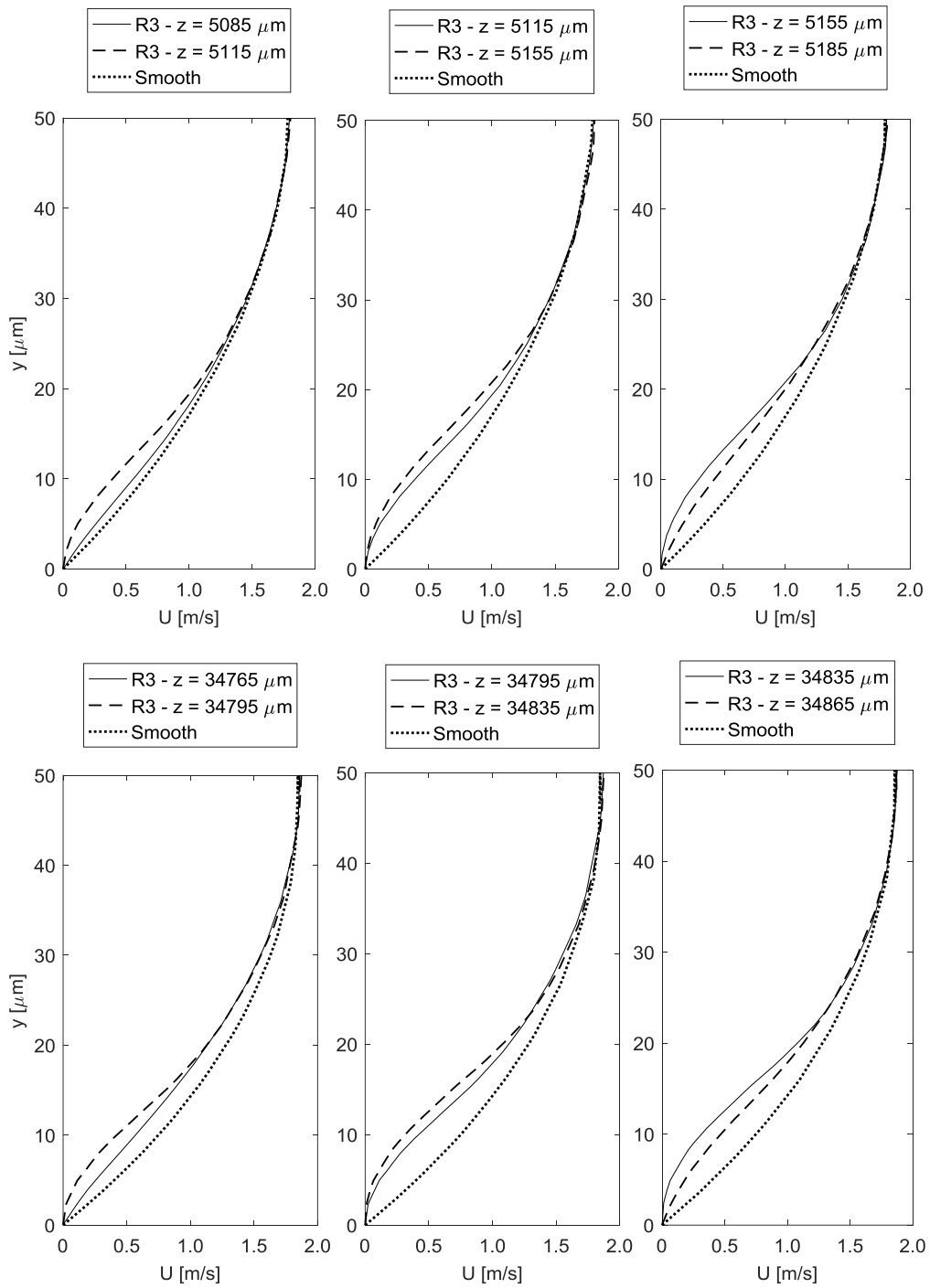


Figure 6.81: Velocity magnitude profiles along the y-direction at  $x = 50 \mu\text{m}$  and various  $z$  locations for the first and last roughness element set of RDC configuration.

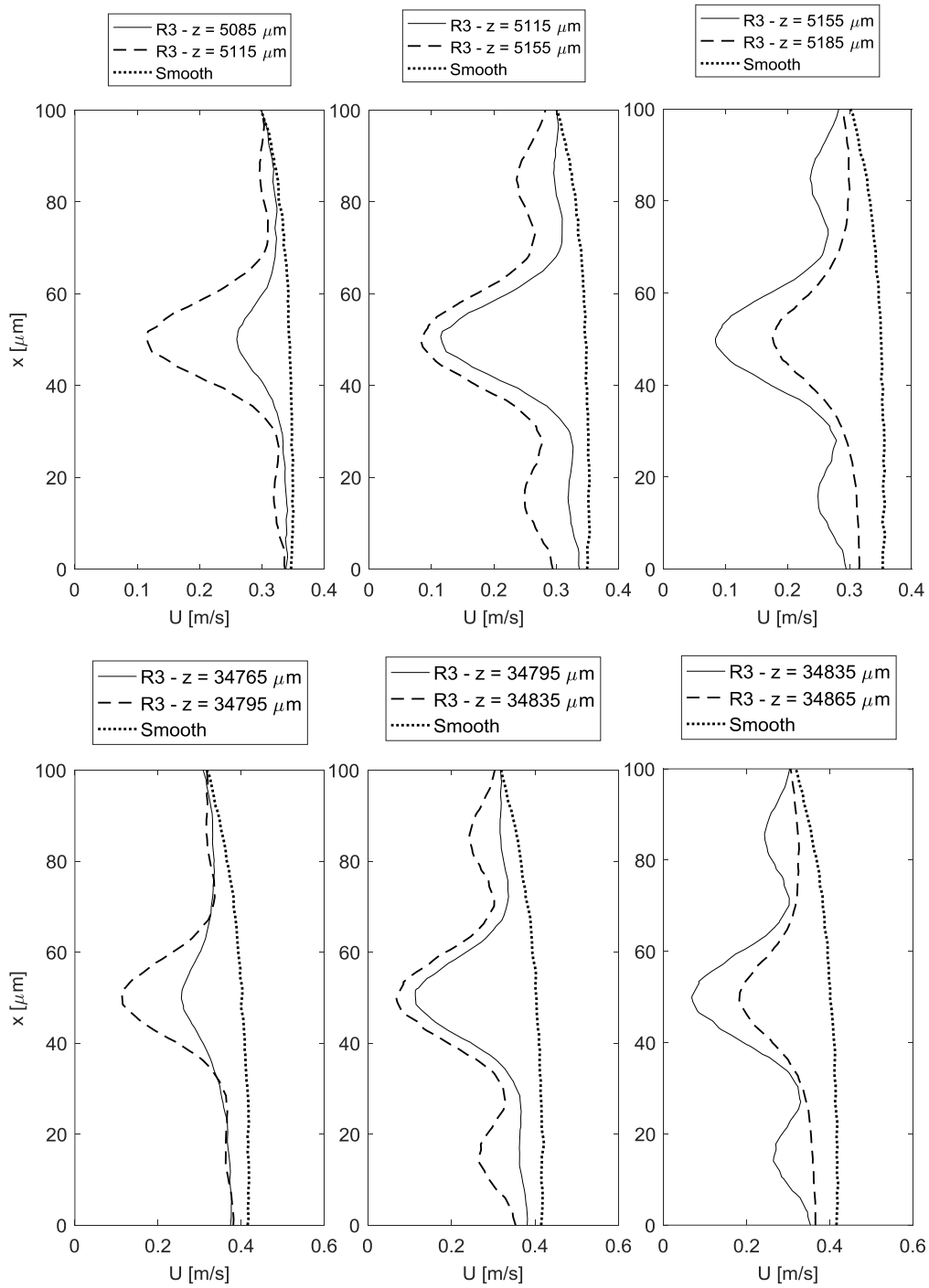


Figure 6.82: Velocity magnitude profiles along the  $x$ -direction at  $y = 5 \mu\text{m}$  and various  $z$  locations for the first and last roughness element set of RDC configuration.

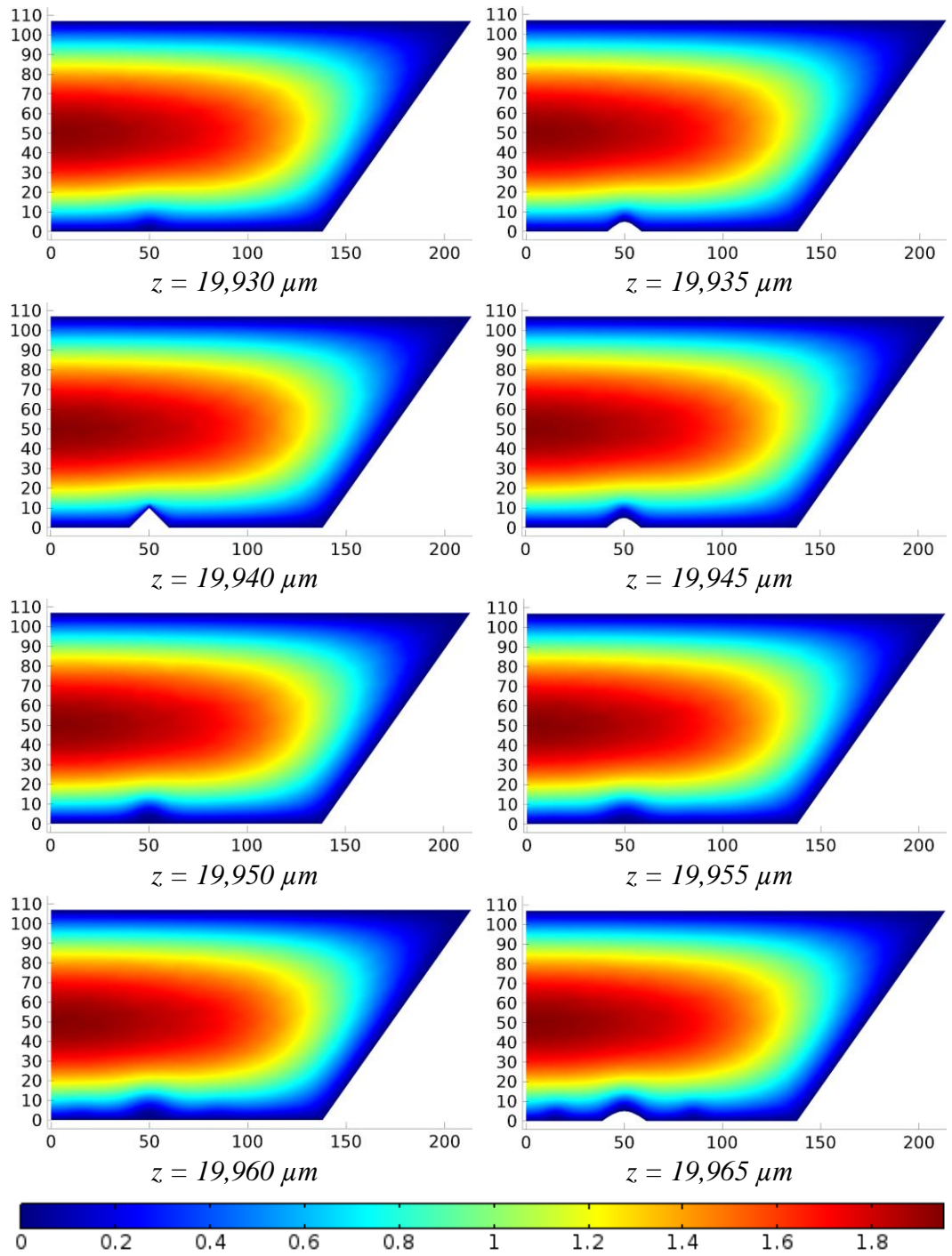


Figure 6.83: Velocity distribution at various cross-sections through the middle roughness element set of RDC configuration in the flow direction ( $G = 1016$  [kg/(m<sup>2</sup>s)]).

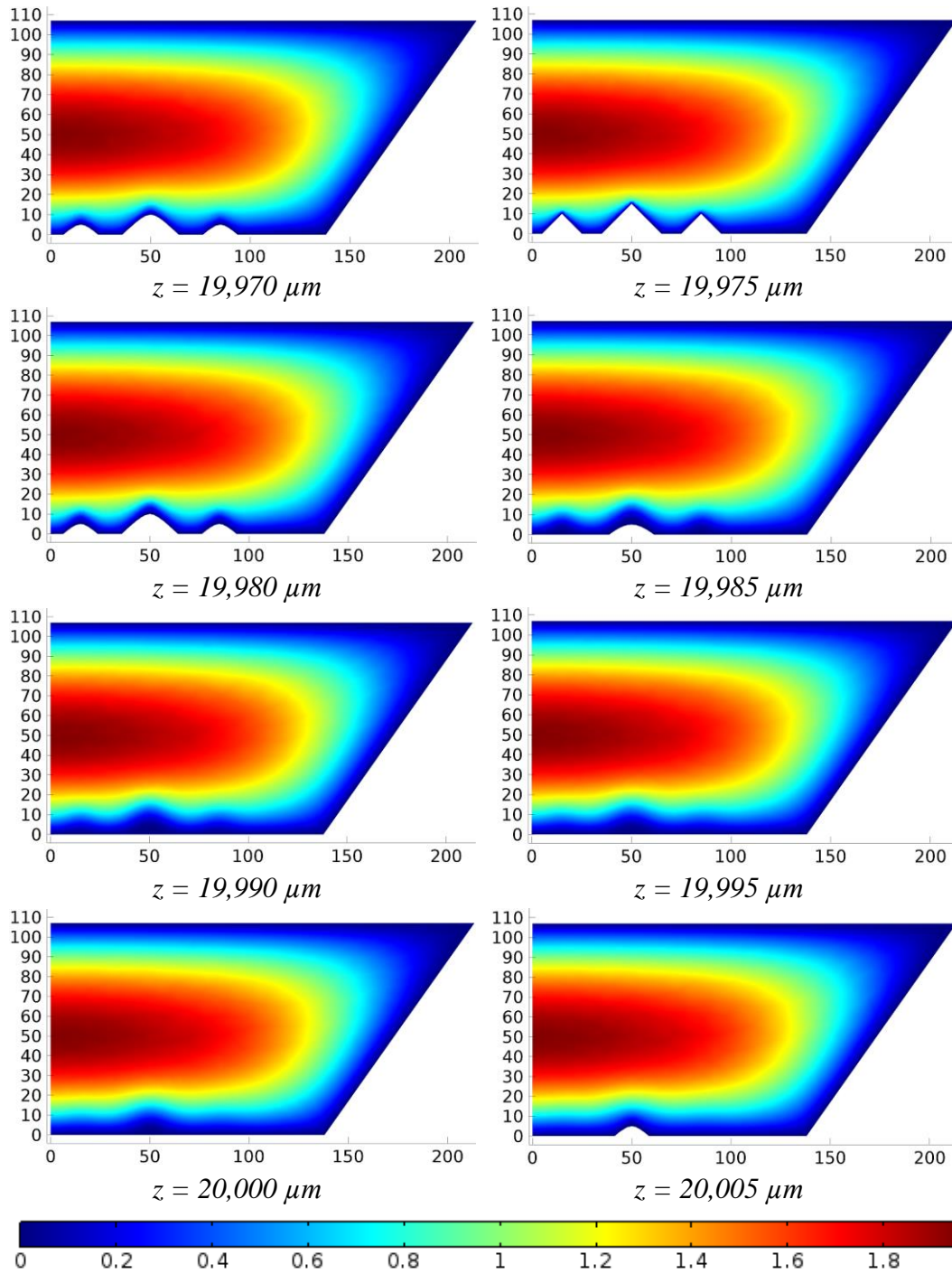


Figure 6.83: Velocity distribution at various cross-sections through the middle roughness element set of RDC configuration in the flow direction ( $G = 1016$  [kg/(m<sup>2</sup>s)]) (*Continued*).

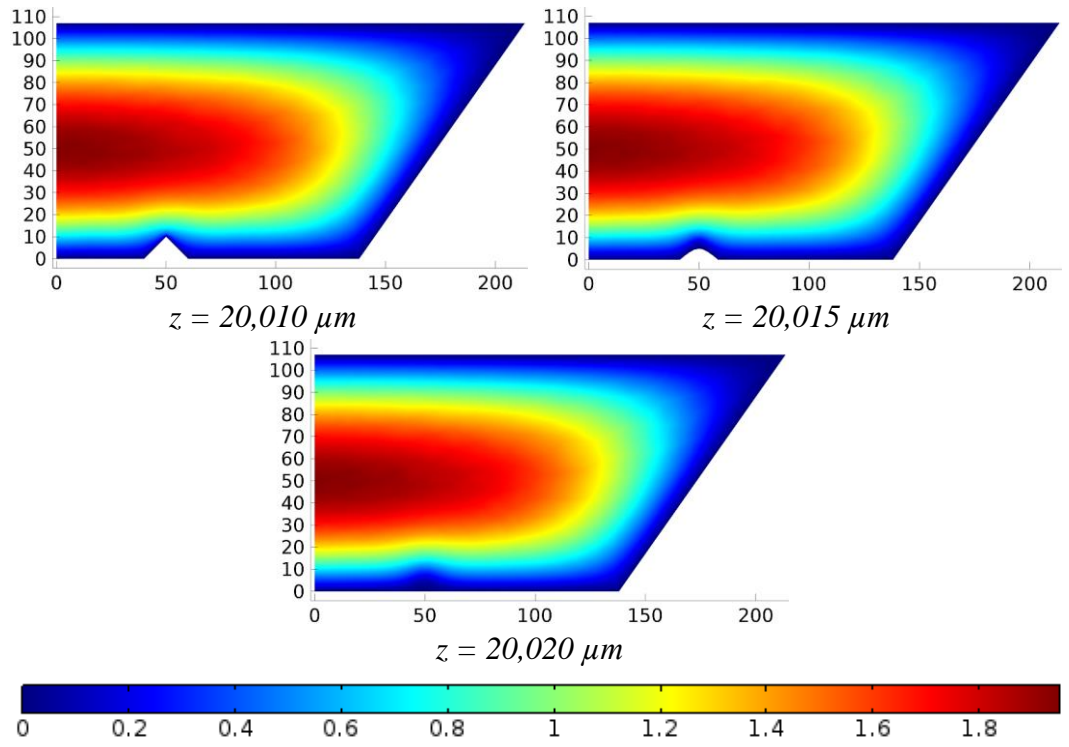


Figure 6.83: Velocity distribution at various cross-sections through the middle roughness element set of RDC configuration in the flow direction ( $G = 1016$   $[\text{kg}/(\text{m}^2\text{s})]$ ) (*Continued*).

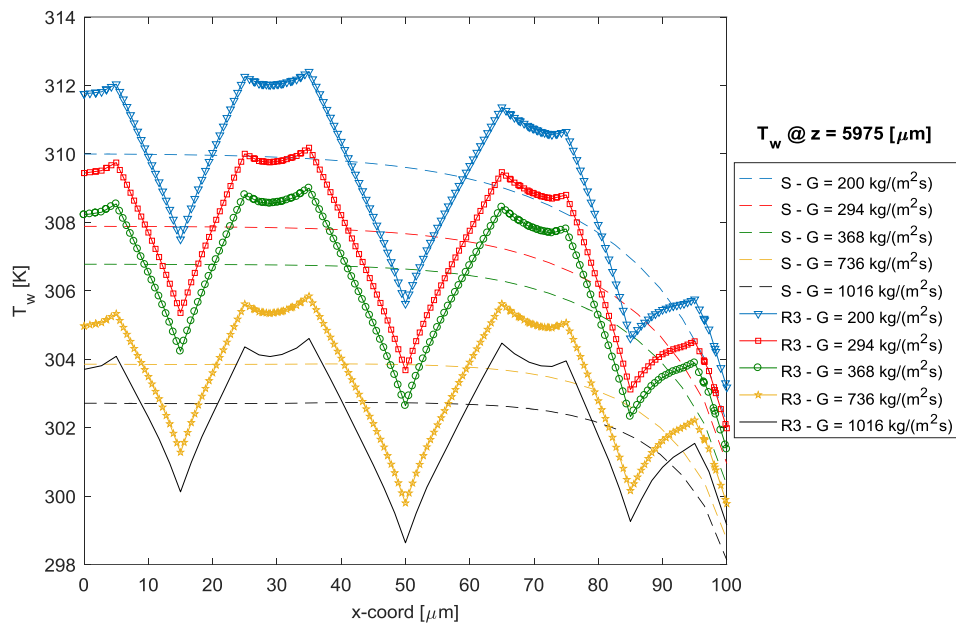


Figure 6.84: Wall temperature distribution at  $z = 5975 \text{ } \mu\text{m}$  location for various inlet mass fluxes for RDC configuration with corresponding smooth values.

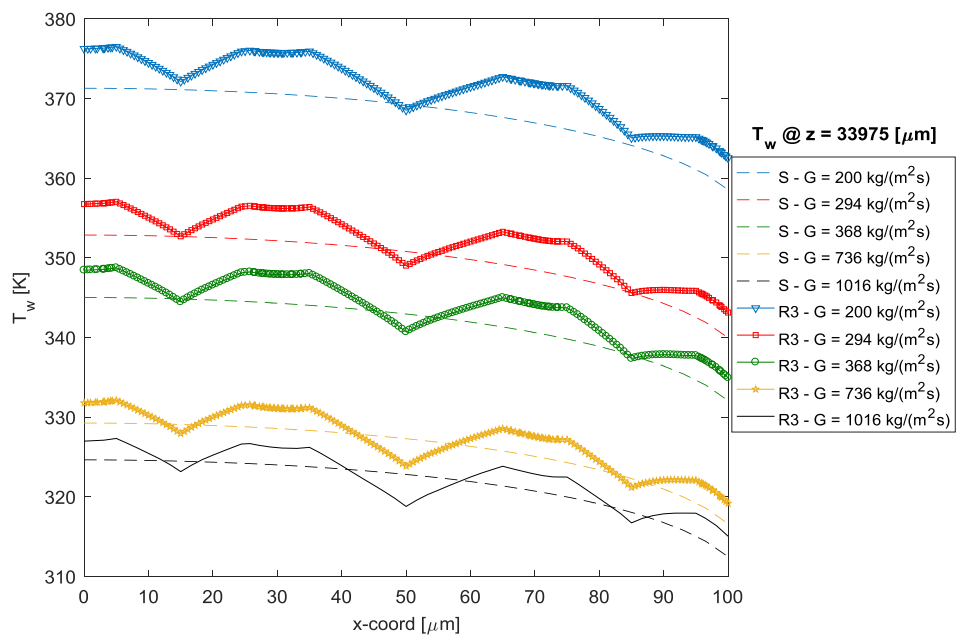


Figure 6.85: Wall temperature distribution at  $z = 33975 \text{ } \mu\text{m}$  location for various inlet mass fluxes for RDC configuration with corresponding smooth values.

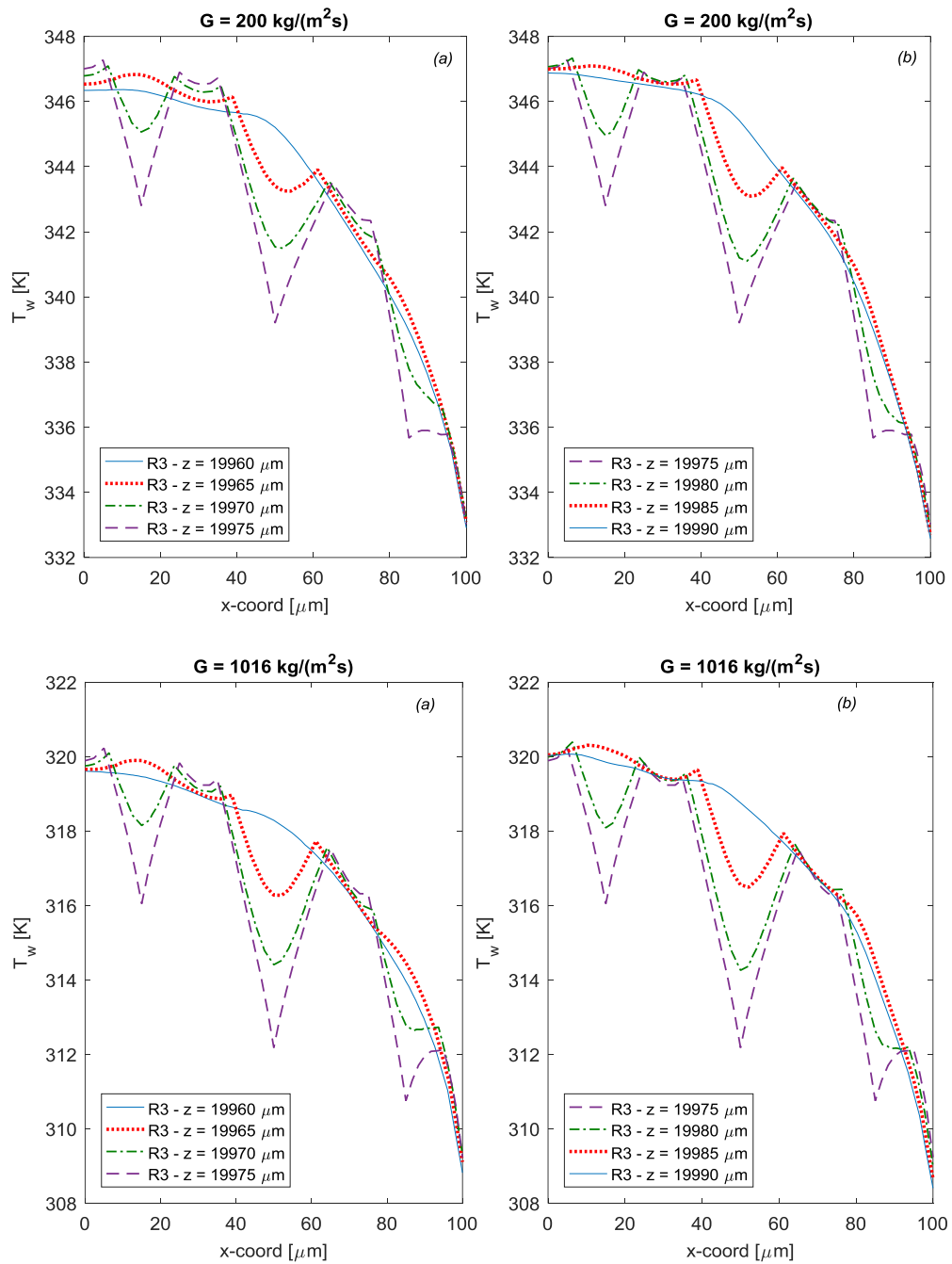


Figure 6.86: Wall temperature distribution around the bigger cone of middle roughness element set of RDC configuration for inlet mass fluxes of  $200 \text{ kg}/(\text{m}^2\text{s})$  and  $1016 \text{ kg}/(\text{m}^2\text{s})$  for (a) flow facing side of the cone, (b) back side of the cone.

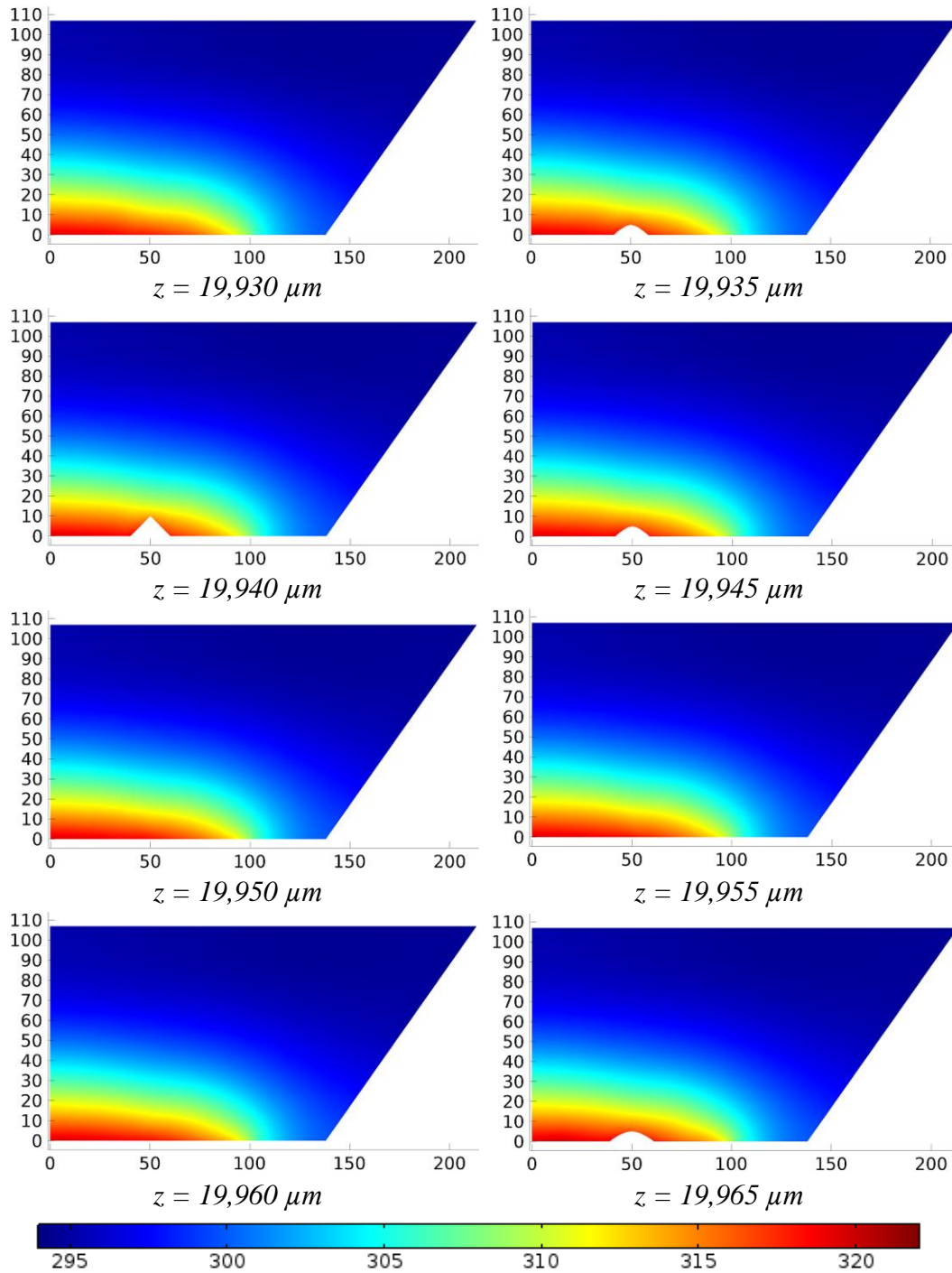


Figure 6.87: Temperature distribution at various cross-sections through the middle roughness element set of RDC configuration in the flow direction ( $G = 1016$  [kg/(m<sup>2</sup>s)]).

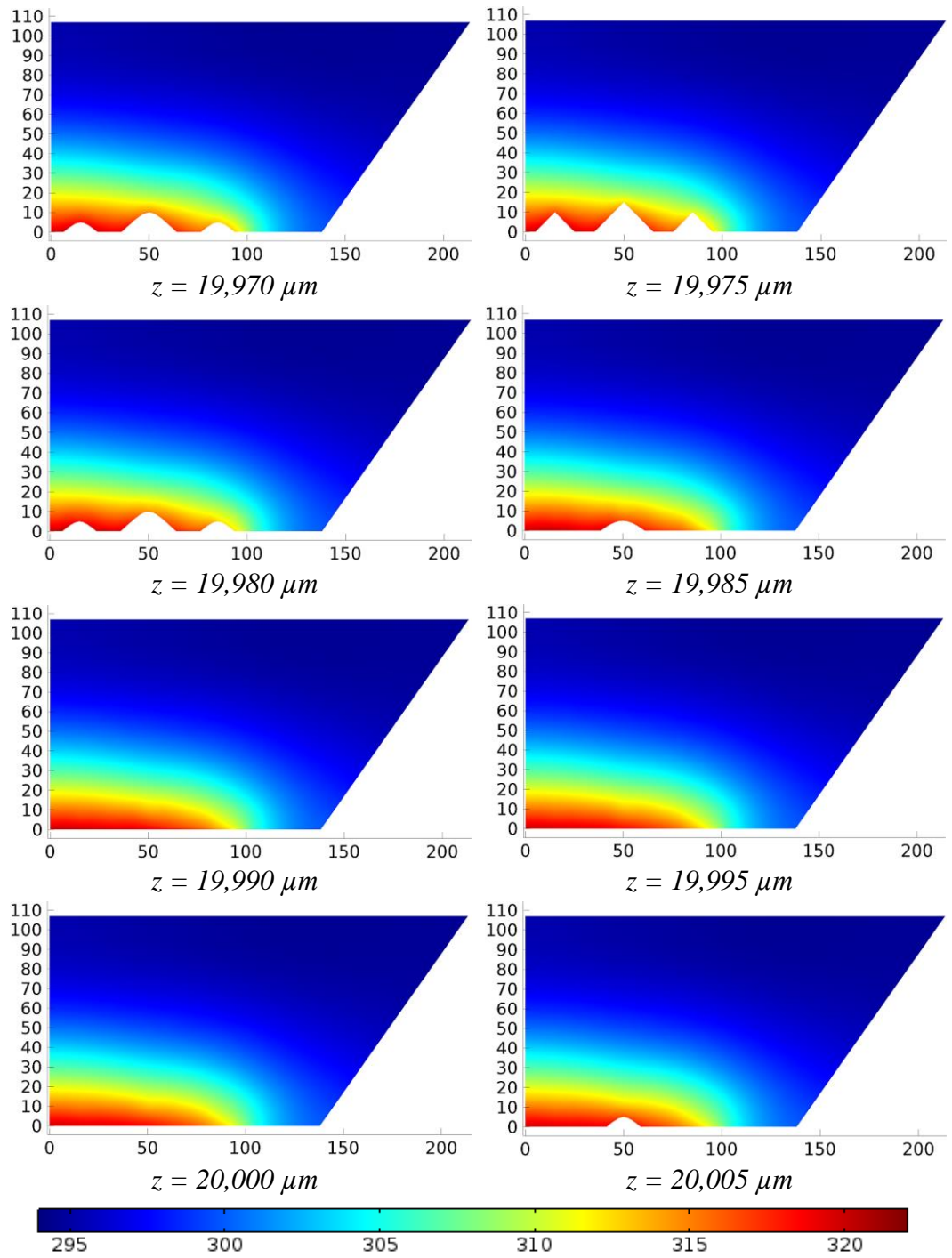


Figure 6.87: Temperature distribution at various cross-sections through the middle roughness element set of RDC configuration in the flow direction ( $G = 1016$   $[\text{kg}/(\text{m}^2\text{s})]$ ) (*Continued*).

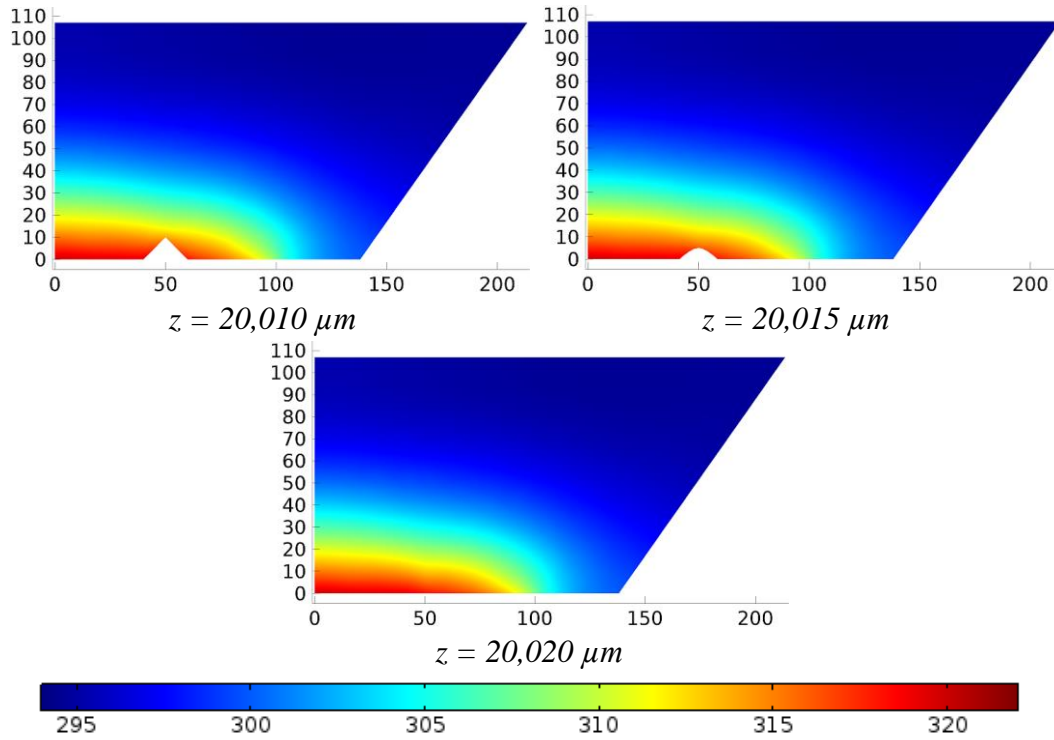


Figure 6.87: Temperature distribution at various cross-sections through the middle roughness element set of RDC configuration in the flow direction ( $G = 1016$   $[\text{kg}/(\text{m}^2\text{s})]$ ) (*Continued*).

Fluid bulk mean temperature distribution over the 7<sup>th</sup> roughness element set and over the last two roughness element sets of RDC configuration are given in Figs. (6.88) and (6.89), respectively. Bulk mean temperatures are calculated in cross-sectional planes  $1 \mu\text{m}$  apart over the roughness element sets, and  $5 \mu\text{m}$  apart between the roughness element sets in the  $z$ -direction. Calculated bulk mean temperatures are nearly the same as the ones obtained for R2LC configuration for each inlet mass flux.

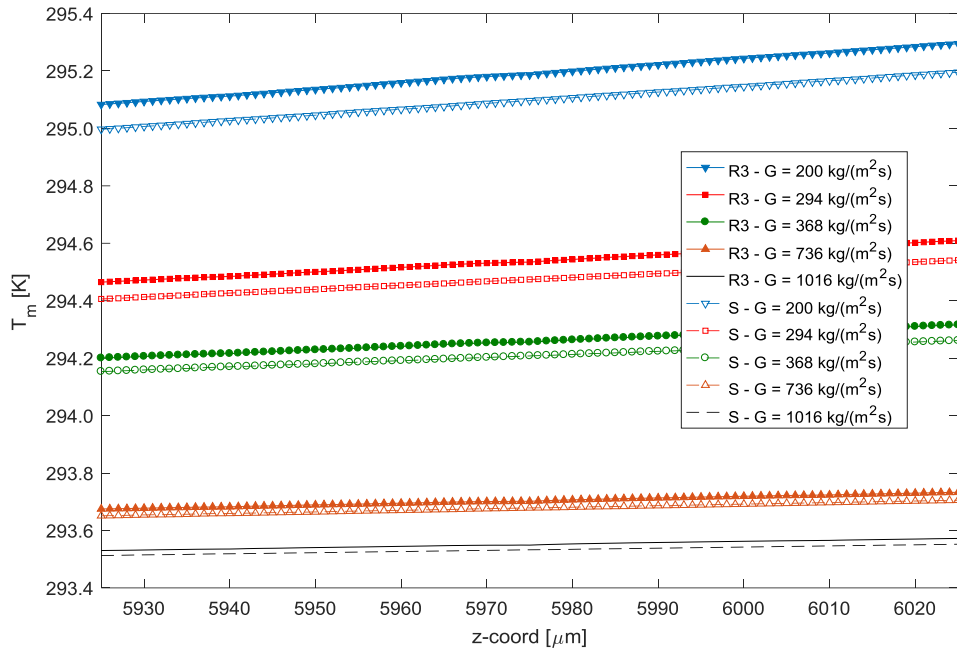


Figure 6.88: Fluid bulk mean temperature distribution over the 7<sup>th</sup> roughness element set of RDC configuration.

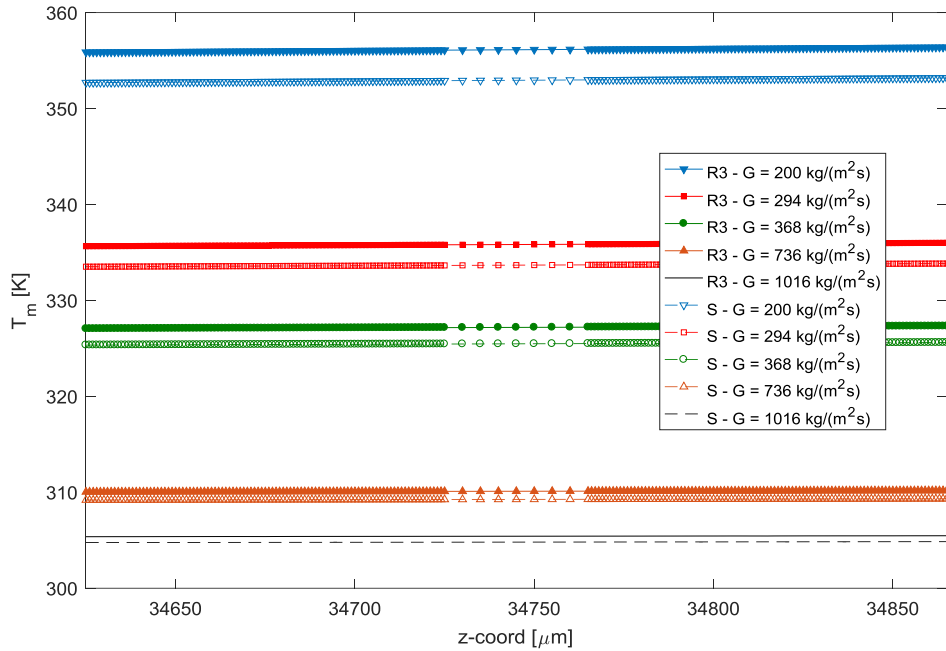


Figure 6.89: Fluid bulk mean temperature distribution over the last two roughness element sets of RDC configuration.

Wall mean temperatures are calculated 1  $\mu\text{m}$  apart over the roughness element sets, and 5  $\mu\text{m}$  apart between the roughness element sets in the  $z$ -direction. Wall mean temperature distribution over the first two, middle, and last two roughness element sets, around the middle roughness element, and over the last two roughness element sets of RDC configuration are shown in Figs. (6.90), (6.91), and (6.92) respectively. Except the inlet part, wall mean temperatures over the roughness element sets takes higher values than the corresponding smooth channel values. As the inlet mass flux increases, the difference between the smooth channel and RDC configuration wall mean temperatures reduces.

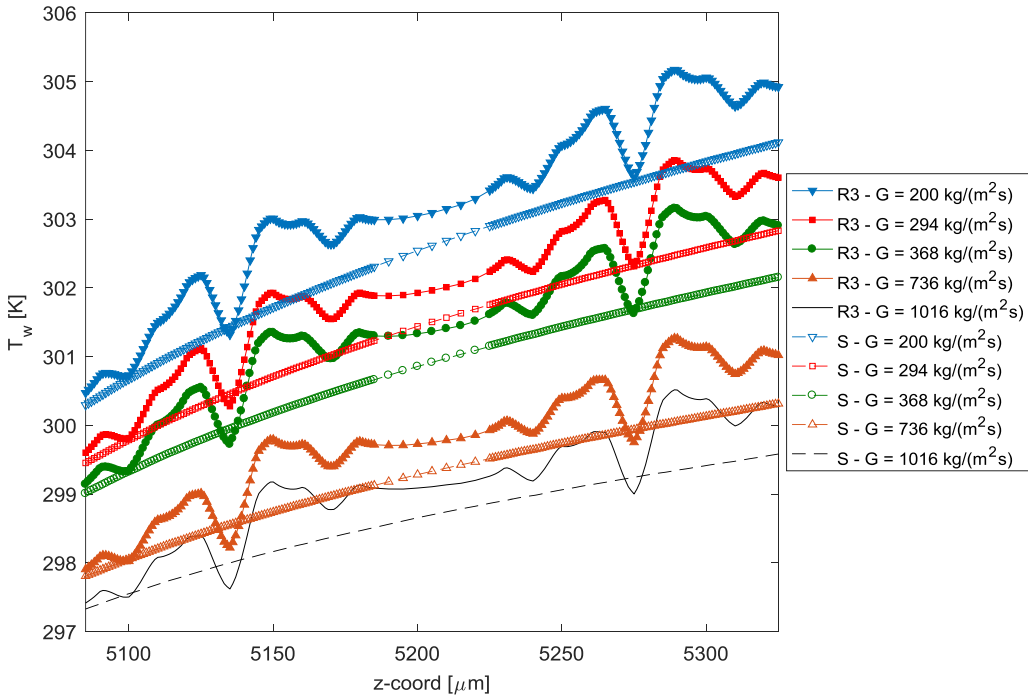


Figure 6.90: Wall mean temperature distribution over the first two roughness element sets of RDC configuration.

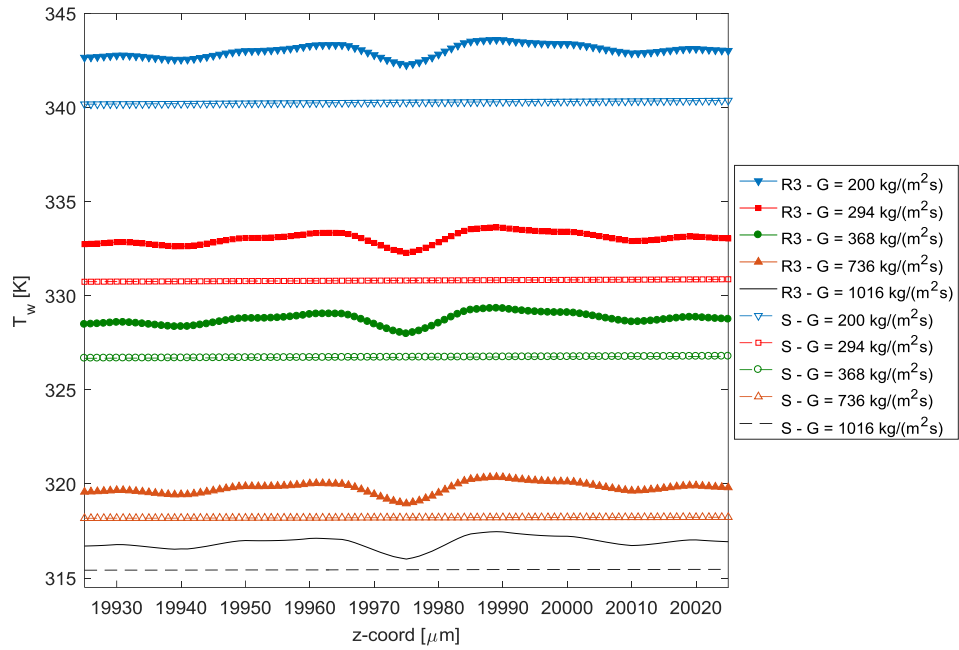


Figure 6.91: Wall mean temperature distribution over the middle roughness element set of RDC configuration.

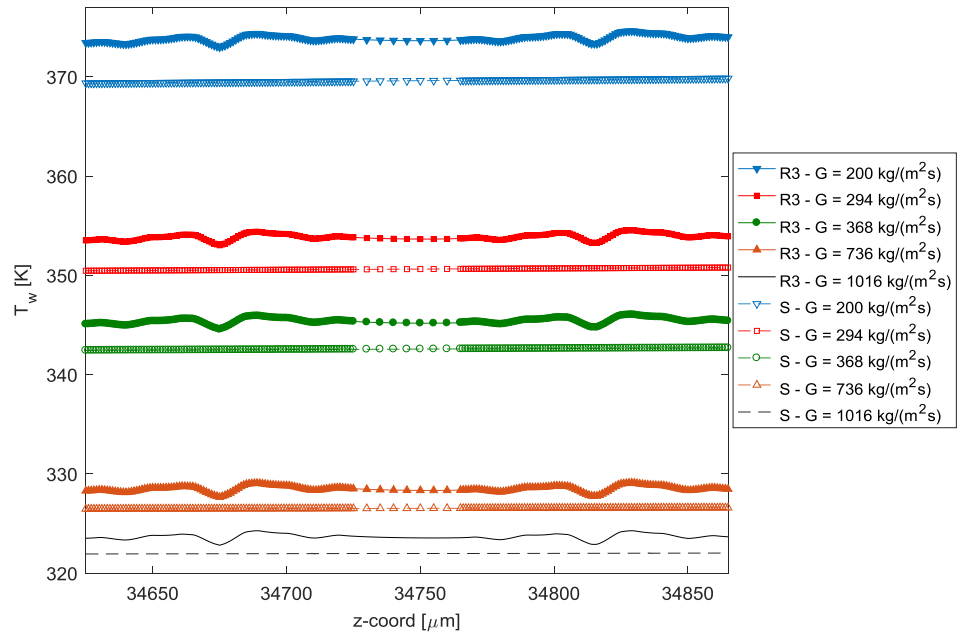


Figure 6.92: Wall mean temperature distribution over the last two roughness element sets of RDC configuration.

Surface temperature around the middle roughness element set of RDC configuration with arrows representing convective heat flux in the fluid at  $y = 5 \mu\text{m}$  plane and  $y = 7.5 \mu\text{m}$  plane is shown in Fig. (6.93) for an inlet mass flux of  $1016 \text{ kg}/(\text{m}^2\text{s})$ . In this figure, the sizes of the arrows are scaled to the magnitude of convective heat flux in the fluid. Similar to R1LC and R2LC configuration, convective heat flux is reduced at downstream sides of cones, which is more obvious between the middle line cones, due to reduced velocity regions.

Variation of density, viscosity, and thermal conductivity of water at  $x = 50 \mu\text{m}$  plane over the last two roughness element set of RDC configuration for  $G = 1016 \text{ kg}/(\text{m}^2\text{s})$  is shown in Fig. (6.94). As the temperature of the working fluid increases through the exit of heated section, thermophysical properties vary both in flow direction and channel height. Density and viscosity reduce while thermal conductivity increases around the conical elements, where the temperature is higher than the other parts of the channel.

Local Nusselt distribution over the first two, the middle, and the last two roughness element sets of RDC configuration are also shown in Figs. (6.95), (6.96), and (6.97) respectively. Similar to previous configurations, local  $Nu$  increases through the tip of the cones, especially over the bigger middle cone where the cone is subjected to relatively colder and faster flow. However, low velocity regions near the base circumference of the conical elements and increased thermal conductivity of the fluid with increased temperature difference between the wall and mean fluid temperature cause reduction in the local  $Nu$  significantly inside the roughness pattern.

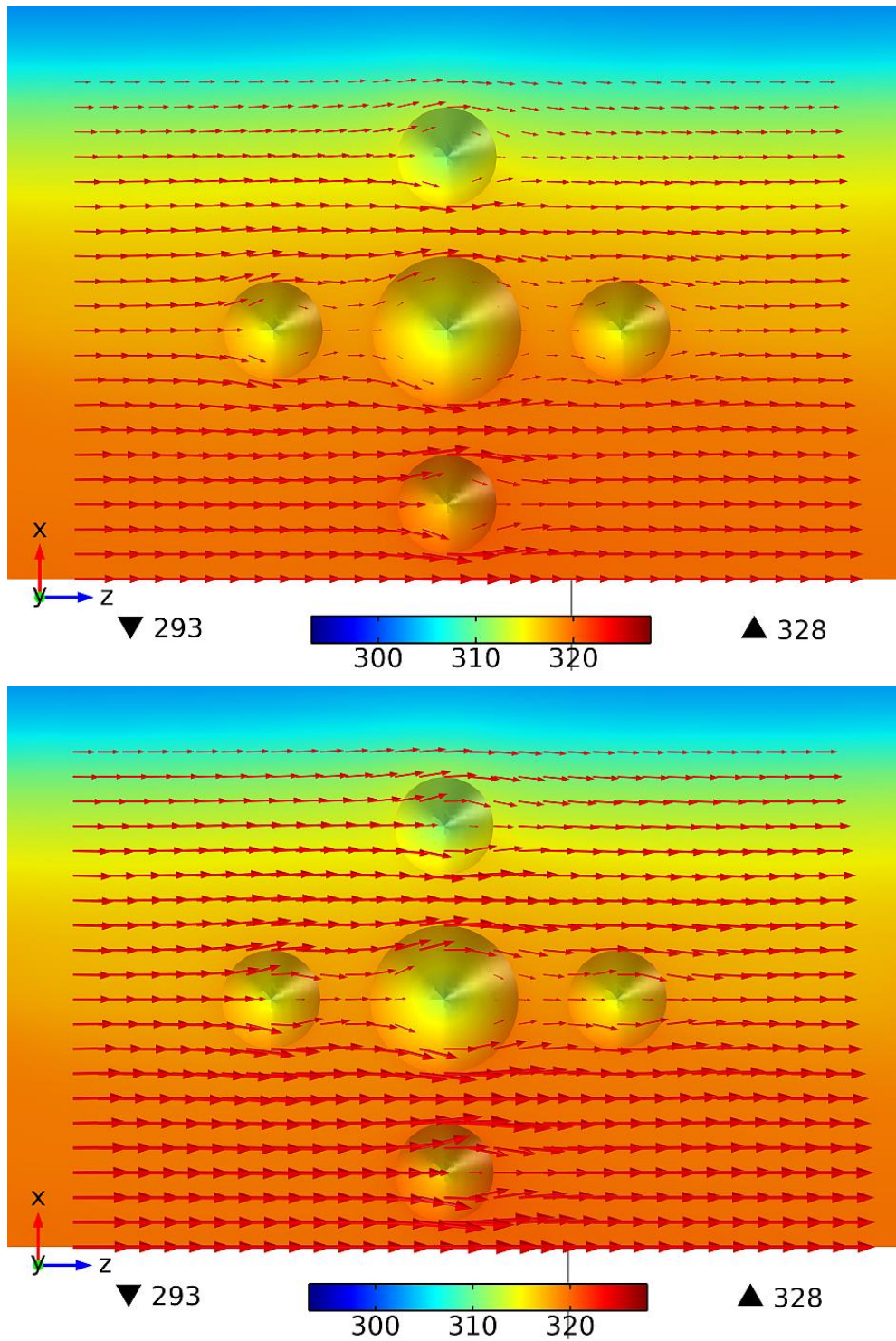


Figure 6.93: Surface temperature around the middle roughness element set of RDC configuration and convective heat flux in the fluid at  $y = 5 \mu\text{m}$  plane (top) and  $y = 7.5 \mu\text{m}$  plane (bottom) for  $G = 1016 \text{ kg}/(\text{m}^2\text{s})$ .

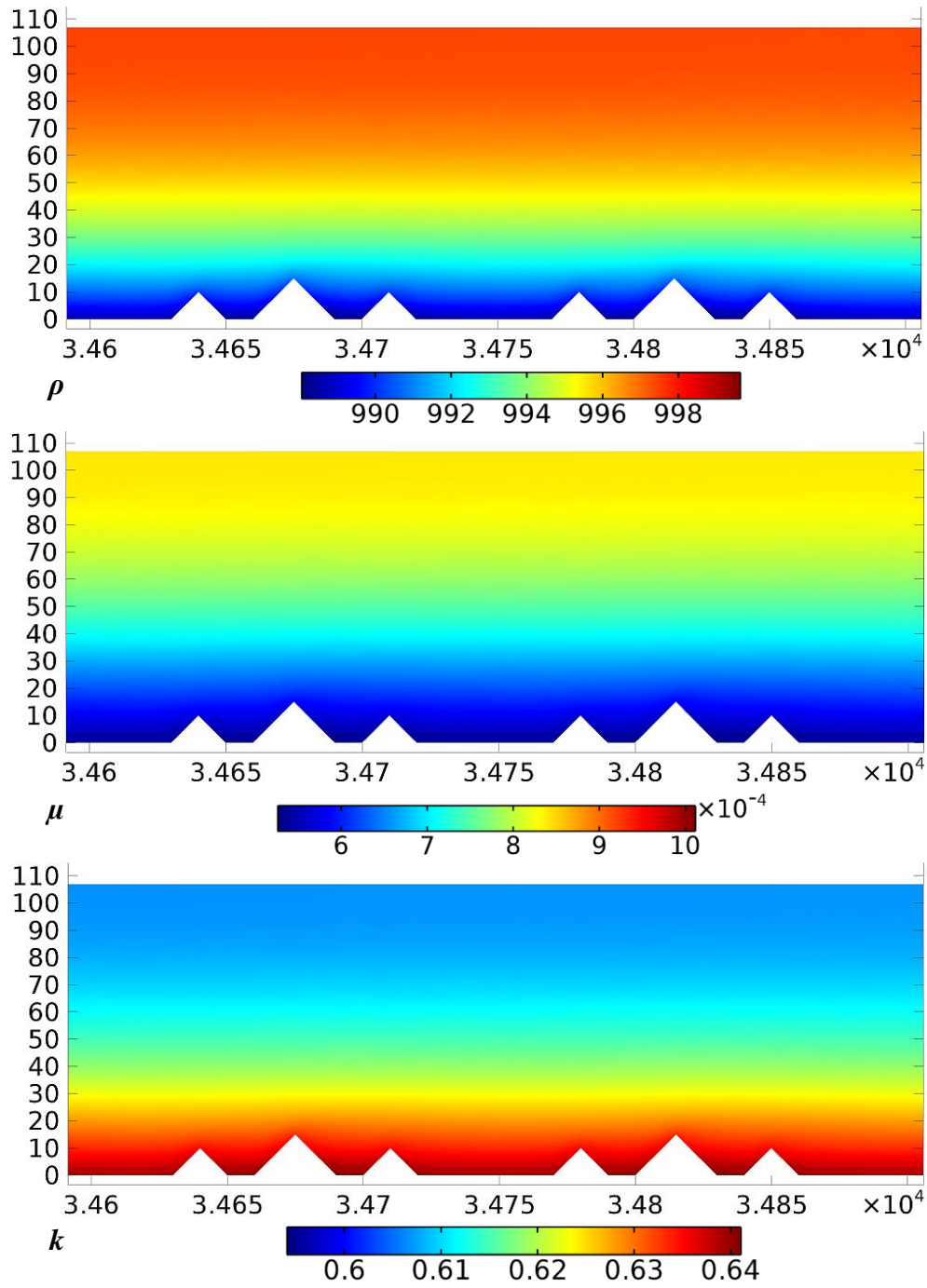


Figure 6.94: Variation of  $\rho$ ,  $\mu$ , and  $k$  over the last two roughness element set of RDC configuration at  $x = 50 \mu\text{m}$  plane for  $G = 1016 \text{ kg}/(\text{m}^2\text{s})$ .

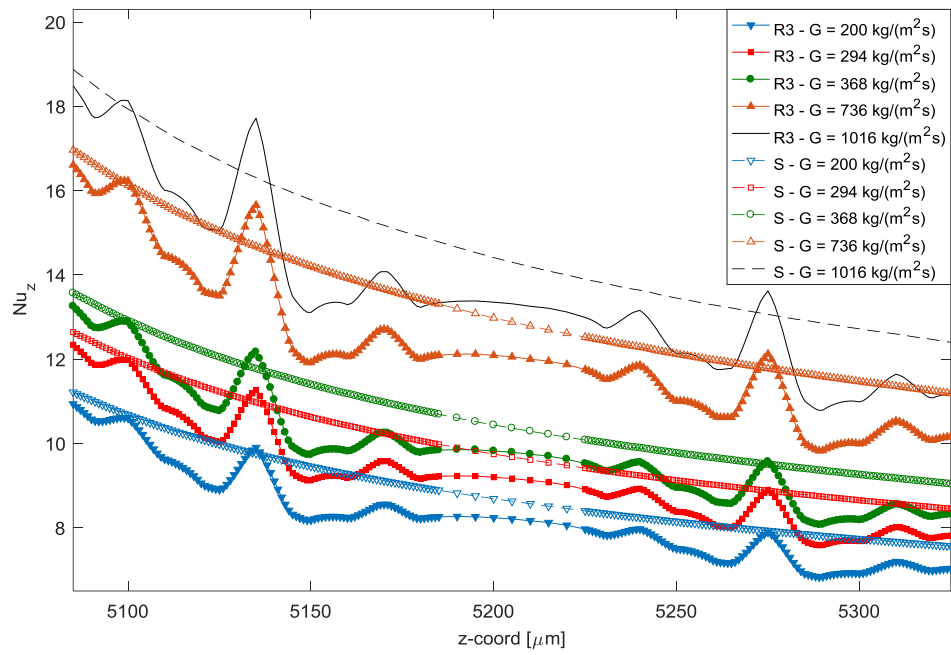


Figure 6.95: Local Nusselt distribution over the first two roughness element sets of RDC configuration.

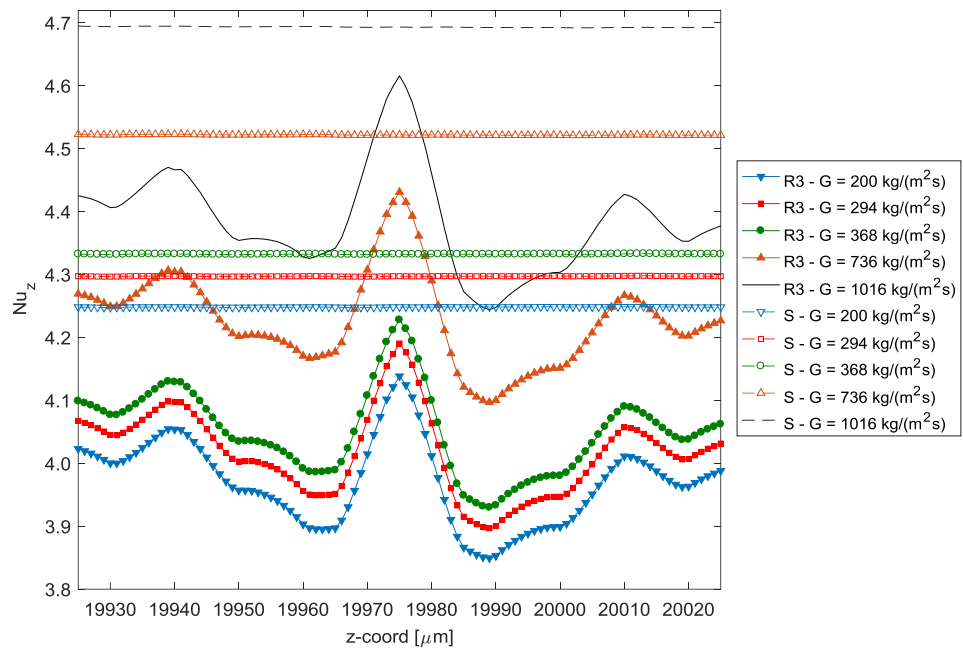


Figure 6.96: Local Nusselt distribution over the middle roughness element set of RDC configuration

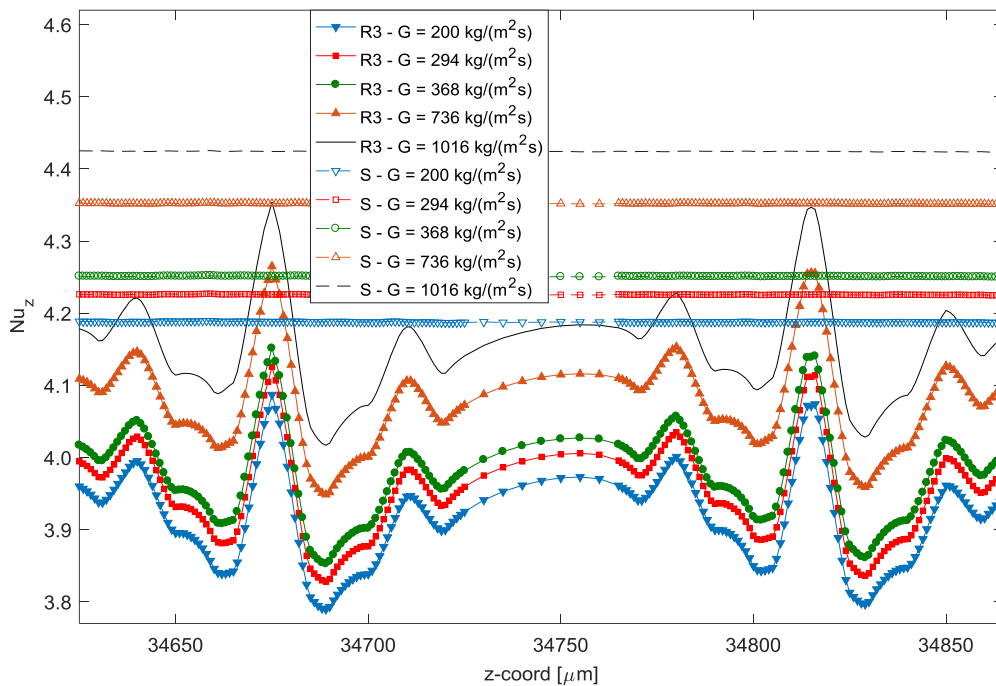


Figure 6.97: Local Nusselt distribution over the last two roughness element sets of RDC configuration.

## 6.6 COMPARISONS OF SMOOTH AND ROUGH CHANNELS

Up to now results from the simulations of one smooth and three rough channels with five different inlet mass fluxes are compared by means of local values. In this section, mean and global values between the inlet and exit of the heated section for the mentioned cases are compared.

Pressure drop between the inlet and exit of the heated section of smooth and rough channels for various inlet mass fluxes is shown in Fig. (6.98). Pressure drop remains nearly same for the smooth and tested rough patterns for lower inlet mass fluxes. As the inlet mass flux increases, pressure drop in the rough microchannels differs slightly compared to the smooth microchannel. In theory, R1LC and R2LC

configurations both have the same relative roughness values of 9.68%. With respect to the smooth channel, R1LC configuration caused about 1% increase in pressure drop for the upper limit of inlet mass flux of this study. However, when the number of conical elements is doubled but the relative roughness is kept constant, like in R2LC configuration, pressure drop increases about 3.2% for the same inlet mass flux with respect to smooth channel. In addition to that, RDC configuration has a more complex pattern than the other cases with slightly lower relative roughness, and caused slightly lower increase in surface area than R2LC with respect to the smooth channel, but yielded slightly greater pressure drop than R2LC configuration. This indicates that, considering the relative roughness height alone to characterize the pressure drop is not sufficient. Other parameters, such as density of the roughness elements and their configuration should also be considered.

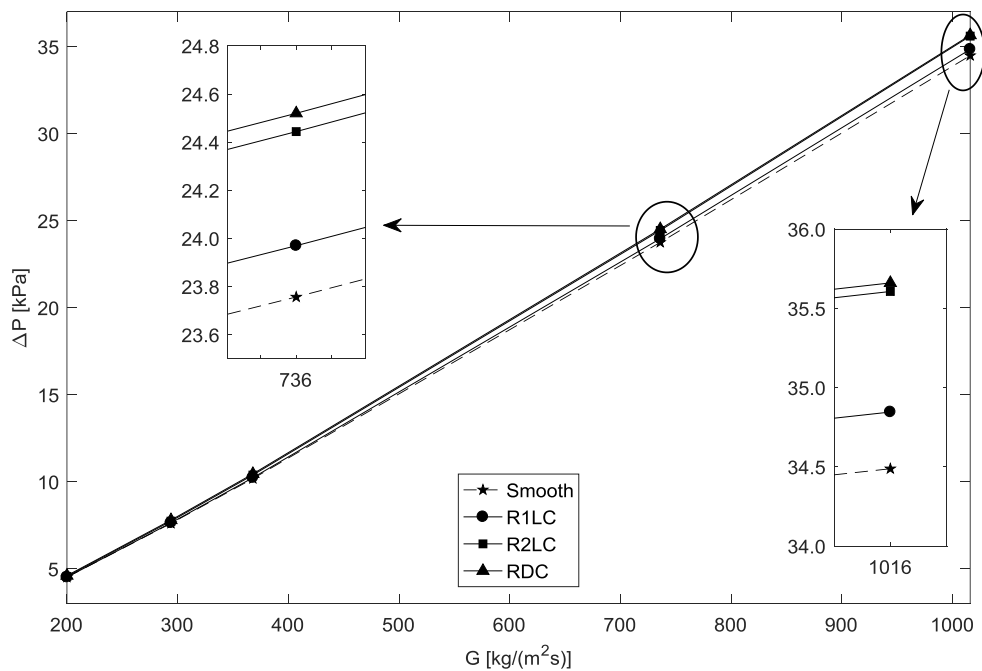


Figure 6.98: Pressure drop between the inlet and exit of heated section of smooth and rough channels for various inlet mass fluxes.

Temperature difference between the inlet and outlet of heated section of smooth and rough channels for various inlet mass fluxes is shown in Fig. (6.99). Ranking of the roughness configurations in temperature difference between the inlet and exit of the heated section follows the ranking of increase in surface area of the configurations. R2LC configuration yielded the maximum temperature difference increase of 7.1% to 9.1% compared to the smooth channel with 5.84% surface area increase, followed by RDC configuration and R1LC configuration, which reduces as the inlet mass flux increases. Temperature difference between the inlet and exit of the heated section increased between 5.3% and 6.1% with respect to the smooth channel for RDC configuration with 5.77% increased surface area. For the R1LC configuration, increase in temperature difference is between 3.9% and 5.6% compared to smooth channel with 2.92% surface area increase.

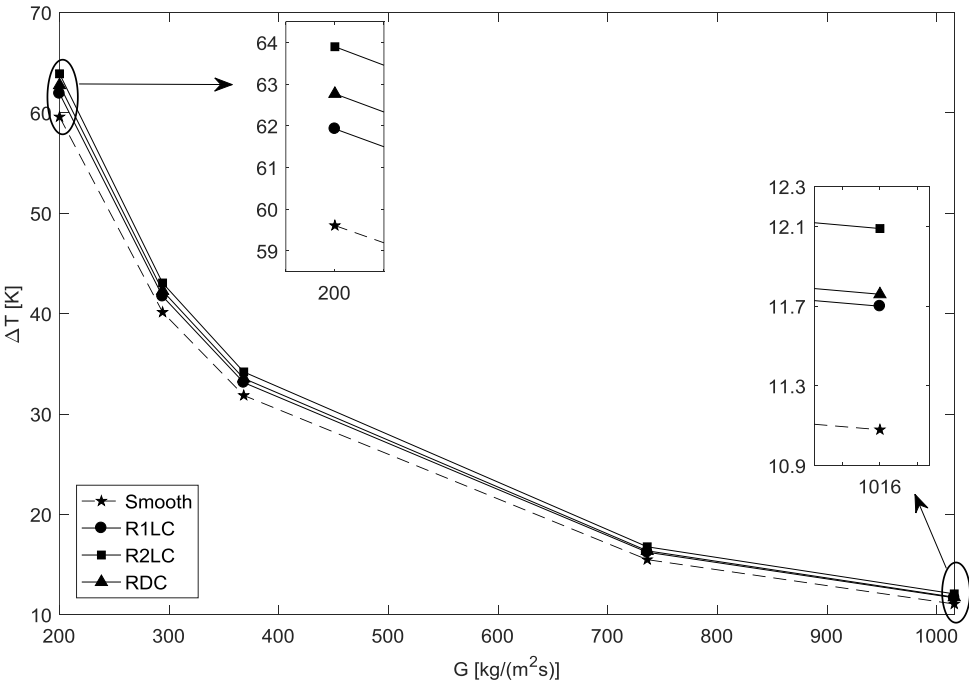


Figure 6.99: Temperature difference between the inlet and outlet of heated section of smooth and rough channels for various inlet mass fluxes.

Increase in mean temperature from inlet to exit also causes increase in thermal conductivity and reduction in viscosity and density since thermophysical properties in simulations are considered as temperature dependent. These changes in thermophysical properties, especially the reduction in viscosity, which is more obvious for low inlet mass fluxes, also cause increase in  $Re$  value through the outlet. On the other hand, increase in mean velocity, which is squared in the calculation of friction factor, overcomes the increasing effects of increased pressure drop and reduced density in friction factor calculation, and cause reduction in friction factor as the inlet mass flux increases. This reduction in friction factor is more effective than the increase in mean  $Re$ , which in the end results in lower  $Po$  values as the inlet mass flux increases, which is shown in Fig. (6.100). Similar to temperature difference comparisons, R2LC configuration yields higher friction factor and  $Po$  values than the RDC configuration.

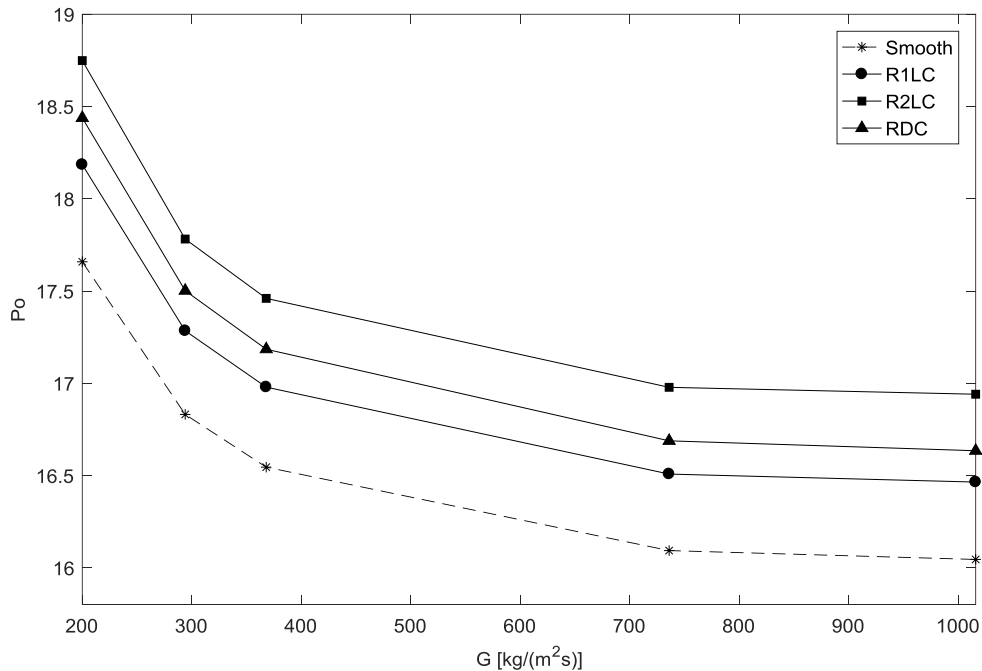


Figure 6.100: Change in  $Po$  value with inlet mass flux in smooth and rough channels.

Calculated mean values of  $Re$  and  $f$ , corresponding  $Po$  values, and temperature and pressure differences between the inlet and exit of heated section are summarized in Table – (6.6) for each microchannel geometry with percentage differences compared to smooth channel values.

Table 6.6: Mean  $Re$ ,  $f$ , and  $Po$  values with temperature and pressure difference between the inlet and exit of the heated section for each geometry.

<b>Smooth</b>										
$G$ [kg/(m <sup>2</sup> s)]	$Re_{in}$	$Re_m$	$f_m$	$Po$	$\Delta p$ [kPa]	$\Delta T$ [K]				
200	31	54.52	0.323885	17.659	4.52	59.61				
294	45	67.03	0.251097	16.831	7.62	40.15				
368	57	77.36	0.213872	16.546	10.19	31.86				
736	114	129.63	0.124151	16.094	23.76	15.50				
1016	157	169.91	0.094437	16.046	34.49	11.08				
<b>RILC</b>							Increase in Surface Area (wrt. Smooth) :			2.92 %
$G$ [kg/(m <sup>2</sup> s)]	$Re_{in}$	$Re_m$	$f_m$	$Po$	(S) <sub>Po</sub> %	$\Delta p$ [kPa]	(S) <sub><math>\Delta p</math></sub> %	$\Delta T$ [K]	(S) <sub><math>\Delta T</math></sub> %	
200	31	55.22	0.329292	18.185	2.980	4.52	0.044	61.93	3.892	
294	45	67.51	0.256026	17.285	2.692	7.64	0.355	41.73	3.935	
368	57	77.75	0.218398	16.979	2.622	10.24	0.501	33.14	4.018	
736	114	129.71	0.127270	16.508	2.576	23.97	0.897	16.24	4.774	
1016	157	169.83	0.096950	16.465	2.613	34.85	1.038	11.70	5.596	
<b>R2LC</b>							Increase in Surface Area (wrt. Smooth) :			5.84 %
$G$ [kg/(m <sup>2</sup> s)]	$Re_{in}$	$Re_m$	$f_m$	$Po$	(S) <sub>Po</sub> %	$\Delta p$ [kPa]	(S) <sub><math>\Delta p</math></sub> %	$\Delta T$ [K]	(S) <sub><math>\Delta T</math></sub> %	
200	31	56.04	0.334545	18.749	6.174	4.57	1.040	63.90	7.197	
294	45	68.17	0.260852	17.782	5.647	7.74	1.668	43.06	7.248	
368	57	78.34	0.222867	17.460	5.528	10.39	2.003	34.20	7.345	
736	114	130.12	0.130481	16.978	5.497	24.44	2.892	16.78	8.258	
1016	157	170.10	0.099594	16.941	5.580	35.61	3.245	12.09	9.116	
<b>RDC</b>							Increase in Surface Area (wrt. Smooth) :			5.77 %
$G$ [kg/(m <sup>2</sup> s)]	$Re_{in}$	$Re_m$	$f_m$	$Po$	(S) <sub>Po</sub> %	$\Delta p$ [kPa]	(S) <sub><math>\Delta p</math></sub> %	$\Delta T$ [K]	(S) <sub><math>\Delta T</math></sub> %	
200	31	56.37	0.327111	18.438	4.415	4.61	1.991	62.77	5.301	
294	45	68.74	0.254606	17.502	3.984	7.80	2.429	42.28	5.305	
368	57	79.08	0.217310	17.185	3.863	10.46	2.651	33.55	5.304	
736	114	131.59	0.126819	16.688	3.695	24.52	3.212	16.38	5.677	
1016	157	172.12	0.096645	16.635	3.672	35.66	3.401	11.76	6.137	

## CHAPTER 7

### SUMMARY, CONCLUSIONS AND SUGGESTIONS FOR FUTURE WORK

In this work, effects of channel geometrical properties and surface roughness properties on laminar flow and heat transfer characteristics in microchannels are investigated numerically. For this purpose, two-dimensional parallel plate microchannels, and three-dimensional trapezoidal macro and microchannels with different geometrical properties and roughness configurations are modeled in addition to the smooth ones. Modelling of the channels, and fluid flow and heat transfer simulations are conducted with the commercial CFD program COMSOL Multiphysics. Extensive mesh independence tests are done for each geometry and are presented separately. For the post-processing, MATLAB and COMSOL's LiveLink for MATLAB module are used.

Two-dimensional simulations are conducted in parallel plate microchannels, with constant wall temperature, as an extension of a previous study. In these channels, roughness is modeled as triangular obstructions on one of the parallel plates. Water in laminar regime is used as the working fluid. Considered relative roughness values are 1.325%, 2.00%, 2.65%, and the  $Re$  range is  $5 \leq Re \leq 100$ . Effect of surface roughness is investigated with the combined effect of variable thermophysical properties of water and viscous dissipation.

Results of 2D simulations showed that tested roughness elements reduced the heat transfer performance with increasing relative roughness, due to formation of low velocity regions behind the roughness peaks and between the roughness elements. Existence of triangular roughness elements increased pressure drop up to 11%.

Among the tested geometries and considered flow conditions, effect of viscous dissipation is found to be negligible. Additionally, effect of using constant or variable fluid properties on temperature difference,  $Nu$ , and pressure drop is found to be less than 1% for the considered flow conditions. Local  $Nu$  distributions for each rough geometry showed similar distribution. Local  $Nu$  takes lower values than the corresponding smooth channel values around the base of the triangular roughness elements and between the consecutive roughness elements due to reduced velocity and convective heat transfer. Near the tip of the triangular elements, local  $Nu$  takes higher values than the smooth channels and peaks at the tip point, which increases with increasing relative roughness height and  $Re$  value.

Three-dimensional simulations are separated into two parts. In the first part, flow without heat transfer is considered in macroscale smooth and microscale smooth and rough trapezoidal channels. In the second part, flow with heat transfer is considered in microscale smooth and rough trapezoidal microchannels. In three-dimensional simulations, roughness is modeled as conical obstructions with different heights, base radii, and spacing that are placed on the base of the trapezoidal channel. The reason of using conical obstructions as the roughness elements is to mimic the naturally occurring roughness in chemically wet etched silicon microchannels and the microstructures that exist on lotus leaves. Three different roughness configurations are considered, namely *1LineCone (R1LC)*, *2LineCone (R2LC)*, and *DaisyCone (RDC)* configurations. Obtained results for smooth and rough channels, are compared with each other.

For flow simulations in macroscale smooth trapezoidal channels, four channels are considered; aspect ratios and side angles are taken from literature, calculated  $Po$  values are compared with the analytical ones that exist in the literature. Maximum difference between the numerical solutions and analytical ones are below 0.7%. For flow simulations in microscale smooth trapezoidal channels, five channels are considered. Four of these channels have the same aspect ratios and side angles as the macroscale channels. The other geometry is taken from an experimental study

that exists in the literature and constitutes the basis of the rough channels. Smooth microchannel  $Po$  values are found to be slightly higher than the smooth macroscale  $Po$  values. Difference between the macro and microchannel  $Po$  values are found to be maximum for the channel having the smallest aspect ratio and lowest side angle among the considered geometries on the order of about 1.9%. Difference between the channels having high aspect ratio is below 0.46% and can be considered as negligible since mesh independence simulations are truncated after the relative error dropped below 0.5%.  $Po$  values calculated for rough microchannels are found to be 3.0%, 5.9%, and 4.2% higher than the smooth microchannel  $Po$  value for R1LC, R2LC, and RDC configurations, respectively. R1LC and R2LC configurations have the same relative roughness value, but surface area increase relative to smooth microchannel is twice in R2LC configuration, which also nearly doubles the increase in  $Po$  value. On the other hand, relative roughness and surface area increase relative to smooth microchannel in RDC configuration is slightly lower than R2LC configuration. However, increase in  $Po$  value is much lower than R2DC configuration and closer to R1LC configuration. These results indicate that there is not a linear relationship between the  $Po$  value and relative roughness height or increase in surface area.

For flow and heat transfer simulations in three-dimensional trapezoidal microchannels, one smooth and the three rough microchannels mentioned above are used. Simulations are carried out for various inlet mass fluxes and one uniform heat flux value. Results obtained for wall temperature and  $Nu$  values for smooth microchannel simulations are compared with the ones that exist in the literature. Good agreement is achieved. In rough channels, the heated section surface area is increased about 2.92%, 5.84%, and 5.77% for the R1LC, R2LC, and RDC configurations compared to the smooth one, respectively. Depending on the inlet mass flux, relative to smooth channel value, 2.57% to 2.98% increase in  $Po$  for the R1LC configuration, 5.49% to 6.17% increase in  $Po$  for the R2LC configuration, and 3.67% to 4.41% increase in  $Po$  for the RDC configuration is observed. Pressure drop between the inlet and the exit of the heated section increases with increasing

inlet mass flux, and is found to be highest for RDC configuration. Temperature difference between the inlet and exit of heated section reduces with increasing inlet mass flux, and is found to be highest for R2LC configuration. Similar to two-dimensional simulations, local  $Nu$  takes the highest values near the tips of the cones. However, except the first few cones at the inlet, local  $Nu$  values are generally lower than the corresponding smooth channel values. Low velocity regions occur at the downstream part of the cones, which reduces the local convective heat transfer. It is also observed that, as the inlet mass flux increased, flow around the conical elements is more disturbed, and the difference between the rough channel and smooth channel local  $Nu$  values reduces.

Since the thermophysical properties of the fluid are temperature dependent, thermal conductivity of the fluid increases gradually while viscosity and density reduce between the conical elements along the flow direction due to constant heating of the fluid. Thermophysical properties of the fluid also varied in other directions, from the symmetry plane to the sidewall and from the heated base to the top wall of the channel, due to unheated side and top walls and unheated regions at the base.

Wall temperatures reduced through the tips of the cones, where the cone tips are subjected to higher velocity flow. Wall temperatures for the rough channels take slightly higher values than the smooth microchannel wall temperatures on the locations where there is no cone.

The most commonly used definition of surface roughness in the literature is the relative roughness height, which is the ratio of average roughness height to the hydraulic diameter. The R1LC and R2LC configurations used in this study have the same relative roughness heights with different number of cones. However, these configurations yield different results of  $f$ ,  $Po$  and  $Nu$  in magnitude. The RDC configuration has a slightly lower relative roughness value with surface area increment close to R2LC configuration and a more complex pattern, resulting in lower friction factors than the R2LC configurations.

Combining the results that are obtained from the reviewed literature and the results that are obtained in this study, it is clear that the relative roughness height definition is not sufficient to resolve the effect of roughness phenomena alone. Other geometrical parameters, such as roughness cross-sectional shapes, spacing between them, density of the used roughness elements in a unit area, uneven distribution of roughness if any, should also be considered in the investigations of the effect of roughness on flow and heat transfer parameters. A systematic approach, that is changing one of the mentioned geometrical parameters and keeping others the same in a test geometry, is necessary to investigate the effect of roughness geometrical parameters despite the huge workload.

Since each roughness configuration results in different parameters for each flow case, this work must be extended by using different patterns of conical elements. By this way, an optimum configuration of conical elements can be obtained to increase heat transfer without causing much increase in friction or pressure drop. Studies in the literature also showed that each roughness geometry is more effective in certain flow velocities. Extending the simulations to different velocities will reveal the best flow conditions for conical roughness elements patterns.

If the main objective of using or investigating engineered rough surfaces is to reduce the friction, such as to produce coatings for planes and submarines, this work should be extended to higher flow velocities. Studies that exist in open literature showed that closely placed roughness elements have the potential of reducing friction at higher velocities.

Moreover, if the sole objective is to increase the amount of heat transfer and to use the roughness as fins in heat sinks, this work should be extended by keeping the heat supply area constant and including the substrate material properties, and then conducting three-dimensional conjugate heat transfer simulations for more realistic results.



## REFERENCES

- [1] MEMS and Nanotechnology Exchange (MNX), <https://www.memsnet.org/about/what-is.html>, last visited on August 2017.
- [2] M. Gad-el-Hak, *The MEMS Handbook: Introduction and Fundamentals*, 2<sup>nd</sup> Ed., Taylor & Francis, 2005.
- [3] G. Karniadakis, A. Beskok, and N. Aluru, *Microflows and Nanoflows, Fundamentals and Simulation*, Springer, 2005.
- [4] P. Rosa, T.G. Karayiannis, and M.W. Collins, Single-phase heat transfer in microchannels: The importance of scaling effects, *Applied Thermal Engineering*, vol. 29, pp. 3447-3468, 2009.
- [5] G. L. Morini, Single-phase convective heat transfer in microchannels: a review of experimental results, *International Journal of Thermal Sciences*, vol. 43, pp. 631-651, 2004.
- [6] University of Missouri Electron Microscopy Core Facility, Training, Courses-Student Projects, Scanning Electron Microscope (SEM) View of Silicon Microchannels, Rosalynn M. Manor, [www.emc.missouri.edu/Manor.htm](http://www.emc.missouri.edu/Manor.htm), last visited on January 2009 (Archived web page).
- [7] PSI Institute Materials Group, <http://materials.web.psi.ch/Research/Structuring/MFC.htm?forprint>, last visited on May 2009 (Archived web page).
- [8] B. Bhushan and Y. C. Jung, Natural and biomimetic artificial surfaces for superhydrophobicity, self-cleaning, low adhesion, and drag reduction, *Progress in Materials Science*, vol. 56, pp. 1-108, 2011.
- [9] A. Malshe, K. Rajurkar, A. Samant, H. N. Hansen, S. Bapat, and W. Jiang, Bio-inspired functional surfaces for advanced applications, *CIRP Annals – Manufacturing Technology*, vol. 62, pp. 607-628, 2013.

- [10] G. Hetsroni, A. Mosyak, E. Pogrebnyak, and L. P. Yarin, Heat transfer in microchannels: Comparison of experiments with theory and numerical results, *International Journal of Heat and Mass Transfer*, vol. 48, pp. 5580-5601, 2005.
- [11] G. Hetsroni, A. Mosyak, E. Pogrebnyak, and L. P. Yarin, Fluid flow in microchannels, *International Journal of Heat and Mass Transfer*, vol. 48, pp. 1982-1998, 2005.
- [12] M. E. Steinke, and S. G. Kandlikar, Single-phase liquid friction factors in microchannels, *International Journal of Thermal Sciences*, vol. 45, pp. 1073-1083, 2006.
- [13] R. Dey, T. Das, and S. Chakraborty, Frictional and heat transfer characteristics of single-phase microchannel liquid flows, *Heat Transfer Engineering*, vol. 33, pp. 425-446, 2012.
- [14] A. M. Adham, N. M-Ghazali, and R. Ahmad, Thermal and hydrodynamic analysis of microchannel heat sinks: A review, *Renewable and Sustainable Energy Reviews*, vol. 21, pp. 614-622, 2013.
- [15] M. Asadi, G. Xie, and B. Sunden, A review of heat transfer and pressure drop characteristics of single and two-phase microchannels, *International Journal of Heat and Mass Transfer*, vol. 79, pp. 34-53, 2014.
- [16] B. Dai, M. Li, and Y. Ma, Effect of surface roughness on liquid friction and transition characteristics in micro- and mini-channels, *Applied Thermal Engineering*, vol. 67, pp. 283-293, 2014.
- [17] G. L. Morini, Scaling effects for liquid flows in microchannels, *Heat Transfer Engineering*, vol. 27, pp. 64-73, 2006.
- [18] G. L. Morini, Laminar-to-turbulent flow transition in microchannels, *Microscale Thermophysical Engineering*, vol. 8, pp. 15-30, 2004.

- [19] W. Qu, G. M. Mala, and D. Li, Pressure-driven water flows in trapezoidal silicon microchannels, *International Journal of Heat and Mass Transfer*, vol. 43, pp. 353-364, 2000.
- [20] W. Qu, G. M. Mala, and D. Li, Heat transfer for water flow in trapezoidal silicon microchannels, *International Journal of Heat and Mass Transfer*, vol. 43, pp. 3925-3936, 2000.
- [21] H. Y. Wu, and P. Cheng, Friction factors in smooth trapezoidal silicon microchannels with different aspect ratios, *International Journal of Heat and Mass Transfer*, vol. 46, pp. 2519-2525, 2003.
- [22] H. Y. Wu, and P. Cheng, An experimental study of convective heat transfer in silicon microchannels with different surface conditions, *International Journal of Heat and Mass Transfer*, vol. 46, pp. 2547-2556, 2003.
- [23] P-F. Hao, F. He, and K-Q. Zhu, Flow characteristics in a trapezoidal silicon microchannel, *Journal of Micromechanics and Microengineering*, vol. 15, pp. 1362-1368, 2005.
- [24] L. Renaud, C. Malhaire, P. Kleimann, D. Barbier, and P. Morin, Theoretical and experimental studies of microflows in silicon microchannels, *Materials Science and Engineering C*, vol. 28, 910-917, 2008.
- [25] H. Wu, X. Wu, and Z. Wei, Flow friction and heat transfer of ethanol-water solutions through silicon microchannels, *Journal of Micromechanics and Microengineering*, vol. 19, 045005, 2009.
- [26] G. Wang, L. Hao, and P. Cheng, An experimental and numerical study of forced convection in a microchannel with negligible axial heat conduction, *International Journal of Heat and Mass Transfer*, vol. 52, pp. 1070-1074, 2009.
- [27] L. Chai, G. Xia, and J. Qi, Experimental and numerical study of flow and heat transfer in trapezoidal microchannels, *Heat Transfer Engineering*, vol. 33, pp. 972-981, 2012.

- [28] V. S. Duryodhan, A. Singh, S. G. Singh, and A. Agrawal, Convective heat transfer in diverging and converging microchannels, *International Journal of Heat and Mass Transfer*, vol. 80, pp. 424-438, 2015.
- [29] R. Sadasivam, R. M. Manglik, and M. A. Jog, Fully developed forced convection through trapezoidal and hexagonal ducts, *International Journal of Heat and Mass Transfer*, vol. 42, pp. 4321-4331, 1999.
- [30] R. K. Shah, Laminar flow friction and forced convection heat transfer in ducts of arbitrary geometry, *International Journal of Heat and Mass Transfer*, vol. 18, pp. 849-862, 1975.
- [31] L. Zhuo, T. Wen-Quan, and H. Ya-Ling, A numerical study of laminar convective heat transfer in microchannel with non-circular cross-section, *International Journal of Thermal Sciences*, vol. 45, pp. 1140-1148, 2006.
- [32] M. Bahrami, M. M. Yovanovich, and J. R. Culham, Pressure drop of fully-developed laminar flow in microchannels of arbitrary cross-section, *Journal of Fluids Engineering*, vol. 128, pp. 1036-1044, 2006.
- [33] E. Sadeghi, M. Bahrami, and N. Djilali, Estimation of Nusselt number in microchannels of arbitrary cross section with constant axial heat flux, *Heat Transfer Engineering*, vol. 31, pp. 666-674, 2010.
- [34] Y. Chen, C. Zhang, M. Shi, and J. Wu, Three-dimensional numerical simulation of heat fluid flow in noncircular microchannel heat sinks, *International Communications in Heat and Mass Transfer*, vol. 36, pp. 917-920, 2009.
- [35] P. Gunnasegaran, H. A. Mohammed, N. H. Shuaib, and R. Saidur, The effect of geometrical parameters on heat transfer characteristics of microchannels heat sink with different shapes, *International Communications in Heat and Mass Transfer*, vol. 37, pp. 1078-1086, 2010.
- [36] H. Wang, Z. Chen, and J. Gao, Influence of geometric parameters on flow and heat transfer performance of micro-channel heat sinks, *Applied Thermal Engineering*, vol. 107, pp. 870-879, 2016.

- [37] J. P. McHale, and S. V. Garimella, Heat transfer in trapezoidal microchannels of various aspect ratios, *International Journal of Heat and Mass Transfer*, vol. 53, pp. 365-375, 2010.
- [38] M. Lorenzini, G. L. Morini, Single-phase laminar forced convection in microchannels with rounded corners, *Heat Transfer Engineering*, vol. 32, pp. 1108-1116, 2011.
- [39] D. Sharma, P. P. Singh, and H. Garg, Comparative study of rectangular and trapezoidal microchannels using water and liquid metal, *Procedia Engineering*, vol. 51, pp. 791-796, 2013.
- [40] N. Tran, Y-J. Chang, J. Teng, and R. Greif, A study on five different channel shapes using a novel scheme for meshing and a structure of a multi-nozzle microchannel heat sink, *International Journal of Heat and Mass Transfer*, vol. 105, pp. 429-442, 2017.
- [41] B. Cao, G. W. Chen, and Q. Yuan, Fully developed laminar flow and heat transfer in smooth trapezoidal microchannel, *International Communications in Heat and Mass Transfer*, vol. 32, pp. 1211-1220, 2005.
- [42] H. Niazmand, M. Renksizbulut, and E. Saeedi, Developing slip-flow and heat transfer in trapezoidal microchannels, *International Journal of Heat and Mass Transfer*, vol. 51, pp. 6126-6135, 2008.
- [43] L. Kuddusi and E. Çetegen, Thermal and hydrodynamic analysis of gaseous flow in trapezoidal silicon microchannels, *International Journal of Thermal Sciences*, vol. 48, pp. 353-362, 2009.
- [44] L. Kuddusi, First and second law analysis of fully developed gaseous slip flow in trapezoidal silicon microchannels considering viscous dissipation effect, *International Journal of Heat and Mass Transfer*, vol. 54, pp. 52-64, 2011.
- [45] Gh. M. Mala, and D. Li, Flow characteristics of water in microtubes, *International Journal of Heat and Fluid Flow*, vol. 20, pp. 142-148, 1999.

[46] C. Kleinstreuer, and J. Koo, Computational analysis of wall roughness effect for liquid flow in micro-conduits, *Journal of Fluids Engineering*, vol. 126, pp. 1-9, 2004.

[47] J. Koo, and K. Kleinstreuer, Analysis of surface roughness effects on heat transfer in micro-conduits, *International Journal of Heat and Mass Transfer*, vol. 48, pp. 2625-2634, 2005.

[48] S. G. Kandlikar, S. Joshi, and S. Tian, Effect of surface roughness on heat transfer and fluid flow characteristics at low Reynolds numbers in small diameter tubes, *Heat Transfer Engineering*, vol. 24, pp. 4-16, 2003.

[49] S. G. Kandlikar, D. Schmitt, A. L. Carrano, and J. B. Taylor, Characterization of surface roughness effects on pressure drop in single-phase flow in minichannels, *Physics Fluids*, vol. 17, 100606, 2005.

[50] J. B. Taylor, A. L. Carrano, and S. G. Kandlikar, Characterization of the effect of surface roughness and texture on fluid flow-past, present, and future, *International Journal of Thermal Sciences*, vol. 45, pp. 962-968, 2006.

[51] A. S. Rawool, S. K. Mitra, and S. G. Kandlikar, Numerical simulation of flow through microchannels with designed roughness, *Microfluid Nanofluid*, vol. 2, pp. 215-221, 2006.

[52] T-Y. Lin, and S. G. Kandlikar, An experimental investigation of structured roughness effect on heat transfer during single-phase liquid flow at microscale, *Journal of Heat Transfer (ASME)*, vol. 134, 101701, 2012.

[53] R. N. Wagner, and S. G. Kandlikar, Effects of structured roughness on fluid flow at the microscale level, *Heat Transfer Engineering*, vol. 33, pp. 483-493, 2012.

[54] V. V. Dharaiya, and S. G. Kandlikar, A numerical study on the effects of 2d structured sinusoidal elements on fluid flow and heat transfer at microscale, *International Journal of Heat and Mass Transfer*, vol. 57, pp. 190-201, 2013.

- [55] G. Croce, and P. D'Agaro, Numerical analysis of roughness effect on microtube heat transfer, *Superlattices and Microstructures*, vol. 35, pp. 601-616, 2004.
- [56] G. Croce, and P. D'Agaro., Numerical simulation of roughness effect on microchannel heat transfer and pressure drop in laminar flow, *Journal of Physics D: Applied Physics*, vol. 38, pp. 1518-1530, 2005.
- [57] G. Croce, P. D'Agaro, and C. Nonini, Three-dimensional roughness effect on microchannel heat transfer and pressure drop, *International Journal of Heat and Mass Transfer*, vol. 50, pp. 5249-5259, 2007.
- [58] G. Croce, P. D'Agaro, and A. Filippo, Compressibility and rarefaction effects on pressure drop in rough microchannels, *Heat Transfer Engineering*, vol. 28, pp. 688-695, 2007.
- [59] G. Croce, and P. D'Agaro, Compressibility and rarefaction effect on heat transfer in rough microchannels, *International Journal of Thermal Sciences*, vol. 48, pp. 252-260, 2009.
- [60] Y. Ji, K. Yuan, and J.N. Chung, Numerical simulation of wall roughness on gaseous flow and heat transfer in a microchannel, *International Journal of Heat and Mass Transfer*, vol. 49, pp. 1329-1339, 2006.
- [61] M. B. Turgay, and A. G. Yazicioglu, Effect of surface roughness in parallel-plate micro-channels on heat transfer, *Numerical Heat Transfer, Part A*, vol. 56, pp. 497-514, 2009.
- [62] C. Zhang, Y. Chen, and M. Shi, Effects of roughness elements on laminar flow and heat transfer in microchannels, *Chemical Engineering and Processing: Process Intensification*, vol. 49, pp. 1188-1192, 2010.
- [63] S. Hossainpour, and M. H. Khadem, Investigation of fluid flow and heat transfer characteristics of gases in microchannels with consideration of different roughness shapes at slip flow regime, *Nanoscale and Microscale Thermophysical Engineering*, vol. 14, pp. 137-151, 2010.

- [64] C. Liu, J. Yang, and Y. Ni, A multiplicative decomposition of Poiseuille number on rarefaction and roughness by lattice Boltzmann simulation, *Computers and Mathematics with Applications*, vol. 61, pp. 3528-3536, 2011.
- [65] J. Cui, W. Li, and W-H. Lam, Numerical investigation on drag reduction with superhydrophobic surfaces by lattice–Boltzmann method, *Computers and Mathematics with Applications*, vol. 61, pp. 3678-3689, 2011.
- [66] L. Ding, W. Shi, and H. Luo, Numerical simulation of viscous flow over non-smooth surfaces, *Computers and Mathematics with Applications*, vol. 61, pp. 3703-3710, 2011.
- [67] Y. Chen, P. Fu, and M. Shi, Numerical simulation of laminar heat transfer in microchannels with rough surfaces characterized by fractal Cantor structures, *International Journal of Heat and Fluid Flow*, vol. 31, pp. 622-629, 2010.
- [68] R. Xiong, Fluid flow in trapezoidal silicon microchannels with 3D random rough bottoms, *Journal of Fluids Engineering*, vol. 133, 031102, 2011.
- [69] Y. Liu, J. Cui, Y. X. Jiang, and W. Z. Li, A numerical study on heat transfer performance of microchannels with different surface microstructures, *Applied Thermal Engineering*, vol. 31, pp. 921-931, 2011.
- [70] J. Cui, Y. Fu, A numerical study on pressure drop in microchannel flow with different bionic micro-grooved surfaces, *Journal of Bionic Engineering*, vol. 9, pp. 99-109, 2012.
- [71] C. Liu, J. Teng, J-C. Chu, Y. Chiu, S. Huang, S. Jin, T. Dang, R. Greif, and H-H. Pan, Experimental investigations on liquid flow and heat transfer in rectangular microchannels with longitudinal vortex generators, *International Journal of Heat and Mass Transfer*, vol. 54, pp. 3069-3080, 2011.
- [72] M. A. Ahmed, N. H. Shuaib, M. Z. Yusoff, and A. H. Al-Falahi, Numerical investigations of flow and heat transfer enhancement in a corrugated channel using nanofluid, *International Communications in Heat and Mass Transfer*, vol. 38, pp. 1368-1375, 2011.

[73] S. Ndao, H. J. Lee, Y. Peles, and M. K. Jensen, Heat transfer enhancement from micro pin fins subjected to an impinging jet, *International Journal of Heat and Mass Transfer*, vol. 55, pp. 413-421, 2012.

[74] A. Tamayol, J. Yeom, M. Akbari, and M. Bahrami, Low Reynolds number flows across ordered arrays of micro-cylinders embedded in a rectangular micro / minichannels, *International Journal of Heat and Mass Transfer*, vol. 58, pp. 420-426, 2013.

[75] K. L. Kirsch and K. A. Thole, Pressure loss and heat transfer performance for additively and conventionally manufactured pin fin arrays, *International Journal of Heat and Mass Transfer*, vol. 108, pp. 2502-2513, 2017.

[76] L. Gong, and B. Wei, The characteristics of fluid flow and heat transfer in wavy, dimple and wavy-dimple microchannels, *Applied Mechanics and Materials*, vol. 394, pp. 173-178, 2013.

[77] G. D. Xia, J. Jiang, J. Wang, Y. L. Zhai, D. D. Ma, Effects of different geometric structures on fluid flow and heat transfer performance in microchannel heat sinks, *International Journal of Heat and Mass Transfer*, vol. 80, pp. 439-447, 2015.

[78] Y. Li, G. Xia, Y. Jia, D. Ma, B. Cai, and J. Wang, Effect of geometric configuration on the laminar flow and heat transfer in microchannel heat sinks with cavities and fins, *Numerical Heat Transfer, Part A*, vol. 71, No. 5, pp. 528-546, 2017.

[79] T. Kim, R. Shin, M. Jung, J. Lee, C. Park, and S. Kang, Drag reduction using metallic engineered surfaces with highly ordered hierarchical topographies: nanostructures on micro-riblets, *Applied Surface Science*, vol. 367, pp. 147-152, 2016.

[80] K. Tsougeni, P. S. Petrou, D. P. Papageorgiou, S. E. Kakabakos, A. Tserepi, and E. Gogolides, Controlled protein adsorption on microfluidic channels with engineered roughness and wettability, *Sensors and Actuators B: Chemical*, vol. 161, pp. 216-222, 2012.

[81] J. Oeffner and G. V. Lauder, The hydrodynamic function of shark skin and two biomimetic applications, *The Journal of Experimental Biology*, vol. 215, pp. 785-795, 2012.

[82] M. A. Samaha, H. V. Tafreshi, and M. Gad-el-Hak, Superhydrophobic surfaces: From the lotus leaf to the submarine, *Comptes Rendus Mecanique*, vol. 340, pp. 18-34, 2012.

[83] E. Luong-Van et al., Review: Micro- and nanostructured surface engineering for biomedical applications, *J. Mater. Res.*, vol.28, No.2, 2013.

[84] S-M. Chang, H. T. Kim, J-H. Shin, and Y. G. Kim, The feasibility of multidimensional CFD applied to calandria system in the moderator of CANDU-6 PHWR using commercial and open-source codes, *Science and Technology of Nuclear Installations*, vol. 2016, 3194839, 2016.

[85] W. Jeong and J. Seong, Comparison of effects on technical variances of computational fluid dynamics (CFD) software based on finite element and finite volume methods, *International Journal of Mechanical Sciences*, vol. 78, pp. 19-26, 2014.

[86] COMSOL, Inc., COMSOL Multiphysics, <https://www.comsol.com>.

[87] A.A.Y. Al-Waaly, M.C. Paul, and P. Dobson, Liquid cooling of non-uniform heat flux of a chip circuit by subchannels, *Applied Thermal Engineering*, vol. 115, pp. 558-574, 2017.

[88] R. Brinda, R.J. Daniel, and K. Sumangala, Effect of aspect ratio on the hydraulic and thermal performance of ladder shape micro channels employed micro cooling systems, *Procedia Engineering*, vol. 38, pp. 2022-2032, 2012.

[89] Y. Han, Y. J. Lee, and X. Zhang, Trapezoidal microchannel heat sink with pressure-driven and electro-osmotic flows for microelectronic cooling, *IEEE Transactions on Components, Packaging and Manufacturing Technology*, vol. 3, No. 11, 2013.

- [90] Y. Kim, M. Kim, C. Ahn, H. U. Kim, S-W. Kang, and T. Kim, Numerical study on heat transfer and pressure drop in laminar-flow multistage mini-channel heat sink, *International Journal of Heat and Mass Transfer*, vol. 108, 1197-1206, 2017.
- [91] X. Yu, C. Woodcock, J. Plawsky, and Y. Peles, An investigation of convective heat transfer in microchannel with Piranha Pin Fin, *International Journal of Heat and Mass Transfer*, vol. 103, pp. 1125-1132, 2016.
- [92] S-Q. Lin, T-M. Shih, R. R-G. Chang, and Z. Chen, Optimization of cooling effects with fins of variable cross-sections, *Numerical Heat Transfer, Part A*, vol. 69, No. 8, pp. 850-858, 2016.
- [93] Q. Yao, T-M. Shih, R. R-G. Chang, Z. Chen, Y-L. Gao, and Y-J. Lu, Optimization of the cooling characteristics in high-voltage LEDs, *Numerical Heat Transfer, Part A*, vol. 69, No. 11, pp. 1242-1252, 2016.
- [94] K. S. Rao, K. G. Sravani, G. Yugandhar, G. V. Rao, and V. N. Mani, Design and analysis of fluid structure interaction in a horizontal micro channel, *Procedia Materials Science*, vol. 10, pp. 768-788, 2015.
- [95] A. Bejan, A. Almerbati, S. Lorente, A. S. Sabau, and J. W. Klett, Arrays of flow channels with heat transfer embedded in conducting walls, *International Journal of Heat and Mass Transfer*, vol. 99, pp. 504-511, 2016.
- [96] Y. Luo, W. Liu, L. Wang, and W. Xie, Heat and mass transfer characteristics of leaf-vein-inspired microchannels with wall thickening patterns, *International Journal of Heat and Mass Transfer*, vol. 101, pp. 1273-1282, 2016.
- [97] M.C. Rajagopal, and S.K. Das, Analyses of drag on viscoelastic liquid infused bio-inspired patterned surfaces, *Journal of Non-Newtonian Fluid Mechanics*, vol. 228, pp. 17-30, 2016.
- [98] V. Ionescu, and A-A. Neagu, Finite element analysis of a MEMS-based heat exchanger with different channel geometries, *Energy Procedia*, vol. 112, pp. 158-165, 2017.

- [99] W. Yaici, M. Ghorab, and E. Entchev, 3D CFD study of the effect of inlet air flow maldistribution on plate-fin-tube heat exchanger design and thermal-hydraulic performance, *International Journal of Heat and Mass Transfer*, vol. 101, pp. 527-541, 2016.
- [100] J. H. K. Haertel and G. F. Nellis, A fully developed flow thermofluid model for topology optimization of 3D-printed air-cooled heat exchangers, *Applied Thermal Engineering*, vol. 119, 10-24, 2017.
- [101] A. F. Al-Neama, N. Kapur, J. Summers, and H. M. Thompson, An experimental and numerical investigation of the use of liquid flow in serpentine microchannels for electronics cooling, *Applied Thermal Engineering*, vol. 116, pp. 709-723, 2017.
- [102] S. A. Patel, and R. P. Chhabra, Effect of the angle of incidence on laminar forced convection from an elliptic cylinder in Bingham plastic fluids, *Numerical Heat Transfer, Part A*, vol. 70, No. 8, pp. 917-937, 2016.
- [103] I. Amber, and T.S. O'Donovan, A numerical simulation of heat transfer in an enclosure with a nonlinear heat source, *Numerical Heat Transfer, Part A*, vol. 71, No.11, pp. 1081-1093, 2017.
- [104] V. Gerlich, K. Sulovska, and M. Zalesak, COMSOL Multiphysics validation as simulation software for heat transfer calculation in buildings: Building simulation software validation, *Measurement*, vol. 46, pp. 2003-2012, 2013.
- [105] B. Stute, V. Krupp, and E. von Lieres, Performance of iterative equation solvers for mass transfer problems in three-dimensional sphere packings in COMSOL, *Simulation Modelling Practice and Theory*, vol. 33, pp. 115-131, 2013.
- [106] M. B. Turgay, Effect of Surface Roughness in Microchannels on Heat Transfer, M.Sc. Thesis, Middle East Technical University, Ankara, Turkey, 2008.
- [107] M. B. Turgay, A. G. Yazıcıoğlu, and S. Kakaç, Roughness effect on the heat transfer coefficient for gaseous flow in microchannels, *Proc. of the ASME International Heat Transfer Conference 14*, Washington DC, USA, Aug. 8-13, 2010.

[108] COMSOL Multiphysics Reference Manual, Version 4.4, November 2013, COMSOL.

[109] R. K. Shah and A. L. London, Laminar Flow Forced Convection in Ducts: A Source Book for Compact Heat Exchanger Analytical Data, Academic Press, 1978.



## APPENDIX A

### NOTES ON BOUNDARY LAYER MESH

In numerical simulations of high speed or turbulent fluid flow, use of proper boundary layer mesh is an important issue to effectively and accurately resolve the flow characteristics near the solid boundaries. However, this accuracy comes with huge computational cost increase, especially for large problems. On the other hand, for slow flows, same accuracy could be achieved without use of boundary layer mesh when the mesh is properly adjusted and small enough to obtain similar resolution. To test the need of using boundary layer mesh with geometries and flow conditions considered in this work, several different meshes are constructed in both rough 2D and 3D with *1LineCone* pattern test geometries and results are extracted in several locations for comparison.

#### A.1 TESTS IN 2D GEOMETRY

For the 2D tests, 14 different meshes are created in the test geometry. 10 of these meshes include 3, 5, and 7 boundary layers to investigate the effect of different boundary layer numbers with the change of element numbers and sizes, and 4 of them do not include any boundary layers. After the simulations completed,  $x$ -velocity components ( $u$ ) are extracted along the 5 lines located around the first, middle, and last roughness elements, resulting total of 210 data sets for comparison. Also, mean  $u$ -velocities are calculated and compared along these lines. Schematics of the test geometry and the location of the data lines are given in Fig. (A.1). Coordinates of the data extraction lines are presented in Table – (A.1), and

properties of used meshes and the solution times are given in Table – (A.2). Among the constructed meshes given in Table – (A.2), mesh groups (1-2-3), (4-5-6), and (7-8-9) have similar element sizes inside the domain and different number of boundary layers. All the simulations are conducted in a workstation with two Xeon X5660 CPU and 48 GB physical RAM running Windows 7 Enterprise Edition. Since the mesh element numbers are low enough, direct solvers are used in each simulation.

Figure (A.2) shows the base and middle close-up views of  $u$ -velocity distribution along the  $R1-L4$  line, and Fig. (A.3) shows the  $u$ -velocity distribution along the line passing through the tip point of the middle roughness ( $R2$ ) element. Except for the coarsest meshes both with and without boundary layers, all other meshes resulted very similar velocity distribution, which is similar to the other data lines. Moreover, at some data lines, solutions are nearly indistinguishable.

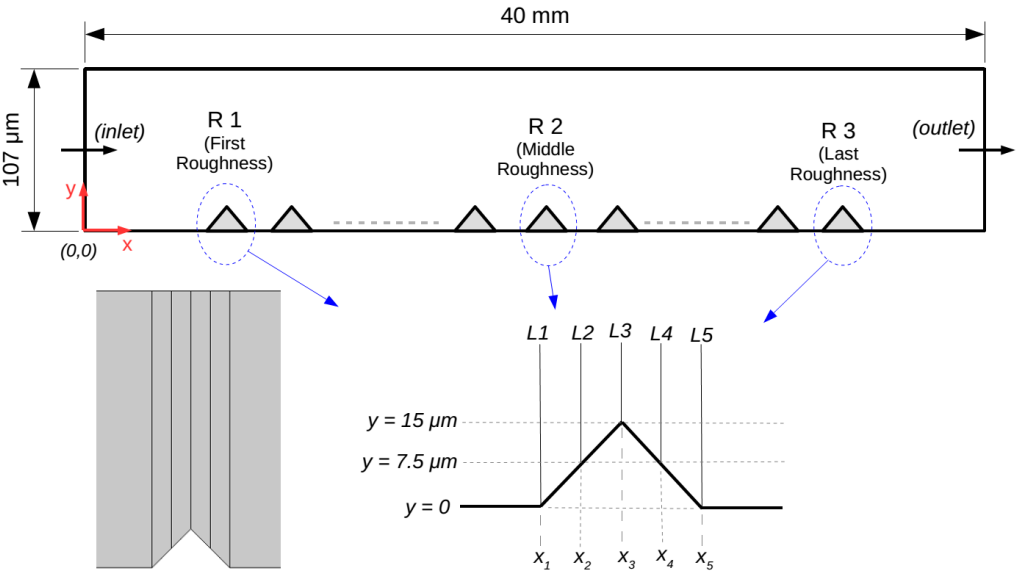


Figure A.1: Schematics of 2D test channel and the locations of data extraction lines.

Table A.1: Coordinates of the data extraction lines.

<i>R1</i>		<i>x</i> [ $\mu\text{m}$ ]	<i>y</i> [ $\mu\text{m}$ ]	<i>R2</i>		<i>x</i> [ $\mu\text{m}$ ]	<i>y</i> [ $\mu\text{m}$ ]	<i>R3</i>		<i>x</i> [ $\mu\text{m}$ ]	<i>y</i> [ $\mu\text{m}$ ]
	<i>L1</i>	5,085.0	0.0		<i>L1</i>	19,985.0	0.0		<i>L1</i>	34,885.0	0.0
	<i>L2</i>	5,092.5	7.5		<i>L2</i>	19,992.5	7.5		<i>L2</i>	34,892.5	7.5
	<i>L3</i>	5,100.0	15.0		<i>L3</i>	20,000.0	15.0		<i>L3</i>	34,900.0	15.0
	<i>L4</i>	5,107.5	7.5		<i>L4</i>	20,007.5	7.5		<i>L4</i>	34,907.5	7.5
	<i>L5</i>	5,115.0	0.0		<i>L5</i>	20,015.0	0.0		<i>L5</i>	34,915.0	0.0

Table A.2: Properties of constructed meshes and solution times.

Mesh	# of BL	# of elements	Min. Elem Quality	Avg. Elem Quality	Physical Memory	Virtual Memory	CPU Time
<b>1</b>	3	1,061,822	0.06558	0.83530	6.55 GB	7.06 GB	3m:17s
<b>2</b>	5	1,125,122	0.05295	0.78780	6.78 GB	7.38 GB	4m:07s
<b>3</b>	7	1,188,422	0.04136	0.74320	7.51 GB	8.20 GB	4m:09s
<b>4</b>	3	1,866,484	0.06773	0.85740	9.71 GB	10.59 GB	5m:48s
<b>5</b>	5	1,953,662	0.06026	0.81850	10.70 GB	11.68 GB	7m:20s
<b>6</b>	7	2,040,840	0.04684	0.78140	11.75 GB	12.85 GB	8m:10s
<b>7</b>	3	2,956,118	0.06883	0.84170	14.90 GB	16.31 GB	9m:31s
<b>8</b>	5	3,126,284	0.05211	0.79540	16.77 GB	18.39 GB	10m:42s
<b>9</b>	7	3,296,450	0.02760	0.74970	18.66 GB	20.48 GB	14m:13s
<b>10</b>	no	2,251,154	0.44270	0.92860	10.79 GB	11.67 GB	7m:43s
<b>11</b>	no	3,081,402	0.42540	0.92840	13.85 GB	15.06 GB	9m:03s
<b>12</b>	no	4,206,237	0.39770	0.92880	18.60 GB	20.31 GB	15m:09s
<b>13</b>	no	7,125,428	0.42180	0.93030	33.58 GB	36.79 GB	25m:45s
<b>14</b>	3	4,779,004	0.05242	0.85610	25.83 GB	28.17 GB	16m:19s

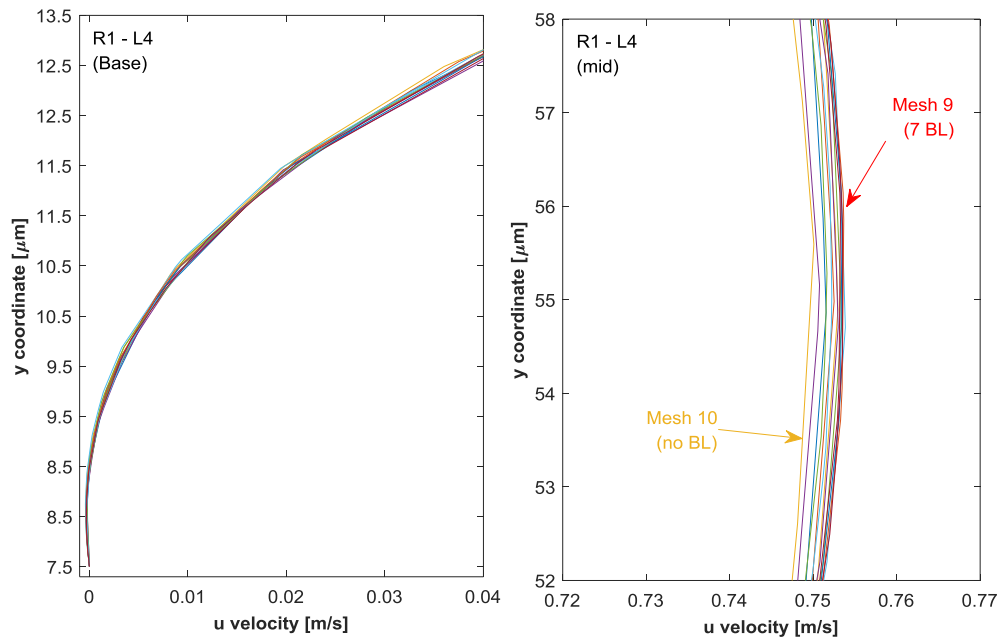


Figure A.2: Close-up views of velocity distributions near the base and around the middle of the *R1-L4* line.

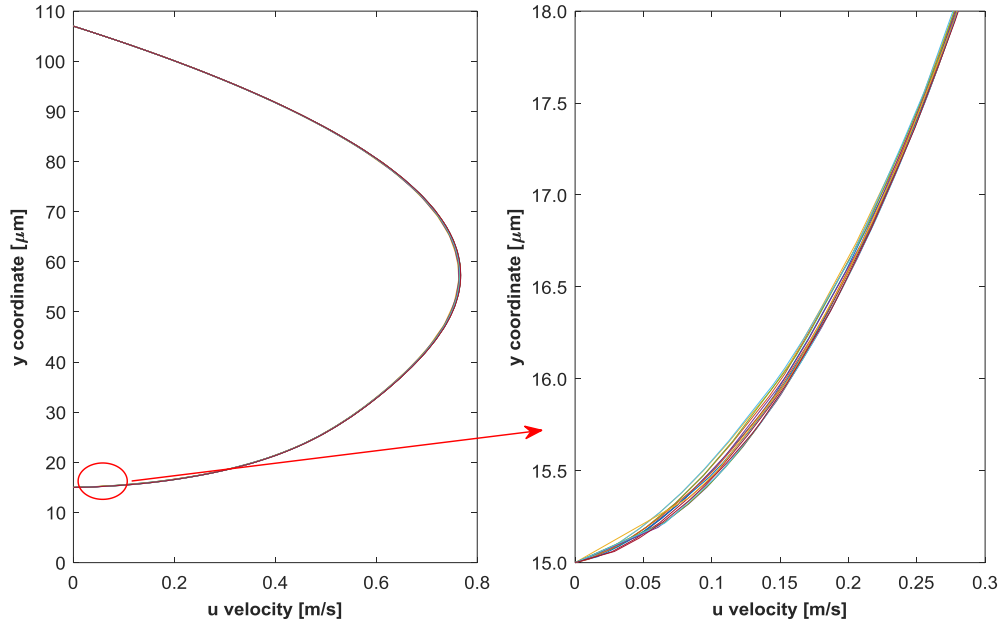


Figure A.3: Velocity distributions over the tip point of middle roughness element (along the *R2-L3* line) and close-up view near the tip point.

In addition, percentage difference between calculated mean velocities from the meshes 7-8-9 (with 3, 5, and 7 boundary layers) and meshes 11 and 12 (no boundary layers) for  $R1$  and  $R3$  roughness locations are given in Table – (A.3), respectively. Maximum difference is below 0.36%.

Table A.3: Percentage differences of mean velocities calculated along the lines around  $R1$  and  $R3$  for meshes 7, 8, 9, 11, and 12.

	<b><i>R1-L1</i></b>	<b><i>R1-L2</i></b>	<b><i>R1-L3</i></b>	<b><i>R1-L4</i></b>	<b><i>R1-L5</i></b>
<b><i>%(m7-m11)</i></b>	0.323	0.318	0.308	0.325	0.324
<b><i>%(m8-m11)</i></b>	0.338	0.332	0.323	0.339	0.339
<b><i>%(m9-m11)</i></b>	0.357	0.349	0.342	0.357	0.358
	<b><i>R3-L1</i></b>	<b><i>R3-L2</i></b>	<b><i>R3-L3</i></b>	<b><i>R3-L4</i></b>	<b><i>R3-L5</i></b>
<b><i>%(m7-m12)</i></b>	0.258	0.261	0.260	0.256	0.260
<b><i>%(m8-m12)</i></b>	0.240	0.243	0.242	0.237	0.242
<b><i>%(m9-m12)</i></b>	0.226	0.228	0.226	0.223	0.226

## A.2 TESTS IN 3D GEOMETRY

For the 3D tests, 7 different meshes are created in the test geometry. 3 of them includes 3, 5, and 7 boundary layers, and 4 of them do not include boundary layers. Similar to the 2D cases, after the simulations completed,  $z$ -velocity components ( $w$ ) are extracted along the 9 lines located around the first, middle and last conical roughness elements, resulting total of 189 data sets for comparison. Also, mean  $w$ -velocities are calculated and compared along these lines. Schematics of the test geometry and the location of the data lines are given in Fig. (A.4). Coordinates of the data lines are presented in Table – (A.4), and properties of used meshes and the solution times are given in Table – (A.5). Simulations are carried out at the same

computer as in the 2D cases. Since the number of elements and unknowns are too much to solve with direct solvers with the available physical RAM, iterative multigrid methods are used in these tests.

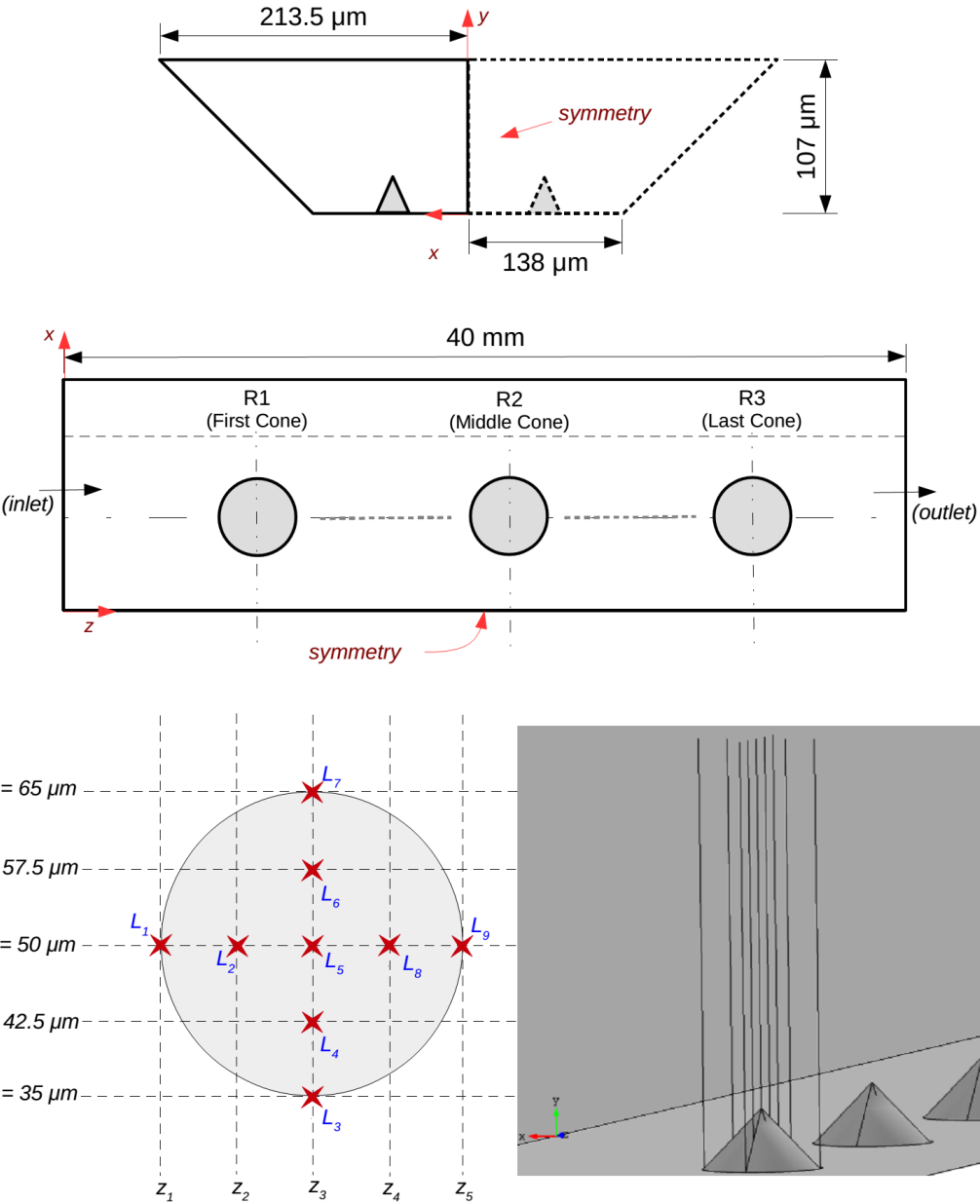


Figure A.4: Schematics of 3D test channel and the locations of data extraction lines.

Table A.4: Coordinates of the data extraction lines (all in  $\mu\text{m}$ ).

<b><i>R1</i></b>	<b><i>L1</i></b>	<b><i>L2</i></b>	<b><i>L3</i></b>	<b><i>L4</i></b>	<b><i>L5</i></b>	<b><i>L6</i></b>	<b><i>L7</i></b>	<b><i>L8</i></b>	<b><i>L9</i></b>
<i>x</i>	50	50	35	42.5	50	57.5	65	50	50
<i>y</i>	0	7.5	0	7.5	15	7.5	0	7.5	0
<i>z</i>	5085	5092.5	5100	5100	5100	5100	5100	5107.5	5115
<b><i>R2</i></b>	<b><i>L1</i></b>	<b><i>L2</i></b>	<b><i>L3</i></b>	<b><i>L4</i></b>	<b><i>L5</i></b>	<b><i>L6</i></b>	<b><i>L7</i></b>	<b><i>L8</i></b>	<b><i>L9</i></b>
<i>x</i>	50	50	35	42.5	50	57.5	65	50	50
<i>y</i>	0	7.5	0	7.5	15	7.5	0	7.5	0
<i>z</i>	19985	19992.5	20000	20000	20000	20000	20000	20007.5	20015
<b><i>R3</i></b>	<b><i>L1</i></b>	<b><i>L2</i></b>	<b><i>L3</i></b>	<b><i>L4</i></b>	<b><i>L5</i></b>	<b><i>L6</i></b>	<b><i>L7</i></b>	<b><i>L8</i></b>	<b><i>L9</i></b>
<i>x</i>	50	50	35	42.5	50	57.5	65	50	50
<i>y</i>	0	7.5	0	7.5	15	7.5	0	7.5	0
<i>z</i>	34885	34892.5	34900	34900	34900	34900	34900	34907.5	34915

Table A.5: Properties of the used meshes and solution times.

<b>Mesh</b>	<b># of BL</b>	<b># of elements</b>	<b>Min. Elem Quality</b>	<b>Avg. Elem Quality</b>	<b>Physical Memory [GB]</b>	<b>Virtual Memory [GB]</b>	<b>CPU Time</b>
<b>1</b>	3	8,176,939	0.00249	0.63170	45.94	47.99	1h:59m:20s
<b>2</b>	5	9,036,965	0.00098	0.57070	46.64	64.78	8h:39m:52s
<b>3</b>	7	7,778,450	3.015E-07	0.49400	47.56	57.03	8h:43m:13s
<b>4</b>	no	11,907,405	0.09156	0.76950	32.83	33.30	2h:00m:43s
<b>5</b>	no	13,652,197	0.08304	0.76400	45.86	46.41	2h:14m:13s
<b>6</b>	no	16,895,208	0.09393	0.76890	46.44	53.3	3h:11m:38s
<b>7</b>	no	14,768,853	0.07938	0.76000	46.92	49.56	2h:32m:34s

Figures (A.5) and (A.6) shows the  $w$ -velocity distribution along the second line of first roughness element with close-up views of base and mid-channel regions. By default, COMSOL generates mesh first over the surfaces by specifying the necessary parameters such as maximum element size, minimum element size, resolution of narrow ranges, element growth rate, and curvature factor, over these surfaces. It

should be noted here, these parameters are not applied exactly as it is, but with a close approximation. Then, progress through the domain. Meshes 1 to 6 created by this way.

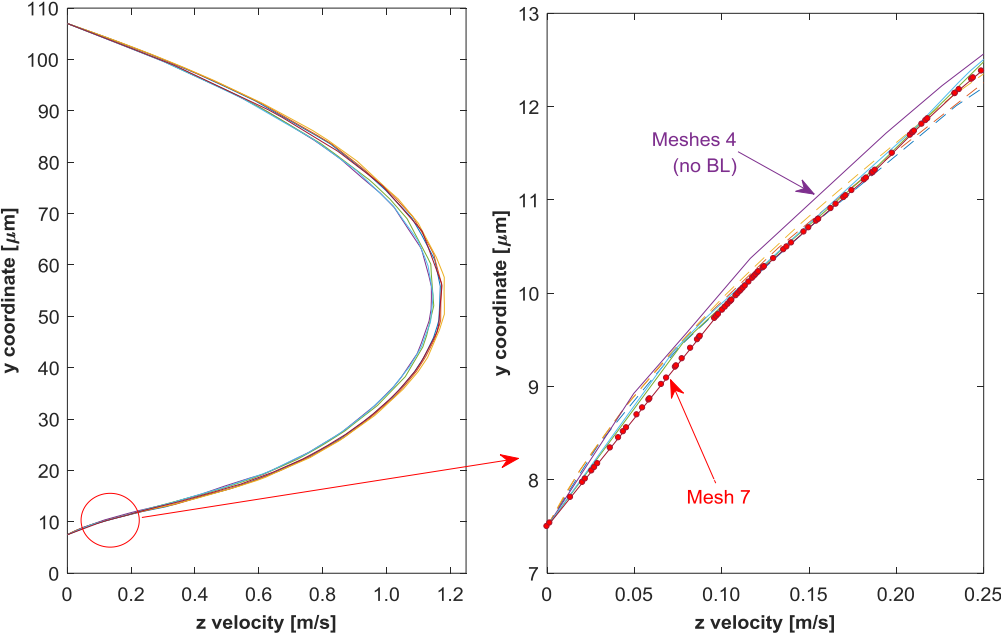


Figure A.5:  $w$ -velocity distributions along the second line of first roughness element and close-up view of the base section.

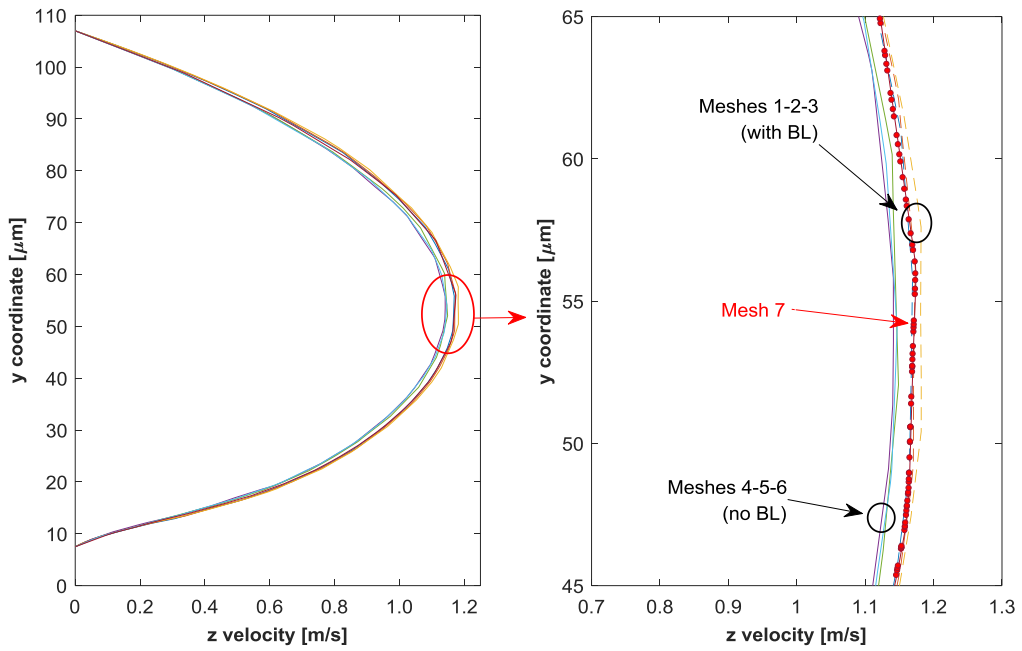


Figure A.6:  $w$ -velocity distributions along the second line of first roughness element and close-up view of the middle section.

However, not using boundary layers with this type of mesh generation leads to deviation starting from a couple of micrometers away from the surface and reaches a maximum of 5% at the center, which can be seen in Figs. (A.5) and (A.6). The second way of generating mesh is to define element numbers directly over all of the edges of the geometry and progress through the domain by another set of size definitions. Mesh 7 is created by this way. This method leads to better handling of the mesh size and better results in shorter solution time.

### A.3 CONCLUSION

Adding boundary layers reduces the minimum and average element qualities significantly. In 2D cases, needed element numbers are generally low and direct

solvers can be used. Thus, low element quality of mesh or solution time do not create much problem. Adding boundary layers only increases the meshing time starting about 20% and goes up to 50% depending on the element number, compared to the no boundary layer mesh used cases.

On the other hand, in 3D cases, much more element numbers are needed for a mesh independent solution and direct solvers cannot be used with the available RAM amount. Thus, iterative solver used throughout the tests. However, success of the iterative solvers also depend on the element quality, with other parameters. Adjusting the necessary parameters of the iterative solvers becomes very difficult and very time consuming.

Despite obtaining better resolution without any modifications and not tackling much with the mesh, other problems observed while using the boundary layers are the increase of the memory needed which restricts the total number of elements that can be used, increase in solver time, and significant increase in meshing time.

For the reasons of the meshing time, solver time, difficulties, and available memory, using boundary layers is not feasible. However, by carefully modifying the triangular or tetrahedral mesh and using enough elements on the boundaries, good results can be obtained in the 1% band of the results obtained by using the boundary layer mesh with the available computational power.

## APPENDIX B

### NUMERICAL CONSIDERATIONS IN COMSOL MULTIPHYSICS

#### B.1 MEMORY REDUCTION STUDIES

To reduce the memory usage of COMSOL, some modifications can be made in the solvers of the COMSOL without affecting the accuracy of the results. One of the many methods is disabling the row reordering option exist in the solver menu and enabled by default.

Memory reduction by disabling the row reordering option of solver without affecting the solution is shown in this section with examples. For this purpose, two different meshes is considered in smooth microchannels in which the geometry and flow conditions are taken from [26]. Simulations are run for inlet mass flux of 1016 kg/(m<sup>2</sup>s) and uniform heat flux of 300 kW/m<sup>2</sup>. Relative tolerance is set to 10<sup>-6</sup>. Each case is solved with both enabling and disabling the row reordering option. Then, wall mean temperatures, fluid bulk mean temperatures, and mean thermal conductivity of the fluid over the microheaters are extracted and compared with each other.

Used memory and CPU times are summarized in Table – (B.1) for the two example meshes. Important amount of reduction in memory usage is obtained with identical results, which are shown in Table – (B.2) for test mesh 2, as an example.

Table B.1: Memory usage and CPU times of two test cases with and without row preordering option.

<i>Mesh</i>	<i># of Elements</i>	<i>CPU Time</i>	<i>Physical Memory</i>	<i>Virtual Memory</i>
<i>(with row preordering)</i>				
<b>1</b>	10,061,865	14h:54m:46s	42.57 GB	43.18 GB
<b>2</b>	11,052,299	16h:29m:13s	45.71 GB	46.38 GB
<i>(without row preordering)</i>				
<b>1</b>	10,061,865	11h:02m:15s	29.42 GB	29.78 GB
<b>2</b>	11,052,299	12h:48m:45s	32.06 GB	32.46 GB

Table B.2: Some of the checked parameters for *Mesh-2* of row preordering test (*mh*: microheater).

	<i>(without row preordering)</i>			<i>(with row preordering)</i>		
	$T_w$ [K]	$T_b$ [K]	$k$ [W/(mK)]	$T_w$ [K]	$T_b$ [K]	$k$ [W/(mK)]
<b>mh.01</b>	300.406	293.711	0.595174	300.406	293.711	0.595174
<b>mh.02</b>	303.028	294.426	0.596372	303.028	294.426	0.596372
<b>mh.03</b>	304.470	295.113	0.597519	304.470	295.113	0.597519
<b>mh.04</b>	305.466	295.813	0.598685	305.466	295.813	0.598685
<b>mh.05</b>	306.442	296.527	0.599869	306.442	296.527	0.599869
<b>mh.06</b>	307.298	297.257	0.601070	307.298	297.257	0.601070
<b>mh.07</b>	308.127	297.995	0.602278	308.127	297.995	0.602278
<b>mh.08</b>	308.777	298.739	0.603487	308.777	298.739	0.603487
<b>mh.09</b>	309.651	299.490	0.604697	309.651	299.490	0.604697
<b>mh.10</b>	310.538	300.248	0.605909	310.538	300.248	0.605909
<b>mh.11</b>	311.582	301.010	0.607118	311.582	301.010	0.607118
<b>mh.12</b>	312.445	301.772	0.608316	312.445	301.772	0.608316
<b>mh.13</b>	313.385	302.538	0.609511	313.385	302.538	0.609511
<b>mh.14</b>	314.573	303.311	0.610704	314.573	303.311	0.610704
<b>mh.15</b>	315.717	304.085	0.611887	315.717	304.085	0.611887

## B.2 EFFECT OF STABILIZATION METHODS

COMSOL offers users two types of stabilization methods, namely consistent stabilization and inconsistent stabilization. Consistent stabilization also includes two options; streamline diffusion (upwind) and crosswind diffusion. With the use of stabilization methods, artificial diffusion is added to reduce the cell Peclet number. Inconsistent stabilization adds more artificial diffusion than the consistent stabilizations and suppresses the solution everywhere in the domain while consistent stabilizations add only the regions where needed. Thus, it is advised to use the inconsistent stabilization in highly oscillating problems with caution since it will change the solution. However, streamline diffusion must be used for convergence.

To see the effects of stabilization methods, a medium size mesh with linear elements is used. A mesh with 7,289,865 DOFs is used for the simulations with COMSOL v4.4. Also, a mesh with same meshing parameters and sizes is constructed with COMSOL v5.2a, to see the differences between the two different versions of the program. However, since the meshing procedure is updated in the newer version with many other things, slightly different mesh resulting 7,299,195 DOFs is obtained with the same parameters. Same iterative multigrid solvers and solver parameters are used in all cases. Simulations are carried out for effective heat flux of  $300 \text{ kW/m}^2$  and inlet mass flux of  $1016 \text{ kg/(m}^2\text{s)}$ . It should also be noted that newer version performed about 20% better in solution time. Heated surface average temperatures, maximum temperatures, and  $Po$  values calculated for these cases are given in Table – (B.3).

Table B.3:  $Po$  values, average, and maximum heater surface temperatures for stabilization method test cases.

Case	Stabilization		$T_{ave,HS}$		$T_{max,HS}$		$Po$	
	C.S.	I.S.	v4.4	v5.2a	v4.4	v5.2a	v4.4	v5.2a
1	FH – B	-	308.357	312.516	316.674	322.523	16.604	16.731
2	FH – S	-	314.347	314.975	325.238	326.077	16.136	16.639
3	F – S, H – B	-	308.360	312.487	316.644	322.423	16.420	16.639
4	F – B, H – S	-	314.346	314.989	325.248	326.119	16.316	16.731
5	FH – S	$id = 0.25$	300.432	300.449	306.566	306.601	47.516	43.612
<p><b>C.S.:</b> Consistent Stabilization      - <b>I:</b> Inconsistent Stabilization  <b>F:</b> Fluid Flow Module                - <b>H:</b> Heat Transfer Module  <b>S:</b> Streamline Diffusion              - <b>B:</b> Both Streamline and Crosswind Diffusion  <b>id:</b> Inconsistent diffusion constant  <b>HS:</b> Heated Surface</p>								

Wall mean temperatures calculated with COMSOL v4.4 and v5.2a are shown in Fig. (B.1) while  $Nu$  values calculated with COMSOL v4.4 are shown in Fig. (B.2). Inconsistent stabilization with a diffusion coefficient of 0.25 causes overdamped temperatures and changes the whole nature of the problem. Thus,  $Nu$  values are not shown for this case. Fluid flow part of the problem seems not affected by the chosen method since *Case-2* and *Case-4* resulted nearly same temperature and  $Nu$  profile. However, when crosswind diffusion is applied to heat transfer part, temperatures are overdamped. On the other hand, when the two versions are compared, it is seen that difference between temperatures in each profile is smaller which indicates an ongoing development in stabilization schemes.

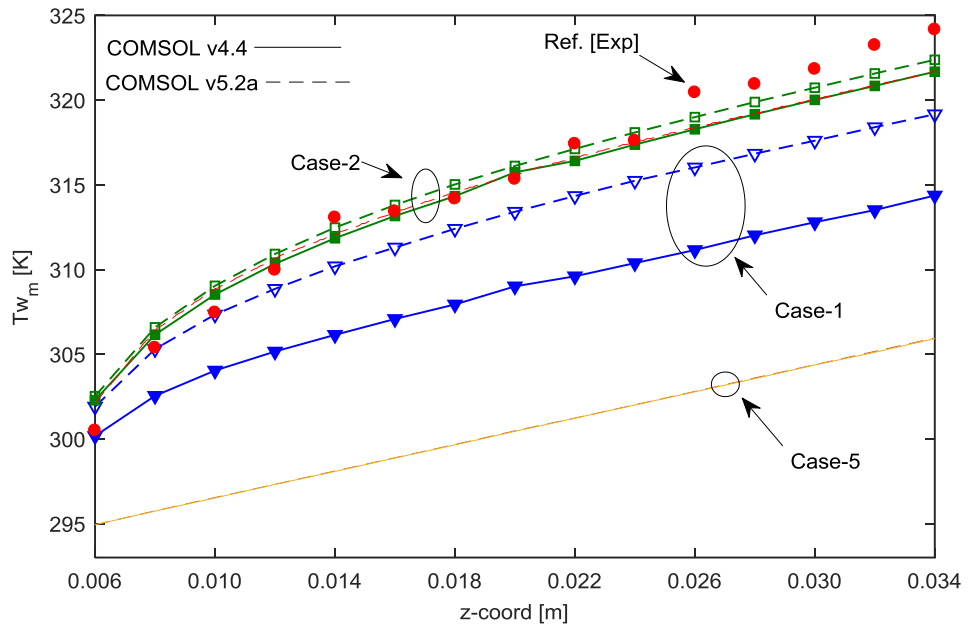


Figure B.1: Wall mean temperatures calculated with COMSOL v4.4 and v5.2a for test cases of stabilization methods.

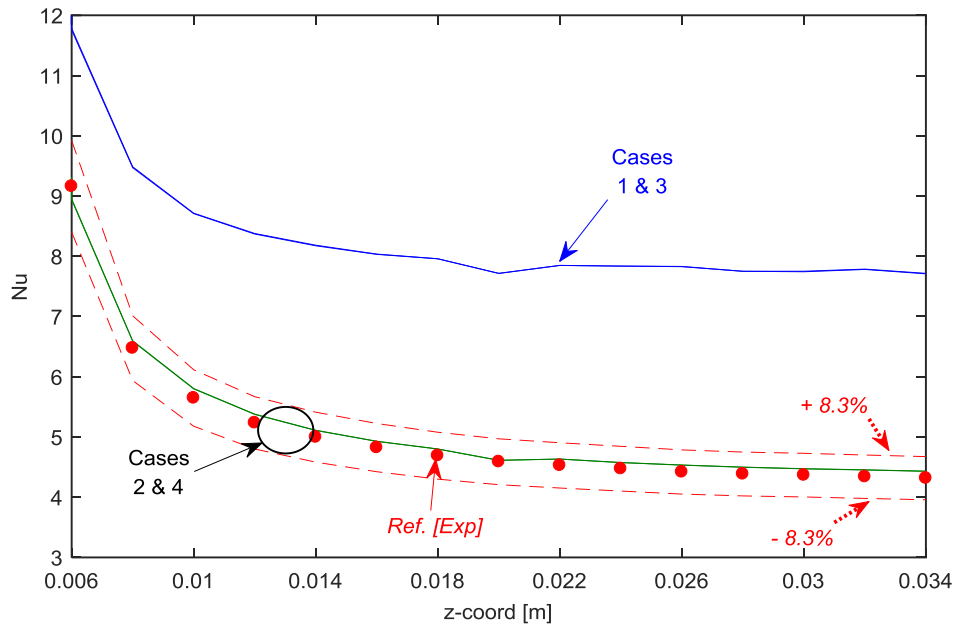


Figure B.2: Local  $Nu$  values for test cases of stabilization methods.

### B.3 EFFECT OF ELEMENT DISCRETIZATION

As the order of the elements increases, calculation points in a mesh element also increases and similar or better results can be obtained with less elements. However, computational cost also increases with the element order. Thus, a balanced point should be found. To observe the effect of element order on this specific problem 5 different mesh is used with linear (P1+P1-L), and second order (P2+P1 for flow and quadratic (Q) for temperature) elements. Relative tolerance in these simulations is set to  $10^{-3}$ , except *Case-4* in which it is set to  $10^{-6}$ . Mesh properties, solution times, and memory requirements are indicated in Table – (B.4) with the heated surface maximum temperature. In addition, wall mean temperature distribution is shown in Fig. (B.3).

Table B.4: Mesh properties and parameters for discretization comparison.

<i>Case</i>	<i>Discr.</i>	<i>Elem. #</i>	<i># of DOFs</i>	<i>S</i>	<i>CPU Time [s]</i>	<i>PM</i>	<i>VM</i>	<i>T<sub>max,HS</sub></i>
<b>1</b>	(a) P2+P1 - Q	316,352	3,136,202	I	3,552	16.28	16.51	324.706
	(b) P1+P1 - L		513,570	D	253	5.48	5.70	328.652
<b>2</b>	(a) P2+P1 - Q	649,767	6,328,442	I	7,977	31.53	31.91	324.793
	(b) P1+P1 - L		1,029,370	D	590	10.86	11.24	327.185
<b>3</b>	(a) P2+P1 - Q	1,287,106	10,588,290	I	9,497	47.46	61.22	324.898
	(b) P1+P1 - L		1,716,650	I	968	7.98	13.03	324.402
<b>4</b>	P1+P1 - L	7,559,401	7,289,865	I	14,072	29.21	29.61	325.237
<b>5</b>	P1+P1 - L	12,176,164	11,554,880	I	17,560	45.26	53.41	325.102
<b>S:</b> Solver <b>I:</b> Iterative <b>D:</b> Direct				<b>PM:</b> Physical Memory <b>VM:</b> Virtual Memory				

Similar to the mesh independence tests, coarser meshes with linear elements results lower wall mean temperatures at the beginning and higher over the rest of the microheaters (Cases 1b, 2b, 3b). As expected, with second order elements results that are more comparable can be obtained at the expense of memory, since the number of DOFs increases nearly six times (Cases 1a, 2a, 3a). However, it is obvious that on both cases, number of DOFs should be much enough for good resolution. Fine resolution also can be achieved linear elements with lower memory need but with longer computational time (Cases 4-5).

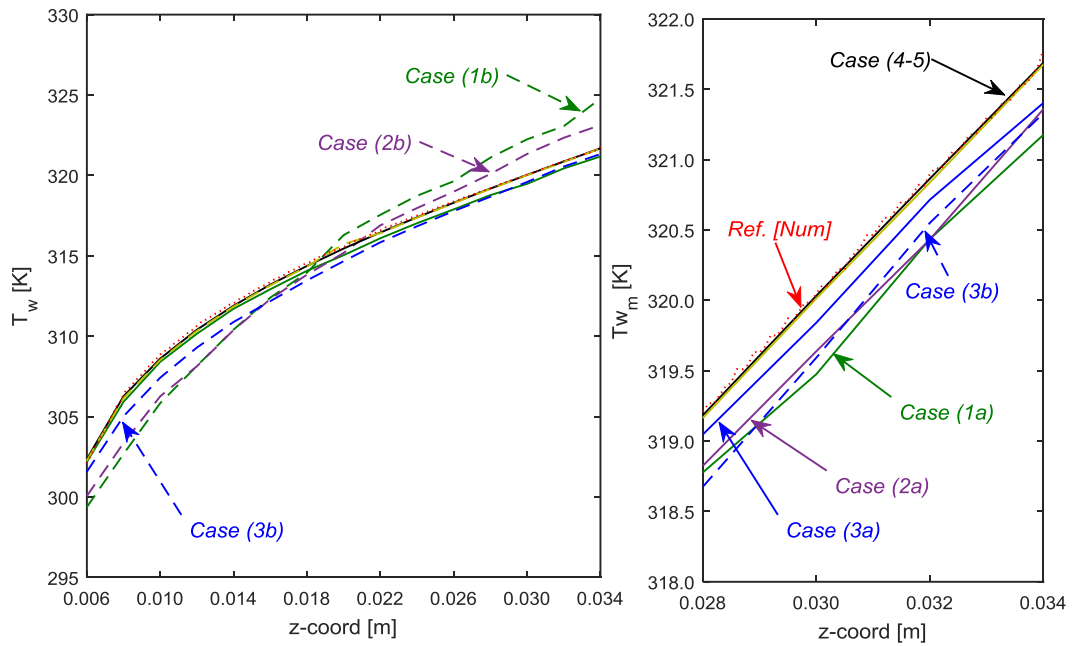


Figure B.3: Wall mean temperature distribution over the heated section for first and second order mesh elements.

#### B.4 EFFECT OF RELATIVE TOLERANCE

In many numerical studies, relative error tolerance is generally set to a value between  $10^{-3}$  and  $10^{-6}$ . In conventional sense, as the relative tolerance reduces, accuracy of the results increases up to a level. Meanwhile, computational cost also increases. To test its effect, three different meshes is used and each case is solved with both  $10^{-3}$  and  $10^{-6}$  relative tolerances by COMSOL v4.4. Number of DOFs, calculated  $Po$  values and heated surface maximum temperatures are summarized in Table – (B.5) with solution times. In *Case-I*, both of the previously mentioned consistent stabilizations are used to see the effects of relative tolerance on overdamped solution.

It is observed that for relatively coarser mesh, difference between the two results is more obvious, on the order of relative tolerance for  $Po$  and on the order of  $10^{-2}$  for maximum temperature. As the DOFs are increased, difference becomes miniscule for this specific problem. However, CPU times increases about two times at minimum, depending on the solver type and memory requirement. As stated before, physical RAM is extended to hard disk, which has much lower reading and writing speeds than RAM. With those results, it can be stated that, higher relative tolerances can be used for mesh independence studies to gain time if it does not change the nature of the solution, and main simulations can be done with lower relative tolerances for better accuracy.

Table B.5: Used cases for the relative tolerance tests and obtained results for 300 kW/m<sup>2</sup> effective heat flux and 1016 kg/(m<sup>2</sup>s) inlet mass flux.

<i>Case</i>	<i># of DOFs</i>	<i>Rel. Tol.</i>	<i>Solver</i>	<i>CPU Time [s]</i>	<i>Po</i>	<i>T<sub>max,HS</sub></i>
<b>1</b>	(a)	10 <sup>-6</sup>	Direct	12,450	17.845664	313.128954
		10 <sup>-3</sup>	Direct	3,122	17.842817	313.186499
<b>2</b>	(a)	10 <sup>-6</sup>	Iterative	14,072	16.136053	325.237023
		10 <sup>-3</sup>	Iterative	8,913	16.136025	325.237615
<b>3</b>	(a)	10 <sup>-6</sup>	Iterative	146,583	16.045549	325.101274
		10 <sup>-3</sup>	Iterative	17,560	16.045520	325.102202



## CURRICULUM VITAE

### PERSONAL INFORMATION

Surname, Name: Turgay, Metin Bilgehan  
Nationality: Turkish (TC)  
Date and Place of Birth: 11 May 1980, Sinop  
Marital Status: Engaged  
GSM: +90 543 515 6689  
E-mail: metinturgay@gmail.com

### EDUCATION

Degree	Institution	Year of Graduation
M.Sc.	METU Mechanical Engineering	2008
B.Sc.	Gazi University, Mechanical Engineering	2005
High School	Sinop Anadolu High School	1998

### WORK EXPERIENCE

Year	Place	Enrollment
2011-2013	EDEA Makina San. ve Tic. Ltd. Şti.	Research Engineer
2004 July-August	ALFA Makina Kazan Sanayi A.Ş.	Intern Engineering Student
2003 July	TEMSAN – Türkiye Elektromekanik Sanayi A.Ş.	Intern Engineering Student

## **FOREIGN LANGUAGES**

English

## **COMPUTER SKILLS**

MATLAB, COMSOL Multiphysics, CATIA V5, Debian GNU/Linux

## **PUBLICATIONS**

[1] M. B. Turgay, Effect of Surface Roughness in Microchannels on Heat Transfer, M.Sc. Thesis, Middle East Technical University, Ankara, Turkey, 2008.

[2] M. B. Turgay, and A. G. Yazıcıoğlu, Effect of surface roughness in parallel-plate microchannels on heat transfer, Numerical Heat Transfer, Part A, vol. 56, pp. 497-514, 2009.

[3] M. B. Turgay, A.G. Yazıcıoğlu, and S. Kakaç, Roughness effect on the heat transfer coefficient for gaseous flow in microchannels, Proc. of the ASME International Heat Transfer Conference 14, Washington DC, USA, Aug. 8-13, 2010.

[4] M. B. Turgay, and A. G. Yazıcıoğlu, Numerical simulation of fluid flow and heat transfer in a trapezoidal microchannel with COMSOL Multiphysics – A case study, *submitted to Numerical Heat Transfer, Part A for publication, NHT17/7475.*

## **PROJECTS**

[1] Sürekli ve Geçici Rejimde Mikrokanallarda Konveksiyonla Isı Transferi, TÜBİTAK 1001 Proje No: 106M076, 07/2006-07/2009, Bursiyer Öğrenci.

[2] Mikrokanallardaki Yüzey Pürüzlülüğünün Akışa ve Isı Transferine Etkisinin Üç Boyutlu Sayısal Analizi, BAP-03-02-2011-003, 01/01/2011-31/12/2011, Ana Araştırmacı.